Study of Shape Effect of Pd Promoted Ga_2O_3 Nanocatalysts for Methanol Synthesis and Utilization

By

Mr. Xiwen Zhou (BSc, MSc)

458063

Wolfson College

A dissertation submitted for the degree of Doctor of Philosophy at the

Inorganic Chemistry Laboratory, Department of Chemistry,

University of Oxford

2013

Study of Shape Effect of Pd Promoted Ga_2O_3 Nanocatalysts for Methanol Synthesis and Utilization

By

Mr. Xiwen Zhou (BSc, MSc)

458063

Wolfson College

Supervisor

Prof. S. C. Edman Tsang

Internal Assessor

Dr. Kylie Vincent

A dissertation submitted for the degree of Doctor of Philosophy at the

Inorganic Chemistry Laboratory, Department of Chemistry,

University of Oxford

2013

Table of contents

Table of contents i

Declaration ii

Dedication iii

Acknowledgements iv

Abstract vi

List of figures viii

List of tables xix

List of schemes xxi

List of symbols and abbreviations xxii

List of publications xxvii

Chapter 1 Introduction……...1

Chapter 2 Analytical techniques……...67

Chapter 3 Experimental.....…….....96

Chapter 4 Synthesis and characterization of morphologically different Ga_2O_3 particles.....……122

Chapter 5 Shape effect of Pd promoted Ga_2O_3 nanocatalysts for methanol synthesis from CO_2 hydrogenation……150

Chapter 6 Shape effect of Pd promoted Ga_2O_3 nanocatalysts for H_2 evolution from methanol photodecomposition……...186

Chapter 7 Conclusion and perspective.....…….....221

Declaration

I confirm that the presented research in this thesis is from my own work unless stated otherwise and the use of all materials from other sources has been properly and fully acknowledged.

Xiwen Zhou

Dedication

To my parents

Acknowledgements

First of all, I would like to thank Prof. S. C. Edman Tsang, my supervisor, for providing me the excellent opportunity to work in his laboratory. I am very grateful for his help, discussion, and guidance on my research project throughout my D.Phil. study. I like to thank University of Oxford and my college Wolfson College for the support during the course of pursuing my D.Phil. study. I also would like to thank my college advisor Prof. Christina Redfield for her advice and support.

In addition, my research work presented in this thesis would not have been possible without the help and assistance by the following people and their expertise. I would like to thank Prof. Xinlin Hong and Mr. Ziyan Zeng (Wuhan University, China) for their assistance in some catalytic testings and SEM images; Dr. Phil Wisemen (ICL, University of Oxford) for the training on the XRD; Dr. Tong Li (Materials, University of Oxford) and Mr. Abdul Mahadi in our group for their assistance in TEM analysis; Dr. Jeffery Harmer (ICL, University of Oxford) and Dr. Qin Lu (US Naval Research Laboratory) for the training in EPR; Dr. Kai Man Kerry Yu in our group for his technical support on training of GC, TPR, BET and testing equipments; Prof. John. S. Foord and Dr. Jingping Hu (PTCL, University of Oxford) for the XPS analysis; Mr. Feng Xu (ICL, University of Oxford) for the help in CV and CO stripping analysis; Mr. Jin Qu (ICL, University of Oxford) for the DFT calculations and modeling; Dr. Lin Ye and Prof. Heyong He (Fudan University, China) for ssNMR characterization and CO_2 TPD; Dr. Waiming Kwok and his group (Hong Kong Polytechnic University)

for the PL and TRPL analysis; Mr. Weiran Zheng, Miss. Tiantian Jia, Mrs. Amy Kolpin and Mr. Aaron Lau (ICL, University of Oxford) for useful discussions; The Royal Society of Chemistry for the permission to use content from my published paper; Mr. Ashleigh Hewson for lab and equipment repairing service; Mrs. Terri Adams for glassblower service; Mr. Bill Thompson, Mr. Leigh Bennett and Mr. Levi Dash for stores assistance; Mrs. Pam Cox and Miss. Aga Borkowska for administrative assistance; All other staff in the Chemistry Department and Wolfson College for their help during the course of my D.Phil. Study. Last but not the least, apart from our group members mentioned above, I would like to spread my thanks to all the other members within the Tsang group at present and past, for their help and support throughout my D.Phil. study.

Abstract

The area of methanol synthesis and utilization has been attracting research interests due to its positive impact on the environment and also from energy perspectives. Methanol synthesis from CO_2 hydrogenation not only produces methanol which is a key platform chemical and a clean fuel, but can also recycle CO_2 which is one of the major greenhouse gases causing global warming. As a mobile energy carrier (particularly as a hydrogen carrier), methanol is a versatile molecule which is able to generate H_2 via its decomposition. Catalysis plays a decisive role in the success of both methanol synthesis from CO_2 hydrogenation and its reverse decomposition reaction. Pd/Ga_2O_3 binary catalyst has recently been identified as an active catalyst for the methanol synthesis reaction. In this thesis, it is reported the shape effect of Pd promoted Ga_2O_3 for this reaction. The catalytic H_2 evolution from methanol photodecomposition has also been studied over these catalysts. Three shapes of Ga_2O_3 nanomaterials (i.e. rod and plate β-Ga_2O_3, and particle γ-Ga_2O_3) have been synthesized, followed by doping with Pd metal to form corresponding Pd/Ga_2O_3 nanocatalysts.

It was found that a (002) polar Ga_2O_3 surface which was dominantly presented on the plate form was unstable, giving a higher degree of oxygen defects and mobile electrons in the conduction band than the other non-polar (111) and (110) surfaces of the rod form. It was shown that a significantly stronger metal support interaction was found between the (002) polar Ga_2O_3 on the plate form and Pd, which gave higher

methanol yield and selectivity.

For methanol photodecomposition, it was found that, for pure Ga_2O_3 catalysts of different shapes, the plate form with a highest degree of defects (unstable polar surface) could encourage a non-radiative catalytic recombination of electron and hole pairs upon irradiation, hence giving a highest photocatalytic activity for H_2 production. Once Pd was introduced onto these oxide surfaces, it was noted that there was a fast and readily electron transfer from the conduction band of Ga_2O_3 to Pd due to the formation of a Schottky junction between the two materials. This produces metal sites for hydrogen production and further enhances the rate of the photocatalytic reaction over the radiative recombination of excitons. However, it was also found that at higher Pd content (>1%), the significantly shortened exciton lifetimes reduce the catalytic rate hence giving an overall volcanic response of activity to increasing Pd content for each shape of Ga_2O_3. At the higher Pd content, the plate form appeared to sustain a longer lifetime for photocatalysis compared to the other forms at the equivalent Pd loading.

Keywords: Heterogeneous catalysis, Ga_2O_3, Pd/Ga_2O_3, CO_2 hydrogenation, photodecomposition, methanol, shape effect, polar surface, non-polar surface, strong metal support interaction.

List of figures

Figure 1.1 An illustration of a typical heterogeneous catalytic process.

Figure 1.2 A volcano plot illustrating the Sabatier principle. Catalytic rate is maximum at optimum adsorption strength. On the left of the Sabatier maximum, the rate of reaction has a positive order in reactant concentration, and on the right of the Sabatier maximum the rate has a negative order. Reprinted with permission from ref. 12, copyright 2010 Wiley-VCH.

Figure 1.3 Bottom up versus top down approach for the preparation of nanostructures. Reprinted with permission from ref. 20, copyright 2008 John Wiley & Sons, Inc.

Figure 1.4 A typical reactor for reacting solids under a gas atmosphere. Reprinted with permission from ref.19, copyright 2005 Taylor & Francis Group, LLC.

Figure 1.5 Typical HAADF-STEM images of three different colloids: ((a), (b)) are colloids showing Au nanoparticles with mean diameter of 1.3 nm; ((c), (d)) depict colloids with mean diameter of 2.1 nm; ((e), (f)) colloids with mean diameter of 6.9 nm. Due to the Z-contrast, Au particles appear as bright spots. Reprinted with permission from ref. 40, copyright 2008 Springer Science + Business Media, LLC.

Figure 1.6 The CO_2 formation rate on rutile TiO_2 as a function of bandgap.

Reprinted with permission from ref. 41, copyright 2005 Springer Science + Business Media, Inc.

Figure 1.7 Illustrative bimetallic surface configurations with one monolayer of 3d metal (red) deposited on Pt (111) substrate (grey). Reprinted with permission from ref. 45, copyright 2012 American Chemical Society.

Figure 1.8 A Plot of rates of room temperature formic acid decomposition on Ag/Pd core-shell with different ratios of Ag:Pd (1:1 is the optimal ratio) (a); Production of CO_2+H_2 by decomposing formic acid at room temperature, compared with an ordinary Ag/Pd alloy and Pd only (b). Modified with permission from ref. 58, copyright 2011 Nature Publishing Group.

Figure 1.9 A summary of different shapes of various metal nanocrystals that have been achieved. Reprinted with permission from ref. 14, copyright 2009 Wiley-VCH.

Figure 1.10 TEM images of Ag nanoparticles: truncated triangular nanoplates (a), near-spherical nanoparticles (b) and nanocubes (c), and the insets showing the SEM images (left) and selected area electron diffraction patterns (right); The catalytic performance of the Ag nanoparticles for oxidation of styrene with TBHP (tert-butyl hydroperoxide) (d). Modified with permission from ref. 59, copyright 2006 Wiley-VCH.

Figure 1.11 TEM images of Pt nanocubes (a) and nanopolyhedra (b), with scale bar of 20 nm; A scheme illustrates adsorption and stepwise

hydrogenation of pyrrole to n-butylamine on Pt surface. (blue atom stands for nitrogen) (c). Modified with permission from ref. 66, copyright 2009 American Chemical Society.

Figure 1.12 Two illustrative atomistic models showing polar (001) surface (a) and non-polar (100) surface (b) of ZnO crystals. Both of the images are side views.

Figure 1.13 TEM images of Co_3O_4 nanoparticles (a) and nanorods (b); CO conversion as a function of time on stream over Co_3O_4 nanoparticles and nanorods (c). Modified with permission from ref. 75, copyright 2009 The Royal Society of Chemistry.

Figure 1.14 Normalized fluorescence intensities on clean SCNSs TiO_2 (calcined to remove capped F atoms), F atoms capped SCNSs TiO_2 (as synthesized), and Degussa P25 TiO_2. Reprinted with permission from ref. 81, copyright 2009 American Chemical Society.

Figure 1.15 Global demand for methanol from 1990 to 2007. Reprinted with permission from ref. 84, copyright 2009 Wiley-VCH.

Figure 1.16 Schematic photoexcitation in a semiconductor solid followed by deexcitation processes. Reprinted with permission from ref. 96, copyright 1995 American Chemical Society.

Figure 1.17 The overall energy profile and reaction pathway for 1,3-butadiene hydrogenation to butene on {203} facets of the AuOH/t-ZrO_2 catalyst. IS=initial state, TS=transition state, M=intermediate and FS=final

state. The atom colors are red (O), blue (Zr), yellow (Au), light grey (H) and Dark grey (C). Reprinted with permission from ref. 99, copyright 2006 Wiley-VCH.

Figure 2.1 The illustrative basic phenomenon of physical techniques. The incident beam is defined by arrows pointed towards the sample, and the emitted beam is defined pointed away from the sample. Reprinted with permission from ref. 1, copyright 2012 Wiley-VCH.

Figure 2.2 An illustration of interfered Bragg reflection.

Figure 2.3 Layout of the optical components in a basic TEM.

Figure 2.4 An illustration of the spin state energy splitting in the presence of magnetic field and the resonance when sweeping the field.

Figure 2.5 A typical layout of an EPR spectrometer.

Figure 2.6 Schematic components in a typical XPS spectrometer (UHV system is not included in the figure). Reprinted with permission from ref. 1, copyright 2012 Wiley-VCH.

Figure 2.7 An illustration of Photoelectron emission upon X-ray irradiation on solid catalyst (exemplified by metal). Modified with permission from ref. 1, copyright 2012 Wiley-VCH.

Figure 2.8 A picture showing a typical TPR instrument.

Figure 2.9 Illustrative processes of spontaneous fluorescence (a) and phosphorescence (b).

Figure 2.10 Set up of optical components in a conventional

spectrophotofluorimeter. 1, lamp; 2, monochromator; 3, cell; 4, sample; 5, light trap; 6, mirror; 7, filters; 8, monochromator; 9, detector. Reprinted with permission from ref. 1, copyright 2012 Wiley-VCH.

Figure 2.11 A typical sequence of time-resolved photoluminescence measurements. Reprinted with permission from ref. 1, copyright 2012 Wiley-VCH.

Figure 2.12 Components of an illustrative cyclic voltammetry system (C: counter electrode; W: working electrode; R: reference electrode). Modified with permission from ref. 16, copyright 1993 Wiley-VCH.

Figure 2.13 A schematic diagram showing components in a typical gas chromatographic system. Reprinted with permission from ref. 17, copyright 2009 John Wiley & Sons, Inc.

Figure 4.1 PXRD pattern of the rod form orthorhombic GaOOH.

Figure 4.2 TEM images of the GaOOH nanorods.

Figure 4.3 PXRD pattern of the monoclinic rod form Ga_2O_3.

Figure 4.4 TEM image, lattice fringes and electron diffraction pattern at the edge region of a rod Ga_2O_3 (a) and SEM image of Ga_2O_3 rods (b).

Figure 4.5 Raman spectrum of the rod form β-Ga_2O_3.

Figure 4.6 UV-Vis absorption spectrum of the rod Ga_2O_3 (a) and corresponding plot used to determine its bandgap value (b).

Figure 4.7 PXRD pattern of the $KGaO_2$ Powder.

Figure 4.8 TEM image of the GaOOH nanoplates (a) and a higher magnification image (b).

Figure 4.9 PXRD pattern of the Ga_2O_3 nanoplates.

Figure 4.10 TEM image, lattice fringes and electron diffraction pattern at edges of plate Ga_2O_3 (a) and SEM image of plate Ga_2O_3 (b).

Figure 4.11 Raman spectrum of the plate form β-Ga_2O_3.

Figure 4.12 UV-Vis absorption spectrum of the plate Ga_2O_3 (a) and corresponding plot for the determination of its bandgap value (b).

Figure 4.13 PXRD pattern (a) and TEM image of the prepared particle form Ga_2O_3 (b).

Figure 4.14 Raman spectrum of γ-Ga_2O_3 particles.

Figure 4.15 UV-Vis absorption spectrum of the particle form Ga_2O_3 (a) (blue line is the measured spectrum, and two dotted red lines are fitted curves) and corresponding plot used to determine its bandgap value (b).

Figure 4.16 PXRD patterns of prepared γ-Ga_2O_3 under various reaction time.

Figure 4.17 PXRD patterns of γ-Ga_2O_3 prepared with different oleic acid/Ga^{3+} ratios.

Figure 4.18 PXRD patterns of γ-Ga_2O_3 prepared with different oleylamine/Ga^{3+} ratios (a) and a representative TEM image with oleylamine/Ga^{3+} ratio at 8 (b).

Figure 4.19 (a) Comparison of PXRD results of γ-Ga_2O_3 (red curve: oleic acid/Ga^{3+}=1 and oleylamine/Ga^{3+}=1; black curve: oleic acid/Ga^{3+}=1);

(b) PXRD results of γ-Ga_2O_3 prepared with various oleyamine/oleic acid molar ratios, with oleic acid/Ga^{3+} =1 for all; (c) A representative TEM image of γ-Ga_2O_3 prepared with oleylamine/oleic acid ratio at 1.

Figure 5.1 (a) Comparison of PXRD patterns of rod and plate monoclinic β-Ga_2O_3; (b) PXRD patterns of Ga_2O_3 rod with Pd doping from 0-5 wt %; (c) PXRD patterns of Ga_2O_3 plate with Pd doping from 0-5 wt%.

Figure 5.2 (a) TEM image of a rod Ga_2O_3 nanocrystal (an insert represents the Fourier transform electron diffraction pattern near the edge region of the crystal); (b) lattice fringe separation of 2.58 Å with (111) facet on rod Ga_2O_3 surface; (c) TEM image of 5% Pd/rod Ga_2O_3; (d) enlarged TEM image of 5% Pd/rod Ga_2O_3.

Figure 5.3 (a) TEM image of plate Ga_2O_3 nanocrystals (an insert represents the Fourier transform electron diffraction pattern near the edge region of a crystal); (b) lattice fringe separation of 2.81 Å with (002) facet on plate Ga_2O_3 surface; (c) TEM image of 5% Pd/plate Ga_2O_3; (d) enlarged TEM image of 5% Pd/plate Ga_2O_3.

Figure 5.4 Comparison of CO_2 conversion (a), methanol selectivity (b) and methanol yield (c) of rod and plate Ga_2O_3 forms, each with different Pd loading levels.

Figure 5.5 (a) CV curves of rod Ga_2O_3 and (b) CV curves of plate Ga_2O_3 with

and without Pd loadings, scanned from 0.0 V to 1.2 V (vs. SHE) at 50 mV/s. The stable 20th cycle was recorded for each sample.

Figure 5.6 Comparison of CV curves of rod and plate forms Ga_2O_3 at (a) 1% Pd, (b) 2% Pd and (c) 5% Pd; representative consecutive CV of all 20 cycles for 5% Pd on rod (d) and plate (e) Ga_2O_3. All the measurements shown were scanned from 0.0 V to 1.2 V (vs. SHE) at 50 mV/s.

Figure 5.7 Comparison of the first cycle of CO stripping curves of rod and plate forms Ga_2O_3 doped with 5% Pd (a); consecutive CO stripping profiles of rod (b) and plate (c) Ga_2O_3 with 5% Pd loading. Measurements were scanned from 0.0 V to 1.2 V (vs. SHE) at 50 mV/s.

Figure 5.8 EPR spectra of rod and plate Ga_2O_3.

Figure 5.9 TPR profiles of rod Ga_2O_3 with and without 5% Pd (a); plate Ga_2O_3 with and without 5% Pd (b); TPR comparison of 5% Pd on rod and plate Ga_2O_3 (c).

Figure 5.10 CO_2 TPD profiles of pure rod and plate forms of Ga_2O_3.

Figure 5.11 XPS data of O 1s for rod form Ga_2O_3 with and without 5% Pd (a); O 1s for plate form Ga_2O_3 with and without 5% Pd (b); comparison of O 1s for rod and plate form Ga_2O_3 with 5% Pd (c).

Figure 5.12 XPS data of Ga 2p 3/2 on 5% Pd/plate Ga_2O_3 (a); Pd 3d 3/2 and Pd 3d 5/2 data for both forms of Ga_2O_3 with 5% Pd loading (b).

Figure 5.13 Atomistic model showing (110) non-polar surface of Ga_2O_3 (O: red,

Ga: blue) (a); DOS of (110) surface in comparison with bulk Ga_2O_3 (b); DOS of (110) surface with orbital contributions from O (c) and Ga (d).

Figure 5.14 Atomistic model showing (111) non-polar surface of Ga_2O_3 (O: red, Ga: blue) (a); DOS of (111) surface in comparison with bulk Ga_2O_3 (b); DOS of (111) surface with orbital contributions from O (c) and Ga (d).

Figure 5.15 Atomistic models showing (002) polar surfaces of Ga_2O_3 with oxygen termination (a) and gallium termination (b) (O: red, Ga: blue); DOS of (002) polar surfaces with O termination (c) and Ga termination (d) in comparison with bulk Ga_2O_3; O orbital contributions to DOS of O terminated (e) and Ga terminated (f) (002) polar surfaces; Ga orbital contributions to DOS of O terminated (g) and Ga terminated (h) (002) polar surfaces.

Figure 6.1 H_2 evolved from methanol photodecomposition on rod, plate and particle Ga_2O_3 with various Pd loadings. All reaction time was 5 hours.

Figure 6.2 Results of H_2 production from methanol decomposition at different reaction time over the selected 0.5% Pd/γ-Ga_2O_3 particle catalyst.

Figure 6.3 Results of methanol concentration effect on H_2 evolution from methanol decomposition over 5 hours. Selected catalyst: 0.5% Pd/γ-Ga_2O_3 particles.

Figure 6.4 PXRD patterns of 0.5% Pd doped Ga_2O_3 before (a) and after (b) reaction; PXRD patterns of particle Ga_2O_3 with Pd loadings before reaction (c).

Figure 6.5 TEM image (a) and enlarged image (b) of 0.5% Pd/rod Ga_2O_3. Typical high resolution TEM images of the edges of 0.5% Pd/rod Ga_2O_3 ((c), (d)).

Figure 6.6 TEM image (a) and enlarged image (b) of 0.5% Pd/plate Ga_2O_3. A representative high resolution TEM image near the edge of 0.5% Pd/plate Ga_2O_3 (c).

Figure 6.7 TEM image (a) and enlarged image (b) of 0.5% Pd/particle Ga_2O_3.

Figure 6.8 The absorption EPR data of rod (a), plate (b) and particle (c) forms Ga_2O_3.

Figure 6.9 Raman spectra of rod (a), plate (b) and particle (c) Ga_2O_3 with Pd loadings.

Figure 6.10 UV-Vis spectra of rod (a), plate (b) and particle (c) Ga_2O_3 with Pd loadings.

Figure 6.11 ^{31}P ssNMR spectra of four pure Ga_2O_3 samples.

Figure 6.12 (a) The polar Ga_2O_3 (002) with two types of surface Ga ions, namely, octahedral gallium ions and tetrahedral gallium ions; the calculated Bader charge densities are: Ga1 (oct) 11.1862; Ga2 (tetra) 11.2344. The average Bader charge density of Ga_2O_3 (002) is 11.2103 (left: sideview; right: topview; blue: Ga ion; red: O ion).

Figure 6.12 (b) The non-polar Ga_2O_3 (111) with four types of surface Ga ions, namely, octahedral gallium ions and tetrahedral gallium ions; the calculated Bader charge densities are: Ga1 (tetra) 11.2282; Ga2 (oct) 11.1775; Ga3 (oct) 11.1575; Ga4 (tetra) 11.2074. The average Bader charge density of Ga_2O_3 (111) is 11.1926 (left: sideview; right: topview; blue: Ga ion; red: O ion).

Figure 6.13 Static photoluminescence (PL) spectra ((a)-(c)) and PL kinetic decay curves ((d)-(f)) obtained with excitation at 255 nm in solid state of Ga_2O_3 rod ((a), (d)), plate ((b), (e)), and particle ((c), (f)) without or with varied Pd loadings.

Figure 6.14 Comparison of luminescence decay profiles obtained with 255 nm excitation of solid state Ga_2O_3 rod (□), plate (Δ) and particle (○) without (a) or with increasing Pd loadings ((b),(c)). The solid lines are the fittings of experimental data.

Figure 6.15 Time-resolved photoluminescence spectra recorded at the denoted time intervals after excitation at 255 nm for rod ((a)-(c)), plate ((d)-(f)) and particle ((g)-(i)) Ga_2O_3 without and with varied Pd loadings.

Figure 6.16 Static photoluminescence spectra recorded with 255 nm excitation of solid state Ga_2O_3 in rod, plate and particle forms.

List of tables

Table 3.1 Variation of oleic acid/Ga^{3+} molar ratio for the synthesis of γ-Ga_2O_3 nanoparticles.

Table 3.2 Variation of oleylamine/Ga^{3+} molar ratio for the synthesis of γ-Ga_2O_3 nanoparticles.

Table 3.3 Variation of oleylaime/oleic acid molar ratio for the synthesis of γ-Ga_2O_3 nanoparticles (with oleic acid/Ga^{3+} ion ratio kept at 1).

Table 3.4 Details of the preparation of catalysts for the photoreaction.

Table 3.5 Methanol photodecomposition on commercial Ga_2O_3 and commercial TiO_2 P25 catalysts doped with various metals (reaction time: 5 hours).

Table 5.1 Summary of catalytic performance of Pd loaded Ga_2O_3 nanocatalysts.

Table 5.2 The quantitative spin number obtained over two pure forms of Ga_2O_3.

Table 5.3 Summary of CO_2 TPD data.

Table 5.4 Summary of catalytic performance of 5% Pd on rod and plate Ga_2O_3 crystals in comparison with Cu on rod and plate ZnO.

Table 6.1 Summary of methanol photodecomposition results on three different forms of Ga_2O_3 (i.e. β-Ga_2O_3 rods, β-Ga_2O_3 plates and γ-Ga_2O_3 particles) and with various amounts of Pd. All reaction time was 5 hours.

Table 6.2 Summary of control experiments (reaction time: 5 hours, at 253.7 nm).

Table 6.3 Effect of reaction time on methanol photodecomposition. Selected

catalyst: 0.5% Pd/γ-Ga_2O_3 particles.

Table 6.4 Effect of methanol concentration on methanol photodecomposition (total volume of liquid mixture: 100 mL; reaction time: 5 hours; selected catalyst: 0.5% Pd/γ-Ga_2O_3 particles).

Table 6.5 Methanol photodecomposition on commercial β-Ga_2O_3 and commercial TiO_2 P25 catalysts doped with various metals (1 wt% metal for each catalyst; reaction time: 5 hours; the UV at 253.7 nm, unless indicated).

Table 6.6 Summary of bandgap values of Ga_2O_3 with and without Pd.

Table 6.7 Kinetic analysis of ns-TRPL decay profiles (τ: time constant; a: associated amplitude).

List of schemes

Scheme 5.1 Electronic levels match of Pd-Ga_2O_3 and Cu-ZnO pairs for SMSI.

List of symbols and abbreviations

A	Absorbance
B_0	Magnetic field (or magnetic flux density)
CO_{ad}	Adsorbed CO
d_{hkl}	Interplanar spacing of (hkl) lattice plane where h, k, l are Miller indices.
$e\Phi_{spec}$	Work function of XPS spectrometer
E_B	Electron binding energy
E_g	Bandgap energy
E_{kin}	Electron kinetic energy
g	Intrinsic factor of a paramagnetic sample
ΔG	Change in Gibbs free energy
hν	Light energy
ΔH_{ad}	Change in enthalpy of adsorption
ΔH_{298K}	Change in enthalpy of reaction at 298 K
M_s	Electron spin quantum number
Q_{co}	Charge for CO desorption
R	Reflectance
S	Scattering coefficient
S_{BET}	Surface area measured by the Brunauer−Emmett−Teller method
μ_B	Bohr magneton

λ	Wavelength
τ	Time constant
τ_{av}	Average time constant
AES	Auger electron spectroscopy
BET	Brunauer−Emmett−Teller
CB	Conduction band
CCD	Charge coupled device
CV	Cyclic voltammetry
CVD	Chemical vapor deposition
CW-EPR	Continuous wave-electron paramagnetic resonance
DFT	Density functional theory
DI	Deionized water
DME	Dimethyl ether
DOS	Density of states
EAS	Electrochemically active surface
ED	Electron diffraction
EPR	Electron paramagnetic resonance
FAT	Fixed analyzer transmission
FID	Flame ionization detector
FTIR	Fourier transform infrared spectroscopy
GGA	Generalized gradient approximation
GHG	Greenhouse gas

HAADF-STEM	High angle annular dark field scanning transmission electron microscopy
HPLC	High-performance liquid chromatography
HRTEM	High resolution transmission electron microscopy
ICCD	Intensified charge coupled device
IMP	2-Isopropul-6-methyl-4-pyrimidinol
IRF	Instrument response function
ISC	Intersystem crossing
KE	Kinetic energy
MAS	Magic angle spinning
MM	Molecular mechanics
MSI	Metal support interaction
NHE	Normal hydrogen electrode
NIR	Near infrared
OPA	Optical parametric amplifier
ORR	Oxygen reduction reaction
PAW	Projector-augmented wave
PBE	Perdew–Burke–Ernzerhof
PL	Photoluminescence
ppb	Parts per billion
ppm	Parts per million
PTFE	Polytetrafluoroethylene

PVP	Polyvinyl pyrrolidone
PXRD	Powder X-ray diffraction
RWGS	Reverse water gas shift
SAED	Selected area electron diffraction
SCE	Saturated calomel electrode
$SCNS_S$	Single crystal nanosheets
SE	Semiempirical
SEM	Scanning electron microscopy
SHE	Standard hydrogen electrode
SMSI	Strong metal support interaction
ssNMR	Solid state nuclear magnetic resonance
s.t.p.	Standard temperature and pressure
TA	Terephthalic acid
TBHP	Tert-butyl hydroperoxide
TCD	Thermal conductivity detector
TEM	Transmission electron microscopy
TMP	Trimethylphosphine
TOA	Trioctylamine
TOF	Turnover frequency
TPDRO	Temperature programmed desorption/ reduction/oxidation
TPR/D	Temperature programmed reduction/desorption
TPR/D-MS	Temperature programmed reduction/desorption coupled with mass

	spectroscopy
TPR/D-IR	Temperature programmed reduction/desorption coupled with infrared spectroscopy
TRPL	Time-resolved photoluminescence
UHV	Ultra high vacuum
UVA	Ultraviolet A
UVC	Ultraviolet C
UV-Vis	Ultraviolet-visible
VASP	Vienna ab initio simulation package
VB	Valence band
v/v	Volume to volume
w/w	Weight to weight
XPS	X-ray photoelectron spectroscopy
XRD	X-ray diffraction

List of publications

1. X. Zhou, J. Qu, F. Xu, J. Hu, J. S. Foord, Z. Zeng, X. Hong, and S. C. E. Tsang, *Chem. Commun.*, 2013, **49**, 1747-1749.
2. Y. Zhao, X. Zhou, L. Ye and S. C. E. Tsang, *Nano Reviews*, 2012, **3**, 17631 (p1-p11).

Chapter 1 Introduction

Chapter 1 Introduction 1

1.1 Catalysis 3

1.1.1 Classification of catalysis 5

1.2 Heterogeneous catalysis 7

1.2.1 Adsorption on catalyst surface 8

1.2.2 Activity, selectivity and catalyst deactivation 10

1.2.3 Support effect 12

1.3 Nanoparticle /catalyst synthesis and manipulation 13

1.3.1 Methods for nanoparticle fabrication 15

1.3.2 Methods for preparation of heterogeneous catalysts 19

1.3.3 Nanoparticle manipulations 21

1.4 Shape effect of metal oxide in heterogeneous catalysis 36

1.4.1 Polar surface enhanced shape dependent catalysis 40

1.4.2 Non-polar surface enhanced shape dependent catalysis 43

1.5 Methanol synthesis from CO_2 hydrogenation 45

1.5.1 Overview 45

1.5.2 Studies on catalyst development 47

1.6 Photocatalytic decomposition of methanol for H_2 evolution 51

1.6.1 Overview 51

1.6.2 Studies on catalyst development 53

1.7 Computational approach in heterogeneous catalysis.....54

1.7.1 DFT approach in heterogeneous catalysis 54

1.8 Project objectives 56

1.9 Thesis outline 57

1.10 References.....59

1.1 Catalysis

Catalysis makes an extremely important contribution to our modern industrial economy. Without it life today would be quite different from what we see around us. Currently, it is estimated that more than 90% of the global chemical manufacturing processes involve catalysis at one stage or another.[1,2] As one of the vital technologies in our modern world, we rely on effective catalysis to produce essential materials such as plastics, fertilizers, fabrics, medicines, fuels and even functioning parts of our own bodies.[1] Therefore, it is no doubt that catalysis plays a key role for today's economic and societal prosperities across the world. The catalysis directed research made by the world's scientific communities has been growing rapidly during the past decades, and will continue to contribute to the advancement of understanding and employment of catalysis.

The word "catalysis" (meaning "loosening down" in Greek) was first introduced by Swedish chemist Berzelius in 1836. Later in 1885, Armstrong proposed the term "catalyst".[3] Based on these pioneering endeavors, Ostwald gave the definition of catalyst which is a substance that increases the rate of attainment of chemical equilibrium without itself undergoing chemical change.[3,4] There is no change in thermodynamic equilibrium, but merely accelerates the rate for achieving this equilibrium, by lowering down the activation barrier of the reactions. In 1813, the first catalytic phenomenon was discovered by Thenard. He noted the dissociation of ammonia occurs in contact with various metals.[5] Since the early start of the 19th century, the experimental findings of catalysis have accumulated rapidly and

instigated continuous research interests among many scientists. During the progress of catalysis, some milestone developments, which have brought profound societal changes, are worth highlighting:

(1) The Haber-Bosch process of producing ammonia from nitrogen and hydrogen in the presence of a reduced magnetite (Fe_3O_4) catalyst (1909).

(2) The Fischer-Tropsch process of converting syn-gas to hydrocarbons (1938).

(3) Catalytic hydrogenation of oils and fats into production of foodstuffs using metallic nickel catalyst by Norman (1901).

(4) Hydrocarbon catalytic cracking by synthetic zeolite catalyst demonstrated by Plank and Rosinsky (1964).

(5) Ziegler-Natta polymerization permits the production of polyethylene and crystalline stereoregular polypropylene by using a mixture of aluminum trialkyls and, as the key component of the Ziegler-Natta catalyst, titanium chloride ($TiCl_3$) (1960).[2]

With the development of industry and economy, some other major themes in catalysis have emerged to bring societal attentions. Many of these reflect the growing concern and commitment to protecting the environment and tackling energy shortage, aiming for sustainable development and growth of human prosperity. Therefore, the global catalysis research and industrial communities spend huge effort on tackling these challenges.

1.1.1 Classification of catalysis

Catalysis is a very comprehensive topic and it is classified by different criteria including the phases of reactants and catalysts, the effects of catalysts, the activation ways of catalysis, applications of catalysts, etc. A generally accepted classification of catalysis is as follows:

(1) Homogeneous catalysis.

(2) Heterogeneous catalysis.

(3) Biocatalysis.

Homogeneous catalysis occurs with both the reagents and catalysts present in the same phase. This normally means that they present as solutes in a liquid reaction mixture. Many important homogeneously catalyzed reactions are carried out by using organometallic compounds and coordination complexes. The scope of homogeneous catalysis ranges from hydrogenation, oxidation and a host of other catalytic processes.[4] One classic example of homogeneous catalysis is alkene metathesis reactions. The reactions are now popularly catalyzed by a homogeneous ruthenium alkylidene compound (known as Grubb's catalyst[4,6]) that enables a significant control on production distribution. The key step of the reaction mechanism is to dissociate a ligand from the ruthenium metal center to enable an alkene molecule to coordinate. Although homogeneous catalysis is attractive due to its high selectivity towards the target products, the big challenge and difficulty of product separation from the catalyst is the major limitation. The less than ten percent of the catalysis market share by homogeneous catalysis also reflects this disadvantage which prevents it from being

widely and industrially utilized.

Heterogeneous catalysis is a fascinating alternative which is extensively applied in industries. It has much better economic impact than its homogeneous counterpart, and accounts for more than 80% of the global market of catalysis. Heterogeneous catalysis is carried out by having catalysts and reactants in different phases, which typically involves applying solid catalysts to reactants in either the liquid or gas phase.[7] There are many advantages of using heterogeneous catalysis, two of which are worth highlighting particularly. Firstly, many of these solid heterogeneous catalysts are robust at high temperatures and therefore they show great tolerance towards a wide range of operating conditions,[4] particularly some harsh conditions. The second very attractive feature is that heterogeneous catalysis does not require extra steps to separate products from catalysts, leading to more efficient and environmentally friendly processes. Regarding these advantages, heterogeneous catalysis is widely used in industries and plays an essential role in the success of many important reactions, such as hydrogenations, ammonia synthesis, sulfur dioxide oxidation,[4] catalytic cracking reactions, Fischer-Tropsch synthesis, etc. The more detailed aspects regarding heterogeneous catalysis will be introduced later in this chapter, because of the presented study in this D.Phil. research project being in the field of heterogeneous catalysis.

In biocatalysis, enzymes are used to catalyze reactions. Enzyme catalysis is not simply categorized into either the homogeneous or the heterogeneous classification. Biocatalysis contribution was a small proportion of the catalysis market. But, over the

past 20 years, enzyme catalysis has gained more and more attention due to many breakthroughs in this area.[8] Enzyme catalysis features some advantages such as high selectivity and mild operating conditions (normally at ambient temperatures and pH and preferentially in aqueous media). Currently, enzymes are able to catalyze an increasing breadth of reactions such as biodiesel production.[9]

1.2 Heterogeneous catalysis

As introduced in the previous section, numerous industrial applications are facilitated by employing heterogeneous catalysis. Therefore, investigation and development of heterogeneous catalysts are of great practical importance. Heterogeneous catalysts commonly consist of active noble or transition metal nanoparticles on a high surface area support material, such as metal oxides, activated carbon and zeolites. Particularly, the combination of a dispersed active metal and an active support often produces superior catalytic performance because of strong metal support interaction (SMSI). It is well acknowledged that the use of catalysts can provide an alternative reaction pathway with a much lower activation energy barrier. The use of catalysts only accelerates the rate of reaction under a low energy barrier scenario, leading to a faster attainment of chemical equilibrium. However, the catalysts cannot change or alter the equilibrium position, which means catalysts cannot make a reaction happen if it is thermodynamically unfavorable.

An illustration of a heterogeneous catalytic process is shown in Figure 1.1. It clearly depicts the energy barrier for a catalyzed reaction is much lower than that of the same

uncatalyzed reaction. The reactants are firstly adsorbed onto a catalyst surface, followed by the subsequent reactions to obtain final products in adsorbed states. Finally, products are desorbed from the catalyst's surface, and the catalyst is thus regenerated.

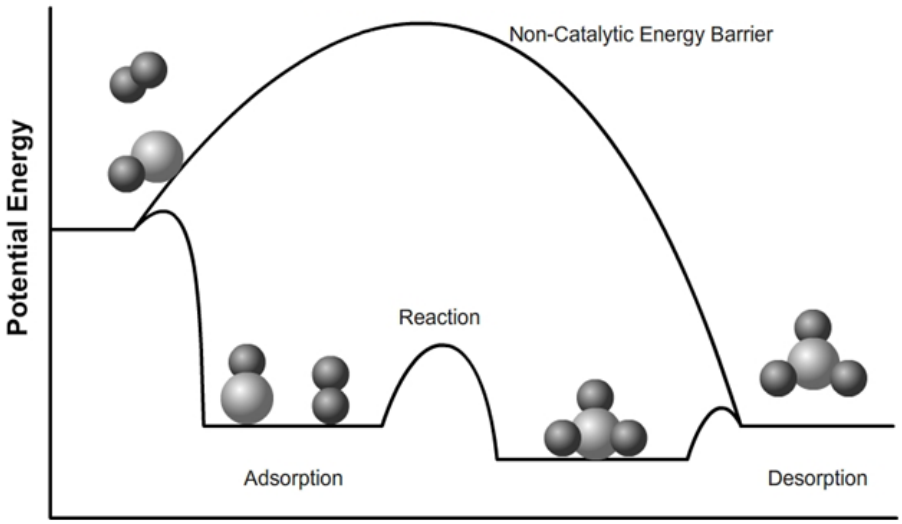

Figure 1.1 An illustration of a typical heterogeneous catalytic process.[10]

In the scope of heterogeneous catalysis, there are some important considerations, including the adsorption of reactants, activity and selectivity of catalysts, stability and deactivation of catalysts, and the support effect. Detailed discussions regarding the importance of these aspects are presented in the following sections.

1.2.1 Adsorption on catalyst surface

Adsorption is a crucial and first reactive step in heterogeneous catalysis.[11] The heterogeneous catalytic process must always be preceded by adsorbing at least one of the reactants at the surface of solid catalyst for a significant period of time.[2] It is commonly accepted that the adsorption is almost invariably an exothermic process.

This view can be justified by the thermodynamic proof. The Gibbs free energy for a spontaneous event must decrease (i.e. $\Delta G<0$), and the adsorption is such a process. In addition, the adsorption process is always accompanied by a decrease in entropy, which means the enthalpy needs to be a negative value (i.e. $\Delta H_{ad}<0$).[2]

Although the adsorption of reactants onto the catalyst's surface is an essential step in heterogeneous catalysis, the strength of adsorption should not be too strong or too weak. If the adsorption is too strong, it will block active sites on the catalyst, hindering the subsequent reaction steps and thus making desorption of products from the catalyst surface a rate-limiting step. On the other hand, a very weak adsorption cannot precede reactions properly, with the hindrance of dissociative adsorption as a limiting factor. Therefore, the ideal adsorption strength should be in the intermediate range to effectively promote the catalyzed reaction: this is also well known as the Sabatier principle.[12] An illustrative volcano plot which describes this feature is shown in Figure 1.2. In light of this consideration, adsorption energy of some group 8-10 noble metals such as palladium (Pd), platinum (Pt), ruthenium (Ru) and iridium (Ir) are just around the Sabatier maximum for many catalytic reactions, making them important components when designing catalysts.

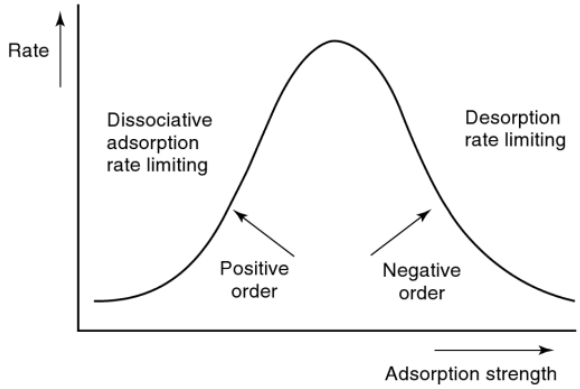

Figure 1.2 A volcano plot illustrating the Sabatier principle. Catalytic rate is maximum at optimum adsorption strength. On the left of the Sabatier maximum, the rate of reaction has a positive order in reactant concentration, and on the right of the Sabatier maximum the rate has a negative order. Reprinted with permission from ref. 12, copyright 2010 Wiley-VCH.

The surface structure and nature are also important to the adsorption and subsequent reaction steps.[1] It is evident that the coordination of atoms at surfaces is different on different surface planes. In addition, the acidic or basic nature of surfaces is also an important factor for many reactions. Regarding this, morphological control over a catalyst with well-defined surfaces has become an attractive topic in catalysis and has recently been attracting tremendous research interest.[13-16]

1.2.2 Activity, selectivity and catalyst deactivation

The most important feature of a catalyst is how efficiently it can convert reactants to products, and this can be reflected by activity and selectivity.

The activity reflects how quickly the catalyst can convert reactants to products. It is defined as the rate of consumption of the reactant, although activity to a particular product can also be specified.[1] Therefore, the fractional conversion of a reactant

within a certain time period can be used as a direct reflection of activity and is also a good indicator for comparing catalytic activity. In addition, catalytic rate can also be expressed in a way called turnover frequency (TOF), which is defined as the number of molecules of a given product per unit time per unit surface area.[2] However, it is not a comprehensively used parameter as some low surface area catalysts may give a high TOF value, but are still associated with an overall lower activity.

Selectivity is another parameter to evaluate the performance of a catalyst. It is the ability of a catalyst to direct the reaction undergoing a specific pathway for obtaining desired products. Selectivity is defined as the fraction of the total products which a particular substance represents.[1]

As the selectivity of a catalyst is an even more intrinsic property compared to activity, the nature of catalytic surface must have great impact on it. Designing more selective catalysts has been set as one of the important pursued goals for catalysis scientists. The tailoring of surface feature by morphological control provides an exciting way to achieve this goal.

As an effective catalyst, it should have both good activity and selectivity, but it also needs to have sufficient stability over the catalytic duration and is not easily passivated or deactivated. There are many types of catalytic deactivations, such as poisoning, sintering, evaporation, coking, corrosion, leaching and mechanical damage.[17] Poisoning is one of the major deactivations which substantially reduces the lifetime of catalysts. It occurs via the strong adsorption of impurities in the feed or from undesirable reaction pathways. Poisoning by sulfur compounds is often

encountered by many large-scale catalytic processes using metal catalysts.[17] In order to prolong the lifetime of active catalysts, modification and improvement of catalyst particles by increasing the resistance to catalytic deactivation is necessary. Engineering advance is also another necessary way to reduce the catalyst deactivation by tailoring the reactors and processes, and optimizing reaction conditions for a large-scale production.

1.2.3 Support effect

The most common materials used in heterogeneous catalysis are metals and metal oxides of various kinds.[1] Conventionally, metals are prepared as small particles with high surface area, therefore, they are active for many catalytic reactions. However, the easily occurred sintering of metal particles reduces its atom usage (loss in metal surface area) in modern advanced catalytic processes. Metal oxides, apart from being active catalysts by themselves, can be used as supports for metals to promote a better metal dispersion and reduce metal sintering significantly. As a consequence, metal oxide supported catalysts are extensively utilized in many industrial manufacturing processes.

Apart from the purely supporting effect, it is noted in many catalytic reactions that various metal oxide supports, such as zinc oxide (ZnO), titanium oxide (TiO_2), cerium oxide (CeO_2) and gallium oxide (Ga_2O_3), can enhance the performance of catalysts (i.e. giving better activity and selectivity than using metals solely). These metal oxides are considered as “active” supports, compared to the conventional inert

supports such as carbon, alumina (Al_2O_3) or silica (SiO_2) which only physically provide a high surface area for metal dispersion. The active supports usually show very strong metal support interactions at some particular exposed surfaces with unique features, and therefore their synergetic effect with doped metal particles can greatly enhance catalytic performance in many reaction processes. By investigating the SMSI between metal and different surfaces of metal oxides, it can provide valuable information on rational design of next generation superior catalysts via the route of maximizing the metal oxide surfaces[13] which give best interactions with metals and therefore improves catalytic performance for target reactions.

With the help of the nano-chemical synthesis approach, one can produce catalysts within the nano regime, which behave quite differently from their bulk counterparts. In addition, with the advances of nanotechnology, controllable synthesis of nanomaterials with some specific morphologies will give additional variables to affect catalyst performance.

1.3 Nanoparticle /catalyst synthesis and manipulation

A nanomaterial is a substance which exhibits physical and chemical properties different from bulk and molecular states as a consequence of having at least one spatial dimension in the size range of 1-1000 nm.[18] The unique properties of nanomaterials such as excellent optical, electronic, magnetic, mechanical and interfacial features are making them great candidates for many applications in catalysis, materials and devices manufactures, medicines, food industries, etc.

The fabrication of nanoscale entities is generally categorized into two approaches, i.e. top-down and bottom-up approaches[4,18,19] (Figure 1.3 shows illustrative processes of both methods). The top-down method is based on engineering techniques to physically carve out or add on nanoscale features to a bulk material. One most common and well-known top-down process is photolithography for the printing of silicon chips.[19] Although this process can easily produce nanoscale materials in large quantities, the poor control over material sizes and morphologies greatly limits its usage in catalysis and many other important areas. The bottom-up approach is to chemically build up nanostructures by manipulating the arrangements of atoms and molecules. This method is superior in terms of the size and shape control of materials, and thus can produce tailor-made nanomaterials with desired features for various applications. The quantity of nanomaterials produced via this approach is limited in one single batch, compared to the top-down large-scale routes.

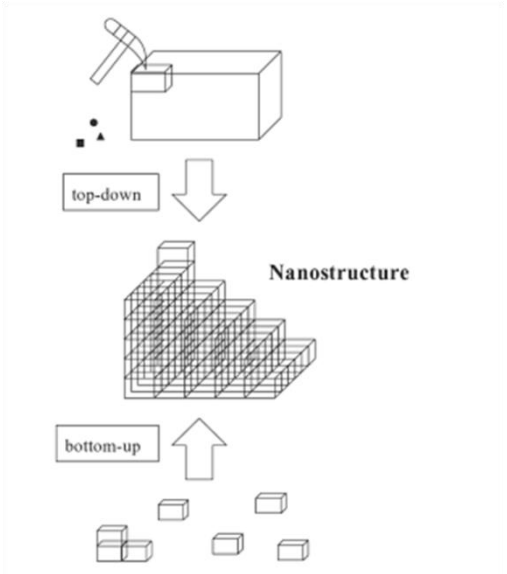

Figure 1.3 Bottom up versus top down approach for the preparation of nanostructures. Reprinted with permission from ref. 20, copyright 2008 John Wiley & Sons, Inc.

Since surface properties are crucial to catalysis, the use of the bottom-up approach enables the study of catalytic features and interactions of various exposed surfaces by controllable synthesis of nanocatalysts with desired shapes. The emphasis of this section is on the chemical bottom-up approach, and thus some common bottom-up methods for nanoparticle fabrication will be discussed, followed by an introduction of some common methods for catalyst preparation and discussion of some important scenarios regarding the nanoparticles' manipulation and modification.

1.3.1 Methods for nanoparticle fabrication

There are many methods which are utilized in the process of the synthesis of nanomaterials, and they are classified by various criteria. Generally, they can be categorized as solution based, solid state, or vapor phase methods according to their phase conditions. Otherwise they can be classified as self-assembled or template assisted methods. In this section, some commonly and very popularly applied chemical bottom-up methods for preparing nanomaterials are presented. Various metals and metal oxides nanomaterials can be manufactured by these methods as follows:

(1) Solution based direct precipitation method

The solution based simple precipitation is widely used in preparation for nanoparticles and nanostructures because it is very easy to use. By adding the chemical agents such as hydroxides or carbonates to the metal containing precursors, precipitation between the intimately mixed reactant components undergoes in solution and forms the nuclei

for the subsequent growth. In order to produce monodispersed precipitates (i.e. nanoparticles), a nucleation process should occur in the first stage, followed by growth without further nucleation. However, in reality, in many precipitating processes, the nuclei grow to nanoparticles, with other new nuclei formed simultaneously. Therefore, both processes will compete to consume the remaining reactants, and also particles will undergo Ostwald ripening,[4] leading to large variation in the size and morphology of the final products. As some important factors such pH value and temperature affect the nucleation and growth processes, the optimization of these parameters to produce monodispersed nanoparticles is of practical importance.

(2) Hydrothermal method

The hydrothermal method is usually using aqueous media to host precursor materials or preliminary precipitates of targeted nano-products, and in some cases, directing or templating agents such as surfactants are incorporated to enhance the directed crystal growth. These reactant mixtures are put in a sealed pressurized thermal reactor to undergo reactions at certain elevated temperatures. The hydrothermal method is a good way to produce nanomaterials with well-defined crystal structures due to the high pressures, controlled temperatures and pH values. As a result, the small variation of these parameters allows the system to produce uniformly distributed nanostructures. Therefore, controlling these parameters is important to the outcome of the synthesis.

(3) High temperature ceramic method

The ceramic method is simple and widely used in the preparation of inorganic solid materials including mixed metal oxides, sulfides, nitrides and many others.[19,21] By

careful adjustment of reactant sizes, compositions, contacts and reaction conditions, the materials can be easily synthesized with sizes in the nano-regime. Typically, the reaction is carried out by heating two non-volatile stoichiometric solids together in a small quartz boat placed in a tube in a horizontal tube furnace, with a specific gas atmosphere applied during synthesis. For example, when making metal oxide nanoparticles, compressed air or oxygen is used to flow over the solids during the synthesis and a bubbler is also attached at the down end to monitor the gas flow rate (An illustrative synthetic process with a gas flow is shown in Figure 1.4). The solids are heated below their melting points, and therefore the reaction takes place in the solid state. A rule of thumb suggests that the temperature of about two-thirds of the melting points of solids will give an efficient process and reasonable reaction time.[19] The solid state reaction can only happen at the interface of the two solids. Therefore, the reactants need to consistently diffuse to the solid interface to make the reaction occur thoroughly. Although the relatively high operating temperature (typically ranging from 500 ℃ to 2000 ℃) can promote diffusion, it is not sufficient in some cases to solely increase the reaction temperature. In order to achieve efficient diffusion and also to avoid the use of too high an operating temperature with a large amount of energy consumption, two starting solid materials are often mixed extensively by making their milled powder into pelletized form. This will maximize the contact surface area and will also reduce the diffusion distance of the two reactants. The nanoparticles synthesized by this approach can also exhibit a wide variety of morphologies.

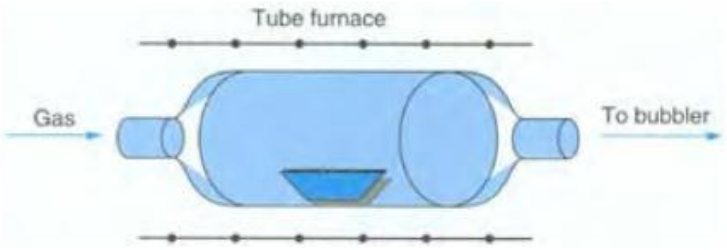

Figure 1.4 A typical reactor for reacting solids under a gas atmosphere. Reprinted with permission from ref.19, copyright 2005 Taylor & Francis Group, LLC.

(4) Chemical vapor deposition method

Chemical vapor deposition (CVD) is another widely used method to prepare nanomaterials, especially nanofilms. During a typical CVD process, a vapor of molecules chemically interact or decompose at or near a substrate surface, where they adsorb onto the surface and combine with other species to produce a solid and residual gaseous products.[4] The decomposition of gaseous reactants is achieved by using high temperatures, lasers or plasmas, and these reactant species are grown to form films under the directing assistance of the substrate. The CVD technique can be used to produce very high quality films if the process is finely tuned. However, CVD also has some drawbacks, including the turbulent gas flow in the reaction chamber, the usage of toxic chemicals, very demanding reaction conditions in terms of cleanliness and energy supply, and the impurities incorporated in products due to the incomplete decomposition of gaseous reactants.[4]

(5) Colloidal method for nanoparticle synthesis

Colloidal method is also often used to produce nano sized metal and metal oxide particles. Generally, in colloidal synthesis, stabilizers such as surfactants and polymers are used in the liquid reaction media to prevent the agglomeration of

particles and also provide extra tunable control over the particle sizes or even shapes.[22] The surfactants or polymers stabilize particles in an electrostatic or steric way, or in a combined approach. In the case of colloidal metal particle synthesis, metal precursors need to be reduced before the stabilizer comes into effect to bind onto the surface of particles. One typical well-known process of producing noble metal colloidal nanoparticles with controlled shapes is called the 'polyol process' which uses, as an example, polyvinyl pyrrolidone (PVP) as a surface capping agent. Metal precursor salts are first dissolved in polyol liquid such as ethylene glycol for later homogeneous nucleation and growth.[22] The PVP is demonstrated to both prevent uncontrolled particle agglomeration and multi-directional growth of metal particles such as Au, Ag, Pt and their alloys.[23-26] Metal oxide nanoparticles can also be synthesized by the colloidal way. The solvothermal method which uses organic solvents with high boiling points such as trioctylamine (TOA) and benzyl ether are often used to thermally decompose appropriate organometallic compounds to produce targeted metal oxide particles. This approach usually produces particles with very narrow particle size distributions, and can be applied to control particle morphologies in many cases.

1.3.2 Methods for preparation of heterogeneous catalysts

In heterogeneous catalysis, metal or metal oxide itself can be effectively prepared through the nanochemical synthesis in a controlled manner, and used directly in various catalytic reactions. However, in many catalytic processes, the combined use

of metal supported on metal oxides is applied to enhance the performance, compared to using metal or metal oxide alone. Therefore, during the synthesis of heterogeneous catalysts, metal and metal oxide are commonly brought together (i.e. loading metal onto metal oxide supports) to maximize the catalytic performance. In this section, two commonly used principal methods in heterogeneous catalyst preparation: coprecipitation and impregnation are introduced.

(1) Coprecipitation

This method is often used in the preparation of heterogeneous catalysts. It is achieved by mixing the active precursors in a solution media, with the addition of other salts, acids or bases to conduct the precipitation. The condensed precipitates are normally dried, calcined and reduced in subsequent steps to get the final active metal oxide supported metal catalysts. The advantage of this method is that it can provide an intimate contact between metal and metal oxide components to achieve a high level of interaction, and thus often give high metal loading of up to 60%.[27] This is very beneficial when high metal loadings are required in some specific reactions. The disadvantage of this method is that it cannot control particle morphology during the process because the metal and metal oxide precursors are precipitated at the same time. As discussed in the previous section, the precipitation technique can be used to produce specific shapes of either metal or metal oxide nanoparticles if the reaction parameters are correctly adjusted. However, during the coprecipitation process, the nucleation and crystal growth processes of the coprecipitated components interfere with each other, leading to rather poor control of the catalyst's shape.

(2) Impregnation

The impregnation method, due to its simplicity, is widely used not only at a laboratory scale, but also in an industrial scale to prepare supported metal catalysts. Generally, there are two forms of impregnation processes classified according to the volume of metal precursor solution added. The first type is called “dry” or “incipient wetness” impregnation which is often used when loading metals into pores of the porous supports (e.g. zeolites) due to the necessity of conducting reactions mainly in the pore space. The metal precursor is prepared in an aqueous solution with the volume equal to the pore volume of the target support. In the case of proper wetting, there is no excess solution remaining outside the porous space.[27] On the other hand, for most metal oxides, a second type named “wet” impregnation is carried out in diffusional conditions.[1,27] In this case, metal precursor solution with excess volume is added to the dry support powder. This method is widely used to produce metal oxide supported catalysts, and is a very useful technique to dope metal components onto metal oxides with different shapes, enabling the investigation of interactions between metal oxide surfaces and doped metals. The impregnated samples usually undergo filtration or a gentle evaporation process to remove the solvents, followed by calcination and reduction to produce final forms of active catalysts.

1.3.3 Nanoparticle manipulations

As described previously, metal and metal oxide nanoparticles can be synthesized by various nanochemical routes. The prepared nano sized particles exhibit unique

properties including electronic, optical, magnetic and other features, which are distinctive from bulk and molecular states. By varying parameters such as sizes, electronic structures, morphologies or compositions, the properties of the nanoparticles can be further tuned to meet specific needs. Therefore, tuning of properties and performance of nanoparticles via a controllable nanochemical approach has great scientific and practical importance. The uniqueness of the properties of nanoparticles enables them to become good candidates for many practical applications. Here, discussion is restricted in some important manipulative methods in nanoparticle engineering including size control, bimetallic formation and shape control, and their influences in catalysis.

(1) Manipulation of particle sizes

Particle sizes of nanocrystals play an important role in many catalytic reactions. By controlling the starting materials, synthetic conditions and post-treatment processes, sizes of nanoparticles can be tuned consequently. As the particle size drops into the nano regime, one direct consequence is significantly large specific surface area, which is much greater than that for bulk materials. Therefore, the control of particle sizes in nanoparticles can maximize the surface area, which is desired in catalytic applications. Nanoparticles, particularly metal nanocrystals, with small sizes are often thermodynamically unstable due to their high surface energy, and they tend to aggregate with each other to increase stability, which will adversely affect catalysis. Therefore, in practice, metal nanoparticles with small sizes are prepared by either using stabilizing ligands bound to particle surface for inhibition of aggregation and

crystal growth, or by dispersing metal nanocrystals onto metal oxides to maintain the adequate surface area required in catalysis. As the particle size decreases, the imperfection level of particle compositions increases. Nanoparticles with small sizes are often found to lack perfect stoichiometry due to the loss of certain sites. Therefore, the atoms with lower coordination numbers are easily observed on the surfaces of small nanoparticles. This feature is closely related to the sizes and manipulation of this will give rise to distinctive catalytic performance.

Changes in particle sizes can also modify the electronic properties of nanomaterials. The appearance of quantum size effect is a direct effect of reducing particle size. With the decrease of particle size, the movement of the electrons is confined and leads to discrete electronic energy levels.[28] The quantum size effect has been investigated over the past years on both metal and semiconductor nanoparticles. The semiconducting nanomaterials have gained much greater research attention due to numerous marketable applications based on the quantum size effect, which shows considerable impact on tuning the electronic and optoelectronic properties of semiconductors. The optical bandgaps of semiconducting nanomaterials are tuned based on the manipulation of particle size, and this consequently affects the energy of their light absorption.[29,30] In photocatalysis where semiconducting nanocrystals are widely used, particle size control is a critical way to increase the catalytic performance.

One famous example of the particle size effect in catalysis is gold nanoparticles. Gold has been considered to be catalytically inert for a long time.[31] However, gold becomes very active if its particle size drops down to less than 3 nm,[32] and is found to be even

superior to other noble metal catalysts for many reactions. Two significant observations in 1980s advanced the research in heterogeneously catalyzed reactions by Au nanoparticles. Pioneering work by Haruta *et al.* discovered that supported Au nanoparticles with fine sizes were very active for the low temperature CO oxidation;[33] prior to this finding Hutchings *et al.* also reported that Au was the best catalyst for ethylene hydrochlorination but without recognition of the size effect of the Au particles.[34,35] Since then, the size effect of Au nanoparticles has been extensively studied and the exploration of Au/supported Au catalysis are growing rapidly by being applied to many important reactions such as low temperature CO oxidation, selective oxidation of alcohols and hydrogenations.[31,36-39]

Haider *et al.* reported recently a remarkable size dependence of supported Au nanoparticles for the aerobic oxidation of benzyl alcohols.[40] They fabricated Au colloidal nanoparticles ranging from 1.3 to 11.3 nm (shown in Figure 1.5). Their findings suggested that the highest activity for oxidizing benzyl alcohols was conducted by catalysts containing Au nanoparticles with the size of around 6.9 nm, irrespective of the support used. Therefore, they attributed the results to the size effect of the gold nanoparticle.

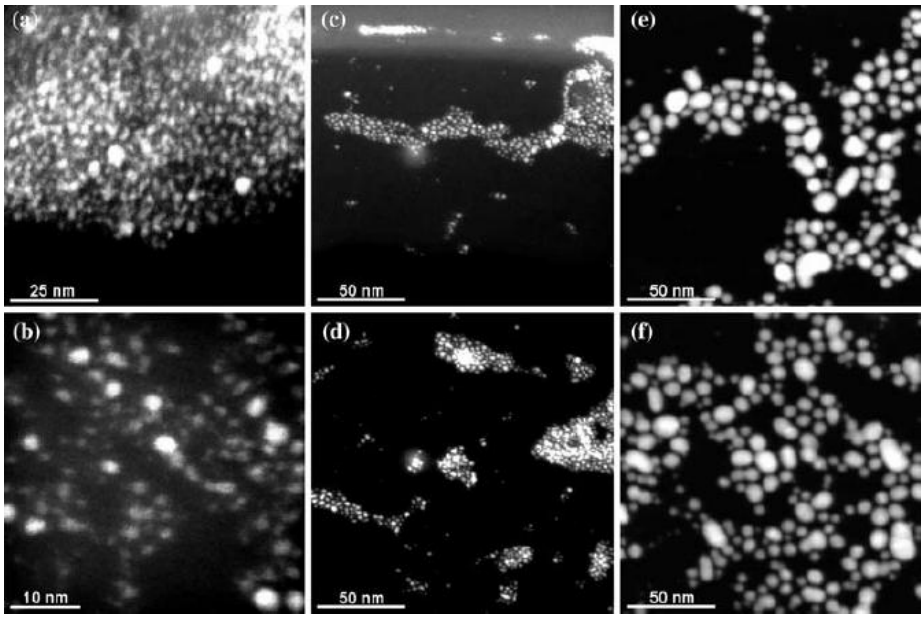

Figure 1.5 Typical HAADF-STEM images of three different colloids: ((a), (b)) are colloids showing Au nanoparticles with mean diameter of 1.3 nm; ((c), (d)) depict colloids with mean diameter of 2.1 nm; ((e), (f)) colloids with mean diameter of 6.9 nm. Due to the Z-contrast, Au particles appear as bright spots. Reprinted with permission from ref. 40, copyright 2008 Springer Science + Business Media, LLC.

A few more examples of semiconductor particle size control showing tunable photocatalytic performance are also worth highlighting. Lee and co-workers investigated the TiO_2 bandgap modulation by preparing rutile TiO_2 nanoparticles of various sizes. They tested TiO_2 catalysts using the probe reaction of oxidation of 2-isopropul-6-methyl-4-pyrimidinol (IMP).[41] The authors found that catalytic activity for oxidation of IMP (measured by CO_2 formation rate) increased with deceasing particle sizes. The results are shown in Figure 1.6. They interpreted this phenomenon as being due to the increase of band position of the conduction band by tuning the band width via manipulation of the particle size of rutile TiO_2. The increased

conduction band positions enable a more effective half-reaction of reduction, and consequently, the other half oxidative reaction and the overall activity for the process of oxidation of IMP can be enhanced. Stroyuk *et al.* investigated various semiconductor nanoparticles such as ZnO, CdS and CdTe, and concluded that the particles size can cause band width modification by a strong quantum size effect.[42]

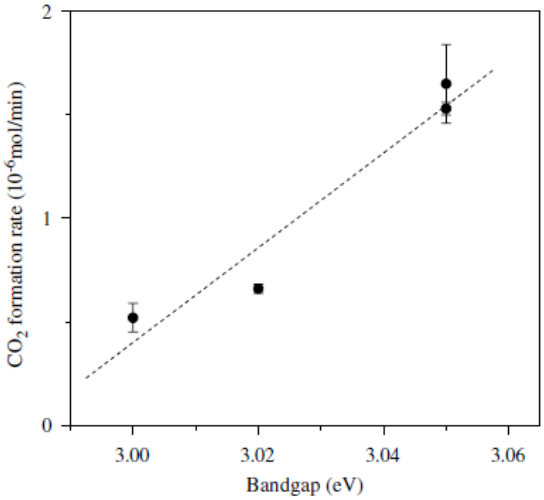

Figure 1.6 The CO_2 formation rate on rutile TiO_2 as a function of bandgap. Reprinted with permission from ref. 41, copyright 2005 Springer Science + Business Media, Inc.

(2) Bimetallic manipulation

Development of bimetallic catalysis is a very popular research area both academically and industrially. The intense research interests on this topic were stimulated by the pioneering work of Sinfelt in the 1960s.[43,44] Bimetallic formation is achieved by modifying a monometallic nanoparticle with the addition of a second foreign metal. The bimetallic modification or alloy formation often gives rise to unique electronic and chemical properties which are very different from the parental monometallic components. In light of these unique properties, studies for understanding bimetallic surfaces and exploring their applications in catalysis are growing rapidly.

Generally, there are two crucial factors that affect the electronic and chemical properties of a metal at the bimetallic interface.[45] The first one is due to the formation of heteroatomic bonds which alter the local electronic environment of the metal surface, modifying its electronic structure via a so called ligand effect. The geometric effect is another factor that plays an important role. In many cases, the bimetallic structure is very different from that of the monometallic parent metals. The average metal-metal distance is often changed due to the formation of the bimetallic structure, and this can create lattice strain affecting the metal electronic structure by changing the degree of metal orbital overlap.[45,46] Particularly, the d-orbitals of metals are often involved in forming bimetallic structures which are important for various catalytic applications. Thus, on formation of a bimetallic surface, the surface d-band width is often changed due to the combination of both ligand and strain effects. Because the d-band filling is hardly changed, the d-band width and d-band center position are closely correlated to each other. The correlation is manifested in the way that the average d-band energy increases while the d-band is getting broader; and the d-band center is higher when this band width becomes narrower.[46] The tunable d-band energy will affect the adsorption behaviors of reactant molecules and consequently change the catalytic properties of the bimetallic surfaces.

Bimetallic catalysts are widely used in many catalytic reaction processes, such as hydrogenation of hydrocarbons[47] and reforming of oxygenates including alcohols, polyols and many others. The CO oxidation process is also a good example of using bimetallic catalysts.[44] Pt based bimetallic catalysts are the most studied and

commonly used bimetallic systems in the interest of both academic research and industrial applications.[48-51] Fukuoka and co-workers reported highly active PtFe alloy catalysts for CO hydrogenation for producing methanol.[49] They attributed the good catalytic performance to the interactions between Pt and Fe in the bimetallic clusters. Pawelec *et al.* investigated PtNi catalysts and their effectiveness in methane reforming with CO_2.[52] They found by varying the composition ratio of Pt to Ni, this could change the degree of methane conversion. This modification altered the electronic structure at the surface by varying its composition, and consequently caused distinctive results in catalysis. Other Pt based bimetallic catalysts such as PtCu, PtRh, and PtRu have also been extensively investigated in catalysis.[53-55] Support materials such as SiO_2 and activated carbon are often used to enhance the bimetallic advantage by providing better dispersions of the bimetallic catalysts.

Nowadays, bimetallic catalysts are often synthesized in a core-shell structured manner. Generally, there are three basic types of surface configurations which can occur when forming a bimetallic surface. Taking Pt and 3d transition metal bimetallic formation as an example as shown in Figure 1.7.[45] When a 3d transition metal is deposited onto the Pt (111) surface at ambient temperature, it is located on the outer surface of the Pt and forms a 3d-Pt-Pt configuration. As the temperature is increased during the preparation, the monolayer of 3d metal atoms diffuses into the matrix of Pt and forms an intermixed bimetallic structure, and this may also be exaggerated to a total subsurface embedded Pt-3d-Pt configuration. Based on the first type of illustrative configuration in which the 3d metal only deposits on the outermost surface of the parental metal,

adoption of proper reaction conditions and use of a sequential deposition technique can make the second metal homogeneously cover the outer surface and allow the parental metal to be encapsulated, ultimately achieving a core-shell structure.

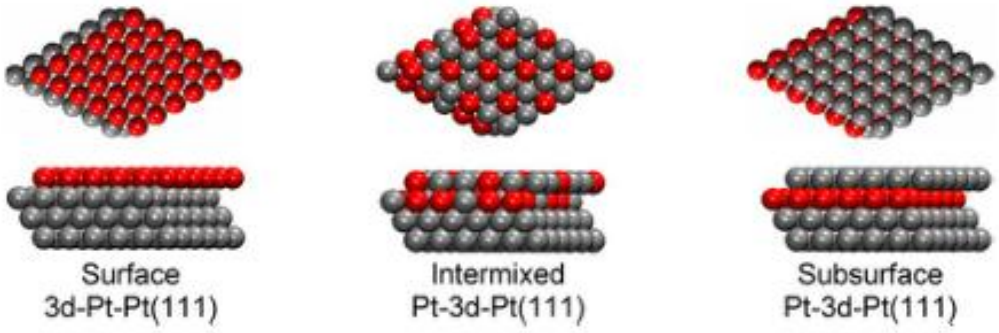

Figure 1.7 Illustrative bimetallic surface configurations with one monolayer of 3d metal (red) deposited on Pt (111) substrate (grey). Reprinted with permission from ref. 45, copyright 2012 American Chemical Society.

By forming the core-shelled structure, not only the properties of the outer shell metal can be tuned by the inner core metal based on the classic bimetallic mechanism, but also it can maximize the surface exposure of the metal at the shell layer compared to the normal alloy, optimizing its performance in terms of a higher reaction activity and selectivity. There are a lot of studies currently trying to understand core-shell structured bimetallic catalysts and to apply them to various catalytic reactions.[56,57] Recently, results published from our group by Tedsree *et al.* showed a superior catalytic performance for room temperature hydrogen production by decomposing formic acid on a Ag/Pd core-shell catalyst.[58] Figure 1.8 summarizes the major findings of this study. Thus, electronic modification of Pd by the Ag core via a core-shell interaction can greatly promote the catalytic performance of the Pd.

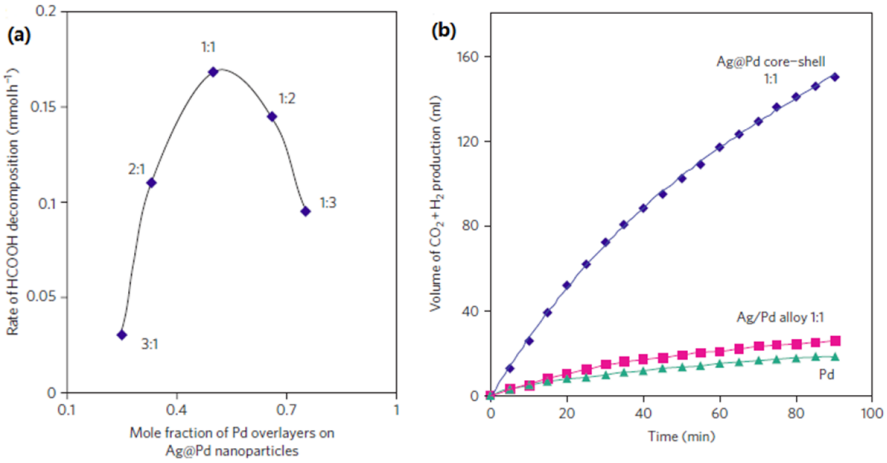

Figure 1.8 A Plot of rates of room temperature formic acid decomposition on Ag/Pd core-shell with different ratios of Ag:Pd (1:1 is the optimal ratio) (a); Production of CO_2+H_2 by decomposing formic acid at room temperature, compared with an ordinary Ag/Pd alloy and Pd only (b). Modified with permission from ref. 58, copyright 2011 Nature Publishing Group.

(3) Manipulation of shapes of nanoparticles

Shape control is a very important approach for engineering nanoparticles, which creates nanocrystals with desired properties. The physical and chemical properties of nanomaterials are not only determined by particle size and chemical composition, but also by morphology. By varying the shape of a nanocrystal, the population of the preferentially exposed surface is changed. The atomic patterns and properties of these surfaces are very distinct from each other, and therefore affect the catalytic processes. Thus, the shape controlled synthesis of nanocrystals introduces a new horizon to the rational design of catalysts with desired catalytically active and selective surfaces. By recognizing the importance over this morphological dependence in catalysis and the advances in shape control synthesis, research activities related to the studies of shape-dependent catalytic behavior have been growing rapidly over the past 10

years.[16]

The growth history of any nanocrystal, regardless of the nature of metal or metal oxide nanoparticle, consists of three sequential stages: nucleation, growth from nuclei to seeds, and growth from seeds to nanocrystals. Once the concentration of the building blocks such as atoms or ions exceeds the critical concentration, they tend to aggregate homogeneously to form nuclei. With a continuous supply of the building blocks, the nuclei will grow bigger and become seeds which can be further grown into nanocrystals.[14]

The morphology and growth rates from seeds to nanocrystals are essentially controlled by two competing forces which are exerted thermodynamically and kinetically. When the growing process is governed by a thermodynamic scenario, the shape of the formed nanocrystal is made up dominantly by most stable surfaces. According to the Gibbs-Wulff theorem, the equilibrium morphology of a nanocrystal is the one with minimum surface energy for a given enclosed volume.[16] Therefore, in this case, the shape of a nanocrystal is often enclosed by facets which have lowest possible surface energy. However, the shape controlled synthesis of nanocrystals does not always adhere to the classic thermodynamic theorem. In many cases, shapes of nanocrystals with high energy surfaces can also be achieved if the adjustment of reaction conditions is made properly before reaching the equilibrium state of the reaction. In this regard, kinetic control is a crucial factor which can lead to nanocrystals with shapes lacking in the case of thermodynamic synthesis. By modifying some parameters such as the concentration of precursors, use of capping

agents, reaction pH, or temperature, the growth rates of different crystal facets can be tuned, giving various shapes of the same crystal. One illustrative example of manipulation over various metal nanocrystal shapes reported by Xia and co-workers[14] is summarized in Figure 1.9.

Structures	Shapes	Schematic drawings	Metals
single-crystal	perfect/truncated cube[a]		Pd, Ag, Au, Pt, Cu, Rh, Bi, Fe
	perfect/truncated octahedron[a]		Pd, Ag, Au, Pt
	perfect/truncated tetrahedron[a]		Ag, Au, Pt, Rh
	rectangular bar		Pd, Ag, Pt
	octagonal rod		Pd, Au, Fe, Co, Ni
	rectangular or octagonal wire	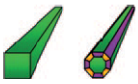	Pb, In, Sn, Sb, Fe, Co
singly twinned	right bipyramid		Pd, Ag
	beam		Ag
multiply twin-ned	decahedron[a]		Pd, Ag, Au
	icosahedron[a]		Pd, Au
	five-fold twinned pentagonal rod		Pd, Ag, Au, Cu
	five-fold twinned pentagonal wire	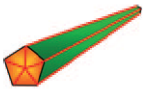	Ag, Au, Cu
	triangular/hexagonal plate		Pd, Ag, Au, Cu, Pb, Bi, Co, Ni
	disc		Sn, Co

[a] Platonic solid.

Figure 1.9 A summary of different shapes of various metal nanocrystals that have been achieved. Reprinted with permission from ref. 14, copyright 2009 Wiley-VCH.

In heterogeneous catalysis, there are lots of reactions which are sensitive to the shapes of the catalysts used. Regarding the importance of this shape dependent feature to

catalysis, a few examples of metal and metal oxide catalysts with different shapes will be highlighted, showing the shape dependent impact on catalytic performance.

Shape controlled synthesis and its impact on catalysis over noble metals such Ag, Pt and Pd are extensively studied, due to the superior catalytic reactivity of those noble metal catalysts. Xu *et al.* reported recently a remarkable shape dependent activity for styrene oxidation by Ag nanoparticles.[59] By proper control of reaction conditions and use of capping agents, they successfully prepared Ag nanoparticles with three different morphologies, namely truncated triangular nanoplates, near nanospheres, and nanocubes. They identified that the major exposed crystal facets were distinctive in three cases. The Ag nanocubes are mainly covered by (100) facet, whereas Ag plates and near spheres are enclosed mainly by (111) surface.(Figure 1.10 (a)-(c)). The testing results surprisingly show a much higher activity of oxidation of styrene on Ag nanocubes, with nanoplates and near spheres showing a much lower and similar performance (Figure 1.10 (d)). They attributed this activity difference to the surface energies. The surface energy of (100) plane is higher than that of (111) surface on Ag nanoparticles, and it leads to an enhanced activity on (100) Ag surface. This example clearly reveals shapes of nanocrystals have profound effect over the catalytic activity and there are many other examples reported with a similar phenomenon.

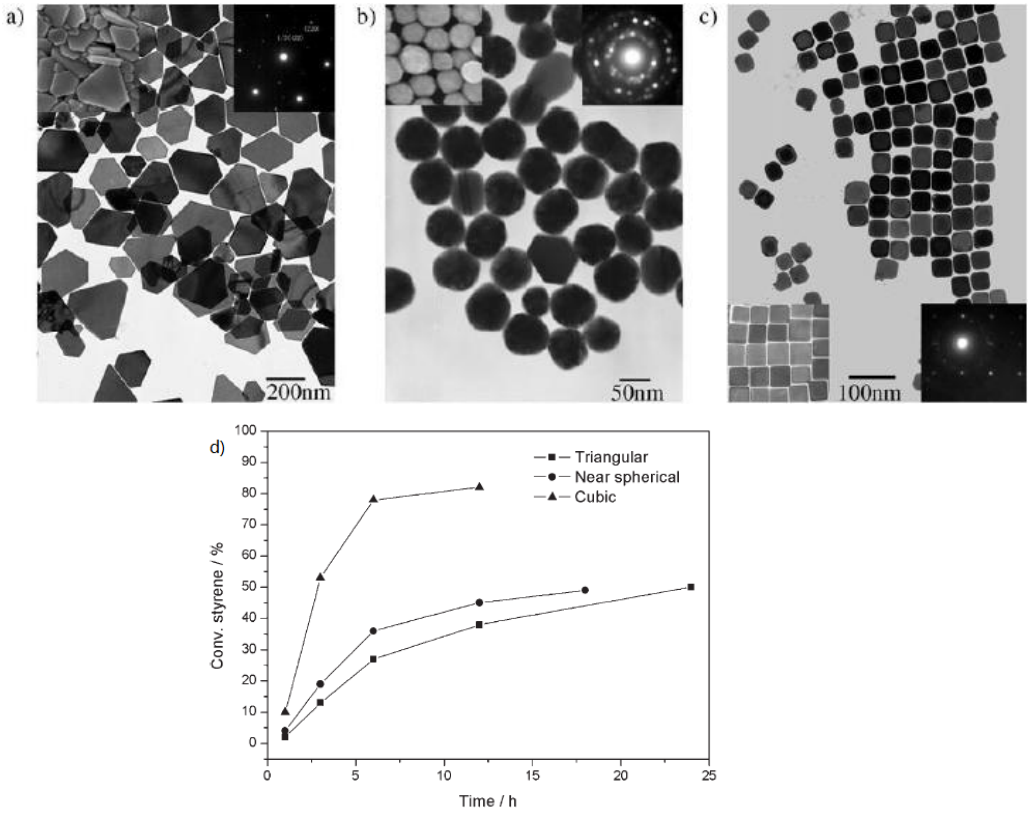

Figure 1.10 TEM images of Ag nanoparticles: truncated triangular nanoplates (a), near-spherical nanoparticles (b) and nanocubes (c), and the insets showing the SEM images (left) and selected area electron diffraction patterns (right); The catalytic performance of the Ag nanoparticles for oxidation of styrene with TBHP (tert-butyl hydroperoxide) (d). Modified with permission from ref. 59, copyright 2006 Wiley-VCH.

Apart from the enhancement of activity, enhancement of reaction selectivity due to shape dependence is also frequently observed in heterogeneous catalysis. Pt is a very valuable noble metal which has excellent catalytic properties for many reactions and its shape effect on activity and selectivity towards various reactions have been extensively studied.[60-65] Yang *et al.* investigated the selectivity dependency over Pt nanocubes and nanopolyhedra (Figure 1.11 (a)-(b)) of the same size (i.e. 5 nm) for pyrrole hydrogenation which is an important model reaction in fuel processing.[66]

They noticed a much more selective ring opening process from pyrrole to n-butylamine by Pt nanocubes (95% selectivity) than that of nanopolyhedra (65% selectivity). The Pt nanocubes were mainly enclosed by the higher energetic (110) facet, whereas the nanopolyhedra were dominantly covered by thermodynamically more stable (111) plane. Their proposed mechanism suggests that the adsorption of pyrrole is through the nitrogen atom bound onto the Pt surface (Figure 1.11 (c)) before the further stepwise hydrogenations. Because the (110) surface is in a higher energy state, it binds the pyrrole more strongly which promotes the ring opening process in the pyrrole molecules, consequently leading to a more selective n-butylamine production on the Pt nanocubes. This example shows that the shape of nanocrystals not only affects its catalytic activity, but also influences its selectivity.

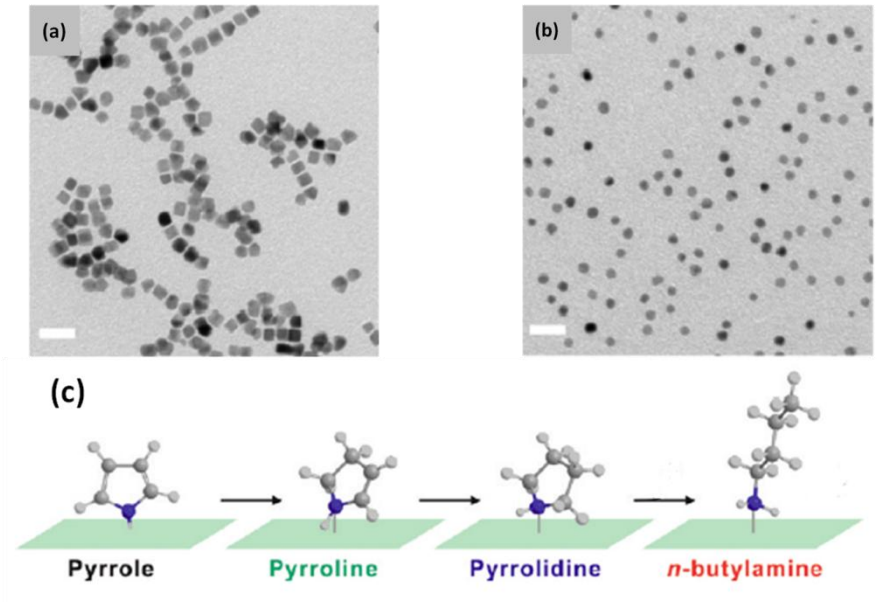

Figure 1.11 TEM images of Pt nanocubes (a) and nanopolyhedra (b), with scale bar of 20 nm; A scheme illustrates adsorption and stepwise hydrogenation of pyrrole to n-butylamine on Pt surface. (blue atom stands for nitrogen) (c). Modified with permission from ref. 66, copyright 2009 American Chemical Society.

Pd is another extremely important noble metal catalyst for a wide range of reactions such as hydrogenation/dehydrogenation reactions, Suzuki coupling reaction, oxygen reduction reaction (ORR), and formic acid oxidation.[14,67,68] With the technique of shape controlled synthesis, Pd nanocrystals have been fabricated into many different morphologies. Studies reported in literature have clearly demonstrated that Pd shapes have profound effect in altering activity and selectivity of many heterogeneous catalytic processes which are shape sensitive.[67]

Apart from metal nanocrystals, shape influence of metal oxide nanocrystals has also been investigated. In heterogeneous catalysis, change of the morphology of metal oxide nanocrystals not only affects their catalytic properties, but also significantly alters the shape dependent metal support interactions (MSI).

1.4 Shape effect of metal oxide in heterogeneous catalysis

Metal oxides are widely investigated and utilized in heterogeneous catalysis, due to their fascinating supporting properties. As discussed in the previous section, metal nanoparticles with different shapes show very distinctive catalytic performance, revealing the important shape-performance relationship in catalysis. The shape dependent catalytic features are also frequently observed in many metal oxides, and in many cases, show even more profound impact than metals. With the bottom-up nanochemical approach, metal oxide nanocrystals can be controllably synthesized with various morphologies by carefully adjusting synthetic parameters such as concentration of precursors, reaction temperature, pH and reaction time. By varying

the shapes of metal oxides nanocrystals, exposed surfaces can be tailored accordingly. The intrinsic surface nature at the atomistic level including composition, structure and electronic property is quite distinct across different surfaces, thus affecting their catalytic properties. Furthermore, strong interactions between metal and a metal oxide support exhibiting a particular surface can, in many cases, results in enhanced catalytic properties.

Defects such as oxygen vacancies are often generated during the synthetic and post-treatment processes of preparing metal oxide nanocrystals. As elusive "invisible" species on oxide surfaces, oxygen vacancies play an important role in tuning physical and chemical properties of metal oxide surfaces.[69] The presence of trapped unpaired electron is often associated with the formation of an oxygen vacancy, and this can be easily detected by electron paramagnetic resonance (EPR). The oxygen vacancy is among the most reactive sites on surfaces of metal oxides, and can provide an active adsorption site for reactant molecules. In addition, the vacant site represents a special source of electrons which modifies surface electronic nature both at localized sites and delocalized band on surfaces. When a metal dopant is introduced onto the metal oxide surface, electrons associated with vacant sites can modify the donor ability of the doped metal, hence enhancing the metal-oxide interaction. Therefore, the understanding and control at an atomistic level of the nature and concentration of oxygen vacancies on different surfaces of metal oxides are essential in exploring the shape-performance relationship of metal oxide catalysts.[69]

Regarding the surfaces of a compound nanocrystal (including metal oxide), it is

simply classified as either polar or non-polar surfaces according to surface polarity.[70,71] The surface polarity originates from a non-zero dipole moment generated within surface repeating units on the termination of a metal oxide surface. Polar surfaces always have higher surface energy due to the presence of a non-zero dipole moment not only at the outer layers, but also on all the repeating units throughout the material.[70] Here, ZnO provides a classic example to illustrate the formation of polarity on such surface termination. ZnO is one of the most well known oxides to have polar surface features. Atomistic models of ZnO surfaces are shown in Figure 1.12. In Figure 1.12 (a), the top oxygen layer is along the (001) surface. It is obvious that the topmost layer is only made up of oxygen atoms, and there is no charge balancing atomic configuration in the same layer. The second layer has the same feature with all positive Zn^{2+} ions. Therefore, a non-zero dipole moment arises at the surface repeating unit, making the (001) plane a polar surface. The Figure 1.12 (b) depicts a typical (100) non-polar surface of ZnO. It is clearly shown that the topmost layer is made up with alternated Zn and O atoms which produces a charge neutral surface, and thus has no dipole moment throughout the surface repeating units, consequently leading to a non-polar surface.

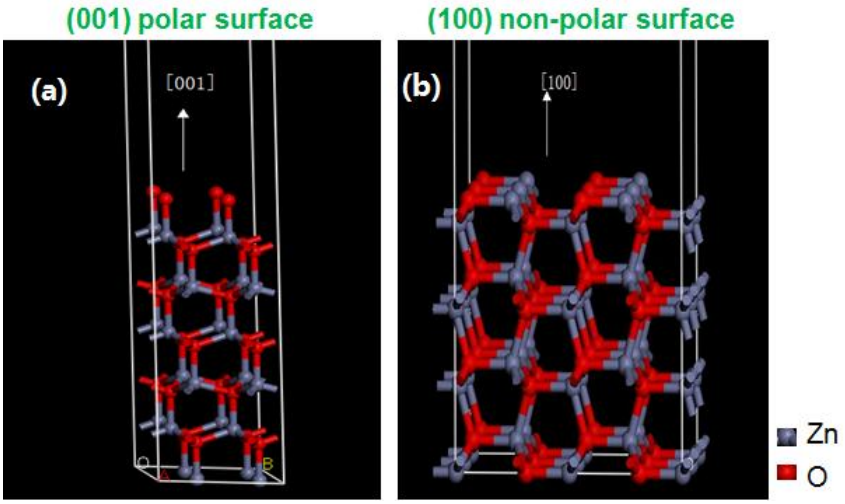

Figure 1.12 Two illustrative atomistic models showing polar (001) surface (a) and non-polar (100) surface (b) of ZnO crystals. Both of the images are side views.

Polar surfaces always feature higher surface energies than non-polar surfaces which are more thermodynamically favorable. In addition, the electrostatic repulsion of the same charged species within the layer on the high energy surface can further render the instability of its structure. In computational models an ideal polar surface is built up without considering the stability of the surface. However, in practice, stabilization of polarity is required in order to make the surface more stable. There are several approaches to stabilize surface polarity, which are listed as follows:

(1) Modification of the surface charges by partially filling surface electronic states.

(2) Reconstruction of surface atomic configuration and composition.

(3) Selective adsorption of foreign charged species.[71]

All these mechanisms are used to stabilize the charged polar surface. The selective adsorption of foreign charged species by the latter method is an energetically favorable, easy and usually observed way to stabilize the polar surface, because stabilization of the surface via reconstruction requires much more energy to take place.

Taking ZnO as an example, both Zn and O terminations of the polar (001) surfaces were observed without much surface reconstruction.[71]. However, for most polar metal oxides, the oxygen terminated polar surface is often stabilized by protons or metal ions, whereas hydroxyl groups are commonly used to stabilize the cation terminated surface. Because most preparations are conducted in solution phase, the use of protons or hydroxyl groups as stabilizing groups can be easily obtained from water molecules.[71] When a metal ion such as Pd^{2+} is added onto a polar surface, it will adsorb strongly on O-terminated surface, and electron transfer between metal and oxide surface often takes place. This is an excellent way not only to stabilize and maintain the unique feature of the polar surface, but also possibly generate a SMSI between metal precursor and the polar oxide surface which might enhance catalytic performance.

Polar surfaces, due to their unique surface arrangement and nature, can alter both the physical and the chemical properties of the oxide surfaces. Such atom arrangements may facilitate the formation of oxygen vacancies which is crucial for many catalytic processes on metal oxides. For nanocrystals of unique shapes, their surfaces can be covered with polar or non-polar surfaces to different degrees. In the next sections, a few examples of shape dependency of metal oxide catalysis will be explored.

1.4.1 Polar surface enhanced shape dependent catalysis

The use of polar surfaces adds an exciting variable to shape dependent catalysis of metal oxide nanocrystals. For many catalytic reactions, oxide with morphologies

mainly covered with polar surface may enhance the catalytic reactivity substantially, compared to other shapes without the polar surface exposure or enrichment.

Recently, Liao and co-workers in our group studied the morphology dependence of ZnO in the Cu/ZnO system for methanol synthesis from CO_2 hydrogenation.[72] They found two forms of ZnO morphologies, namely, the plate form ZnO nanoparticles exhibiting the (002) polar surface and the rod form ZnO exhibiting the (100) non-polar surface. Although both of them showed a hexagonal wurtzite structure, a higher methanol selectivity (64.5%) was observed using the plate form compared to the non-polar ZnO rods (41.0%) at the same level of Cu doping. Detailed characterizations revealed that the higher energetic polar (002) surface on ZnO plates showed a much stronger interaction with the doped Cu metal, and the O-terminated polar (002) surface was easier to generate oxygen vacancies compared to its non-polar counterpart. The electron enriched polar surface shuttled electrons from the conduction band (CB) of ZnO to Cu metal. All these features enhanced the synergic effect between the active components of ZnO and Cu, giving enhanced selectivity towards methanol production on the Cu promoted (002) polar ZnO catalyst.

Meyer *et al.* carried out density functional theory (DFT) calculations on ZnO surfaces doped with Cu atoms for the same reaction.[73] They indeed found that the (002) polar surface exhibited a stronger interaction with adsorbed Cu atoms to give more oxygen vacancies than those of non-polar surfaces.

Co_3O_4 is another example of a metal oxide with a strong shape dependence in catalyzing reactions such as catalytic oxidation of CO and hydrocarbons.[74] Xie and

co-workers studied the shape dependence of Co_3O_4 nanocrystals for low temperature CO oxidation.[75] Morphologies of the spinel structured Co_3O_4 nanoparticles and nanorods were fabricated (Figure 1.13 (a)-(b)). They discovered that the activity of the CO oxidation was much higher on Co_3O_4 nanorods than that on nanoparticles (Figure 1.13 (c)). Detailed characterizations were carried out to understand this phenomenon. They found the Co_3O_4 nanorods mainly exhibited the (110) surface, which is a polar surface.[76] But, the Co_3O_4 nanoparticles mainly exhibited (111) and (001) surfaces. (i.e. They are truncated octahedra consisting of 8 {111} and 6 {001} planes). The (111) plane on Co_3O_4 was also considered as a polar surface, whereas the (001) facet was not. Based on surface studies, it was suggested that the (111) and (001) planes contain only Co^{2+} cations, whereas Co^{3+} cations were the main cations on the polar (110) surface. DFT calculations of CO oxidation revealed that the Co^{3+} was the favorable site for CO adsorption, whereas the Co^{2+} species were inactive.[77] As a consequence, the Co_3O_4 nanorods covered with the (110) polar surface showed a much higher activity towards the CO oxidation.

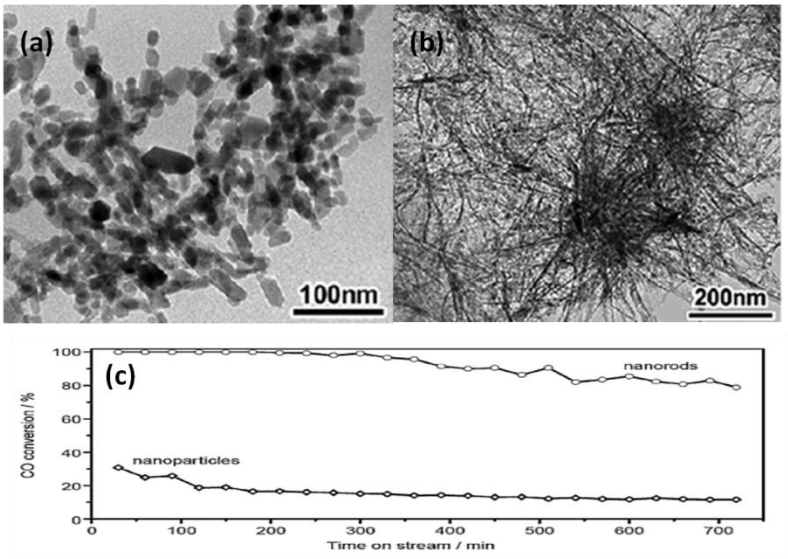

Figure 1.13 TEM images of Co_3O_4 nanoparticles (a) and nanorods (b); CO conversion as a function of time on stream over Co_3O_4 nanoparticles and nanorods (c). Modified with permission from ref. 75, copyright 2009 The Royal Society of Chemistry.

There are many other metal oxide catalysts which can generate polar surfaces at their specific shapes, including MgO, NiO, Fe_2O_3, Fe_3O_4, CeO_2, Ga_2O_3, etc. Among these metal oxides, Ga_2O_3 has gained increasing research interest in catalysis due to its excellent physical and chemical properties. In recent years, various shapes of Ga_2O_3 have been fabricated successfully.[78-80] However, the shape dependent catalytic processes of Ga_2O_3 were not investigated prior to the present study. This provides an opportunity to understand the shape effect of Ga_2O_3 towards selected catalytic processes.

1.4.2 Non-polar surface enhanced shape dependent catalysis

It is not necessarily the case that only polar surfaces can promote catalysis reactions. Metal oxides such as anatase TiO_2 with non-polar surfaces are known to be active for

catalysis. Yang *et al.* synthesized anatase single crystal nanosheets (SCNSs) of TiO_2 with dominant (001) facets via hydrolysis of titanium tetrafluoride (TiF_4).[81] This (001) plane is a non-polar surface.[82] They tested the photoreactivity over various TiO_2 facets including the (001) plane in aqueous solution for the generation of OH radicals which is considered as a very important oxidative agent in many photocatalytic reactions. By using terephthalic acid (TA) as a scavenger (to capture photo-produced OH radicals) and a fluorescent probe, the produced TAOH with fluorescence intensity at 426 nm can be used to measure the photocatalytic activity. The normalized fluorescent intensity on (001) non-polar surface of the SCNSs TiO_2 is found to be the highest (shown in Figure 1.14), which is 5 times higher than that of the commercial Degussa P25 TiO_2 powder (contains about 70% anatase, and 30% of rutile and amorphous phase). Therefore, the results clearly revealed that active OH radicals can be produced at higher rate on the (001) non-polar TiO_2 SCNSs under this photocatalytic reaction. In addition, it was attributed that the surface was characterized with a higher density of 5-fold Ti with an unique electronic structure.[81]

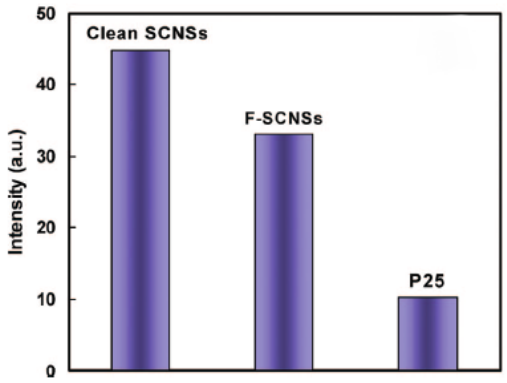

Figure 1.14 Normalized fluorescence intensities on clean SCNSs TiO_2 (calcined to remove capped F atoms), F atoms capped SCNSs TiO_2 (as synthesized), and Degussa P25 TiO_2. Reprinted with permission from ref. 81, copyright 2009 American Chemical Society.

1.5 Methanol synthesis from CO_2 hydrogenation

1.5.1 Overview

Methanol, also called methyl alcohol, is a key platform chemical for present fuel and chemical infrastructures.[83] A lot of added-value chemicals such as formaldehyde, acetic acid and dimethyl ether (DME) are derived from methanol. In addition, methanol itself can also be used as a fuel due to its excellent combustion characteristics. The global demand of methanol production has increased significantly over the past two decades, and in 2007, it reached around 40 million tons per year[84] (shown in Figure 1.15). The demand has been growing even more rapidly since then due to the faster growing pace of industrialization in many areas. Currently, almost all the methanol worldwide is produced from syn-gas which is derived from natural fossil fuels (e.g. natural gas and coal). With consideration of increasing consumption of fossil fuel based energy and possible energy shortage, continuous methanol

production will be severely affected if it continues to rely on fossil fuel based syn-gas. Therefore, an alternative feedstock for methanol synthesis is needed to meet the fast growing demand.

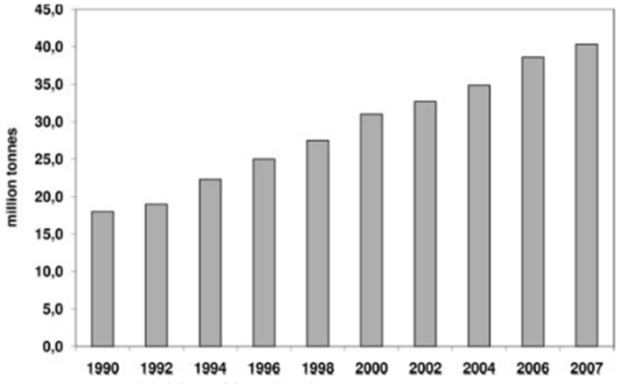

Figure 1.15 Global demand for methanol from 1990 to 2007. Reprinted with permission from ref. 84, copyright 2009 Wiley-VCH.

In recent years, carbon dioxide (CO_2) which is one of the main greenhouse gases has attracted public attention due to the implication of its emissions on climate change.[85] Various sequestration technologies for CO_2 abatement are being considered.[72] There is recognition that CO_2 hydrogenation to generate methanol provides a promising approach to the recycling of CO_2. In addition, this route provides an exciting alternative route for methanol production using CO_2 as feedstock. Meanwhile, methanol synthesis from CO_2 and H_2 has been considered to play an important role in the conversion and the transportation of hydrogen energy derived from non-fossil energies such as solar energy, hydropower and biomass.[86] The success of this methanol synthesis process will not only reduce the global warming via recycling CO_2, but also produce methanol which is crucial to sustainable energy provision. In addition, based on the success of this process and advances in CO_2 recycling, a carbon

neutral cycle can be achieved.

1.5.2 Studies on catalyst development

Regarding this process for methanol synthesis, it is well acknowledged that catalysis plays a key role in the effective methanol production from CO_2 hydrogenation. The typical catalytic process for methanol synthesis from CO_2 hydrogenation involves two major molecular reactions as follows (Equations 1.1-1.2):

$$CO_2 + 3H_2 \leftrightarrow CH_3OH + H_2O\,, \qquad \Delta H_{298K} = -90.70\ \text{kJ/mol} \qquad \text{(Eq. 1.1)}$$

$$CO_2 + H_2 \leftrightarrow CO + H_2O\,, \qquad \Delta H_{298K} = 41.19\ \text{kJ/mol} \qquad \text{(Eq. 1.2)}$$

The formation of methanol is an exothermic process, with the reduction in the number of molecules. Therefore, a decrease in reaction temperature and increase in pressure will favor the forward reaction from a thermodynamic point of view. However, considering the reaction rate and chemically inert nature of CO_2, the process is normally operated above 513 K and at a pressure at 5-10 MPa to facilitate CO_2 activation and methanol formation.[87] In addition, Equation 1.2 is the reverse water gas shift (RWGS) reaction, which is a major side reaction that consumes H_2. Therefore, methanol synthesis from CO_2 hydrogenation requires more effective catalysts with higher activity and selectivity towards methanol but not to CO by the RWGS reaction. During the past decades, a lot of endeavors have been made to develop effective catalysts for this reaction and to investigate the nature of this target reaction over specific catalysts. Catalytic researchers around the world have reported various types of catalysts for this reaction. Particularly, researches have been dominantly focused on

using metal-metal oxide mixed catalysts because of their excellent properties.

The most extensively studied catalysts so far are Cu based catalysts, especially Cu/ZnO based catalysts. These Cu based catalysts are considered to be very promising, and have long been found to be active for traditional methanol synthesis from CO and H_2.[86] During the past decades, many research groups and institutions have been working on developing new but effective Cu-based catalysts for carbon dioxide hydrogenation to methanol. Tagawa *et al.* studied activities of various catalysts containing Cu, Cr, Zn and/or Al, and also investigated the effect of supports on the Cu based catalysts from the viewpoint of their acid-base properties. They found that catalysts containing Cu and Zn were very active.[88-90] They attributed these findings to the high stability and reactivity of formate species, which is the key intermediate for this reaction, on these catalysts' surfaces. Subsequently, other research groups investigated the mechanisms and pointed out that the active sites were derived from a CuZn alloy, which was responsible for the CO_2 activation and subsequent methanol formation. Very recently, our group reported that interactions between Cu and ZnO and the shape of ZnO played a key role in this catalytic process, and they were responsible for the enhanced methanol synthesis. Based on the testing and characterizations, they found that a polar (002) facet-enriched plate form ZnO was more active and selective than the non-polar (100) and (110) facets of rod form ZnO.[72] This study revealed for the first time that a polar surface enhanced shape-dependent catalysis in methanol synthesis. Furthermore, researchers introduced other components to the Cu/ZnO based systems, to study the effects exerted by

various metal oxides on the performance of the catalysts. For instance, Hattori *et al.* examined the activities of Cu/ZnO catalysts combined with ZrO_2, MgO, Al_2O_3, or Cr_2O_3, and found that ZrO_2, MgO, and Al_2O_3 were more effective to enhance the activity of Cu/ZnO.[91] Meanwhile, Saito *et al.* also studied Cu/ZnO based ternary catalysts on the activity of methanol synthesis. Al_2O_3, Cr_2O_3, ZrO_2, and Ga_2O_3 were found to increase the activity of a Cu/ZnO catalyst.[86] Currently, high performance Cu/ZnO based multi-component catalysts have also been designed on the basis of the roles of various metal oxides. The activities of these multi-component catalysts were higher and more stable than that of Cu/ZnO/Al_2O_3. In addition, multi-component Cu/ZnO based catalysts were found to be very stable during long-term operation.[86]

Another category of catalysts investigated are noble metal based catalysts, such as Pd, Pt, Ru or Rh based catalysts for this reaction. Noble metal based catalysts provide an excellent opportunity to develop a high performance catalyst for methanol synthesis. It is because the adsorption strengths of reactant molecules on noble metal surfaces are always at the intermediate state (the Sabatier principle). This is based on the partially filled metal d-orbital or related orbitals with similar energy range, which can electronically interact well with most adsorbed molecules without producing either too strong or too weak an interaction. In addition, due to their high activity, only a very small quantity of metal (around 5 wt%) is required compared to the large metal usage in the Cu based catalysts (Cu: 30 wt%-40 wt%). Therefore, the activity per gram metal basis is much higher than that of Cu. Among those noble metal catalysts, Pd based catalysts have been widely studied, and proven to show high activity

towards methanol synthesis. For example, Fujimoto *et al.* reported that Pd/CeO_2 and Pd/TiO_2 catalysts reduced at 773 K exhibited high selectivity and stability towards methanol formation in continuous methanol synthesis.[92] Other different metal oxides as supports were also investigated, such as Pd/SiO_2, Pd/ZnO, Pd/ZrO_2, and Pd/Ga_2O_3. Interestingly, Fujitani *et al.* found that Pd/Ga_2O_3 catalyst showed the highest activity, and the determined specific activity (turnover frequency) of this catalyst was 25 times higher than that of Cu/ZnO.[93]

Since Fujitani's report on this exceptional Pd/Ga_2O_3 catalyst for CO_2 hydrogenation to methanol was published,[93] research interest in exploring this catalyst has been increasing rapidly. Baltanas *et al.* have also recently reported that Pd/Ga_2O_3 based catalysts showed a high activity towards methanol synthesis.[94] Furthermore, by *in situ* Fourier transform infrared spectroscopy (FTIR) they have proposed a mechanism of stepwise hydrogenation of CO_2 on the Ga_2O_3 surface to generate methanol, with contribution from atomic hydrogen spilled over from the Pd metal surface. Therefore, the Pd/Ga_2O_3 catalyst can be recognized as a bi-functional catalyst for this reaction.

Apart from the traditional study of catalyst development, shape-dependency study over metal-oxide catalysts is of great importance for this important reaction. In addition, the identification of highly active crystal facets could enable rational design of next generation catalysts. The recent shape-dependency study over the Cu/ZnO catalyst reported by our group has also shed a light on this. To the best of our knowledge, there is no reported research to date by others addressing the shape effect of Ga_2O_3 to promote Pd for methanol synthesis from CO_2 hydrogenation.

1.6 Photocatalytic decomposition of methanol for H_2 evolution

1.6.1 Overview

Methanol has been recognized as an excellent hydrogen storage molecule. In this case, methanol is considered as a mobile energy carrier and can be used to produce H_2. Due to its lower splitting energy ($\Delta G = 16.1\ kJ/mol$) than water ($\Delta G = 237.1\ kJ/mol$), H_2 evolution from photocatalytic methanol decomposition is superior than photocatalytic water splitting. The overall reaction of methanol photodecomposition is described by the Equation 1.3:

$$CH_3OH(l) + H_2O(l) \leftrightarrow 3H_2(g) + CO_2\,(g), \quad \Delta G = 16.1\ kJ/mol \qquad (Eq.\,1.3)$$

Although H_2O contributes to the hydrogen production as presented in the reaction equation, the actual photocatalytic process is far more complicated than the stoichiometry implies. Investigation of this reaction has showed that the dominant source for hydrogen is from methanol, but water molecules only contribute a small extent to the H_2 evolution.[95]

At this stage, it is also worth highlighting some core aspects regarding the fundamentals of photocatalytic processes. In a typical photocatalytic process which is shown in Figure 1.16, a semiconductor photocatalyst absorbs UV and/or visible light which has energy equal or greater than the bandgap of the semiconductor. Some electrons in the valence band (VB) then get excited to the conduction band (CB), leaving positive holes (h^+) in the valence band. The electron (e^-) and hole (h^+) pairs generated are called "excitons". After the excitation, the separated electrons and holes

start to diffuse from the inside the bulk to the surfaces of the semiconductor. During this process, there are 3 major fates for the separated electrons and holes. The migrated electrons can be transferred from the semiconductor surface to adsorbed reactant species (electron acceptor) which will be reduced (route C). Holes, on the other hand, can take electrons from other adsorbed reactant molecules (electron donor) to oxidize them (route D). Recombination of electrons and holes are also observed both in the volume (route B) and on the surface (route A) of the semiconductor photocatalyst.[96] Recombination is a dominant deexcitation process which can cause lowering of the exciton lifetime and efficiency of the photocatalysts. Therefore, searching for and modifying semiconductor photocatalysts with slower recombination rates are very important for enhancing the efficiency of photocatalytic processes.

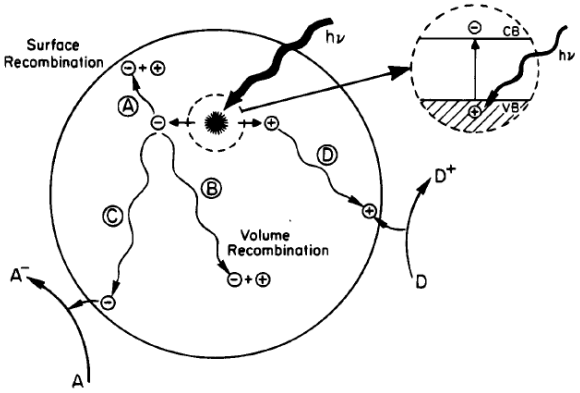

Figure 1.16 Schematic photoexcitation in a semiconductor solid followed by deexcitation processes. Reprinted with permission from ref. 96, copyright 1995 American Chemical Society.

To facilitate a photoreaction, matching respective positions of band edges of the conduction and valence bands and the redox potential levels of adsorbed reactants is essential. Both the reduction and oxidation potentials of the adsorbed species should lie in the bandgap of the photocatalyst. Taking methanol photodecomposition as an

example, the bottom of the conduction band should be more negative than the reduction potential of H^+/H_2 (0 V vs normal hydrogen electrode (NHE)). The top of the valence band should be more positive than the oxidation potential of CO_2/CH_3OH (0.38 V vs NHE). There are quite a few semiconductor materials which meet this thermodynamic requirement. Other factors such as overpotentials, electron mobility, lifetime of the photoseparated electrons and holes, and concentration of reactants are also influential for this reaction.[97]

1.6.2 Studies on catalyst development

Currently, the major class of catalysts studied for this reaction is TiO_2 based materials. TiO_2 has a bandgap of 3.2 eV and is well known to be active for many photocatalytic reactions. It is also often used as a benchmarking catalyst in photocatalysis. Studies over TiO_2 photocatalysts have revealed many important aspects for methanol photodecomposition reaction. For example, the lifetime of electron and hole pairs is a crucial factor for photocatalytic reactivity. Thus, various methods such as the use of metal co-catalysts, and addition of other semiconductors to form a heterojunction structure to prolong the lifetime of excitons are often applied.

Inspired by the literature on the general importance of shape dependent activity in catalysis, I have been particularly interested in studying the shape effect of Ga_2O_3 in the Pd doped Ga_2O_3 catalysts for this photoreaction in this thesis.

1.7 Computational approach in heterogeneous catalysis

With the continuous breakthroughs in computational technology and advent of powerful computers, theoretical approaches by computational chemistry have been making increasing contribution to the field of heterogeneous catalysis. Although so far we cannot directly be told an optimized catalyst for a certain reaction by simply inputting data to a computer program, guidance and predictions provided via computational calculations and modeling show important impacts in various aspects of heterogeneous catalysis. Generally, the main methods used can be classified into five broad classes, namely, molecular mechanics (MM), *ab initio* calculations, semiempirical (SE), density functional theory (DFT) calculations, and molecular dynamics calculations.[98] Among them, the DFT method is an extremely popular and, on the whole, a successful way of dealing with problems in heterogeneous catalysis.[2]

1.7.1 DFT approach in heterogeneous catalysis

Density functional theory is based on the electron density function which determines the ground-state properties of an atom or molecule.[98] It is widely used in theoretical studies of many aspects in heterogeneous catalysis. Some important applications of the DFT method in heterogeneous catalysis are highlighted below:

(1) Calculation and modeling in structures and energies of both surface and bulk for metal or metal oxide catalysts.

(2) Study of adsorption behavior of reactant species, which includes adsorption energy calculations, preferred sites and patterns, on the surfaces of catalysts.

(3) Prediction of reactivity and reaction pathways on a specific catalyst.

(4) Scrutiny of electronic properties of surfaces and bulk states of metal or oxide catalysts.

A good example of DFT calculations is the calculation for the reaction pathway of selective 1,3-butadiene hydrogenation over a tetragonal ZrO_2 (t-ZrO_2) supported gold nanocatalyst.[99] Liu and co-workers conducted this DFT study and found the active gold species was not Au^0, but Au^I (i.e. AuOH) which was the thermodynamically preferred reduced species from Au^{III} precursor and more energetically favorable for subsequent reaction steps. The reaction pathway on the {001} type stepped {203} surfaces was studied due to the fact that this surface gave the lowest reaction pathway energy (as shown in Figure 1.17). The AuOH was first attached to {001} step by Au-$O_{lattice}$ and HO-Zr bonds. During the reaction, the incoming H_2 was dissociated heterolytically by breaking the Au-O_{latt} bond, in which the ZrO_2 support was active for the heterolytic H_2 dissociation. They found 1,3-butadiene only reacted with dissociated hydrogen on HO_{latt}, then the hydrogenated intermediate (C_4H_7) was not stable and transferred onto the Au center where the adsorbed C_4H_7 species could further take hydrogen from hydride to yield the final butene product. A further hydrogenation from butene to butane was not favorable, because butene can be easily desorbed from the Au center and cannot effectively compete with the hydrogenation of 1.3-butadiene. Their calculations agreed very well with the experimental results for this reaction. In addition, the ZrO_2 in this study was also demonstrated to provide active sites for this reaction, rather than acting as a simple catalytic support.

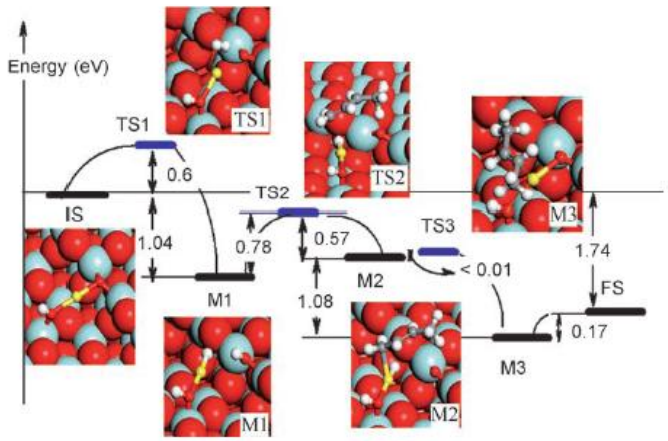

Figure 1.17 The overall energy profile and reaction pathway for 1,3-butadiene hydrogenation to butene on {203} facets of the AuOH/t-ZrO_2 catalyst. IS=initial state, TS=transition state, M=intermediate and FS=final state. The atom colors are red (O), blue (Zr), yellow (Au), light grey (H) and Dark grey (C). Reprinted with permission from ref. 99, copyright 2006 Wiley-VCH.

Although computational approaches for heterogeneous catalysis are progressing very rapidly, to date, it is still hard to study many complex catalytic processes thoroughly. It is expected that further breakthroughs will provide more comprehensive computational guides and predictions in heterogeneous catalysis.

1.8 Project objectives

The objective of this project is to study the shape effect of Ga_2O_3 on Pd/Ga_2O_3 binary nanocatalysts for two important catalytic reactions, namely, methanol synthesis from CO_2 hydrogenation and H_2 evolution from photocatalytic methanol decomposition. The shape dependent properties of metal oxide on the SMSI and the overall effect on catalytic reactions are of great importance in heterogeneous catalysis. To the best of our knowledge, there are no reported studies by others on the shape effect of Ga_2O_3 on

Pd/Ga_2O_3 binary nanocatalysts for these two catalytic reactions.

Thus, detailed effort has been made during the course of this D.Phil. project to achieve this objective. Firstly, morphologically different Ga_2O_3 nanomaterials have been synthesized, based on careful control over parameters. Various types of characterizations have also been applied to study the nature and properties of these Ga_2O_3 nanocrystals with different shapes. Secondly, corresponding Pd doped Ga_2O_3 (i.e. rod and plate forms of β-Ga_2O_3) nanocatalysts have been tested for methanol synthesis from CO_2 hydrogenation. Extensive characterizations and computational calculations have also been carried out to study the SMSI between Pd and these Ga_2O_3 nanocrystals. Lastly, the Pd doped Ga_2O_3 (i.e. rod and plate forms of β-Ga_2O_3, and particulate form of γ-Ga_2O_3) nanocatalysts have also been studied for photocatalytic methanol decomposition.

1.9 Thesis outline

This thesis consists of seven chapters and the outline is listed as follows:

Chapter 1-----Introduces some important basics about heterogeneous catalysis, nanoparticles synthesis, and methods of their manipulations. Shape control over metal oxides is highlighted particularly. Some background information concerning methanol synthesis from CO_2 hydrogenation and H_2 evolution via photocatalytic methanol decomposition is introduced. Computational effort in heterogeneous catalysis is also reviewed.

Chapter 2-----Introduces some of the most common and important techniques for

studying solid catalysts.

Chapter 3-----Describes experimental details concerning synthesis of nanocatalysts, catalytic testings, and material characterizations.

Chapter 4-----Describes the synthesis and characterization of Ga_2O_3 with different shapes.

Chapter 5-----Describes the study of shape effect of Ga_2O_3 (rod and plate forms β-Ga_2O_3) on Pd/Ga_2O_3 nanocatalysts for methanol synthesis from CO_2 hydrogenation.

Chapter 6----- Describes the study of shape effect of Ga_2O_3 (rod and plate forms β-Ga_2O_3, and γ-Ga_2O_3 with particulate form) on Pd/Ga_2O_3 nanocatalysts for H_2 production from methanol photodecomposition.

Chapter 7-----Conclusion and perspective.

1.10 References

1. M. Bowker, *The Basics and Applications of Heterogeneous Catalysis, Oxford Chemistry Primers,* Volume 53, Oxford University Press Inc., New York, USA, 1998.
2. J. M. Thomas and W. J. Thomas, *Principles and Practices of Heterogeneous Catalysis*, VCH Publishers Inc., New York, USA, 1997.
3. K. W. Kolasinksi, *Surface Science: Foundations of Catalysis and Nanoscience, Second Edition*, John Wiley & Sons, Ltd., 2008.
4. P. Atkins, T. Overton, J. Rourke, M. Weller and F. Armstrong, *Shriver & Atkins' Inorganic chemistry, Fifth Edition,* Oxford University Press, 2010.
5. J. K. Smith, *History of Catalysis,* in *Encyclopedia of Catalysis,* John Wiley & Sons, Inc., 2010.
6. P. W. Leeuwen and J. C. Chadwick, *Homogeneous Catalysis: Activity-Stability-Deactivation.,* Wiley-VCH Verlag & Co.KGaA., Weinheim, Germany, 2011.
7. G. Rothenberg, *Catalysis: Concepts and Green Applications,* Wiley-VCH, Weinheim, 2008.
8. A. S. Bommarius and B. R. Riebel, *Biocatalysis: Fundamentals and Applications*, Wiley-VCH Verlag GmbH & Co. KGaA, Weinheim, 2004.
9. M. K. Lam, K. T. Lee and A. R. Mohamed, *Biotech Adv.,* 2010, **28**, 500-518.
10. From the section of *Catalysis*, in *IMPRESS Education* website (access date: 5th June 2013), http://www.spaceflight.esa.int/impress/text/education/index.html.

11. V. J. Inglezakis and S. G. Poulopoulos, *Adsorption, Ion Exchange and Catalysis: Design of Operations and Environmental Applications,* Elsevier B.V., 2006.
12. R. A. V. Santen and Editors (A. Cybulski, J. A. Moulijn and A. Stankiewicz), *Novel Concepts in Catalysis and Chemical Reactors: Improving the Efficiency for the Future,* Wiley-VCH Verlag & Co.KGaA., Weinheim, Germany, 2010.
13. J. A. V. Bokhoven, *ChemCatChem,* 2009, **1**, 363-364.
14. Y. Xia, Y. Xiong, B. K. Lim and S. E. Skrabalak, *Angew. Chem. Int. Ed.*, 2009, **48**, 60-103.
15. Y. Xiong and Y. Xia, *Adv. Mater.*, 2007, **19**, 3385-3391.
16. K. Zhou and Y. Li, *Angew. Chem. Int. Ed.*, 2012, **51**, 602-613.
17. J. A. Moulijn, A. E. V. Diepen and F. Kapteijn, *Appl. Catal. A: Gen.,* 2001, **212**, 3-16.
18. G. A. Ozin, A. C. Arsenault and L. Cademartiri, *Nanochemistry: A Chemical Approach to Nanomaterials.,* Royal Society of Chemistry, Cambridge, UK, 2009.
19. L. E. Smart and E. A. Moore, *Solid State Chemistry: An Introduction., Third Edition,* CRC Press, Taylor & Francis Group, USA, 2005.
20. Y. S. Lee, *Self-Assembly and Nanotechnology: A Force Balance Approach,* John Wiley & Sons, Inc., USA, 2008.
21. M. T. Weller, *Inorganic Materials Chemistry, Oxford Chemistry Primers,* Volume 23, Oxford University Press Inc., New York, USA, 1994.
22. A. Tao, S. Habas and P. Yang, *Small,* 2008, **4**, 310-325.
23. Y. Sun and X. Xia, *Science,* 2002, **298**, 2176-2179.

24. F. Kim, S. Connor, H. Song, T. Kuykendall and P. Yang, *Angew. Chem. Int. Ed.*, 2004, **43**, 3673-3677.

25. H. Song, F. Kim, S. Connor, G. A. Somorjai and P. Yang, *J. Phys. Chem. B.*, 2005, **109**, 188-193.

26. S. B. Han, Y. J. Song, J. M. Lee, J. Y. Kim, D. H. Kim and K. W. Park, *Bull. Korean Chem. Soc.*, 2009, **30**, 2362-2364.

27. M. Lok, E. Marceau, X. Carrier, M. Che and K. P. D. Jong, *Synthesis of Solid Catalysis*, Wiley-VCH Verlag GmbH & Co.KGaA., Weinheim, Germany, 2009.

28. K. Pedersen, in Lecture notes: *Quantum size effect in nanostructures,* pages 1-33, Aalborg University, 2006.

29. Y. Wang and N. Herron, *J. Phys. Chem.*, 1991, **95**, 525-532.

30. A. L. Stroyuk, A. I. Kryukov, S. Y. Kuchmii and V. D. Pokhodenko, *Theor. Exp. Chem.*, 2005, **41**, 67-91.

31. A. S. K. Hashmi and G. J. Hutchings, *Angew. Chem. Int. Ed.*, 2006, **45**, 7896-7936.

32. R. Grisel, K. J. Weststrate, A. Gluhoi and B. E. Nieuwenhuys, *Gold. Bull.*, 2002, **35 (2)**, 39-45.

33. M. Haruta, N. Yamada, T. Kobayashi and S. Iijima, *J. Catal.*, 1989, **115**, 301-309.

34. G. J. Hutchings, *J. Catal.*, 1985, **96**, 292-295.

35. G. J. Hutchings, *Catal. Today*, 2005, **100,** 55-61.

36. M. Haruta, *Catal. Today*, 1997, **36,** 153-166.

37. M. Haruta and M. Date, *Appl. Catal. A: Gen.*, 2001, **222,** 427-437.

38. J. T. Miller, A. J. Kropf, Y. Zha, J. R. Regalbuto, L. Delannoy, C. Louis, E. Bus, and J. A. V. Bokhoven., *J. Catal.*, 2006, **240**, 222-234.

39. O. L. Acevedo, K. A. Kacprzak, J. Akola and H. Hakkinen, *Nat. Chem.*, 2010, **2**, 329-334.

40. P. Haider, B. Kimmercle, F. Krumeich, W. Kleist, J. D. Grunwaldt and A. Baiker, *Catal. Lett.*, 2008, **125**, 169-176.

41. H. S. Lee, C. S. Woo, B. K. Youn, S. Y. Kim, S. T. Oh, Y. E. Sung and H. I. Lee, *Top. Catal.*, 2005, **35**, 255-260.

42. A. L. Stroyuk, A. I. Hryukov, S. Y. Kuchmii and V. D. Pokhodenko, *Theor. Exp. Chem.*, 2005, **41**, 207-228.

43. J. H. Sinfelt, *Bimetallic catalysts: Discoveries, concepts, and applications*, Wiley, New York, 1983.

44. Z. Wei, J. M. Sun, Y. Li, A. K. Datye and Y. Wang, *Chem. Soc. Rev.*, 2012, **41**, 7994-8008.

45. W. Yu, M. D. Porosoff, and J. G. Chen, *Chem. Rev.*, 2012, **112**, 5780-5817.

46. J. R. Kitchin, J. K. Norskov, M. A. Barteau and J. G. Chen, *Phys. Rev. Lett*, 2004, **93**, 156801(1-4).

47. L. Guczi, *Catal Lett.*, 1990, **7**, 205-212.

48. G. W. Huber, J. W. Shabaker, S. T. Evans and J. A. Dumesic, *Appl. Catal B: Environ.*, 2006, **62**, 226-235.

49. A. Fukuoka, T. Kimura, N. Kosugi, H. Kuroda, Y. Minai, Y. Sakai, T. Tominaga and M. Ichikawa, *J.Catal.*, 1990, **126**, 434-450.

50. M. Englisch, V. S. Ranade and J. A. Lercher, *J.Mol. Catal. A: Chem.,* 1997, **121**, 69-80.

51. J. R. Kitchin, N. A. Khan, M. A. Barteau, J. G. Chen, B. Yakshinskiy and T. E. Madey, *Surf. Sci.,* 2003, **544**, 295-308.

52. B. Pawelec, S. Damyanova, K. Arishtirova, J. L. G. Fierro and L. Petrov, *Appl. Catal. A: Gen.,* 2007, **323**, 188-201.

53. J. Y. Park, Y. W. Zhang, S. H. Joo, Y. S. Jung and G. A. Somorjai, *Catal. Today,* 2012, **181,** 133-137.

54. D. Liang, J. Gao, J. Wang, P. Chen, Y. Wei and Z. Hou, *Catal. Commun.,* 2011, **12,** 1059-1062.

55. M. Janyasupab, Y. Zhang, P. Lin, B. Bartling, J. Xu and C. Liu, *J. Nanotechnol.,* 2011,1-6.

56. R. W. J. Scott, O. M. Wilson, S. K. Oh, E. A. Kenik and R. M. Crooks, *J. Am. Chem. Soc.,* 2004, **126,** 15583-15591.

57. N. Toshima, *Pure. Appl. Chem.,* 2000, **72**, 317-325.

58. K. Tedsree, T. Li, S. Jones, C. W. A. Chan, K. M. K. Yu, P. A. J. Bagot, E. A. Marquis, G. D. W. Smith and S. C. E. Tsang, *Nat. Nanotechnol.,* 2011, **6**, 302-307.

59. R. Xu, D. Wang, J. Zhang and Y. Li, *Chem. Asian. J.,* 2006, **1**, 888-893.

60. R. Narayanan and M. A. El-Sayed, *Nano. Lett.,* 2004, **4,** 1343-1348.

61. S. Mostafa, F. Behafarid, J. R. Croy, L. K. Ono, L. Li, J. C. Yang, A. I. Frenkel and B. R. Cuenya, *J. Am. Chem. Soc.,* 2010, **132**, 15714-15719.

62. C. Wang, H. Daimon, T. Onodera, T. Koda and S. Sun, *Angew. Chem. Int. Ed.,*

2008, **47**, 3588-3591.

63. K. M.Bratlie, H. J. Lee, K. Komvopoulos, P. Yang and G. A. Somorjai, *Nano. Lett.*, 2007, **7**, 3097-3101.

64. M. Subhramannia and V. K. Pillai, *J. Mater. Chem.*, 2008, **18,** 5858-5870.

65. C. M. S. Sanchez, J. S. Gullon, F. J. V. Iglesias, A. Aldaz, V. Montiel and E. Herrero, *J. Am. Chem. Soc.*, 2010, **132**, 5622,5624.

66. C. K. Tsung, J. N. Kuhn, W. Y. Huang, C. Aliaga, L. I. Hung, G. A. Somorjai and P. Yang, *J. Am. Chem. Soc.*, 2009, **131**, 5816-5822.

67. H. Zhang, M. Jin, Y. Xiong, B. Lim and Y. Xia, *Acc. Chem. Res.*, 2013, **46**, 1783-1794.

68. R. Wang, H. He, L. Liu, H. Dai and Z. Zhao, *Catal. Sci. Technol.*, 2012, **2**, 575-580.

69. G. Pacchioni, *Chem Phys Chem.*, 2003,**4**, 1041-1047.

70. C. Noguera, *J. Phys.: Condens. Matter.*, 2000, **12**, R367-R410.

71. J. Goniakowski, F. Finocchi and C. Noguera, *Pep. Prog. Phys.*, 2008, **71**, 016501 (55pages).

72. F. Liao, Y. Huang, J. Ge, W. Zheng, K. Tedsree, P. Collier, X. Hong and S. C. Tsang, *Angew. Chem. Int. Ed.*, 2011, **50**, 2162-2165.

73. B. Meyer and D. Marx, *Phys. Rev. B.*, 2004, **69**, 235420 (1-7).

74. Y. Li and W. Shen, *Chem. Scichina.*, 2012, **55**, 2485-2496.

75. X. Xie and W. Shen, *Nanoscale*, 2009, **1,** 50-60.

76. J. Chen and A. Selloni, *J. Phys. Chem. Lett.*, 2012, **3,** 2808-2814.

77. P. Broqvist, I. Panas and H. Persson, *J. Catal.*, 2002, **210**, 198-206.

78. S. Yan, L. Wan, Z. Li, Y. Zhou and Z. Zou, *Chem. Commun.*, 2010, **46**, 6388-6390.

79. Y. Zhao, R. L. Frost and W. N. Materns, *J. Phys. Chem. C.*, 2007, **111,** 16290-16299.

80. Y. Quan, D. Fang, X. Zhang, S. Liu and K. Huang, *Mater. Chem. Phys.*, 2010, **121**, 142-146.

81. H. Yang, G. Liu, S. Qiao, C. Sun, Y. Jin, S. C. Smith, J. Zou, H. Cheng and G. Lu, *J. Am. Chem. Soc.*, 2009, **131,** 4078-4083.

82. M. Lazzeri and A. Selloni, *Phys. Rev. Lett.*, 2001, **87**, 266105 (1-4).

83. L. K. Rihko-Struckmann, A. Peschel, R. Hanke-Rauschenbach, K. Sundmacher, *Ind. Eng. Chem. Res.* 2010, **49**, 11073 – 11078.

84. G. A. Olah, A. Goeppert and G. K. S. Prakash, *Beyond Oil and Gas: The Methanol Economy, Second Edition,* Wiley-VCH Verlag GmbH & Co.KGaA., Weinheim, 2009.

85. K. M. K. Yu, I. Curcic, J. Gabriel, and S. C. E. Tsang, *ChemSusChem,* 2008, **1**, 893– 899.

86. M. Saito, *Catalysis Survey from Japan*, 1998, **2**, 175-184.

87. J. Ma, N. Sun, X. Zhang, N. Zhao, F. Xiao, W. Wei and Y. Sun, *Catal. Today*, 2009, **148**, 221-231.

88. Y. Amenomiya and T. Tagawa, *Proc. 8th Int. Congr. Catal.*, 1984, **2,** 557.

89. T. Tagawa, G. Pleizier and Y. Amenomiya, *Appl. Catal.*, 1985, **18**, 285-293.

90. T. Tagawa and Y. Amenomiya, *Appl. Spectrosc.*, 1985, **39**, 358-360.

91. Z. Xu, Z. Qian, L. Miao, K. Tanabe and H. Hattori, *Bull. Chem. Soc. Jpn.*, 1991, **64**, 1658-1663.

92. L. Fan and K. Fujimoto, *Bull. Chem. Soc. Jpn.*, 1994, **67**, 1773-1776.

93. T. Fujitani, M. Saito, Y. Kanai, T. Watanabe, J. Nakamura and T. Uchijima, *Appl. Catal A: Gen.*, 1995, **125**, 199-202.

94. S. E. Collins, D. L. Chiavassa, A. L. Bonivardi and M. A. Baltanas. *Catal. Lett.*, 2005, **103**, 83-88.

95. K. Lalitha, J. K. Reddy, M. V. P. Sharma, V. D. Kumari and M. Subrahmanyam, *Int. J. Hydrogen. Energ.*, 2010, **35**, 2991-4001.

96. A. L. Linsebigler, G. Q. Lu and J. T. Yates, *Chem. Rev.*, 1995, **95,** 735-758.

97. X. Chen, S. Shen, L. Guo and S. S. Mao, *Chem. Rev.*, 2010, **110**, 6503-6570.

98. E. Lewars, *Computational Chemistry: Introduction to the Theory and Applications of Molecular and Quantum Mechanics*, Kluwer Academic Publishers, New York, 2004.

99. Z. Liu, C. Wang and K. Fan, *Angew. Chem. Int. Ed.*, 2006, **45**, 6865-6868.

Chapter 2 Analytical techniques

Chapter 2 Analytical techniques 67

2.1 Introduction 68

2.2 X-ray diffraction 70

2.3 Transmission electron microscopy 72

2.4 Electron paramagnetic resonance 74

2.5 X-ray photoelectron spectroscopy 77

2.6 Temperature programmed reduction/desorption 81

2.7 Photoluminescence spectroscopy 83

2.8 Cyclic voltammetry 86

2.9 Gas chromatography 90

2.10 References 94

2.1 Introduction

Characterization is of great importance in understanding the nature of catalysts and providing useful guidance for rational design of future effective catalysts. A lot of physical techniques, which are based on microscopy, spectroscopy, adsorption, desorption and others, are frequently used in characterizing solid materials and heterogeneous catalysts. Various information of the studied catalysts can be elucidated, including composition, structure, morphology, surface properties and so on, by these widely applied characterization tools.

Generally, all these techniques used for characterizing solid catalysts are based on the same phenomenon (shown in Figure 2.1). An incident beam attacks the sample. As a consequence, a generated emitted beam, which contains information, is detected and further analyzed. The information reveals "fingerprints" of the solid catalysts and/or of species or reaction intermediates adsorbed on it. According to the sources of incident beam and emitted beam, they can be composed of photons, electrons, neutrons, ions, or electric, magnetic acoustic or thermal fields.[1]

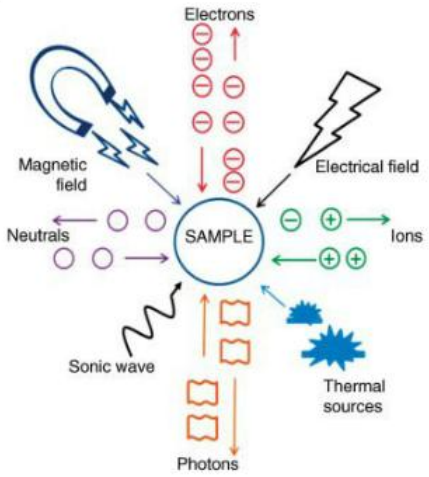

Figure 2.1 The illustrative basic phenomenon of physical techniques. The incident beam is defined by arrows pointed towards the sample, and the emitted beam is defined pointed away from the sample. Reprinted with permission from ref. 1, copyright 2012 Wiley-VCH.

Despite the successful and extensive use of these physical techniques in characterization of solid catalysts, there are also some challenges. The latest challenge is to study solid catalysts under real working conditions, which is the ultimate goal for characterizing solid catalysts. Many characterizations of model systems are now usually conducted at low pressure such as ambient pressure or even ultra high vacuum (UHV) conditions. However, real catalysts are often used under harsh conditions like high pressure, which makes current characterization techniques difficult to apply. Advances in technology enable design of novel characterization-catalytic reactor cells,[1] which can simultaneously characterize the catalyst under the exact reaction conditions and in the same cell while it conducts the catalytic reaction. Extensive effort is being made on the development of the real *in-situ* characterization tools.

In the following sections within this chapter, some of the important characterization techniques which are utilized in characterizing heterogeneous catalysts are discussed

in detail.

2.2 X-ray diffraction

X-ray diffraction (XRD) is one of the basic and most commonly used techniques in characterizing solid catalysts. Various applications, including identification of unknowns and crystalline phases, determination of sample phase purity, determination of lattice parameters, calculation of crystallite sizes (i.e. based on Scherrer equation) and others, can be achieved by this technique and related analysis of the measured XRD patterns of samples.[2] In heterogeneous catalysis, powder X-ray diffraction (PXRD) patterns are frequently measured, because the heterogeneous catalysts are often prepared as fine powder, polycrystalline or even amorphous phases, rather than as single crystals.

Typically, the X-ray is generated from a beam of highly energetic electrons bombarding a target metal plate (e.g. copper in most cases), which ejects an electron from one of the core orbital of the metal atom. The electron vacancy is filled by electron decay from a higher energetic orbital, accompanied by the emission of X-ray radiation. The Cu K_α radiation ($\lambda \approx 1.54$ Å) is the most commonly used radiation source due to its optimized balance between the extent of intensity loss by absorption by the environment and the precision of the XRD measurements.[3] Cu K_α radiation is generated by the emission of electron decaying transition from 2p to 1s orbital, and in copper spectrum, it consists of two neighbored $K_{\alpha1}$ and $K_{\alpha2}$ lines (i.e. λ=1.5406 Å and λ=1.5444 Å, respectively).[2] The K_α line is also the most intense radiation in the

copper spectrum. In order to conduct diffraction measurements, other unwanted radiations including Cu K_β (i.e. transition from 3p to 1s orbital) radiation and bremsstrahlung radiation need to be eliminated, and this may be achieved by applying a crystal monochromator or filter. Therefore, only the narrow wavelength and intense Cu K_α is used as the working radiation source.

When an X-ray beam impinges on a crystalline solid, the scattered waves can interfere with each other. In order to generate this interference, the wavelength has to be the same order of magnitude as the interatomic distances, which is the case for X-ray.[3] The intense reflected X-ray can be generated when scattered X-rays interfere constructively, which happens when the difference of the travel lengths of the X-ray is the integer multiple of the wavelength.

This feature can be illustrated by the following Figure 2.2. The scattering of the X-ray beams from the point B and B' in the neighboring crystalline planes will generate constructive interference when the path difference between A'B'C' and ABC is the integer multiple of the wavelength. The feature is well described by the fundamental equation of XRD, i.e. Bragg's law (Equation 2.1):

$$n\lambda = 2d \sin\theta \qquad \text{(Eq. 2.1)}$$

where integer n is the diffraction order, λ is the wavelength of X-ray, d is the interplanar distance, and θ is the incident angle of the X-ray. Therefore, under constructive interference, the measured diffraction angle 2θ in XRD can reveal the information of lattice spacing d based upon Bragg's law.

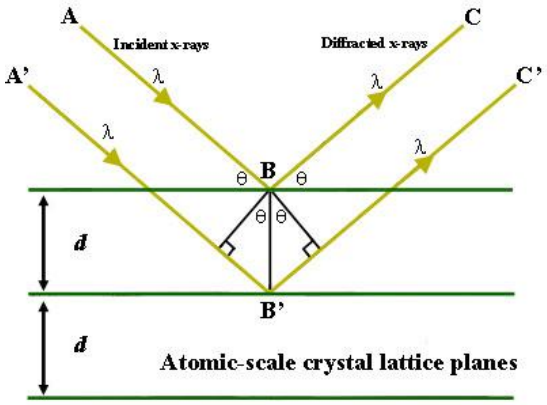

Figure 2.2 An illustration of interfered Bragg reflection.[4]

2.3 Transmission electron microscopy

Transmission electron microscopy (TEM) is capable of yielding information including morphology, size, structure and composition of solid materials. Under ultra high vacuum environment, TEM utilizes a high energetic electron beam to probe the specimen, and collect the trajectories of the transmitted electrons by focusing using a set of lenses, then projecting them onto the fluorescent screen to produce real space images of the thin specimen with high magnifications. The images can be recorded by either a charge coupled device (CCD) camera or by film. The basic layout of the optical components in a typical TEM is displayed in Figure 2.3.

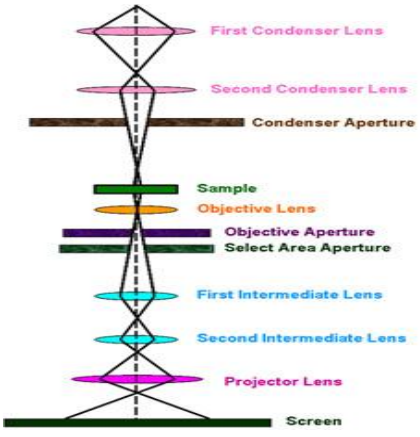

Figure 2.3 Layout of the optical components in a basic TEM.[5]

The wavelength of the electrons can be tuned by the acceleration voltage in TEM. It is well acknowledged that the wavelength of the electron is inversely related to the accelerating voltage V (i.e. $\lambda \propto (V)^{-1/2}$). In addition, it is known from the Rayleigh criteria, $\delta \approx 0.6\ \lambda$, where δ is the smallest distance that can be resolved.[3] Therefore, use of a higher acceleration can substantially increase the resolution of the TEM. For example, the electron wavelength is 0.00251 nm when at 200 kV voltage, and it is down to 0.00164 nm at 400 kV voltage. However, the lenses used in the TEM are electromagnetic lenses, and the resolution it can deliver is far below the level of the electron wavelengths. With the advances in technical design, High resolution TEM (HRTEM) can now probe the atomic scale down to 0.5 Å.[3] HRTEM is also very useful in probing the detailed crystal structure of the specimen. For example, highly magnified HRTEM images can show lattice fringes of the specimen, which helps to determine the exposed crystal planes by measuring the d-spacing between the fringes.

Apart from the function of imaging, another basic mode of a conventional TEM is diffraction. Those scattered electrons after passing the specimen are brought to be focused at the back focal plane of the objective lens. This plane consequently contains the diffraction patterns of the spatial frequencies of the specimen and is often called as reciprocal space or Fourier space. Electron diffraction can be collected by selecting certain area of the specimen by adjusting the aperture placed in the image plane of the objective lens.[3] The diffraction features characterized with selected area electron diffraction (SAED) can reveal information about crystal structure and lattice parameters of the specimen.

2.4 Electron paramagnetic resonance

Electron paramagnetic resonance (EPR) is frequently used in catalysis and related fields as a powerful tool to investigate paramagnetic entities. In other words, the samples studied by the EPR must possess unpaired electron spins. This technique is based on the absorption of the electromagnetic radiation in the microwave frequency range by a paramagnetic featured sample placed in magnetic field.[1] The definition of EPR reveals that it will show no response to any diamagnetic substances which represents the majority of substances. However, this limitation can be considered as an advantage, because the investigated paramagnetic centers (e.g. paramagnetic ions or radicals) are often within complex chemical structures or systems. This enables the study of paramagnetic components free of interference, making EPR a very specialized technique. In addition, EPR is a very sensitive technique, in which trace amounts of paramagnetic species can be unambiguously detected.[6] From EPR investigation, information such as the nature, symmetry and electronic structure of the paramagnetic center and of its surroundings can be elucidated.[1]

The Zeeman Effect is of fundamental importance in understanding EPR, which describes how the electron spin energy level will be split into two levels in the presence of an exerted magnetic field.[1] Because the electron has magnetic momentum, it will behave like a magnet when an external magnetic field (B_0) is exerted on it. The lowest state energy of an electron is presented when the momentum of the electron (μ) is aligned with the magnetic field while a highest energy is presented when μ is anti-aligned with the magnetic field. These two states are labeled by the projection of

the electron spin (M_s) onto the direction of the magnetic field, i.e. designated as aligned state (M_s= -1/2) and anti-aligned state (M_s= +1/2).[7] Therefore, the basic two Equations 2.2-2.3 can be derived as follows based on the quantum mechanics.

$$E = g\mu_B B_0 M_s = \pm\frac{1}{2} g\mu_B B_0 \qquad \text{(Eq. 2.2)}$$

$$\Delta E = g\mu_B B_0 = hv \qquad \text{(Eq. 2.3)}$$

where μ_B is the Bohr magneton and g is an independent and intrinsic factor of the paramagnetic center within a sample and depending only on its electronic configuration. This g-factor is the characteristic parameter of a paramagnetic sample and can indicate its electronic structure or electronic environment. From the Equation 2.3, the resonance happens when the energy difference is equal to the microwave energy. Two possible ways (i.e. sweeping microwave frequency or magnetic field) are capable of achieving this. However, due to the limited frequency range in microwave radiation, samples are usually irradiated with a fixed microwave frequency and sweeping the magnetic field. When the magnetic field arrives at the value that meets the resonance requirement, the spectrum of absorption of microwave is presented. An illustration of these effects and the process is shown in Figure 2.4.

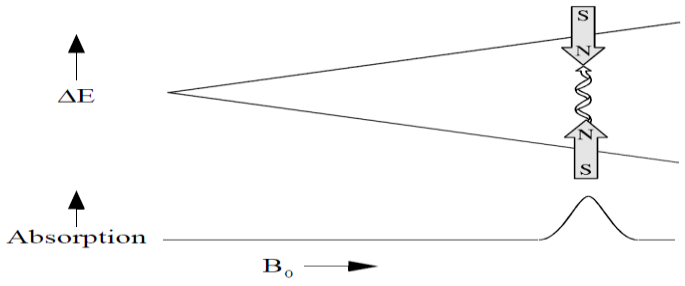

Figure 2.4 An illustration of the spin state energy splitting in the presence of magnetic field and the resonance when sweeping the field.[7]

Unpaired electrons are very sensitive to their environment. In addition, the nuclei of atoms in the compound or molecule often have magnetic momentum as well, which can act as a weak local magnetic field (much weaker than the external field) to the electron. The coupling of the nuclei and the electron can reveal the hyperfine structure by splitting an individual resonance line into components. However, as the number of nuclei increases, the number of signals is increased as well and they may overlap with each other. Therefore, in most cases, we observe the broad signal, rather than the split hyperfine structure. In general, the EPR measurements can be conducted by two approaches. The more common one is irradiating sample with low intensity continuous microwave radiation (i.e. continuous wave or CW-EPR). The other one is using high-powered pulse microwave radiation to irradiate sample and the signal is recorded in the absence of the microwave. The majority of the EPR studies in catalysis are carried out by CW-EPR, and the normal spectral data are presented as the first derivative of the adsorption. A typical layout of an EPR spectrometer is shown in Figure 2.5. It consists of some core parts, including a microwave bridge, a sample cavity, a electromagnet, a detector, and a console. The microwave needs to be controlled properly at low intensity levels, as it will get the EPR intensity saturated if the level is too high, making the information measured less useful.

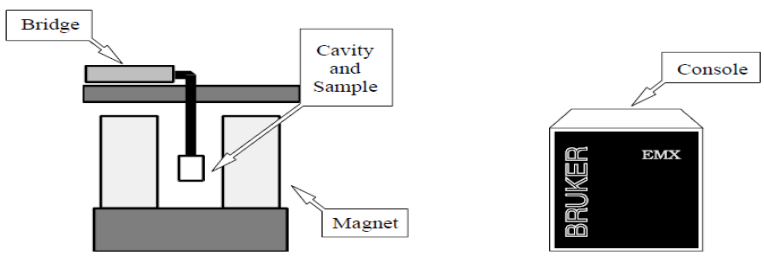

Figure 2.5 A typical layout of an EPR spectrometer.[7]

2.5 X-ray photoelectron spectroscopy

X-ray photoelectron spectroscopy (XPS) is a surface-sensitive technique which is frequently used in the characterization of solid catalysts. Various information including surface elemental composition, and chemical and electronic states of the surface elements can be determined.

In a typical process, an XPS spectrum is recorded by irradiating the sample with a beam of X-ray and simultaneously measuring the kinetic energy (KE) and the number of the escaped electrons from the surface region of the studied sample (i.e. the top 1-10 nm region in the sample).[8] The operating condition in XPS is typically under UHV, because it prevents contamination of the studied surface, and prevents the loss of information embedded in emitted electrons which happens by the collision of these electrons with gas molecules in the environment. The core parts of a typical XPS spectrometer consist of an X-ray source, an UHV system, a sample stage, an electron collection lens, an electron analyzer and an electron detector (shown in Figure 2.6). The X-ray source can be chosen conventionally between aluminum K_α (Al K_α) and magnesium K_α (Mg K_α) irradiations (1486.6 and 1253.6 eV, respectively). Modern high resolution XPS instruments are always fitted with a monochromated Al K_α X-ray.[1] The electrons emitted are focused at the entrance of the analyzer and further counted by detector.

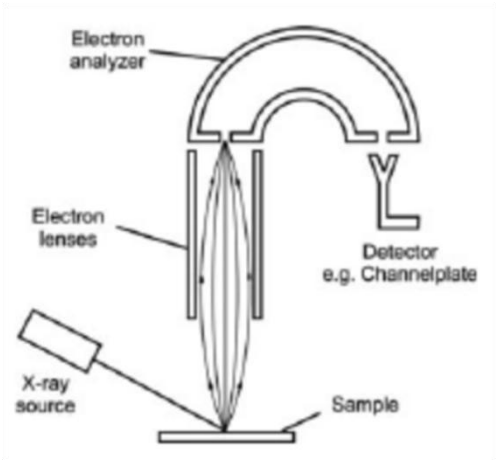

Figure 2.6 Schematic components in a typical XPS spectrometer (UHV system is not included in the figure). Reprinted with permission from ref. 1, copyright 2012 Wiley-VCH.

The principle behind the XPS can be described in the following way, as shown in Figure 2.7. The contact between a solid catalyst exemplified by metal with the spectrometer gives rise to the equalization of their Fermi levels and vacuum levels mismatch. Upon the irradiation with incoming X-ray, the electron with binding energy (E_B), which is related to the Fermi level, is emitted equipped with a kinetic energy (E_{kin}). The energy during this process is written by Equation 2.4:

$$E_B = hv - E_{kin} - e\emptyset_{spec} \quad \text{(Eq. 2.4)}$$

where $e\Phi_{spec}$ is the work function of the spectrometer, reflecting the referencing of the binding energy to the Fermi level rather than vacuum, and is easy to be calibrated. The binding energy of the photoelectron is correlated to the energy of the ionized electron level, indicating the ionized orbital and oxidation state of the emitting elemental atom.[1] Therefore, it is of crucial importance in probing the chemical and electronic states of the surface elements. The measured value of E_B in an unknown sample is compared with the data-based referencing values which are often at the elemental state. Therefore, the binding energy is a good indicator of the electronic and

oxidation state of the surface element in the studied sample. The spectrum of a photoelectron emission is generally doublets, except those from the s orbitals. This is due to the coupling interaction between the spin and the angular momentum which results in energy difference (i.e. parallel or antiparallel states). The difference of binding energies between the split doublets is constant and independent of the chemical state of the atom. In addition, the intensity ratio between the two split lines is fixed. For example, 2:3 for d 3/2 and d 5/2. However, in some cases, superposition of multiplet splitting effect may affect the splitting between the doublets and the superimposed satellites are influential to their intensities.[1]

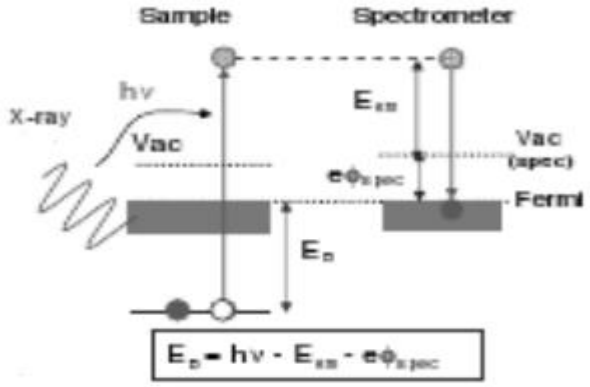

Figure 2.7 An illustration of Photoelectron emission upon X-ray irradiation on solid catalyst (exemplified by metal). Modified with permission from ref. 1, copyright 2012 Wiley-VCH.

For a conducting solid or surface (e.g. metal), the binding energy can be recorded without distortion. However, for non-conducting samples, the surface will become positively charged with accompanying photoelectron emission. This is due to insufficient compensation of ejected electrons by the sample current. This charging effect will cause the measured E_B shifting towards higher values compared to the true value, to an extent depending on the specific instrumental configuration. A steady

state of this charging effect can be achieved by injecting low energetic electrons using a flood-gun. In addition, this charging effect can be corrected by employing an internal E_B reference. The binding energy of C1s of the adventitious carbon (E_B=284.5 eV) is normally used for this propose. The difference between the measured C1s E_B and the 284.5 eV is used as the correction factor. Therefore, the internal referencing process can provide a more accurate E_B of the sample. However, this referencing is based on the assumption that all parts on the surface of the sample are equally charged. The differential charging, for example, may occur in the metal-supported catalysts because of the insufficient contact between the metal and support.[1] Therefore, great attention should be paid when interpreting these data.

Apart from the conventional XPS, Auger electron spectroscopy (AES) is also similarly useful and often regarded as a secondary process of XPS. Upon the emission of the core electron in XPS process, the core hole left behind can be filled by an electron from a higher energy level. The released transition energy by this process can further excite and emit an outer shell electron if this transition energy is greater than its binding energy. The driving force in the Auger process is the intra-atomic transition, therefore, the kinetic energy of the emitted auger photoelectron is independent of the initial external excitation process.[1] AES shows similar capability in determining the surface oxidation states and electronic states of the element, and it is also widely used, on its own, as a surface technique, provided with the proper initial excitation process by various sources.

2.6 Temperature programmed reduction/desorption

Temperature programmed reduction and desorption (TPR/D) are commonly used in characterization of modern catalysts. These thermal methods are very useful in assessing the redox properties of the catalysts, determining thermodynamic and kinetic parameters, studying the type and quantity of the active sites, and investigating the acidic-basic nature of the catalysts.

TPR allows the investigation of the reducibility of catalysts. It is also a destructive method to characterize not only the surface of the catalyst, but also at least partially the bulk.[3] The typical layout of a TPR instrument consists of a furnace and a sample holder, a temperature controller, a gas delivery system and a detector system. A representative TPR instrument is shown in Figure 2.8. Principally, the process of TPR is carried out by placing the sample in the middle of a sandwiched structure covered by quartz wool on both sides and embedded in a reaction quartz tube. Then this internal reactor tube is further covered by an outer quartz shell which is mounted onto a stainless steel lid with gas injection and ejection ports on it. The sample needs to be pretreated by an inert gas in a sufficient low pressure (e.g. ambient pressure) and at elevated temperature (i.e without sample structure degradation) to clean the catalyst's surface. The sample is then heated up in a programmed manner (usually linear), with passing the reducing agent (i.e. H_2 gas in most cases) in an inert gas carrier onto the sample. The amount of the consumed H_2 gas is detected by the thermal conductivity detector (TCD), which can elucidate the amount of the reduced species in the sample based on further quantitative analysis. More importantly, from the acquired profile,

positions of the reduction peaks are of great importance in understanding the reducibility of a catalyst. In the case of a metal-oxide system, it is an indicator of different level of SMSI of the studied catalysts.

Figure 2.8 A picture showing a typical TPR instrument.[9]

TPD is often used to study the acidic and basic nature of the surfaces and the desorption phenomenon of the adsorbed species such as NH_3, CO_2, CO, etc.[3] Compared to TPR, TPD is considered to be a surface technique. The apparatus, sample preparation and pretreatment procedure of the TPD are the same as TPR. After the pretreatment, one or more probe species are then carried onto the catalyst surface by an inert gas at low temperature (e.g. room temperature or lower) until adsorption saturation. After flushing off the weakly adsorbed species by the inert gas, desorption is carried out by heating up the sample (often linearly) while the inert gas takes the desorbed gases into the TCD detector. The peak area in TPD is proportional to the desorbed species and thus correlate to the quantity of the acidic or basic sites on the catalyst surface. The position of the peak maximum is also very useful to determine the interaction level between the adsorbed gas molecule and the solid surface.

Recently, TPR/D has been coupled with Mass spectrometry or Infrared spectroscopy (i.e. TPR/D-MS or TPR/D-IR) to provide advanced quantitative study of the phenomena during the TPR/D processes.

2.7 Photoluminescence spectroscopy

Photoluminescence (PL) spectroscopy is a highly sensitive and nondestructive method to study the electronic properties, particularly at excited states, of materials. The phenomenon of photoluminescence is defined as light emission from a molecule or solid after the absorption of photons (photoexcitation).[1] In catalysis, especially in photocatalytic applications, PL has been widely used to study the defect sites, chemical nature of active sites, and even the mechanism of reactions. Compared to many conventional techniques, the high sensitivity of PL analysis enables it to detect extremely low concentrations of emitting catalysts down to parts per million (ppm) or parts per billion (ppb) levels. Apart from using PL in a static fashion, it can be combined with time-resolved spectroscopy to produce time-resolved photoluminescence (TRPL) to further elucidate the dynamics involved in the catalytic or photocatalytic processes.

Upon the absorption of photon energy, a molecule or a solid material can be transferred to the electronically excited state. The decay processes happen, as a consequence, either in a radiative or nonradiative way in order to return the material to the lower stable state. The nonradiative decay, which is the more common decay process, transfers the excess energy into thermal energy (i.e. heat) or chemical

products (i.e. photocatalysis). While in a radiative way (i.e. photoluminescence), light is emitted to discard its excitation.[10] After the photoexcitation process, a stimulated emission immediately happens which emits the light with the same photon energy as the absorbed photon, and this process is often referred as resonant fluorescence. This process shows no significant internal energy transfer within the material, and thus less interesting for studying the characteristics inside the catalysts. Other radiative processes including spontaneous fluorescence and phosphorescence are crucially related with the internal energy transfer and intrinsic properties of the excited materials. The spontaneous fluorescence emission process (Figure 2.9 (a)) happens between the singlet excited state and singlet ground state. It emits light with a lower frequency than the absorbed photon, due to the internal radiationless energy transfer (e.g. energy loss in vibrational states or trapped states in defects) at the excited state. The unique emitted fluorescence pattern gives rise to the understanding of internal properties of the emitting material such as defects. The time order of spontaneous fluorescence is typically from 10^{-9} to 10^{-5} second.[11] Phosphorescence is another radiative process which involves the intersystem crossing (ISC) between an excited singlet state (S^*) and an excited triplet state (T), and the spontaneous emission from the triplet state to ground state (S) is observed (Figure 2.9 (b)). The singlet-triplet transition is due to the spin-orbit coupling, and it is quite significant when a molecule has moderately heavy atoms. Because the triplet state is a relatively lower excited state, the excited electron can stay in this state longer before relaxing back to the ground state. Therefore, light emission of phosphorescence typically happens in the

time range from 10^{-5} to 10^{-3} second,[11] or even longer. Phosphorescence is also very useful in investigating intrinsic properties of a catalyst. Apart from the studies focused on the catalyst itself, PL can also provide some hints on the reaction processes. Typical chemical reactions occur within the timescale of 10^{-10} to 10^{-5} second,[11] which suggests that the knowledge extracted from fluorescence study is of great importance in exploring the nature of catalytic or photocatalytic reactions.

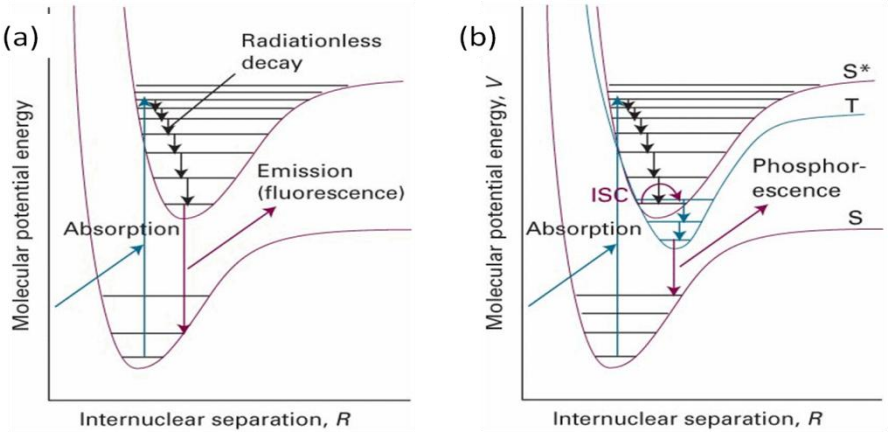

Figure 2.9 Illustrative processes of spontaneous fluorescence (a) and phosphorescence (b).[10]

As previously introduced, the PL measurement itself can be performed in two ways, i.e. static or time-resolved approaches. In a static PL process, a light source of Xe or high pressure Hg lamp, or laser sources are used to excite the sample embedded in the testing cell, and the emitted luminescence is collected by detector for further analysis. A typical set up of the optical parts in a conventional spectrophotofluorimeter is shown in Figure 2.10.

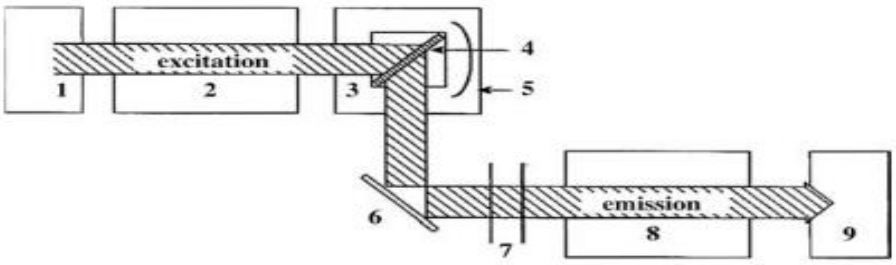

Figure 2.10 Set up of optical components in a conventional spectrophotofluorimeter. 1, lamp; 2, monochromator; 3, cell; 4, sample; 5, light trap; 6, mirror; 7, filters; 8, monochromator; 9, detector. Reprinted with permission from ref. 1, copyright 2012 Wiley-VCH.

The time-resolved photoluminescence measurements are conducted by applying the pulsed form of light excitation from sources such as pulsed lasers or lamps. The TRPL spectra are recorded by collecting radiation data within a certain sampling time, which is after the delay time following the pulse excitation. The process is shown in Figure 2.11.[1] The photoluminescence decay profiles of the emitting material can be given based on the TRPL intensity measurements. TRPL and the related decay profiles are powerful approaches to study the dynamics involved in the photocatalytic processes.

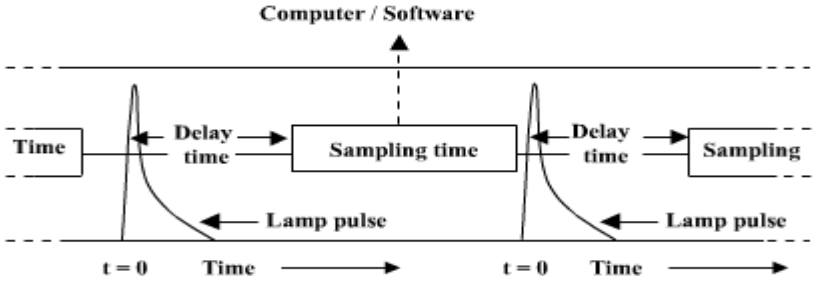

Figure 2.11 A typical sequence of time-resolved photoluminescence measurements. Reprinted with permission from ref. 1, copyright 2012 Wiley-VCH.

2.8 Cyclic voltammetry

Cyclic voltammetry (CV) is one type of potentiodynamic electrochemical

measurement. It is widely used in electrochemistry to study various redox processes within complicated electrode reactions, for obtaining information such as electron transfer, reaction kinetics and intermediates.[12-15] In the field of catalysis, CV is also an attractive technique to study the properties of the catalysts and the related catalytic processes. Characterizations of electrocatalysts by CV for applications such as fuel cells are well established. In this stream, CV is not only considered as a characterization method, but also a reaction process which directly mimics the real electrocatalytic application studied. In addition, as a characterization tool, CV is frequently used to study properties of the catalysts designed for other catalytic applications (i.e. not electrocatalytic applications). For example, metal-oxide catalysts are studied by CV to elucidate the SMSI between metal and oxide components, which can provide crucial information for understanding the related catalytic processes. The CV technique is a highly sensitive method. Therefore, property changes in the catalyst can be well reflected by electrical signal variations in CV, making it a desired approach to study the subtle changes of the catalyst under investigation. Furthermore, the CV technique studies properties of a catalyst at an overall scale, rather than at a selected region from some parts of the catalyst. Therefore, it can reasonably reflect the overall properties of the studied catalyst accurately.

A typical setup of a CV system is depicted by Figure 2.12. An input system, which is basically a function generator, allows the operator to change the experimental parameters such as scan rate and scan range, and send them to the electrochemical station which consists of a potentiostat and a voltage-current convertor. The

potentiostat is used to control the applied potential throughout the measurement and the convertor is used to measure the generated current.[16] The crucial part is the electrochemical cell, which contains three electrodes all immersed in the properly selected electrolyte solution. The three electrodes are:

(1) Working electrode. It is commonly made of glassy carbon, Pt or Au. The electrode is generally encased in an inert rod insulator and with one disk end exposed. The exposed end of the electrode should have a well-defined surface area and shape which are required in accurately interpreting CV results. The catalyst is deposited onto the exposed end of the working electrode to carry out the test.

(2) Counter electrode. This electrode should have excellent conductivity. A Pt wire is commonly used as a counter electrode in CV test. The reaction happens on the counter electrode is not important as long as it conducts the current well.

(3) Reference electrode. It is an electrode with a stable and well known potential. This allows the determination of the potential on the other half cell within an electrochemical cell. A saturated calomel electrode (SCE) is commonly used for this purpose. The potential measured based on the SCE reference can be easily referred to by other types of reference electrodes such as a standard hydrogen electrode (SHE) by simply adding a potential difference of 0.242V (at 25 ℃) between the SCE and SHE.[12]

The three electrodes are all connected to the electrochemical station. Potential is applied between the working electrode and the reference electrode, while the current is measured between the working electrode and the counter electrode. The results are

shown by a cyclic voltammogram (i.e. a plot of current versus potential sweep). An inert gas such as nitrogen (N_2) or argon (Ar) is commonly bubbled into the system before testing to eliminate oxygen which, in many cases, may affect the accuracy of the measurement.

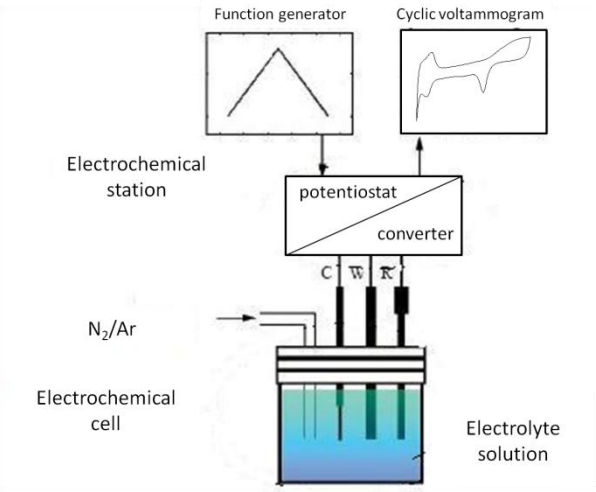

Figure 2.12 Components of an illustrative cyclic voltammetry system (C: counter electrode; W: working electrode; R: reference electrode). Modified with permission from ref. 16, copyright 1993 Wiley-VCH.

In a typical CV measurement, the potential is ramped linearly with a certain scan rate towards a set value, during which the analyte is oxidized (or reduced depending on the initial scan direction) and a current peak is shown. Once the potential reaches the set point, it starts to ramp back to the initial potential point. During the back scan, if the redox couple is reversible, it shows another current peak when the potential reaches the reduction (or oxidation) potential of the analyte. Cyclic scans over the sample are usually conducted in a multiple scans fashion for a single CV test. The oxidation current peak and reduction current peak have the similar shape. However, due to the effects of overpotential or others, a hysteresis may exist, affecting the

reduction and oxidation potential positions and current peak shapes.

Apart from the traditional CV test, CO stripping voltammetry is another helpful CV technique to study the properties of catalysts, because many metal and oxide materials have strong and unique interaction with the CO probe. It shares the same experimental apparatus with the conventional CV. By saturating the catalyst surface with adsorbed CO, under CV operating conditions, the CO oxidation behavior such as on-set potential, peak potential and current peak area, can reveal very useful information about active sites and SMSI of a metal-oxide system.

2.9 Gas chromatography

Gas chromatography (GC) is a commonly used separation technique for molecular analysis. Typical applications of GC include analyzing the purity of a certain substance, separating different components of a mixture and quantitatively determining the amount of individual components in the mixture. The analyte must be vaporizable and stably presented without decomposition in the analytical temperature range.[17] In gas chromatography, the mobile phase is a carrier gas, which is He, Ar or N_2, or other gases such as H_2. The selection of carrier gas is dependent on the specific requirements of the analysis. The solid stationary phase, which is usually made by attaching a layer of microscopic polymer onto an inert solid, is coated inside the wall of the metal tubing which is known as the column. Various packed columns and capillary columns are used in GC analysis, the selection of which is based on the specific analytical purpose. The function of the mobile phase is for carrying gaseous

samples, while the stationary phase is to separate the different gaseous components. During a GC analysis, the gaseous components of a sample interact with the stationary phase in the column. The components elute from the column at different times (i.e. the retention times) due to distinctive levels of interactions between each gaseous component and the stationary phase of the column. Therefore, these gaseous components can be separated and detected. Parameters such as velocity of the carrier gas (controlled through gas pressure), column length and column temperature (controlled by oven temperature) can affect the separation results of the analysis. Generally, higher gas velocity, shorter column length, or higher column temperature, will lead to faster elution rates of gaseous components and less degree of separation. However, due to economical considerations, making the column material and the analysis time to a very long scale is not realistic, although a better level of separation can be achieved in this way. Therefore, the balance between the effectiveness of separation and the economy of analysis should be optimized for an efficient and accurate GC analysis.

A typical schematic diagram of core components in a modern gas chromatograph is shown in Figure 2.13. The flow rate of the carrier gas is maintained at a moderate level (e.g. 50 mL/min) throughout the whole analysis. Gas or liquid samples are introduced through the sample injection system which is designed differently based on the phases of the injected samples. In the case of gaseous samples, the sample is injected directly into instrument and mixed into the line filled with the carrier gas to bring the sample into the analytical system. If the injected sample is in the liquid

phase, the injector port has a different design, where a small chamber is used to hold the liquid sample injected by a gas-tight syringe. The liquid is heated and vaporized in the chamber, and then taken to the analytical system by carrier gas. The column is located statically in the oven and the column temperature is carefully controlled by the oven temperature. In most GC analysis processes, oven temperature is kept constant at a set value, and this is called an isothermal analysis. However, different programmed oven temperatures are also available for some special analytic purposes. The eluted analytes from the column are then collected by the detector for analysis. There are many types of detectors used in GC analysis. The most commonly used detectors are thermal conductivity detector (TCD) or flame ionization detector (FID), both of which are very sensitive. The TCD detector can detect any component other than the carrier gas (i.e. the thermal conductivity of the analyte is different from that of the carrier gas, and this conductivity difference is the origin of the TCD signal).[17] TCD detection is a non-destructive way and thus widely used in GC processes. The FID detector is mainly used to detect hydrocarbons due to its higher sensitivity response to them than that of TCD. The eluted gases from the column at different retention times are pyrolyzed by the flame of the FID placed at the exit of the column, and then get detected. This indicates FID is a destructive detector. Some carbon containing inorganic molecules such as CO_2 and CO can also be detected by FID if a methanator, which can convert these eluted molecules into methane, is placed before the FID. The detection of converted methane can thus reveal the information of those molecules. However, other inorganic compounds cannot be detected by FID.

Apart from the qualitative separation of gaseous analytes, GC can also be applied for quantitative analysis. The peak area of a eluted component in a GC spectrum is proportional to its amount. Therefore, the concentration or the absolute quantity of the gaseous components in a sample can be obtained. They can be calculated by using a calibration curve.

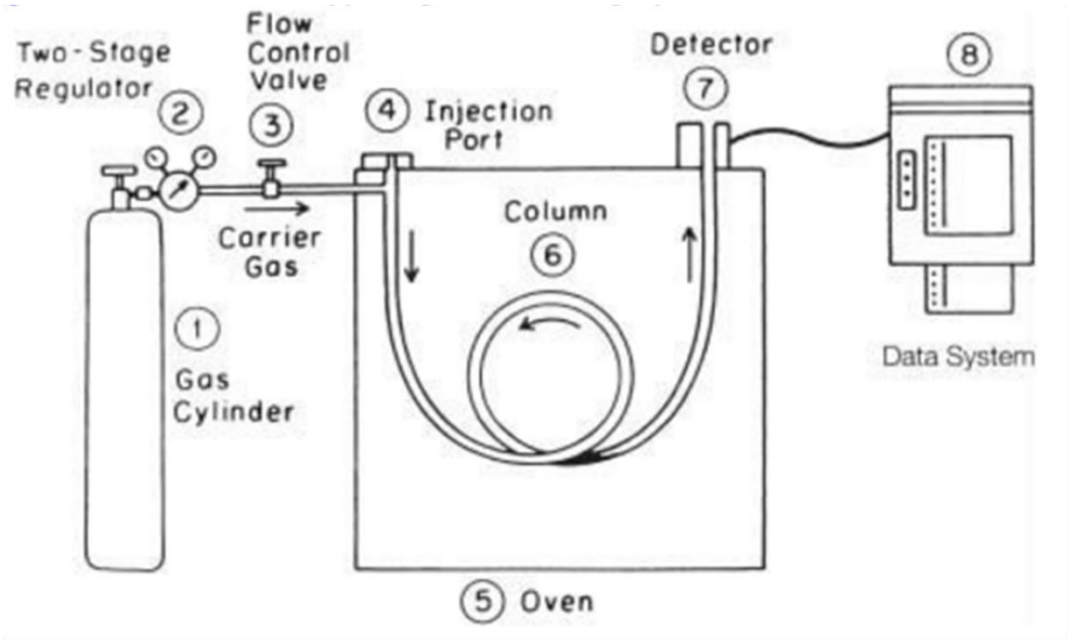

Figure 2.13 A schematic diagram showing components in a typical gas chromatographic system. Reprinted with permission from ref. 17, copyright 2009 John Wiley & Sons, Inc.

2.10 References

1. M. Che and J. C. Vedrine, *Characterization of Solid Materials and Heterogeneous Catalysts*, Volume 1, Wiley-VCH Verlag & Co. KGaA, Weinheim, Germany, 2012.
2. M. T. Weller, *Inorganic Materials Chemistry, Oxford Chemistry Primers*, Volume 23, Oxford University Press Inc., New York, USA, 1994.
3. M. Che and J. C. Vedrine, *Characterization of Solid Materials and Heterogeneous Catalysts*, Volume 2, Wiley-VCH Verlag & Co. KGaA, Weinheim, Germany, 2012.
4. D. Henry, N. Eby, J. Goodge and D. Mogk, in the section of *Bragg's Law*, From the website of *Science Education Resource Center* (access date: 25th June 2013), http://serc.carleton.edu/research_education/geochemsheets/BraggsLaw.html.
5. Y. Ding, in the section of *Fundamental Theory of Transmission Electronic Microscopy*, From the website of *Professor Zhong L. Wang's Nano Research Group* in Georgia Institute of Technology (access date: 26th June 2013), http://www.nanoscience.gatech.edu/zlwang/research/tem.html.
6. J. M. Thomas and W. J. Thomas, *Principles and Practices of Heterogeneous Catalysis*, VCH Publishers Inc., New York, USA, 1997.
7. R. T. Weber, J. Jiang and D. P. Barr, *EMX User's Manual*, Bruker Instruments, Inc., USA.
8. M. G. Clerici and O. A. Kholdeeva, *Liquid Phase Oxidation via Heterogeneous Catalysis: Organic Synthesis and Industrial Applications*, John Wiley & Sons, Inc.,

USA, 2013.

9. *TPR instrument brochure* by CE Elantech, Inc., USA.
10. P. Atkins and J. D. Paula, *Physical Chemistry, Ninth Edition*, Oxford University Press, 2010.
11. A. L. Linsebigler, G. Lu and J. T. Yates, *Chem.Rev.*, 1995, **95**, 735-758.
12. A. J. Bard and L. R. Faulkner, *Electrochemical Methods: Fundamentals and Applications, Second Edition*, John Wiley & Sons, Inc., New York, USA, 2001.
13. A. M. Bond and S. W. Feldberg, *J. Phys. Chem. B*, 1998, **102**, 9966-9974.
14. S. H. Duvall and R. L. McCreery, *Anal. Chem.*, 1999, **71**, 4594-4602.
15. R. S. Nicholson, *Anal. Chem.*, 1965, **37**, 1351-1355.
16. D. K. Gosser, Jr., *Cyclic Voltammetry Simulation and Analysis of Reaction Mechanisms*, Wiley-VCH, Inc., USA, 1993.
17. H. M. McNair and J. M. Miller, *Basic Gas Chromatography, Second Edition*, John Wiley & Sons, Inc., USA, 2009.

Chapter 3 Experimental

Chapter 3 Experimental 96

3.1 Synthesis of rod form β-Ga_2O_3 nanocrystals 98

3.2 Synthesis of plate form β-Ga_2O_3 nanocrystals 99

3.3 Synthesis of particle form γ-Ga_2O_3 nanoparticles 101

3.4 Synthesis of Pd on morphologically different Ga_2O_3 nanocatalysts 102

3.4.1 Pd doped Ga_2O_3 nanocatalysts for methanol synthesis 103

3.4.2 Pd doped Ga_2O_3 nanocatalysts for methanol photodecomposition 104

3.5 Methanol synthesis from CO_2 hydrogenation 105

3.6 Methanol photodecomposition for H_2 evolution 106

3.7 Computational details 109

3.8 Characterizations 111

3.8.1 XRD 111

3.8.2 TEM 111

3.8.3 SEM 112

3.8.4 EPR 112

3.8.5 TPR/D 112

3.8.6 BET 113

3.8.7 XPS 113

3.8.8 CV and CO stripping 114

3.8.9 ssNMR 116

3.8.10 PL and TRPL spectroscopy 116

3.8.11 Raman spectroscopy 118

3.8.12 UV-Visible Spectroscopy 118

3.9 References 120

In this chapter, experimental details of the synthesis of Ga_2O_3 with different shapes are presented. Ga_2O_3 nanocrystals with three distinctive shapes, namely, β-Ga_2O_3 rods, β-Ga_2O_3 plates, and γ-Ga_2O_3 particles, have been prepared successfully. The experimental descriptions for the preparation of corresponding Pd doped (various Pd loading levels) Ga_2O_3 nanocatalysts are also depicted. In addition, details of the catalytic testing conditions for methanol synthesis from CO_2 hydrogenation and H_2 production from methanol photodecomposition are given. Finally, experimental details on material characterizations and computational modeling and calculations are described.

3.1 Synthesis of rod form β-Ga_2O_3 nanocrystals

The rod form β-Ga_2O_3 was synthesized according to the method reported by Zhao *et al.*[1] In a typical synthesis, 0.006 mol $Ga(NO_3)_3$ ($Ga(NO_3)_3.xH_2O$, x≈9; 99.9% trace metal basis, Aldrich) was weighed in a glove box under N_2 atmosphere due to the hygroscopic nature of the sample, and was dissolved in deionized (DI) water in a flask to form a solution A with a metal ion to water molar ratio of 1:100. The mixture was then heated to 80 ℃. With stirring at 430 rpm, a 1.5 mol/L NaOH (pellets, reagent grade, ≥98%, Sigma-Aldrich) solution was added dropwise by a dropping funnel into solution A. A 0.018 mol portion of NaOH, which was three times that of $Ga(NO_3)_3$ was used to form a gallium oxide hydroxide (GaOOH) precipitate. The pH value after mixing was found to be around 6.3-6.5, which was near the neutral point, in order to obtain a maximum amount of precipitate. The mixture was then transferred into a

sealed 50 mL polypropylene centrifuge tube (Corning) which was placed in a shaking bath at a shaking rate of 100 rpm at 80 ℃ for 2 hours for an aging process. The resulting precipitate was recovered by centrifuge (Hettich Universal 320) at 5000 rpm and washed with DI water 4 times to remove any sodium nitrate. Then the rod GaOOH precipitate was re-suspended in DI water (30 mL total volume) under vigorous stirring with a speed of 600 rpm at room temperature for 2 hours. The suspension was transferred into a Teflon cup located in an acid digestion vessel (model 4744, Parr Instrument), which was hydrothermally treated at 100 ℃ in a oven for 2 days and the solid content was washed by DI water 4 times and dried in air at 80 ℃.

The dried rod GaOOH solid was then calcined in a furnace (Caborlite 2416 series) in a flowing stream of air (the air supply was allowed to pass through a twin-columned filter to remove moisture and impurities before entering into a furnace tube) at 900 ℃ for 2 hours, with a heating rate and air flow rate at 2.5 ℃/min and 45 mL/min, respectively. Finally, the calcined sample was allowed to cool down to room temperature naturally. The final product was christened as rod form Ga_2O_3 nanocrystals.

3.2 Synthesis of plate form β-Ga_2O_3 nanocrystals

The plate form β-Ga_2O_3 nanocrystals were prepared through a solid state synthesis method, followed by an ion exchange with various post-treatments according to the method of Yan *et al.*[2] In a typical synthesis, firstly, $KGaO_2$ solid which was a key

precursor was prepared by the following procedure: a stoichiometric mixture of 0.0035 mol K_2CO_3 (anhydrous, 99.99% trace metal basis, Aldrich) and 0.0035 mol Ga_2O_3 (≥99.99% trace metal basis, Aldrich) were ground in a pestle and mortar to make fine powder, which was pelletized into 5 individual pellets with 1 mm thickness. The pellets were heated in a furnace kept at 950 ℃ under an air atmosphere for 12 hours before cooling to room temperature to yield the $KGaO_2$ pellets. The temperature ramping rate and air flow rate for this process were set at 5 ℃/min and 35 mL/min, respectively. The prepared $KGaO_2$ pellets were transferred to a glove box (N_2 atmosphere) from the sealed furnace tube due to the strongly hygroscopic nature of $KGaO_2$. In the glove box, the synthesized $KGaO_2$ was further ground into fine powder before the subsequent preparation of an aqueous $KGaO_2$ solution of designated concentration.

For the preparation of plate form GaOOH, an ion exchange was then employed. In a typical procedure: a 32.5 mL aqueous solution containing $KGaO_2$ (0.2 mol/L) was added dropwise into a 32.5 mL acetic acid solution (0.2 mol/L; volumetric 0.5 mol/L CH_3COOH, Fluka) in a beaker, which was stirred at 500 rpm for 3 hours at room temperature to form the plate form GaOOH nanocrystals. The precipitate was then isolated by centrifugation at 6900 rpm, washed 4 times with DI water and dried in an oven at 60 ℃ overnight.

The plate form β-Ga_2O_3 was obtained by calcination of the as-prepared plate form GaOOH in a furnace at 800 ℃ under an air atmosphere for 3 hours, with a heating rate of 5 ℃/min and air flow rate of 45 mL/min, respectively.

3.3 Synthesis of particle form γ-Ga_2O_3 nanoparticles

The particle form of γ-Ga_2O_3 was synthesized via a modified solvothermal method previously used for ZnO synthesis by our group.[3] In a typical synthesis, the precursor, 6.38 mmol gallium(Ⅲ) acetylacetonate (99.99% trace metal basis, Aldrich), was introduced into 15 mL (33.93 mmol) troictylamine (TOA, 98%, Aldrich) solvent in a 3-necked flask. 2 mL (6.38 mmol) of oleic acid (technical grade, 90%, Aldrich) was then injected into the flask using a plastic syringe (slip-tip, BD^{TM}). The 2 side necks of the flask were fitted with a thermometer and a nitrogen gas supply, respectively. The central neck was connected to a reflux condenser which was circulated with flowing water in an exterior cooling jacket. The mixture was then heated under nitrogen to 290 ℃ and maintained at that temperature for 1 hour in order to decompose the gallium(Ⅲ) acetylacetonate to yield γ-Ga_2O_3. The mixture was magnetically stirred throughout the decomposition process. After the mixture was cooled down to room temperature, the solid product was washed extensively by acetone (≥99.7%, Barrettine) 10 times and centrifuged at 6500 rpm before it was collected as a cake. The collected solid cake was dried in an oven kept at 70 ℃ in air overnight in order to get the final dry particle form of γ-Ga_2O_3.

The particle form of γ-Ga_2O_3 was also used to investigate the effects of varying capping agent and reaction time (kept at 290 ℃ but the reaction time was varied to 10 min, 30 min, 1 hour, 2 hours, and 4 hours, respectively), while keeping all other reaction parameters the same. Oleic acid and oleylamine (technical grade, 70%, Aldrich) were two organic surfactants (i.e. capping agents) frequently used for the

controlled synthesis of metal oxide nanocrystals with various morphologies. The effects of oleic acid or oleylamine and their mixture on the final shape of γ-Ga_2O_3 nanoparticles were therefore studied (experimental details are shown in Table 3.1-3.3, respectively).

Table 3.1 Variation of oleic acid/Ga^{3+} molar ratio for the synthesis of γ-Ga_2O_3 nanoparticles

Surfactant studied	Oleic acid to Ga^{3+} ion molar ratio							
Oleic acid	0	0.4	1	2	3	4	8	10

Table 3.2 Variation of oleylamine/Ga^{3+} molar ratio for the synthesis of γ-Ga_2O_3 nanoparticles

Surfactant studied	Oleylamine to Ga^{3+} ion molar ratio				
Oleylamine	0	1	2	4	8

Table 3.3 Variation of oleylaime/oleic acid molar ratio for the synthesis of γ-Ga_2O_3 nanoparticles (with oleic acid/Ga^{3+} ratio kept at 1)

Surfactant studied	Oleylamine to oleic acid molar ratio			
Oleylamine+oleic acid	1	2	4	8

3.4 Synthesis of Pd on morphologically different Ga_2O_3 nanocatalysts

For the preparation of Pd doped catalysts**,** a modified wet impregnation method was used. $Pd(NO_3)_2$ solution (14.87 wt% Pd assay, Alfa Aesar) was used as the source of soluble metal precursor to coat onto an appropriate type of Ga_2O_3 support. Both rod and plate forms of Ga_2O_3 nanocrystals and their Pd doped counterparts (with various Pd dopings) were studied for methanol synthesis from CO_2 hydrogenation. As for the reaction of methanol photodecomposition to H_2, all three morphologically different Ga_2O_3 materials and their Pd doped nanocatalysts were studied. For this reason, the

detailed experimental procedures for preparing Pd doped Ga_2O_3 nanocatalysts are categorized into the following two groups:

3.4.1 Pd doped Ga_2O_3 nanocatalysts for methanol synthesis

For each shape of Ga_2O_3, Pd/Ga_2O_3 catalysts with corresponding Pd dopings of 1 wt%, 2 wt% and 5 wt% were prepared. In a typical synthesis, a designated amount of $Pd(NO_3)_2$ was added to Ga_2O_3 in the form of an aqueous solution, the resulting slurry was stirred at a speed of 600 rpm at room temperature for 16 hours to achieve the adsorption/desorption equilibrium of the Pd precursor on Ga_2O_3. The mixture was then heated slowly on a hot plate up to 70 ℃ with stirring at 780 rpm to gradually evaporate off the water from the system, and the solid was dried at 70 ℃ in an oven in air overnight.

The dried sample was then calcined in a furnace under a flowing stream of air (50 mL/min), at 300 ℃ for 2 hours, with a ramping rate of 3 ℃/min to get the corresponding PdO/Ga_2O_3. The PdO/Ga_2O_3 sample was then reduced *in-situ* in the reactor under H_2 at 250 ℃ for 1 hour, with a ramping rate of 5 ℃/min and H_2 flow rate of 20 mL/min, in order to get the final Pd/Ga_2O_3 nanocatalyst for the reaction. For the use of reduced Pd/Ga_2O_3 nanocatalyst for some characterizations, the calcined sample was reduced *ex-situ* in a dilute H_2 (molar ratio of H_2/N_2=1:2, gas flow rate at 50 mL/min) at 200 ℃ for 1 hour, with a ramping rate of 5 ℃/min. After cooling to room temperature, the reduced Pd/Ga_2O_3 was placed into a specimen tube without any exposure to air.

3.4.2 Pd doped Ga_2O_3 nanocatalysts for methanol photodecomposition

All the three shapes of Ga_2O_3 (i.e. rod, plate and particle forms) and their Pd doped nanocatalysts were studied for H_2 production from methanol photodecomposition. For each shape of Ga_2O_3, corresponding Pd/Ga_2O_3 nanocatalysts were prepared with the final Pd loadings set at 0.5 wt%, 1 wt%, 2 wt% and 5 wt%, respectively. The preparation procedure was similar to those of catalysts prepared for methanol synthesis described above. All the calcined samples were pre-reduced in a furnace in dilute H_2 (molar ratio of H_2/N_2=1:2) at 200 ℃ for 1 hour, with a ramping rate of 5 ℃/min and a flow rate of 50 mL/min in order to get the final reduced Pd/Ga_2O_3 photocatalysts. The reduced sample was then transferred into a specimen tube without exposure to air, for photoreaction testing and characterization.

For comparison purposes, commercial β-Ga_2O_3, commercial TiO_2 P25, and their corresponding 1 wt% metal doped catalysts were prepared. The experimental details are listed in Table 3.4. Unless stated, all other preparation procedures were kept constant for all the catalysts.

Table 3.4 Details of the preparation of catalysts for the photoreaction

Sample number	Catalyst prepared	Metal precursor	Calcination temperature (℃)	Reduction temperature (℃)
1	1% Pd/β-Ga_2O_3 commercial	$Pd(NO_3)_2$ solution (14.87% Pd assay, Alfa Asear)	300	200
2	1% Pt/β-Ga_2O_3 commercial	$Pt(NO_3)_4$ solution (16.46% Pt assay, Johnson Matthey)	300	200
3	1% Pd/TiO_2 P25	$Pd(NO_3)_2$ solution (14.87% Pd assay, Alfa Asear)	300	200
4	1% Pt/TiO_2 P25	$Pt(NO_3)_4$ solution (16.46% Pt assay, Johnson Matthey)	300	200
5	1% Ag/TiO_2 P25	$AgNO_3$ (BioXtra, ＞99%, Sigma-Aldrich)	450	200
6	1% Cu/TiO_2 P25	$Cu(NO_3)_2$ ($Cu(NO_3)_2.xH_2O$, x≈3; 99.999%, trace metal basis, Aldrich)	500	250

The calcination and reduction temperatures were selected by taking the decomposition and reduction of corresponding metal precursors into consideration, which ensured the metal components in the final catalysts were at the metallic state.

3.5 Methanol synthesis from CO_2 hydrogenation

Catalytic testing for hydrogenation of CO_2 to methanol was conducted in collaboration with Prof. Xinlin Hong and Mr. Ziyan Zeng at Wuhan University, China. The tests were carried out at a total pressure of 5 MPa using a tubular fixed bed reactor (12.7 mm outside diameter) by sandwiching 0.2 g powder catalyst (i.e. the appropriate PdO/Ga_2O_3). The catalytic performance (conversion and yield) below those thermodynamic predicted values was ensured, as the reaction conditions should be selected in a kinetic controlled regime for meaningful catalytic comparisons. A CO_2–H_2 reaction gas mixture with a molar ratio of 1/3 was fed at a flow rate of 20

mL/min through the catalyst bed. The reaction temperature was fixed at 250 ℃. Before each test, the catalyst was first pre-reduced *in situ* at 250 ℃ for 1 hour under a H_2 flow (20 mL/min) and cooled down to room temperature before undergoing further catalytic evaluations at increasing temperatures and pressures. The products (methanol and CO were the only carbon containing products with no methane or dimethylether detected) were analyzed by a calibrated GC equipped with a TCD and FID detectors.

3.6 Methanol photodecomposition for H_2 evolution

The photodecomposition of methanol was conducted in an optical grade round bottom quartz flask with a total volumetric capacity of 300 mL (type 214 quartz; Robson Scientific). In a typical reaction, the starting reagents methanol (≥99.9%, Sigma-Aldrich) and DI water mixture (1:1 v/v, total volume 100 mL) were added into the quartz flask. A sample of 0.1 g of the appropriate catalyst was then added into the flask and this operation was carried out in a glove box under N_2 atmosphere to prevent any unwanted oxidation of Pd. The quartz reactor was then securely sealed with a Suba-Seal rubber cap (Sigma-Aldrich) and applied with high vacuum grease (Dow Corning) inside the neck of the flask. Meanwhile, parafilm (Parafilm ®M, Sigma) was also wrapped inside and outside the cap to further prevent any gas leakage. Before each reaction, with stirring, 5% CH_4/Ar gas was purged into the reaction mixture for 30 min to eliminate air contamination and ensure the reaction environment was under 5% CH_4/Ar. Since CH_4 is one of the most stable organic

molecules, it can be used as an internal standard for GC-TCD analysis as it would remain chemically unchanged under the reaction conditions.

A photoreaction station (LightChem brand) was used to carry out all these reactions at ambient temperature. As for the light source, 12 low pressure mercury lamp bulbs with 7.2 W electrical output (UV output is 2.2 W, G8T5, Ushio) each and illumination peaking at 253.7 nm (UVC) were fitted into the wall of the photoreaction station (four of them were on the left side of quartz flask, with distance about 15 cm to the flask; four were on the right side of the flask with the same distance to the flask; four were on top of flask with distance about 10 cm). The reaction mixture was stirred with medium speed throughout the reaction process. The typical reaction time was 5 hours. After the 5 hours photoreaction, 30 mL gas products were taken by a syringe (slip-tip, BD^{TM}) and injected into a calibrated GC for analysis.

The GC used for analyzing products of this reaction was equipped with a complex configuration with two analytical channels (A and B), two TCD detectors (A and B) and three columns (1, 2 and 3). Once the sample was injected, it was trapped by a 1.0 cc gas sample loop located in each channel. Channel B was first connected for analyzing H_2 gas, using N_2 as a carrier gas (line pressure supply: 50 psig). The column used in this channel B for H_2 was the column 3 which combined two column parts (HayeSep T+Molecular Sieve 5A) into one. The HayeSep T part eluted H_2 first while delaying all other heavier gases which flew into the Molecular Sieve 5A part after finishing the elution of H_2 that was detected by TCD B. All other gas components were then analyzed by connecting Channel A equipped with two separate columns,

namely, column 1 (HayeSep N) and column 2 (Molecular Sieve), using He as a carrier gas (line pressure supply: 50 psig) and TCD A. The outputs from the two TCD signals were combined into one single electrical signal and presented on a computer screen. The temperatures of injector, oven and detector were 100 ℃, 60 ℃ and 200 ℃, respectively. The column head pressures for columns 1, 2 and 3 were set as 18 psig, 18 psig, and 19 psig, respectively.

Liquid phase samples from some selected after-reaction liquids were qualitatively analyzed by a Perkin Elmer 200 series high-performance liquid chromatography (HPLC) system equipped with a refractive index detector.

The tests for all three shapes of Ga_2O_3 and their Pd doped photocatalysts for this reaction were carried out. Additionally, a 0.5% Pd/γ-Ga_2O_3 particle sample was selected as a probe to further study the effects of reaction time and methanol concentration on H_2 production. The reaction time studied was at 2, 5, 8, 11, and 14 hours, with all other reaction parameters kept constant. The methanol concentration (volumetric) was varied from 10%, 30%, 50%, to 70%, respectively, with the total volume of the liquid mixture kept at 100 mL and all other conditions unchanged. Control experiments were also carried out to ensure the data collected were significant.

Finally, for comparison purposes, commercial β-Ga_2O_3, commercial TiO_2 P25, and their corresponding 1 wt% metal doped catalysts were tested. The details are listed in Table 3.5. Unless specified, all other reaction conditions were the same as described in the above typical procedure.

Table 3.5 Methanol photodecomposition on commercial Ga_2O_3 and commercial TiO_2 P25 catalysts doped with various metals (reaction time: 5 hours)

Sample number	Catalysts
1	1% Pd/β-Ga_2O_3 commercial (253.7 nm UV)
2	1% Pt/β-Ga_2O_3 commercial (253.7 nm UV)
3	1% Pd/TiO_2 P25 (253.7 nm UV)
4	1% Pd/TiO_2 P25 (350 nm UV)
5	1% Pt/TiO_2 P25 (350 nm UV)
6	1% Ag/TiO_2 P25 (350 nm UV)
7	1% Cu/TiO_2 P25 (350 nm UV)
8	Pure TiO_2 P25 (350 nm UV)

Notice that 350 nm UV in parenthesis denotes that a catalyst was irradiated using 12 black UVA bulbs (electrical output 8 W each, Hitachi FL8BL-B) with the radiation centered at 350 nm.

3.7 Computational details

Computational modeling and calculations were conducted in collaboration with Mr. Jin Qu in our group for the rod form and plate form Ga_2O_3. Atomistic models, density of states (DOS), Bader charge densities[4-7] and energies to create an oxygen vacancy on Ga_2O_3 slab with (002), (110) and (111) surfaces were developed.

In modeling, all calculations were performed in the framework of DFT by using the Vienna ab initio simulation package (VASP).[8-11] The projector-augmented wave (PAW)

potentials[12,13] were used for the core electron interaction. The Perdew–Burke–Ernzerhof (PBE) functional[14,15] based on the generalized gradient approximation (GGA) was employed to evaluate the non-local exchange-correlation energy.

A plane wave basis set with a cutoff energy of 400 eV and a k-point grid determined by the Monkhorst-Pack method were used. In the bulk and surface unit cells optimizations and DOS calculations, the k-point sampling used a $2\times8\times4$ grid for the bulk, $4\times8\times1$ for the (002) and $4\times4\times1$ for the (110) and (111) slabs. For structure optimization, all the ionic positions were allowed to relax until the forces were less than 0.01 eV/Å.

The unit cell for the bulk Ga_2O_3 optimization contained 4 Ga_2O_3 units. The optimized cell parameters were a=12.255 Å, b=3.052 Å, c=5.828 Å, which was in good agreement with the experimental values (a=12.230 Å, b=3.040 Å, c=5.800 Å). The Ga_2O_3 (002), (110) and (111) surfaces were modeled by periodic models. Each contained 8 Ga_2O_3 molecular units. The 1×1 surface unit cell (6.315×3.052 Å^2) of (002) , (5.828×6.315 Å^2) of (110) and (6.315×6.578 Å^2) of (111) slab were utilized in this study. A vacuum layer of 15 Å along the z direction perpendicular to the surface was employed to prevent spurious interactions between the repeated slabs. Two different terminated energetic Ga_2O_3(002) surface unit cells were built. A non-stoichiometric model was used to keep the top and bottom layer symmetric in the slab. The O-terminated slab contained 26 O atoms and 16 Ga atoms, while the Ga-terminated slab contained 22 O atoms and 16 Ga atoms. The slab unit cell

parameters of the polar (002) were the same as those in its non-polar model. To estimate the energy required to create a surface oxygen vacancy, a 2×2 supercell for (002), a 1×2 supercell for (110) and a 2×1 supercell for (111) were used to make the surface vacancy density the same. The k-point sampling used a 2×4×1 grid for (002) and (111) supercell models, and a 4×2×1 grid for (110) supercell.

3.8 Characterizations

3.8.1 XRD

Powder X-ray diffraction (PXRD) were conducted on a Philips PW1050/81 diffractometer, operating in Bragg-Brentano focusing geometry and using Cu Kα radiation (λ = 1.5418 Å) generated from a Philips PW1729 X-ray generator operated at 40 kV and 30 mA. Typically, a powder sample was dispersed into an appropriate amount of acetone and sonicated before adding dropwise onto a glass specimen slide to achieve a homogeneous sample layer. After the acetone was totally evaporated, the sample slide was measured from 10° to 70° (2θ), with step size and scan time at 0.05°(2θ) and 25 min, respectively.

3.8.2 TEM

TEM images were obtained using a JEOL 2010 microscope with a high resolution pole piece. The accelerating voltage was 200 kV. A typical sample was prepared by placing a drop of very low-concentrated nanoparticle ethanol (ACS reagent, absolute, ≥99.8%, Sigma-Aldrich) suspension onto a carbon-coated copper grid, and allowing

the solvent to evaporate. For selected samples, HRTEM and SAED were examined for further in-depth analysis.

3.8.3 SEM

Scanning electron microscopy (SEM) images were obtained on a FEI Quanta 200 microscope at Wuhan University, China. The accelerating voltage was 30 kV. Before SEM measurement, a typical sample was sputtered by Au under an Ar atmosphere to ensure the conductivity required by SEM.

3.8.4 EPR

EPR was conducted for the three pure Ga_2O_3 of different shapes, i.e. Ga_2O_3 rods, plates and particles, respectively. X-band CW EPR spectra were recorded on a Bruker EMX spectrometer using an Elexsys probehead with 17-40 mg sample placed in 4 mm (outside diameter) quartz tube separately. The handling process of loading a sample into an EPR tube was conducted in glove box under N_2 flow to avoid oxygen contamination. The microwave power was set at 0.6325 mW with attenuation at 25 dB.

3.8.5 TPR/D

TPR was obtained using a CE Intsrument TPDRO1100. For each measurement, a sample with about 25 mg weight was used. The sample was pretreated under He (10 mL/min) and heated from 40 ℃ to 150 ℃ with a ramping rate at 10 ℃/min. After being held at 150 ℃ for 5 min, the sample was then cooled down to 40 ℃. TPR

analysis was then carried out with a ramping rate of 10 ℃/min from 40 ℃ to 800 ℃ under a flowing stream of 5% H_2/Ar (20 mL/min). Samples were held for 30 min at 800 ℃ before cooling to room temperature.

The TPD profile of a sample was obtained using a Micromeritics Chemisorb 2720. The sample was firstly pretreated under He from room temperature to 750 ℃ with a ramping rate of 10 ℃/min, and kept at 750 ℃ for 30 min before cooling to room temperature. For the analysis, CO_2 was flowed over the sample for 60 min at room temperature for adsorption, and then He was flowed through for another 60 min to get rid of weakly adsorbed molecules. Desorption process was then carried out by ramping the sample from room temperature to 800 ℃ with a rate at 10 ℃/min under a flowing stream of He. A sample weighed100 mg was used for each CO_2 TPD.

3.8.6 BET

N_2 sorption was carried out at -196 ℃ (77 K) by a CE instrument Sorptomatic 1990 system for three different shaped Ga_2O_3 samples. For each measurement, a 300 mg sample was used. Prior to measurement, the sample was pretreated under vacuum at 100 ℃ overnight for cleaning its surface and degassing purposes. The Brunauer−Emmett−Teller (BET) method was used within a relative pressure range of p/p_0=0.05～0.35 to elucidate the specific surface area (S_{BET}, m^2/g) of the sample.

3.8.7 XPS

XPS characterization was carried out in collaboration with Prof. John. S. Foord and

Dr. Jingping Hu at University of Oxford. XPS was performed using a Kratos XSAM800 system. A typical sample containing Pd was first pre-reduced in diluted H_2 (H_2/N_2=1:2) at 200 ℃ for 1 hour with a flow rate of 50 mL/min. The sample was then transferred into a glove bag under N_2. The powder sample was placed onto a carbon disc (a double adhesive electrically conductive sheet, Agar Scientific) which was stuck on a sample stub. The prepared sample was presented as a thin and uniform layer covering the carbon disc, which was then transferred in the glove bag to the XPS chamber without exposure to air.

XPS was performed using an Al Kα (1486.6 eV) X-ray source and a hemispherical electron energy analyzer. The acceleration voltage was 10 kV and the emission current was 20 mA. The spectra were acquired at around a 90 degree emission angle. The electron energy analyzer operated in fixed analyzer transmission (FAT) mode, with constant pass energy of 50 eV for both survey (wide) scans and high resolution scans. The peak fitting was conducted using CasaXPS, with a Shirley background subtraction, and a mixed Lorentzian (30%) and Gaussian (70%) lineshape.

3.8.8 CV and CO stripping

The cyclic voltammetry (CV) and CO stripping measurements were collaborated with Mr. Feng Xu in my group and were carried out in a conventional three-electrode cell containing 0.5 mol/L H_2SO_4 at room temperature (25 ℃). Samples which contained Pd components were pre-reduced in diluted H_2 (H_2/N_2=1:2) at 200 ℃ for 1 hour with a flow rate of 50 mL/min. Before each measurement, a 3 mg catalyst, 500 μL

Millipore water (18.2 MΩ · cm, at 25 ℃) and 50 μL perfluorosulfonic acid-PTFE copolymer (5% w/w solution, Alfa Aesar) were ultrasonically mixed for 10 min to form an ink. Then 24 μL ink was pipetted onto a glassy carbon electrode (GC electrode) which was pre-polished to a mirror-like finish using an aluminum oxide (<50 nm) slurry on a polishing cloth (purchased from BASI). The electrode was then dried under vacuum at room temperature for 30 min. The electrode geometric area exposed to the electrolyte was 0.071 cm^2. The Pd loading was 0.092 mg/cm^2. The electrolyte was purged with ultra high purity argon for 30 min before testing. For CO stripping, the GC electrode was immersed in the Ar pre-saturated electrolyte and bubbled with ultra high purity CO for 30 min. After the CO bubbling, the electrode was rinsed with plenty of Millipore water and moved into the testing cell where the electrolyte was also Ar pre-saturated, for a CO stripping measurement. The CV and CO stripping tests were carried out using an Ivium CompactStat instrument. Platinum wire was used as the counter electrode, and a saturated calomel electrode (SCE) was used as reference electrode. The GC electrode, platinum wire and SCE were all purchased from BASI. The scan rate was set at 0.05 V/s. The voltage positions of the measured values were based on referencing to SCE (scanned from -0.242 V to 0.958 V). However, the presented data in CV and CO stripping spectra in further chapters in this thesis were transferred to a standard hydrogen electrode (SHE) reference (plus 0.242 V for the measured voltage positions), in order to facilitate comparison with literature where SHE references were more widely used. The CO stripping was used to calculate the electrochemically active surface (EAS) by means of the Equation 3.1:

$$EAS_{CO} = \frac{Q_{CO}}{[Pd] \times 4.84} \quad \text{(Eq. 3.1)}$$

where Q_{co} is the charge for CO desorption (C), 4.84 (C/m^2) represents the charge density required to oxidize a CO monolayer on Pd surface, and [Pd] represents the Pd loading (g).[16]

3.8.9 ssNMR

Solid state nuclear magnetic resonance (ssNMR) experiments were conducted in collaboration with Prof. Heyong He and Dr. Lin Ye at Fudan University, Shanghai, China. Ga_2O_3 samples without Pd were analyzed. For pretreatment, the sample was placed into a glass tube, which was connected to a vacuum system. A degassing pretreatment was carried out at 300 ℃ for 2 hours under vacuum (10^{-1} Pa). After adding 3 mmol trimethylphosphine (TMP, J&K) per gram of the sample, the glass tube was immersed in liquid nitrogen in vacuum. Then the sealed glass tube was transferred to a glove box. Under N_2 atmosphere, the sample was then transferred to a 4 mm ZrO_2 rotor and closed with Kel-F lids. All ssNMR measurements were performed on a Bruker Advance DSX-300 spectrometer at room temperature. All ^{31}P magic angle spinning (MAS) NMR spectra were obtained at a MAS speed of 12 kHz with a 30 °pulse and a recycle delay of 300 s.

3.8.10 PL and TRPL spectroscopy

The nanosecond time-resolved photoluminescence (referred to ns-TRPL) was conducted with a commercial Ti:Sapphire regenerative amplifier laser system as the

excitation light source. The 255 nm excitation laser pulse was produced from an optical parametric amplifier (OPA) pumped by the 800 nm fundamental (40 fs, 1 kHz) from the Ti:Sapphire laser system. The ns-TRPL were obtained based on a gated method using an intensified CCD (ICCD) as detector for ns-TRPL spectra covering spectral region from 280 to 670 nm. The ICCD was synchronized to the Ti:Sapphire laser system to allow recording ns-TRPL spectra at various designated time intervals after the photo-excitation. The instrument response function (IRF) of the TRPL measurement was 2 ns. As for the time decay profiles, The TRPL intensities were given by integrated area of the TRPL spectra (in wavelength range from 300 to 650 nm) recorded at a series of time intervals after the photoexcitation. To facilitate comparison of the decay dynamics, the intensities of TRPL in the different samples were normalized to those at ~1 ns after the excitation.

Static PL spectra were acquired by a Jobin Yvon FluoroMax-4 spectrofluorometer with a home-built powder sample holder for quantitative measurement of PL spectrum and intensity.

All the ns-TRPL and static PL measurements were performed at room temperature and atmospheric pressure with the samples in solid state.

Kinetic analysis of TRPL decay profiles (I(t)) acquired from the ns-TRPL measurements (from 0 to ten μs) required fitting with multi-exponential function (Equation 3.2):

$$I(t) = \sum(a_i \times \exp(-t/\tau_i)) \text{ with } \sum a_i = 1 \quad \text{(Eq. 3.2)}$$

where τ_i is the time constant, and a_i is the associated amplitude, indicating percentage

contribution of component τ_i to the overall PL decay. The time constant (τ_i) and related amplitude (a_i) derived from fittings of experimental ns-TRPL decay profiles for the three morphology types of Ga_2O_3 samples without or with different Pd loadings are listed in Table 6.7. Included also in the table are the amplitude weighted average time constant τ_{av} ($\tau_{av} = \Sigma(a_i \times \tau_i)$) for each sample system.

3.8.11 Raman spectroscopy

Measurements were conducted by a Perkin Elmer RamanStation 400F spectrometer. The spectrometer was equipped with a monochromator, a filter system and a CCD detector. The powder sample was placed onto the center of a microscope slide and pressed to a flat surface before loading into a sample compartment. The sample was excited by a near infrared (NIR) 785 nm laser (at 10% laser power) with a resolution of 2 cm^{-1} in the range of 100 to 900 cm^{-1} . A USB CCD video camera with auto video focus was used for the alignment of sample before analysis.

3.8.12 UV-Visible Spectroscopy

Ultraviolet-Visible (UV-Vis) spectra were acquired by using a Perkin Elmer Lambda 750S UV/Vis/NIR spectrometer from 800 nm to 200 nm. The spectrometer was equipped with a dual-lamp light system which consisted of a tungsten halogen lamp and a deuterium lamp. During each measurement (started from 800 nm to 200 nm), the working lamp changed from the tungsten lamp to the deuterium lamp at a set position of 319.2 nm. The measurements were taken using solid samples. Typically,

0.1 g catalyst was mixed with 500 mg KBr (BioXtra, ≥99.0%, Sigma-Aldrich) using a mortar and pestle and was then pressed into a pellet. The pellet was mounted onto the sample holder and transferred into the sample compartment. It was important to use diluted catalyst (0.1 g in 500 mg KBr) which ensured the absorbance was below 1.

3.9 References

1. Y. Zhao, R. L. Frost and W. N. Materns, *J. Phys. Chem. C.,* 2007, **111**, 16290-16299.
2. S. Yan, L. Wan, Z. Li, Y. Zhou, Z. Zou, *Chem. Commun.*, 2010, **46**, 6388-6390.
3. A. McLaren, T. V. Solis, G. Li and S. C. Tsang, *J. Am. Chem. Soc.*, 2009, **131**, 12540-12541.
4. R. F. W. Bader, *Atoms in Molecules*, in *Encyclopedia of Computational Chemistry*, John Wiley and Sons, Ltd, 2002.
5. W. Tang, E. Sanville, and G. Henkelman, *J. Phys.: Condens. Matter.,* 2009, **21**, 084204 (pages 1-7).
6. E. Sanville, S. D. Kenny, R. Smith, and G. Henkelman, *J. Comput. Chem.*, 2007, **28**, 899-908.
7. G. Henkelman, A. Arnaldsson, and H. Jonsson, *Comput. Mater. Sci.*, 2006, **36**, 254-360.
8. G. Kresse and J. Hafner, *Phys. Rev. B,* 1993, **47**, 558-561.
9. G. Kresse and J. Hafner, *Phys. Rev. B,* 1994, **49**, 14251-14269.
10. G. Kresse, and J. Furthmüller, *Comput. Mat. Sci.*, 1996, **6**, 15-50.
11. G. Kresse, and J. Furthmüller, *Phys. Rev. B,* 1996, **54**, 11169-11186.
12. P. E. Blochl, *Phys. Rev. B,* 1994, **50**, 17953-17979.
13. G. Kresse, and D. Joubert, *Phys. Rev. B,* 1999, **59**, 1758-1775.
14. J. P. Perdew, K. Burke, and M. Ernzerhof, *Phys. Rev. Lett.*, 1996, **77**, 3865-3868.
15. J. P. Perdew, K. Burke, and M. Ernzerhof. Erratum, *Phys. Rev. Lett.*, 1997, **78**,

1396.

16. A. Pozio, M. D. Francesco, A. Cemmi, F. Cardellini and L. Giorgi, *J. Power Sources*, 2002, **105**, 13-19.

Chapter 4 Synthesis and characterization of morphologically different Ga_2O_3 particles

Chapter 4 Synthesis and characterization of morphologically different Ga_2O_3 particles 122

4.1 Introduction 124

4.2 Synthesis and characterization of rod form Ga_2O_3 126

4.2.1 Preparation of rod form GaOOH 126

4.2.2 Preparation and characterization of rod form Ga_2O_3 127

4.2.2.1 PXRD, TEM, SEM and BET 127

4.2.2.2 Raman spectroscopy 130

4.2.2.3 UV-Visible Spectroscopy 130

4.3 Synthesis and characterization of plate form Ga_2O_3 132

4.3.1 Preparation of plate form GaOOH 132

4.3.2 Preparation and characterization of plate form Ga_2O_3 134

4.3.2.1 PXRD, TEM, SEM and BET 134

4.3.2.2 Raman and UV-Visible spectroscopy 136

4.4 Synthesis and characterization of particle form Ga_2O_3 138

4.4.1 PXRD, TEM and BET 138

4.4.2 Raman and UV-Visible spectroscopy 139

4.4.3 Investigation of synthetic parameters 141

4.4.3.1 Effect of reaction time 141

4.4.3.2 Effect of oleic acid/ Ga^{3+} molar ratio 142

4.4.3.3 Effect of oleylamine/Ga^{3+} molar ratio 144

4.4.3.4 Effects of using oleylamine and oleic acid mixture and their molar ratios to Ga^{3+} 145

4.5 Conclusion 146

4.6 References 148

4.1 Introduction

Ga_2O_3 is an important semiconducting material with a wide bandgap of around 4.9 eV at room temperature.[1] It has versatile applications in optoelectronic devices, high-temperature stable gas sensors, and heterogeneous catalysis and photocatalysis. Ga_2O_3 is known to exhibit 5 different possible polymorphs, which are α, β, γ, δ and ε phases, respectively. Among these polymorphs, the monoclinic β-Ga_2O_3 is the most chemically and thermally stable structure (with melting point around 1725 ℃), and it was also reported to be commonly formed under ordinary synthetic conditions.[2] Other phases of Ga_2O_3 can be made under different designated synthetic conditions, and these polymorphs are all converted into the monoclinic β-Ga_2O_3 if thermally treated above 850 ℃.[3] Polymorphs including α, δ and ε phases are far less applied and studied due to either poorer thermal stability or greater difficulty in determination of their crystal structures. Apart from the most extensively investigated β-Ga_2O_3, γ-Ga_2O_3 (a metastable cubic structure but with much less crystallinity) has been attracting increasing attention for its optical and photocatalytic properties.[4]

In the field of heterogeneous catalysis and photocatalysis, Ga_2O_3 has been proven to be active for various reactions. For example, in recent years, Ga_2O_3 when mixed with Pd can catalyze methanol formation from CO_2 hydrogenation.[5-7] In addition, the semiconducting nature of Ga_2O_3 makes it a good potential candidate for a variety of industrial photocatalytic applications ranging from photocatalytic water splitting, wastewater treatment, aromatic compounds photodecomposition, to methanol photodecomposition.[8] Nanostructured Ga_2O_3 is of particular interest for the above

applications. Thus, nanosized Ga_2O_3 materials with a large variety of morphologies such as nanorods, nanoplates, nanosheets, nanowires and nanotubes have been synthesized successfully.[1] By tuning the morphology of Ga_2O_3 nanomaterials, the exposed surface can be varied, and thus will affect their catalytic performance. As a result, synthesis and characterization of morphologically different Ga_2O_3 nanomaterials will provide advancements in understanding their shape dependent catalytic properties.

In this chapter, the focus is placed upon the synthesis and characterization of Ga_2O_3 nanomaterials with three different shapes, namely, β-Ga_2O_3 rods, β-Ga_2O_3 plates, and γ-Ga_2O_3 particles. The rod form of Ga_2O_3 was prepared via a precipitation method followed by hydrothermal treatment and calcination,[9] whereas the plate form of Ga_2O_3 was fabricated through a solid state synthesis with subsequent ion exchange and calcination.[1] Finally, metastable γ-Ga_2O_3 particles were synthesized via a solvothermal protocol.[10] Investigations into the effects of reaction time and the use of surfactants on directing particle growth were also studied over the γ-Ga_2O_3 system. Characterizations including PXRD, TEM (including HRTEM and ED), SEM, BET surface area measurement, Raman spectroscopy and UV-Visible absorption spectroscopy were conducted in order to assess the fundamental physicochemical properties of these shape-varied Ga_2O_3 nanomaterials. This chapter will also provide information to underpin the studies of their interaction(s) with metal nanoparticles and their corresponding catalytic and photocatalytic properties which will be presented in the following two chapters.

4.2 Synthesis and characterization of rod form Ga_2O_3

4.2.1 Preparation of rod form GaOOH

The rod form of Ga_2O_3 was synthesized based on the initial formation of GaOOH rods which was prepared via precipitation and hydrothermal treatment.[9] The GaOOH was prepared by precipitating the $Ga(NO_3)_3$ with NaOH at 80 ℃ and the final pH was controlled in the range of 6.3-6.5. Due to the amphoteric nature, the final pH was kept at this neutral value in order to maximize the formation of GaOOH precipitate. The crucial GaOOH rod formation process was found to take place during the 2 hours aging time of the fluffy precipitate as demonstrated by Zhao *et al.*[9] The subsequent hydrothermal treatment at 100 ℃ was conducted to promote further growth of the GaOOH rods. The prepared GaOOH rods were analyzed by PXRD and TEM and the results are shown in Figures 4.1 and 4.2 respectively.

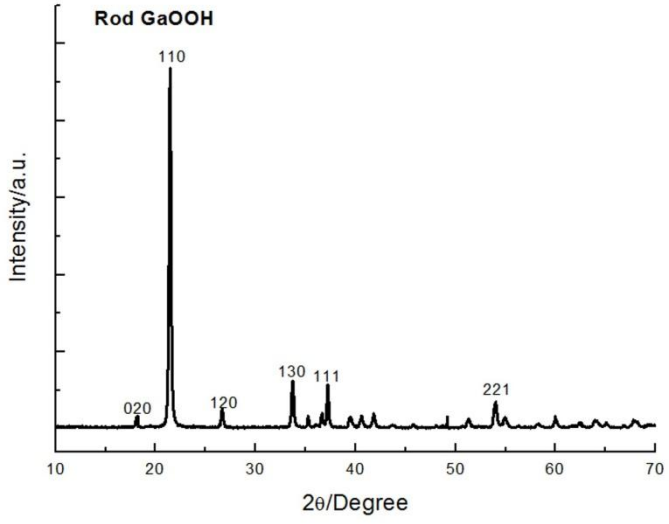

Figure 4.1 PXRD pattern of the rod form orthorhombic GaOOH.

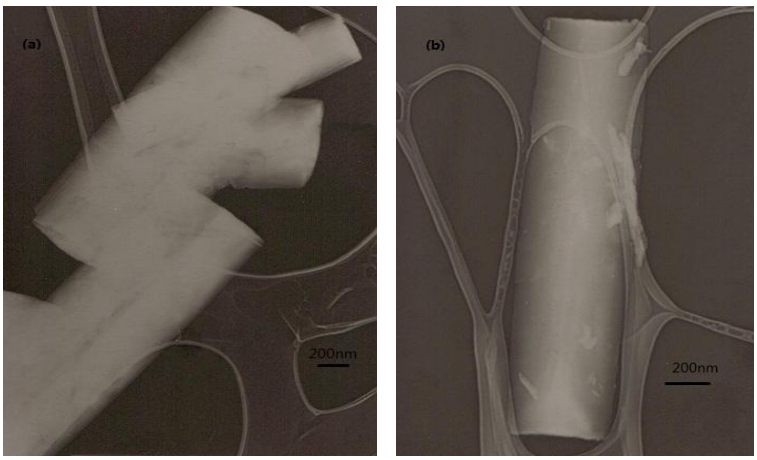

Figure 4.2 TEM images of the GaOOH nanorods.

From the PXRD pattern, the prepared GaOOH can be identified with an orthorhombic structure with lattice parameters: a=4.573 Å, b=9.804 Å, c=2.972 Å and α=β=γ=90° (JCPDS 06-0180). TEM images shown in Figure 4.2 also suggest that the synthesized GaOOH rods are highly crystalline with an average diameter of 400-500 nm and length of 2 μm.

4.2.2 Preparation and characterization of rod form Ga_2O_3

The dried GaOOH rods were then calcined under a controlled air atmosphere to yield the final rod form of Ga_2O_3. The obtained Ga_2O_3 rods were characterized by various techniques including PXRD, TEM (associated by HRTEM and ED), SEM, BET, Raman and UV-Visible spectroscopy.

4.2.2.1 PXRD, TEM, SEM and BET

The PXRD pattern of the rod form Ga_2O_3 (Figure 4.3) can be assigned to a monoclinic β-Ga_2O_3 system, with lattice constants: a=12.225 Å, b=3.039 Å and c=5.801 Å (JCPDS 43-1012), α=γ=90 ° and β=103.7°. This PXRD pattern also

suggests a highly crystalline nature of β-Ga_2O_3 rods. Peaks corresponding to the (110), (002) and (111) crystallographic planes are the three most intense peaks observed. The interplanar spacings (d_{hkl}) of these crystal planes in monoclinic structure can be calculated by the Equation 4.1:

$$\frac{1}{d^2} = \frac{1}{\sin^2\beta}\left(\frac{h^2}{a^2} + \frac{k^2\sin^2\beta}{b^2} + \frac{l^2}{c^2} - \frac{2hl\cos\beta}{ac}\right) \quad \text{(Eq. 4.1)}$$

where integers h, k and l are the Miller indices of a (hkl) lattice plane. The calculated d-spacing values for (110), (002) and (111) planes are 2.944 Å, 2.817 Å and 2.549 Å, respectively.

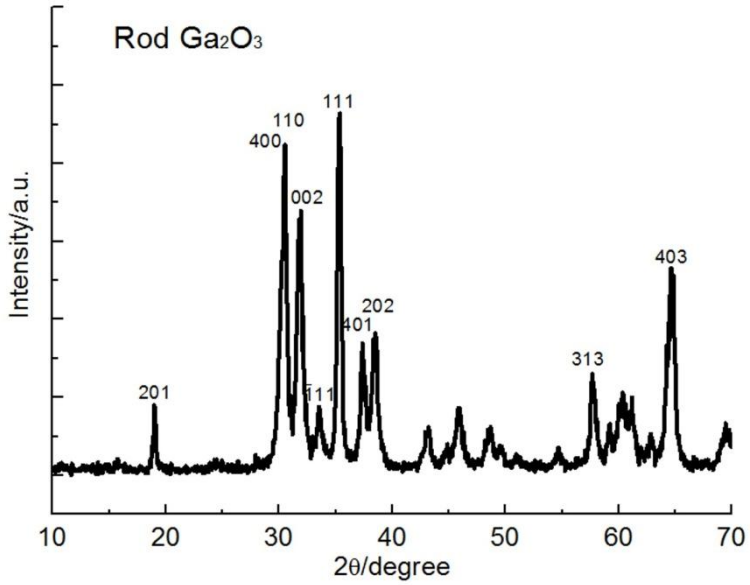

Figure 4.3 PXRD pattern of the monoclinic rod form Ga_2O_3.

The TEM and SEM analysis in Figure 4.4 indeed confirm the rod shape β-Ga_2O_3. The average size of a typical rod Ga_2O_3 is around 400-550 nm in diameter and 2.5 μm in length. The surface of the formed Ga_2O_3 rods does not appear as smooth as those of GaOOH rods, suggesting that the calcination process under high temperature might have led to the formation of some pits in this structure. The pores distributed along the

rod surfaces might be useful for catalysis as they will enhance surface area and provide defective sites for catalysis (e.g. formation of oxygen vacancies). Analysis near the edge of a rod Ga_2O_3 nanocrystal by TEM and electron diffraction (ED) suggested the majority of the surfaces were terminated with either (111) or (110) faces, with the rod growth extending along the [110] direction. The high intensities for both (110) and (111) facet peaks by these diffraction techniques also reflect such a crystal orientation. A representative high resolution TEM image presented in Figure 4.4 (a) shows a lattice fringe separation of 2.58 Å, running along with the Ga_2O_3 rod axis, which corresponds to the (111) crystal facet termination. Thus, this measured value is in good agreement with the theoretically calculated d_{111} spacing. Such stable low index terminations are expected in high temperature synthesis and the rod shape particle reflects this feature. The measured specific surface area of Ga_2O_3 rods by the N_2 BET method was around 16.69 m^2/g (S_{BET}).

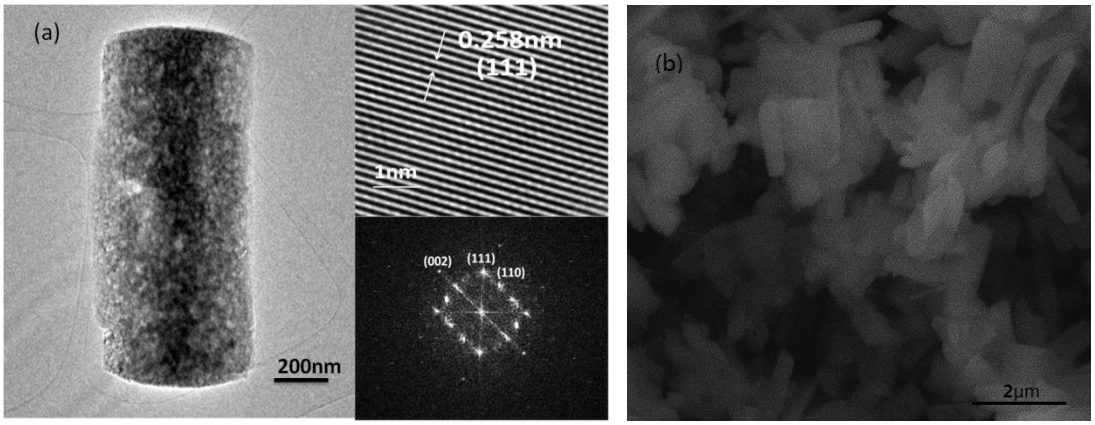

Figure 4.4 TEM image, lattice fringes and electron diffraction pattern at the edge region of a rod Ga_2O_3 (a) and SEM image of Ga_2O_3 rods (b).

4.2.2.2 Raman spectroscopy

Raman spectroscopy was used to characterize the structure of the rod form Ga_2O_3. Figure 4.5 shows the Raman spectrum of rod Ga_2O_3, which reveals characteristic Raman peaks of monoclinic β-Ga_2O_3. According to Zhao *et al.* and Rao *et al.*,[11,12] these characteristic Raman peaks can be categorized into the following groups. Raman bands observed at 766, 652, and 632 cm^{-1} are the stretching and bending of GaO_4 tetrahedra units. Raman peaks at 476, 416, 346 and 318 cm^{-1} are the symmetric bending and stretching vibrations of GaO_2 octahedra units. The low frequency peaks (below 200 cm^{-1}) arise from the libration and translation of tetrahedral-octahedra chains,[13] with a sharp band at 200 cm^{-1} assigned to O-Ga-O bending modes.

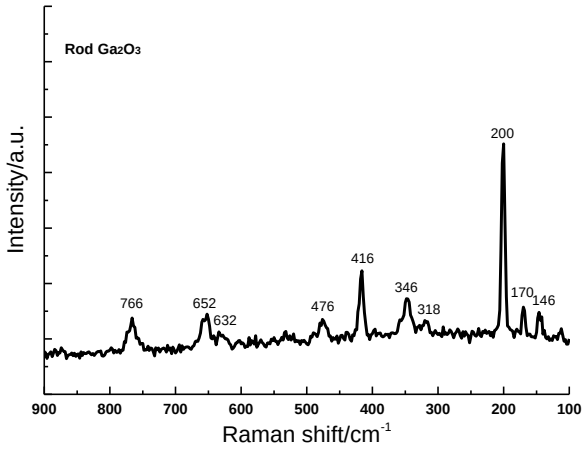

Figure 4.5 Raman spectrum of the rod form β-Ga_2O_3.

4.2.2.3 UV-Visible Spectroscopy

Considering the semiconducting nature of Ga_2O_3, UV-Visible absorption spectroscopy was carried out from 800 nm to 200 nm over the different forms of Ga_2O_3 in order to probe their optical properties and to determine their bandgap values. Here in this

section, a typical UV-Visible spectrum of rod Ga_2O_3 is displayed in Figure 4.6 (a). From the Figure 4.6 (a), it can be seen that Ga_2O_3 rods start to absorb UV light from the wavelength of below 274 nm, which reflects the wide bandgap of the Ga_2O_3. Notice that KBr is used as diluent, which is transparent for the whole range of wavelengths studied. It was found that such dilution was essential to avoid problems such as false absorptions from contaminated impurities and the highly absorbing nature of samples such as Pd doped Ga_2O_3. There is a disturbance region between 350 nm and 274 nm caused by changing lamps (the "changing position" was set at 319.2 nm). Luckily, this region does not overlap with the typical absorption region of Ga_2O_3, and thus does not affect the measurements.

As a result, the bandgap of the rod form Ga_2O_3 was determined by applying the Kubelka-Munk equation (Equation 4.2) to the diffuse reflectance spectroscopy as follows:

$$F(R) = \frac{(1-R)^2}{2R} = \frac{\alpha}{s} \quad \text{(Eq. 4.2)}$$

where R is the reflectance of the measured sample, α is the absorption coefficient and s is the scattering coefficient. In addition, the following two equations (Equations 4.3-4.4) are also required and are listed as follows:

$$A = -\lg(R) \quad \text{(Eq. 4.3)}$$

$$\alpha h\nu = C(h\nu - E_g)^{1/2} \quad \text{(Eq. 4.4)}$$

where A is the absorbance, hν is the light energy, C is the constant and E_g is the bandgap. Substitution of R by A, combining all the three equations, and plotting $(F(R)\times h\nu)^2$ (y-axis) versus hν (x-axis), E_g can be obtained by the intercept of the

tangent line with the x-axis (at y=0), as shown in Figure 4.6 (b). Based on this method, the obtained bandgap value for Ga_2O_3 rods was found to be 4.85 eV, which was in good agreement with the reported value.[9]

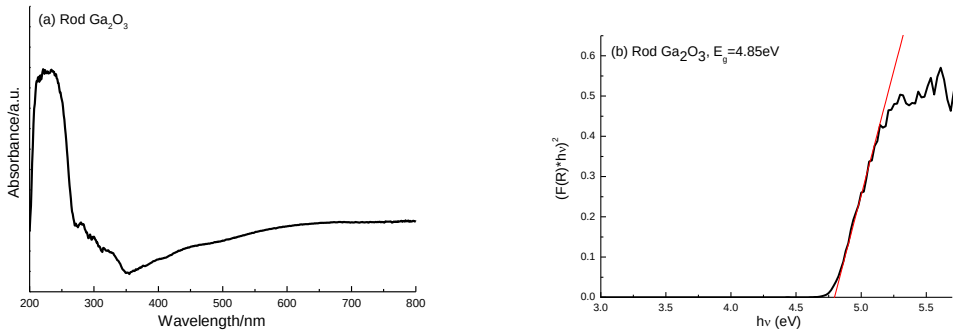

Figure 4.6 UV-Vis absorption spectrum of the rod Ga_2O_3 (a) and corresponding plot used to determine its bandgap value (b).

4.3 Synthesis and characterization of plate form Ga_2O_3

4.3.1 Preparation of plate form GaOOH

The plate form Ga_2O_3 was synthesized based on the initial formation of GaOOH nanoplates which were prepared through a solid state synthesis and ion exchange reaction.[1] For the preparation of GaOOH nanoplates, $KGaO_2$ powder was firstly obtained by the solid state reaction of commercial K_2CO_3 and Ga_2O_3 powder at 950 ℃ for 12 hours. Figure 4.7 displays the PXRD pattern of the prepared $KGaO_2$ powder, which is in a good agreement with JCPDS 80-1194.

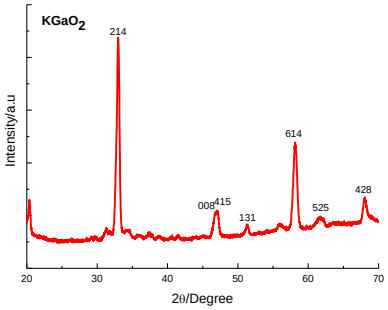

Figure 4.7 PXRD pattern of the $KGaO_2$ Powder.

The GaOOH nanoplates were then obtained from the ion exchange of $KGaO_2$ in an aqueous solution containing CH_3COOH at room temperature. It was demonstrated by Yan and co-workers[1] that the use of CH_3COOH was crucial for the formation of crystalline GaOOH with the plate shape control. Using a strong acidic solution such as hydrochloric acid (HCl) would unfortunately lead to an amorphous product due to uncontrolled fast reaction process. Therefore, the moderate exchange reaction rate between $KGaO_2$ and CH_3COOH was beneficial for the nucleation and growth processes to form the GaOOH plates.

As a result, the PXRD of the formed GaOOH was indexed to an orthorhombic structure (JCPDS 06-0180), and the relative intensity of peaks was nearly identical to those of GaOOH rod pattern, which was described previously. TEM images in Figure 4.8 confirm the regular rhombic shape of the GaOOH crystals with a diameter of around 150-200 nm. Although some stacking of plates can be seen from the TEM images, the surfaces of the formed GaOOH nanoplates appear to be highly crystalline and are sharp and smooth without any pore formation.

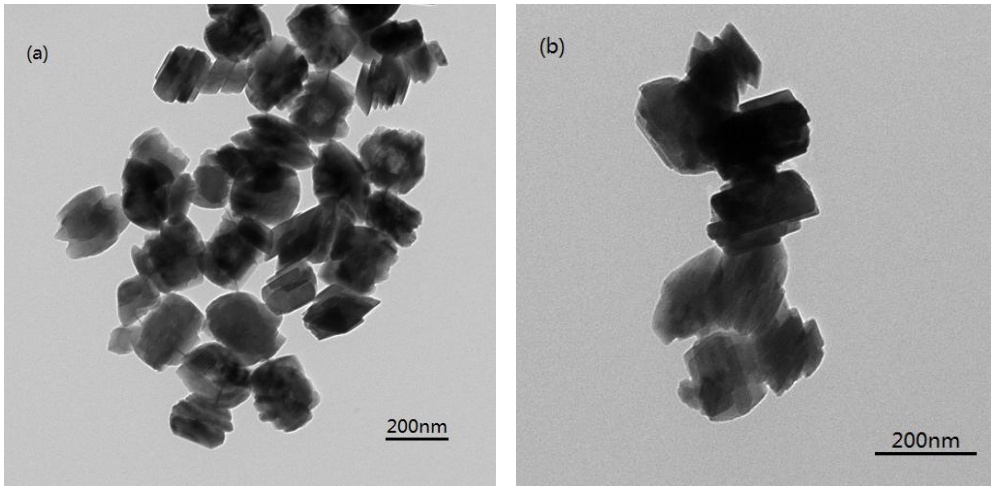

Figure 4.8 TEM image of the GaOOH nanoplates (a) and a higher magnification image (b).

4.3.2 Preparation and characterization of plate form Ga_2O_3

Ga_2O_3 nanoplates were obtained by the calcination of the prepared GaOOH nanoplates under an air atmosphere. The formed plate form Ga_2O_3 was also extensively characterized by the same techniques described for the characterization of the rod material. Focus was therefore placed on the distinctive features of the plate form Ga_2O_3 from its counterparts.

4.3.2.1 PXRD, TEM, SEM and BET

The PXRD of the Ga_2O_3 nanoplates shown in Figure 4.9 can be indexed as a highly crystalline monoclinic β-Ga_2O_3 (JCPDS 43-1012). The most interesting feature is that the plate form indeed displays higher (002) and lower (110) peak intensities compared to the rod form with reference to (111) peak. This unique feature suggests that the (002) enriched termination might be the dominant facet for this morphology.

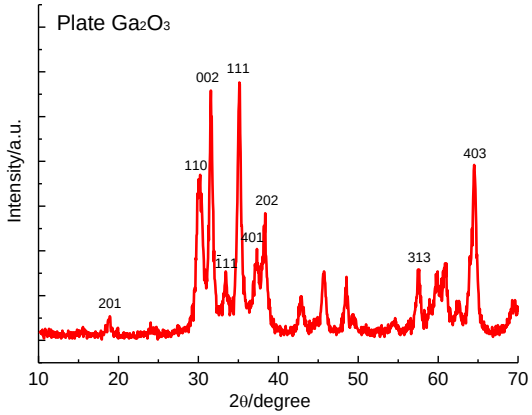

Figure 4.9 PXRD pattern of the Ga_2O_3 nanoplates.

TEM and SEM images shown in Figure 4.10 (a) and (b) confirm the 'plate' morphology of the synthesized β-Ga_2O_3. In addition, it is clearly seen from the TEM image that the Ga_2O_3 gives uniform rhombic shape particles after the high temperature treatment. Unlike the GaOOH plates, the prepared Ga_2O_3 nanoplates exhibit some porous texture. It can be attributed to the fact that under high temperature calcination, pore formation associated with defects can occur. Analysis near the edges of the plate Ga_2O_3 by TEM and ED showed that a more open, higher energetic (002) facet was commonly observed, suggesting a higher preference for this surface termination. A representative high resolution image in Figure 4.10 (a) shows a lattice fringe separation of 2.81 Å, running along with the Ga_2O_3 plate surface, which corresponds to the (002) crystal facet termination. This d-spacing value is in a very good agreement with the theoretically calculated value (monoclinic d_{002}=2.817 Å). The higher (002) PXRD intensity in Figure 4.9 also reflects the higher content of this (002) crystal termination in plate form than rod form Ga_2O_3. The BET surface of the plate form Ga_2O_3 was found to be 21.87 m^2/g. The S_{BET} for both plate and rod forms

were generally quite low and comparable to each other due to the high temperature calcination.

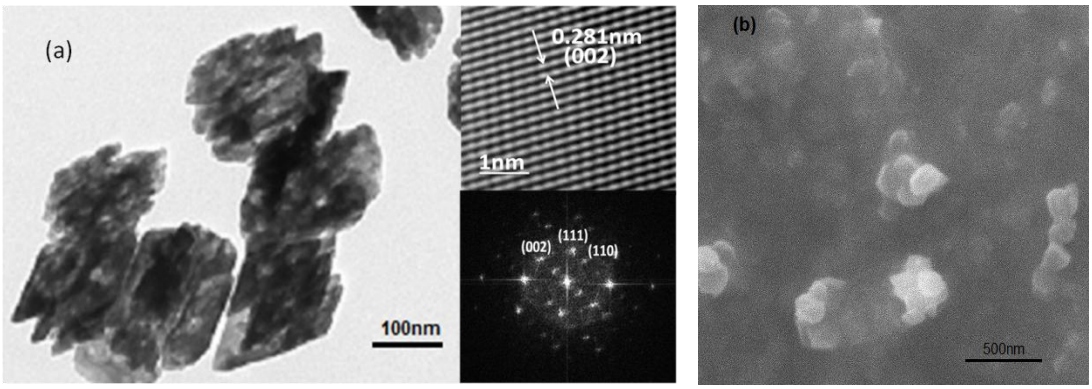

Figure 4.10 TEM image, lattice fringes and electron diffraction pattern at edges of plate Ga_2O_3 (a) and SEM image of plate Ga_2O_3 (b).

4.3.2.2 Raman and UV-Visible spectroscopy

The Raman spectrum of the plate form Ga_2O_3 shown in Figure 4.11 is nearly identical to that for the rod form Ga_2O_3, with no apparent peak shift or peak intensity variation. This similarity in Raman spectra reflects the same internal structure of the both crystals. This monoclinic structure with characteristic lattice movements such as vibrational, rotational and other low-frequency modes are identical in this system. It appears that the difference in crystal morphologies does not affect the intrinsic lattice movements. Nevertheless, the well defined Raman peaks can be used to verify the internal long range crystalline Ga_2O_3 structure.

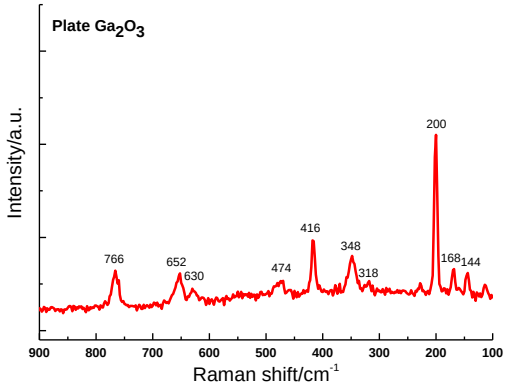

Figure 4.11 Raman spectrum of the plate form β-Ga_2O_3.

The UV-Visible spectrum of Ga_2O_3 nanoplates is displayed in Figure 4.12 (a) and closely resembles the rod form. A large absorption begins at 274 nm and below, with the maximum peak absorption at 235 nm. The bandgap of Ga_2O_3 nanoplates was calculated by the same method as described for the rod form, and the value was found to be 4.87 eV. Taking the instrumental error into account (0.01 eV), the bandgap values for both Ga_2O_3 were found to be similar.

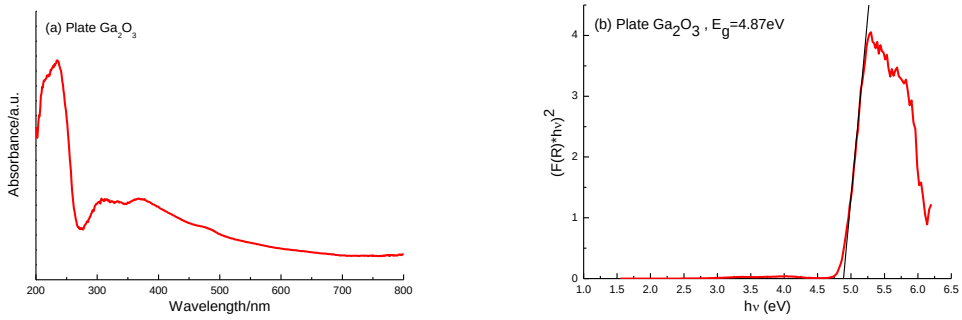

Figure 4.12 UV-Vis absorption spectrum of the plate Ga_2O_3 (a) and corresponding plot for the determination of its bandgap value (b).

In order to probe the nature of the dominant surfaces in the synthesized rod and plate forms of Ga_2O_3 and to investigate their influence on catalytic processes, further

material characterizations and computational simulations were carried out. Detailed results will be presented in Chapters 5 and 6. However, it is worth pointing out that the plate form is predominantly covered with (002) surface, which can introduce surface polarity. This type of surface is more openly packed and more energetic than those of other non-polar (110) and (111) facets, enabling a much easier oxygen vacancy formation. The relationship of surface facets and catalysis will be discussed in the following two chapters.

4.4 Synthesis and characterization of particle form Ga_2O_3

The particle form γ-Ga_2O_3 was prepared through a solvothermal method.[10] Typically, gallium(Ⅲ) acetylacetonate was decomposed in trioctylamine (TOA) solvent with oleic acid added as a capping agent (the oleic acid/Ga^{3+} molar ratio was set at 1). Oleic acid, which is commonly used as a metal nanoparticle stabilizer, is frequently employed in controlling the shape and size of metal nanocrystals.[10,14] The precipitated Ga_2O_3 nanoparticles were separated and purified by extensive washing with acetone.

4.4.1 PXRD, TEM and BET

The PXRD pattern of synthesized γ-Ga_2O_3 particle shown in Figure 4.13 (a) can be indexed as a cubic structure (JCPDS 04-4118). The significant peak broadening indicates the formed particles might be below 5 nm in size. The morphology of the synthesized particles was examined by TEM. From Figure 4.13 (b), it can be seen that the Ga_2O_3 particles appear to be either cubic or spherical shapes (not well defined)

with a narrowly distributed particle size of around 5 nm. The HRTEM images showed no lattice fringes at higher magnification, indicating poor crystallinity of the synthesized γ-Ga_2O_3 particles. The specific surface area measured by N_2 adsorption BET gave the S_{BET} value of 99.45 m^2/g, which represents a high surface area for metal oxide nanomaterials.

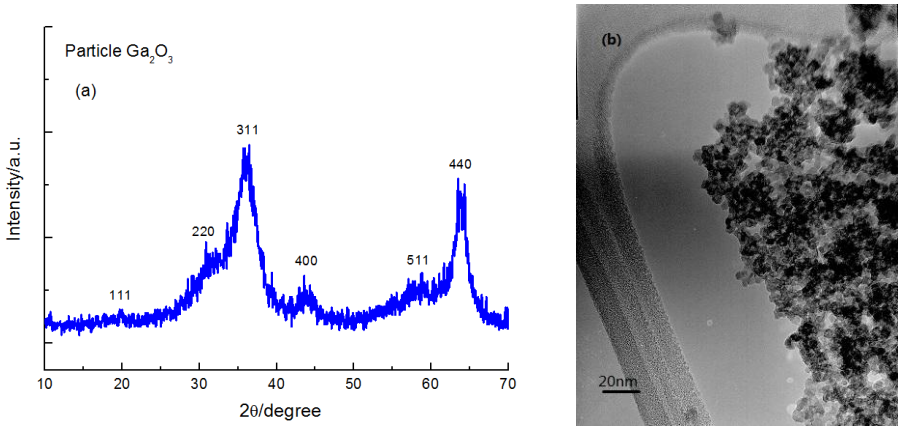

Figure 4.13 PXRD pattern (a) and TEM image of the prepared particle form Ga_2O_3 (b).

4.4.2 Raman and UV-Visible spectroscopy

Raman spectroscopy was used to probe the structural information of γ-Ga_2O_3 particles. The spectrum shown in Figure 4.14 is significantly different from those of rod and plate form Ga_2O_3. The absence of the characteristic Raman peaks is attributed to the lack of a long range crystalline structure of the γ-Ga_2O_3 particles. The high surface area of γ-Ga_2O_3 particles and the absence of Raman peaks have also been recognized by Hou *et al.*[8]

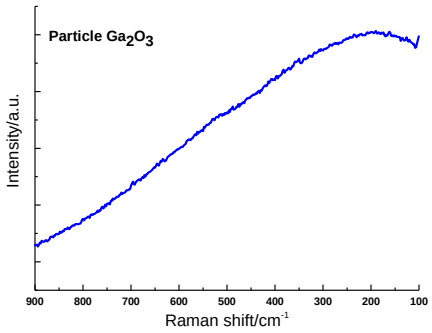

Figure 4.14 Raman spectrum of γ-Ga_2O_3 particles.

The UV-Visible absorption spectrum for γ-Ga_2O_3 particles is shown in Figure 4.15 (a). As seen from the spectrum, the overall peak featuring a shoulder can be resolved into two separate peaks. The first absorption peak positioned at 265 nm (based on fitted peak position) is due to the absorption of oleic acid or TOA residue on the surface of γ-Ga_2O_3 particles. The other peak at 222 nm (based on fitted peak position) is attributed to the band edge absorption of Ga_2O_3. The calculated bandgap of the Ga_2O_3 particles using the 222 nm peaked absorption band was determined to be 5.02 eV (Figure 4.15 (b)), which is higher than those of rod and plate forms Ga_2O_3. This was attributed to the significantly smaller particle size (5 nm) of the γ-Ga_2O_3 particles, which caused the increase in the bandgap value.

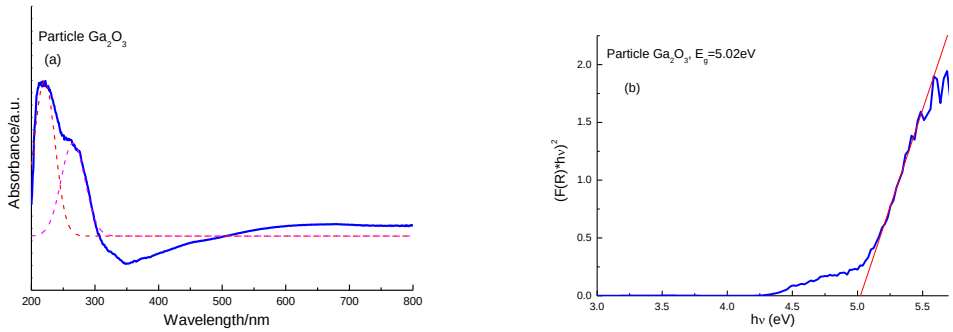

Figure 4.15 UV-Vis absorption spectrum of the particle form Ga_2O_3 (a) (blue line is the measured spectrum, and two dotted red lines are fitted curves) and corresponding plot used to determine its bandgap value (b).

4.4.3 Investigation of synthetic parameters

The effect of reaction time on the shape of γ-Ga_2O_3 was studied and the results are reported in this section. In addition, oleic acid and oleylamine were used as organic capping agents in order to control the morphology of γ-Ga_2O_3. The effect of adding exclusively oleic acid or oleylamine as a capping agent, and the effect of their mixture (with various ratios) were also studied. In order to study these variables each in turn, all other parameters were kept constant and only one variable was investigated.

4.4.3.1 Effect of reaction time

The reaction time for synthesizing γ-Ga_2O_3 was controlled at 10 min, 30 min, 1 hour, 2 hours and 4 hours, respectively. All the solid products were separated and characterized by PXRD and the results are shown in Figure 4.16. It can be clearly seen that the solid product collected after 10 min reaction time at 290 ℃ is

characterized with very broad PXRD peaks, indicative of its amorphous nature. This suggests that defined crystalline particles were not formed over this short time. The corresponding TEM indeed showed small but amorphous particles with no defined shape. On the other hand, typical patterns of cubic γ-Ga_2O_3 products are obtained with the reaction time over 30 min. However, the PXRD patterns shown in Figure 4.16 do not give any change in peak intensity nor position. This indicates that a variation in reaction time beyond the critical time needed for the formation of these nanocrystals (30 min) did not really give much effect on the growth rate and their final shape. In addition, TEM analysis confirmed that the prepared particles under different reaction time were similar in shape with size of around 5 nm. As a result, 1 hour reaction time was selected for other comparative studies.

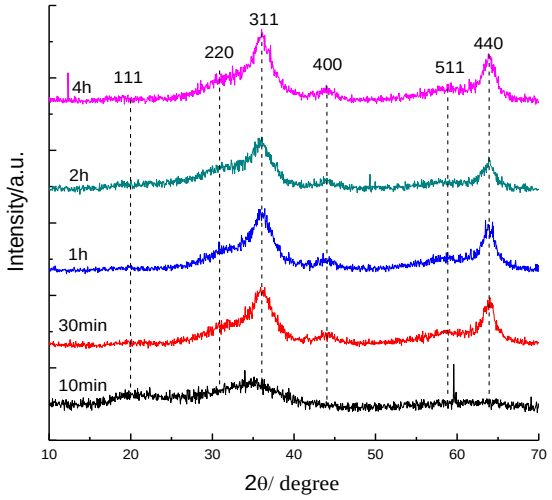

Figure 4.16 PXRD patterns of prepared γ-Ga_2O_3 under various reaction time.

4.4.3.2 Effect of oleic acid/ Ga^{3+} molar ratio

The effect of oleic acid on the shape of γ-Ga_2O_3 was studied by varying the oleic

acid/Ga^{3+} molar ratios between 0 and 10. The PXRD patterns in Figure 4.17 suggest that the particles are basically amorphous under the oleic acid/Ga^{3+} ratios from 0 to 0.4. The result clearly illustrates that sole use of the solvent TOA, or use at its great excess without adding a significant concentration of capping oleic acid, does not result in the controlled growth of crystalline γ-Ga_2O_3. It is believed that the TOA molecules can rapidly decompose the Ga precursor if not protected (capped) by the oleic acid to form highly branched and disordered materials. Thus, the presence of oleic acid as a capping agent to protect the growing sol particles from rapid decomposition is absolutely essential for the controlled growth of the crystalline γ-Ga_2O_3 phase. Notice that as oleic acid/Ga^{3+} ratios were increased to 1, 2, 3, 4, 8 or 10, the crystalline phase of γ-Ga_2O_3 was formed. However, the PXRD patterns of these crystalline products are nearly identical. This may suggest that although oleic acid is an essential capping agent to allow controlled decomposition to yield the crystalline phase, it does not greatly inhibit decomposition indicating that its adsorption on the material surface is quite moderate. The corresponding TEM images collected using different molar oleic acid/ Ga^{3+} ratios from 1, 2, 3, 4, 8 to 10 (not shown) indeed resembled to each other, confirming no subtle change in crystallinity, size and shape was observed in the synthesis.

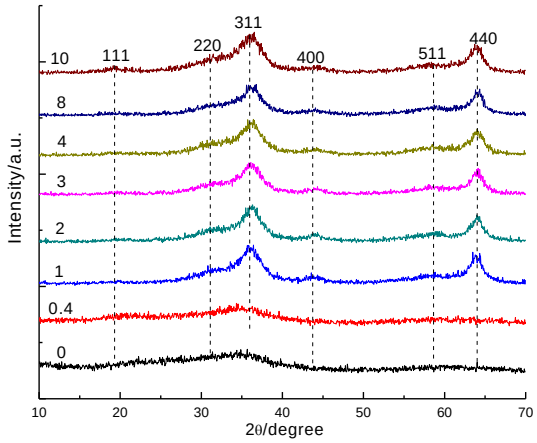

Figure 4.17 PXRD patterns of γ-Ga_2O_3 prepared with different oleic acid/Ga^{3+} ratios.

4.4.3.3 Effect of oleylamine/Ga^{3+} molar ratio

The effect of oleylamine to replace oleic acid on particle size and morphology of γ-Ga_2O_3 was also briefly investigated. The oleylamine/Ga^{3+} ratios were thus varied between 0 and 8. The PXRD results (Figure 4.18 (a)) suggest that the solid products prepared with the oleylaime ratios up to 2 are still amorphous, and a typical cubic γ-Ga_2O_3 is only obtained when the ratio is raised above 4. It reveals that the capping ability of oleylamine appears to be weaker than corresponding oleic acid, as it needs a higher concentration to guide the controlled growth of the seeds. However, similar to oleic acid, the use of oleylamine does not seem to direct the growth of the γ-Ga_2O_3 in a certain direction. A representative TEM image (Figure 4.18 (b)) of the γ-Ga_2O_3 prepared by oleylamine/Ga^{3+} at the molar ratio of 8, still shows the same morphology with the average particle size of 5 nm.

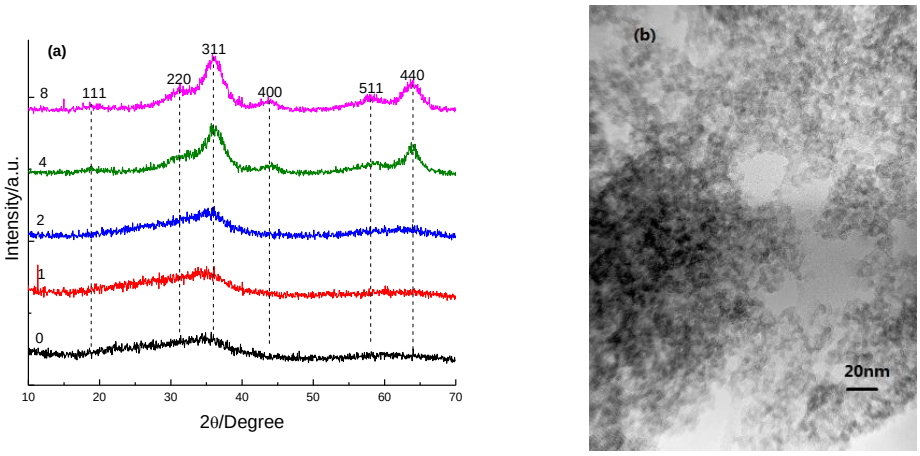

Figure 4.18 PXRD patterns of γ-Ga_2O_3 prepared with different oleylamine/Ga^{3+} ratios (a) and a representative TEM image with oleylamine/Ga^{3+} ratio at 8 (b).

4.4.3.4 Effects of using oleylamine and oleic acid mixture and their molar ratios to Ga^{3+}

The effects of using oleylamine and oleic acid as co-capping agents at different molar ratios on the size and shape of γ-Ga_2O_3 were briefly studied. Figure 4.19 (a) shows a distinctive feature that the (111) peak is enhanced at the expense of the (440) peak as compared to the use of either oleic acid or oleylamine when the mixed surfactants (1:1 molar ratio) are used. This suggests that the mixed surfactants could preferentially promote the synthesis of crystalline γ-Ga_2O_3 with a preferred growth axis perpendicular to the (111) plane while suppressing the [440] direction. Varying the ratios of the surfactant mixture, however, does not give a further variation in the PXRD patterns from that obtained with 1:1 oleylamine/oleic acid ratio (Figure 4.19 (b)). A representative TEM image displayed in Figure 4.19 (c), depicts the γ-Ga_2O_3 prepared with oleylamine/oleic acid ratio at 1. Regarding the weak chelating nature of both capping agents, it is not yet known their synergetic effect on directing the growth

of the γ-Ga_2O_3 phase. Further work is required to investigate this interesting effect.

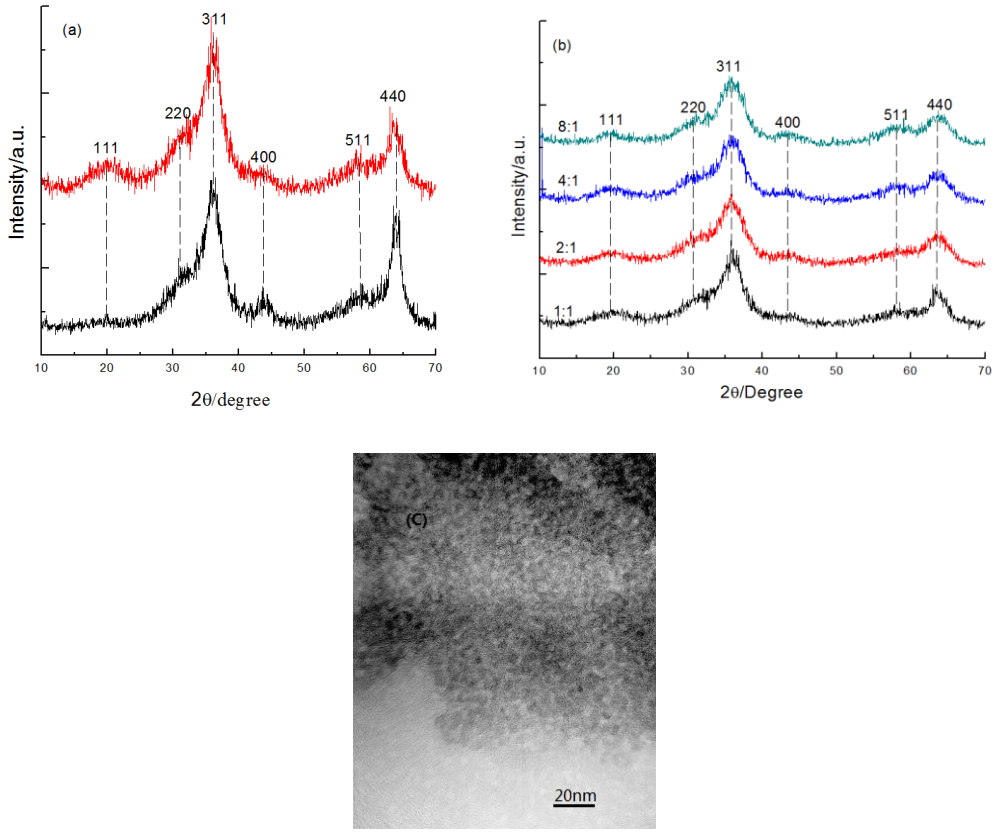

Figure 4.19 (a) Comparison of PXRD results of γ-Ga_2O_3 (red curve: oleic acid/Ga^{3+}=1 and oleylamine/Ga^{3+}=1; black curve: oleic acid/Ga^{3+}=1); (b) PXRD results of γ-Ga_2O_3 prepared with various oleyamine/oleic acid molar ratios, with oleic acid/Ga^{3+} =1 for all; (c) A representative TEM image of γ-Ga_2O_3 prepared with oleylamine/oleic acid ratio at 1.

4.5 Conclusion

Ga_2O_3 with three well defined shapes (i.e. rod, plate and particle forms) was synthesized successfully. Fundamental physiochemical properties of the prepared materials regarding structural, morphological, physical and optical aspects were also extensively characterized. It was found that the surface of the rod form Ga_2O_3 was dominantly covered by either (110) or (111) facets, whereas a more open and higher

energy (002) facet was identified on the surface of the plate form Ga_2O_3. In addition, synthetic parameters including the use of surfactant(s) and their added concentration(s) on the morphology of γ-Ga_2O_3 nanoparticles were briefly investigated. These studies were based on the fact that the relative shape of a nanocrystal should be governed by the relative growth of individual crystal facets in the presence of surfactant, which can be different due to the difference in their surface free energies.[10,15] The use of surfactant(s) and the used ratios could be able to dictate the particle morphology, because of their stabilization for particular crystal planes. In contrast, from the present studies, the use of oleic acid and olelyamine with various ratios did not show any apparent effect on directing the particle growth of γ-Ga_2O_3 to a particular shape. This might be due to their small differences in surface energies for different γ-Ga_2O_3 surfaces, but further work and computational modeling should be required to substantiate this conclusion.

4.6 References

1. S. Yan, L. Wan, Z. Li, Y. Zhou and Z. Zou, *Chem. Commun.*, 2010, **46**, 6388-6390.
2. S. Yoshioka, H. Hayashi, A. Kuwabara, F. Oba, K. Matsunaga and I. Tanaka, *J. Phys.: Condens. Matter.*, 2007, **19**, 346211(11 pages).
3. U. Rambabu, N. R. Munirathnam, T. L. Prakash, B. Vengalrao and S. Buddhudu, *J. Mater. Sci.*, 2007, **42**, 9262-9266.
4. T. Wang, S. S. Farvid, M. Abulikemu and P. V. Radovanovic, *J. Am. Chem. Soc.*, 2010, **132**, 9250-9252.
5. M. Saito, *Catalysis Survey from Japan*, 1998, **2**, 175-184..
6. T. Fujitani and I. Nakamura, *Bull. Chem. Soc. Jpn.*, 2002, **75**, 1393-1398.
7. T. Fujitani, M. Saito, Y. Kanai, T. Watanabe, J. Nakamura and T. Uchijima, *Appl. Catal A: Gen.*, 1995, **125**, 199-202.
8. Y. Hou, L. Wu, X. Wang, Z. Ding, Z. Li and X. Fu, *J. Catal.*, 2007, **250**, 12-18.
9. Y. Zhao, R. L. Frost and W. N. Martens, *J. Phys. Chem. C.*, 2007, **111**, 16290-16299.
10. A. McLaren, T. V. Solis, G. Li and S. C. Tsang, *J. Am. Chem. Soc.*, 2009, **131**, 12540-12541.
11. Y. Zhao, and R. L. Frost, *J. Raman. Spectrosc.*, 2008, **39**, 1494-1501.
12. R. Rao, A. M. Rao, B. Xu, J. Dong, S. Sharma and M. K. Sunkara, *J. Appl. Phys.*, 2005, **98**, 094312(1-5).
13. D. Dohy, G. Lucazeau and A. Revcolevschi, *J. Solid State Chem.*, 1982, **45**, 180-192.

14. T. Andelman, Y. Gong, M. Polking, M. Yin, I. Kuskovsky, G. Neumark and S. O'Brein, *J. Phys. Chem. B.,* 2005, **109**, 14314-14318.

15. Y. Xia, Y. Xiong, B. Lim, and S. E. Skrabalak, *Angew. Chem. Int. Ed.,* 2009, **48**, 60-103.

Chapter 5 Shape effect of Pd promoted Ga_2O_3 nanocatalysts for methanol synthesis from CO_2 hydrogenation

Chapter 5 Shape effect of Pd promoted Ga_2O_3 nanocatalysts for methanol synthesis from CO_2 hydrogenation.....150

5.1 Introduction.....151

5.2 Synthesis and characterization of Pd doped Ga_2O_3 nanocatalysts.....153

5.2.1 PXRD.....154

5.2.2 TEM.....155

5.3 Catalytic performance.....159

5.4 Other characterizations, computational studies and discussions.....163

5.4.1 CV and CO stripping.....163

5.4.2 EPR and TPR/D.....167

5.4.3 XPS.....171

5.4.4 Computational modeling and calculations.....174

5.4.5 Further discussions.....180

5.5 Conclusion.....183

5.6 References.....184

5.1 Introduction

In recent years, CO_2 has become the focus of attention because of the position of CO_2 as one of the primary greenhouse gases and the implication of its emissions on the problem of climate change.[1] Effort on CO_2 abatement has been made extensively to tackle this issue.[2] On the other hand, chemical synthesis of methanol from CO_2 and H_2 has been regarded as an important way in the conversion and transportation of hydrogen gas related energies derived from non-fossil sources such as solar power, hydropower and biomass.[3] Thus, the generation and use of energetic methanol molecules derived from CO_2 hydrogenation for energy provision is strategically more desirable than the approach of only post-capture and storage of CO_2. As a result, CO_2 hydrogenation to methanol is the key route of recycling CO_2 which has promoted recent research effort to develop effective catalysts for this reaction.[4]

Methanol, known as a core chemical,[5] can be produced from CO_2 hydrogenation over Cu based catalysts. Numerous investigations concerning various aspects of Cu on ZnO catalysts have been carried out during the past few decades, making this field relatively well established. On the other hand, Pd is also known to be an active component when combined with active supports for methanol synthesis from CO_2 hydrogenation, which is currently being intensively studied.[6] The report of Pd/Ga_2O_3 catalyst giving a higher activity than the Cu/ZnO formulation for methanol production from CO_2 hydrogenation was first launched by Fujitani *et al.*[7] Based on their pioneering work, the research activities for developing Pd/Ga_2O_3 based catalysts have been growing quickly in recent years.

Apart from the search for different catalyst formulations, study of shape-performance relationships is an emerging important field of research. Particularly, the metal-support interaction plays an important role in heterogeneous catalysis, which stems from geometric and electronic perturbations between catalyst components. It has been clearly shown from literature that by presenting different shapes (i.e. different exposed crystallographic planes) of metal oxide support particles to host metal, there is a great variation in their catalytic performance.[8] This new approach adds an exciting variable in tailoring properties of nanocatalysts for various reactions,[2] which may contribute to rational design of novel highly active and selective nanocatalysts for many catalytic applications. However, little work has been done in this important area for methanol synthesis from CO_2 hydrogenation. Our group have recently reported in a communication note[2] that activity and selectivity dependence on the shape of ZnO plate nanocrystal in Cu/ZnO gave a higher yield for methanol production from CO_2 hydrogenation than other corresponding oxide surfaces. This clearly indicates that the exposed crystallographic plane on the plate form surface of ZnO must show a stronger synergy with metal than other facets, giving enhanced catalysis.[2] However, to the best of our knowledge, there is no reported literature by others addressing the shape effect of Ga_2O_3 for the Pd/Ga_2O_3 system for methanol synthesis from the CO_2 hydrogenation reaction.

Here, in this chapter, two forms of Ga_2O_3 nanocrystals of the same structure but different shapes, namely, β-Ga_2O_3 rods and β-Ga_2O_3 plates were compared. In addition, these two Ga_2O_3 materials were doped with Pd nanoparticles from low to

high loadings progressively and used them as model catalysts to study the morphology-performance relationship for the reaction of methanol synthesis from CO_2 hydrogenation. Within this chapter, careful testing of these model catalysts were carried out in combination with in-depth characterizations including PXRD, TEM, EPR, TPR/D, cyclic voltammetry (CV) and CO stripping, XPS and computational studies. From the above work and systematic comparisons, it aims to produce a more comprehensive understanding of the morphological effect of Ga_2O_3 in the Pd/Ga_2O_3 system for this important catalytic reaction.

5.2 Synthesis and characterization of Pd doped Ga_2O_3 nanocatalysts

The Pd doped rod and plate form Ga_2O_3 nanocatalysts were prepared through a modified wet impregation method at room temperature, by the addition of a prepared Pd precursor solution ($Pd(NO_3)_2$) into the appropriate Ga_2O_3. The designated final Pd loadings were set at 1 wt%, 2 wt% and 5 wt%, respectively. The impregnated mixture was then heated gradually to 70 ℃ to remove water from the system. The dried samples were calcined in air before reduction under H_2 to obtain the final Pd/Ga_2O_3, for the purpose of achieving a better contact and thus better interaction between the metal and oxide components. The whole synthetic procedure of preparing Pd doped Ga_2O_3 did not allow any Pd loss during the process (no filtration process was used), making the control in Pd content precise. The obtained Pd/Ga_2O_3 nanocatalysts were firstly characterized by PXRD and TEM analysis to acquire some initial knowledge of the materials, before they were tested for the CO_2 hydrogenation reaction and further

characterized by other physical techniques.

5.2.1 PXRD

The powder X-ray diffractograms of the two morphologically different β-Ga_2O_3 nanocrystals with and without Pd of different loadings are displayed in Figure 5.1. For a comparison between the rod and plate form Ga_2O_3, the XRD patterns of both pure materials of different shapes without Pd are shown in Figure 5.1 (a). It can be clearly seen from this figure that the most striking feature is that the plate form Ga_2O_3 exhibits a higher (002) peak intensity than the rod form with reference to (111) peak. The dominance of this (002) plane on the plate form surface was also confirmed by corresponding TEM analysis as discussed in Chapter 4. Figure 5.1 (b) and (c) display the XRD patterns of Ga_2O_3 rod and Ga_2O_3 plate with Pd metal loadings varied from 0% to 5%, respectively. Generally, all levels of Pd doping show no Pd peaks with exception of the 5% Pd samples which show very small characteristic Pd (200) peaks. The observed Pd (200) peak sizes in the figures suggest that the dispersion of Pd on the plate form Ga_2O_3 was better than on the rod form at 5% loading, which is indicated by the much smaller Pd peak of the 5% Pd doped Ga_2O_3 plate. It was also confirmed that the crystal structure for both forms was well maintained after the calcination and reduction.

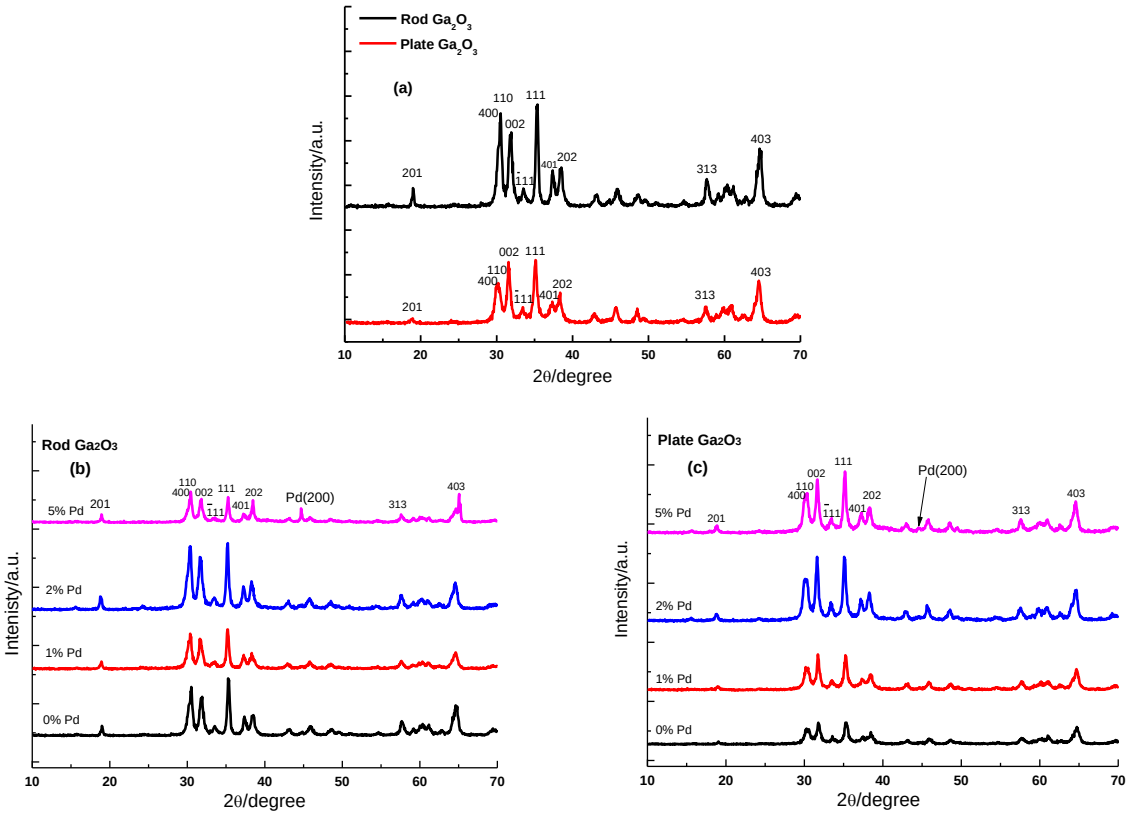

Figure 5.1 (a) Comparison of PXRD patterns of rod and plate monoclinic β-Ga_2O_3; (b) PXRD patterns of Ga_2O_3 rod with Pd doping from 0-5 wt %; (c) PXRD patterns of Ga_2O_3 plate with Pd doping from 0-5 wt%.

5.2.2 TEM

TEM analysis was performed in order to examine the structure and physical appearances of the 5% Pd doped rod and plate forms of Ga_2O_3. The reason for choosing the 5% Pd doped samples was that this level of loading was close to the optimum Pd loading for this target reaction.[6]

The TEM images shown in Figure 5.2 (a)-(d) represent the rod shape Ga_2O_3 with and without Pd. Figure 5.2 (a) shows a typical undoped rod shape Ga_2O_3. The average

dimension of a typical rod Ga_2O_3 is around 400-550 nm in diameter and 2.5 μm in length. In Chapter 4, analysis near the edge region of the rod Ga_2O_3 nanocrystals demonstrated by TEM and electron diffraction (ED) revealed that the majority of their surfaces were terminated with either (111) or (110) faces, with the rod growth extending along the [110] direction. Here, a typical high resolution image presented in Figure 5.2 (b) shows a lattice fringe separation of 2.58 Å, running along the Ga_2O_3 rod surface, which corresponds to the (111) crystal facet termination. It is noted that there are regions of atomic steps and dislocations, suggesting that the quality of the nanocrystals made by this method is far from those of single crystals but the majority of surface atoms in the (111) facet is ascertained. For the Pd doped samples, it is clearly seen that the Pd clusters/nanoparticles are well dispersed on Ga_2O_3 surfaces (Figure 5.2 (c) and (d)), with the Pd metal sizes ranging from 1-8 nm at 5% Pd loading.

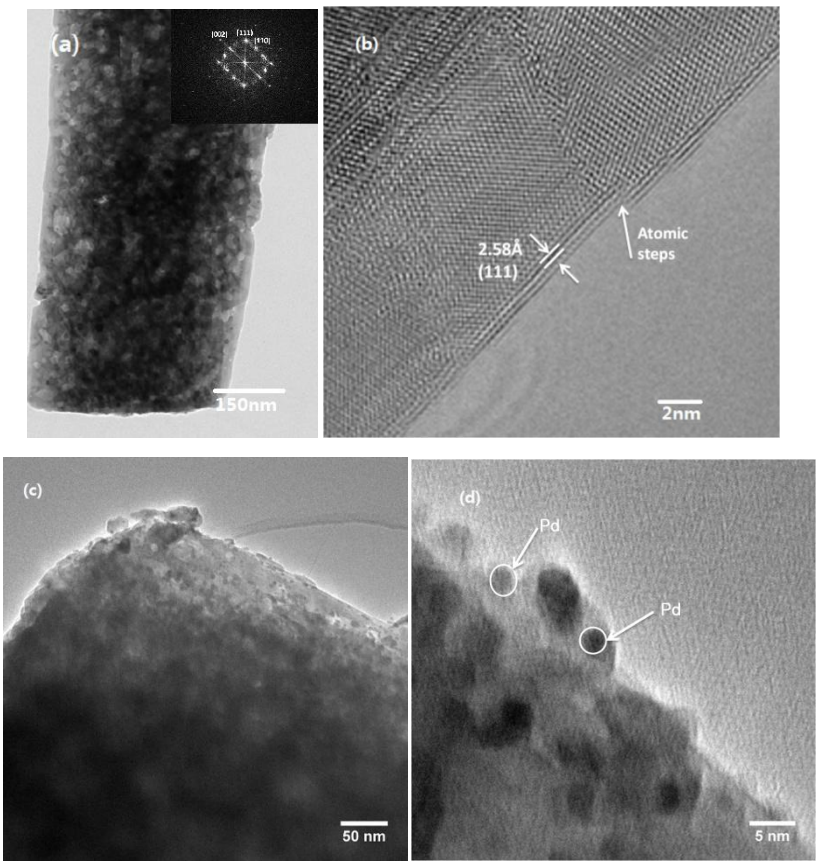

Figure 5.2 (a) TEM image of a rod Ga_2O_3 nanocrystal (an insert represents the Fourier transform electron diffraction pattern near the edge region of the crystal); (b) lattice fringe separation of 2.58 Å with (111) facet on rod Ga_2O_3 surface; (c) TEM image of 5% Pd/rod Ga_2O_3; (d) enlarged TEM image of 5% Pd/rod Ga_2O_3.

The TEM images shown in Figure 5.3 (a)-(d) represent the clusters of plate Ga_2O_3 particles with and without Pd. Figure 5.3 (a) shows a typical undoped Ga_2O_3 plates in aggregation. The individual plate Ga_2O_3 appears to be a regular rhombic shape with a diameter of around 150-200 nm. As discussed in Chapter 4, the most common observed lattice fringe separations of 2.81 Å (002) were found running along the Ga_2O_3 plate surface. A representative high resolution image presented in Figure 5.3 (b) clearly shows the (002) crystal facet termination. Thus, TEM and ED analysis showed

the more open, higher energy polar (002) face was frequently observed, suggesting a high preference for this surface termination. From Figure 5.3 (c), it can also be observed that the Pd clusters/nanoparticles are well dispersed on the Ga_2O_3 plate surfaces after the Pd deposition. An enlarged TEM image from a selected region of Figure 5.3 (c) is shown in Figure 5.3 (d), which indicates the Pd metal sizes ranging from 1-5 nm at the 5% Pd loading. The overall better dispersion and generally smaller Pd particle sizes on plate Ga_2O_3 than rod form suggests there may be a stronger interaction between Pd and plate surface, which can host Pd well with less aggregation.

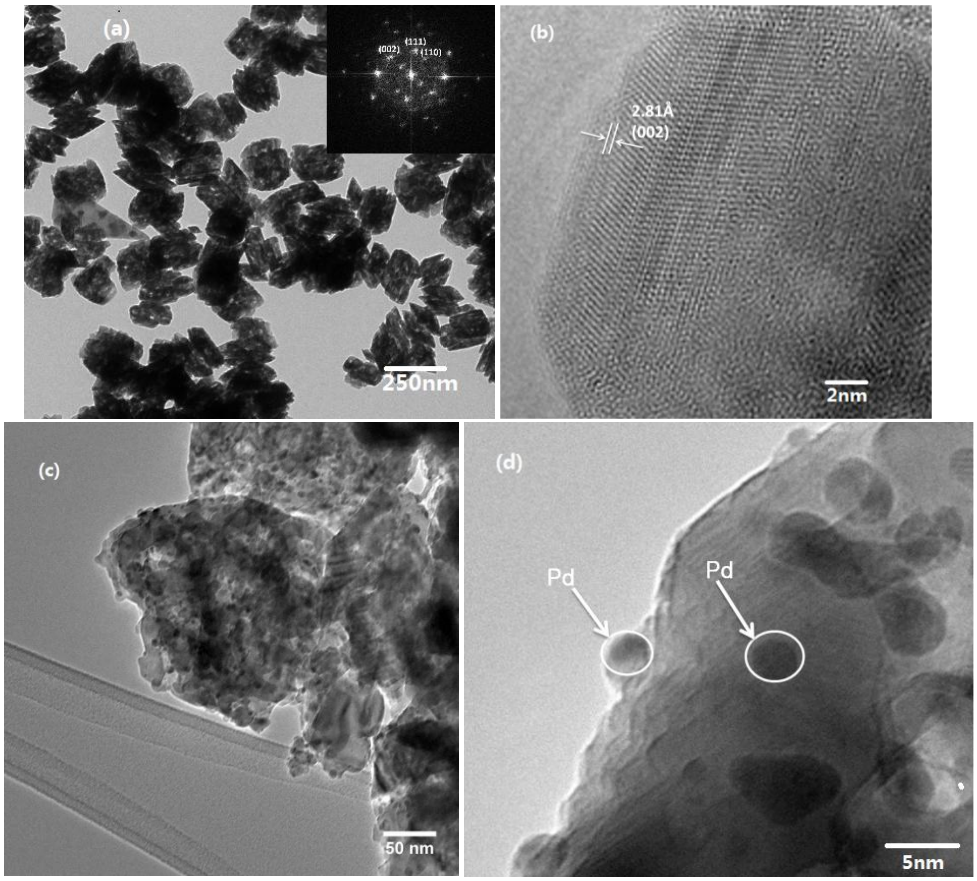

Figure 5.3 (a) TEM image of plate Ga_2O_3 nanocrystals (an insert represents the Fourier transform electron diffraction pattern near the edge region of a crystal); (b) lattice fringe separation of 2.81 Å with (002) facet on plate Ga_2O_3 surface; (c) TEM image of 5% Pd/plate Ga_2O_3; (d) enlarged TEM image of 5% Pd/plate Ga_2O_3.

5.3 Catalytic performance

The N_2 BET surface area measurements for rod and plate forms of β-Ga_2O_3 indicated a low but comparable surface area for the two samples (~16.7-21.9 m^2g^{-1}) due to high temperature calcination (800-900 ℃). However, they showed a very different morphology and surface features. The progressive coverage of Pd on their surfaces may reflect the various degrees of metal-support interaction in catalysis. Catalytic testing for methanol synthesis from CO_2 hydrogenation was carried out under

industrially applicable conditions (5 MPa, 250 ℃), and the results over different Pd doped Ga_2O_3 nanocatalysts are summarized in Table 5.1 and Figure 5.4.

Table 5.1 Summary of catalytic performance of Pd loaded Ga_2O_3 nanocatalysts

Catalysts	CO_2 Conv. (%)	CH_3OH Select. (%)	CH_3OH yield (%)	CO yield (%)	Carbon balance (%)
1% Pd/rod Ga_2O_3	8.65	45.20	3.86	4.68	98.7
2% Pd/rod Ga_2O_3	11.80	45.78	5.31	6.29	98.3
5% Pd/rod Ga_2O_3	11.04	41.27	4.54	6.46	99.7
1% Pd/plate Ga_2O_3	10.95	29.51	3.19	7.62	98.7
2% Pd/plate Ga_2O_3	15.03	43.05	6.35	8.40	98.1
5% Pd/plate Ga_2O_3	17.33	51.62	8.93	8.37	99.8

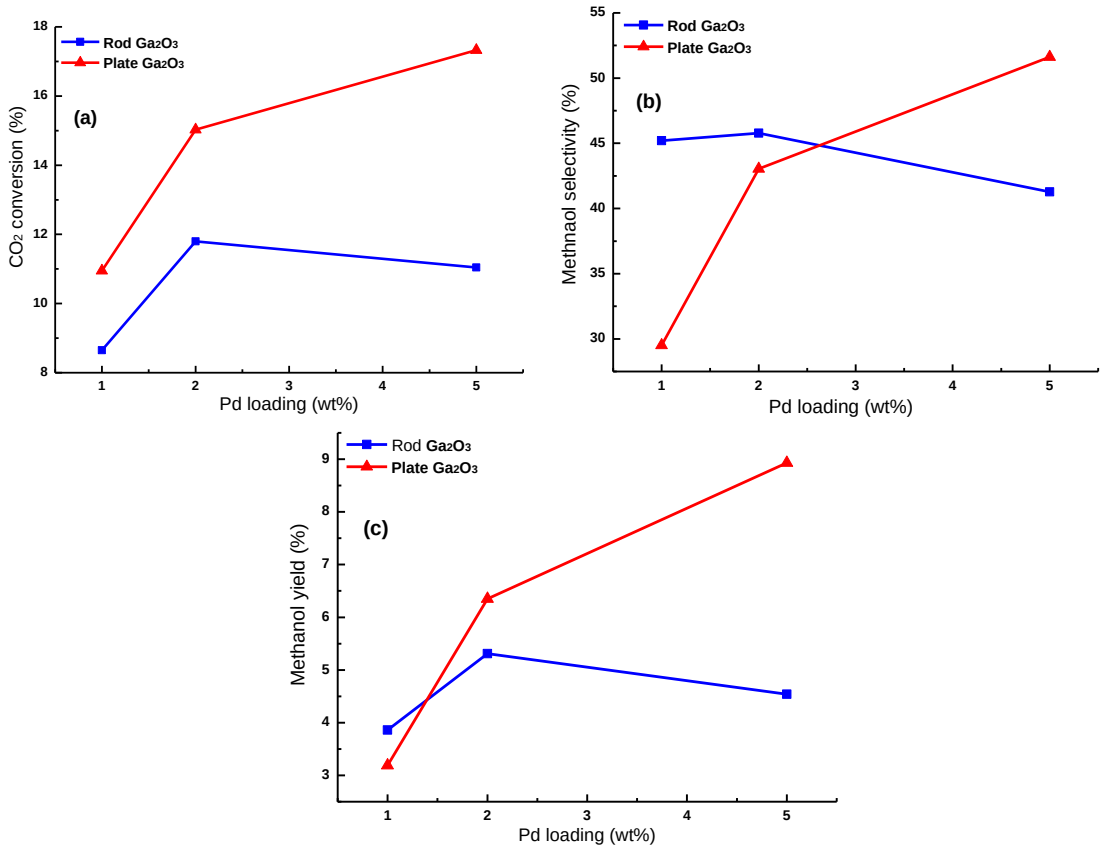

Figure 5.4 Comparison of CO_2 conversion (a), methanol selectivity (b) and methanol yield (c) of rod and plate Ga_2O_3 forms, each with different Pd loading levels.

As seen from the figures and table, CO is the only side product detected in this reaction, and the excellent carbon balance throughout the reaction (≥98%) indicates a very good accuracy for the testing results. By increasing Pd loading from 1 wt% to 2 wt%, both rod and plate forms of β-Ga_2O_3 show a corresponding rise in CO_2 conversion, methanol selectivity and yield as a consequence. It is thought that the increase in Pd loading gives an increase in metal-support contact (both Pd and Ga_2O_3 alone did not give methanol product in this test) and thus higher methanol yield. The Pd deposition is also likely to first take place on defect sites (energetically favorable) before reaching the terraces of Ga_2O_3. The dramatic increase in methanol selectivity (29.51% to 43.05%) from 1 wt% to 2 wt% may suggest that the plate form β-Ga_2O_3 contains more structural defects than the rod form despite its highly crystalline structure. However, the rod form β-Ga_2O_3 behaves in a very different trend from the plate form, which shows a drop in CO_2 conversion, methanol selectivity and methanol yield at 5% Pd loading. This observation is due to the aggregation of Pd at higher Pd loading which leads to the loss of desirable metal-support contact and introduction of unselective sites. The methanol selectivity over the 5%Pd /rod Ga_2O_3 reaches the highest value at 41.27%. On the other hand, the plate form Ga_2O_3 can apparently take up Pd more effectively to give higher effective metal-support contact than the rod form despite their comparable surface area. That means Pd is more interactive and dispersive on the plate form Ga_2O_3 than the rod form, giving higher CO_2 conversion and higher methanol selectivity at the 5% Pd coverage. The major difference between the catalytic performance is believed to be due to the intrinsic nature of the surface

features of these nanocrystals since the two forms are structurally identical with comparable surface area. The difference is attributed to a different degree of metal–support interaction between Pd with rod form Ga_2O_3 ((111)/(110) facets) and plate form Ga_2O_3 ((002) facet). As a result, the optimal methanol yield of the 5% Pd on plate Ga_2O_3 was nearly double that seen using the rod support, indicative of the remarkable activity and selectivity dependence on morphology of the support oxide used. It was further confirmed by PXRD and TEM that the crystal structure and morphologies for both forms were well maintained after the catalytic reaction.

It is well accepted that Pd/Ga_2O_3 binary catalyst is considered as a truly bi-functional catalyst for this target reaction. Baltanas and co-workers suggested in their studies of mechanism that the Pd component was only responsible for the generation of atomic H and spill-over them to the gallia surface, whereas CO_2 was activated and reacted on gallia surface to form methanol product.[4] However, they did not explore the effect of metal support interaction and its impact on this reaction, which was noted in this study and can apparently affect this reaction. In our case, although the observed Pd size on plate Ga_2O_3 (by PXRD and TEM) was slightly smaller than on the rod form, which itself would only facilitate more H_2 for dissociation, the better catalytic performance (activity and selectivity) were mainly attributed to the SMSI between Pd and plate form Ga_2O_3. In addition, the phenomenon of slightly smaller Pd size on the plate form was also due to the better interaction which prevented Pd aggregation and thus a better dispersion, regarding the same preparative procedures of loading Pd and same structure of both forms of Ga_2O_3. Therefore, this SMSI has fundamental

importance to the success of this reaction. Other detailed characterizations and computational studies were carried out, and corresponding results are presented and discussed in the following sections to elucidate this feature more comprehensively.

5.4 Other characterizations, computational studies and discussions

5.4.1 CV and CO stripping

In order to assess the degree of interaction between Pd metal and the surfaces of the plate and rod Ga_2O_3 nanocrystals, the Pd promoted Ga_2O_3 samples were characterized on a glassy carbon electrode by cyclic voltammetry and CO stripping voltammetry. For each CV measurement, 20 cycles of scans were recorded to achieve stable results. Thus the results shown were the recorded stable 20^{th} cycle for each sample, for accurate comparison. It is noted from Figure 5.5 that both Pd/plate Ga_2O_3 and Pd/rod Ga_2O_3 are clearly electrochemically active with H adsorption/desorption below 0.2 V, and Pd oxidation/reduction above 0.7 V. There are no electrochemical signals for the two pure Ga_2O_3 supports (Figure 5.5 (a) and (b)), indicating the activity is only associated with the presence of Pd and interfaces with the oxides. For the rod form sample, the electrochemical signals increase with Pd loading from 1 wt% to 2 wt% but decrease at 5 wt% due to the reduction in metal-support interface because of Pd aggregation (Figure 5.5 (a)). Notice that this sample order matches with the same order from the catalytic evaluation (refer to Figure 5.4). For the plate form sample, the electrochemical signals progressively increase with Pd loading from 1 wt% to 5 wt% (Figure 5.5 (b)), suggesting a clearly stronger metal-support interaction to reduce the

extent of Pd aggregation. At 5% loading for both samples, there are observable shifts in the signal positions compared to their corresponding lower loadings due to an extensive interaction of increased Pd with the Ga_2O_3 surfaces.

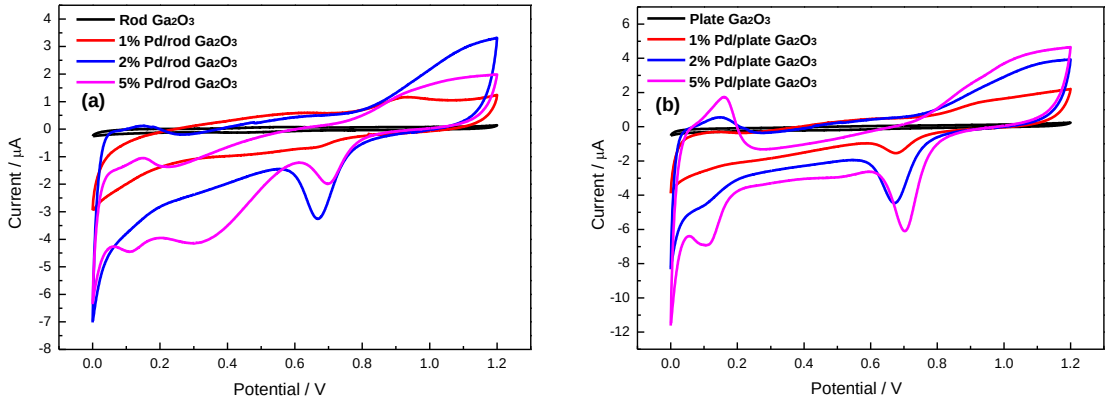

Figure 5.5 (a) CV curves of rod Ga_2O_3 and (b) CV curves of plate Ga_2O_3 with and without Pd loadings, scanned from 0.0 V to 1.2 V (vs. SHE) at 50 mV/s. The stable 20th cycle was recorded for each sample.

Corresponding CV curves are then compared at 1%, 2% and 5% Pd loadings on the two forms of Ga_2O_3 for further analysis (Figure 5.6 (a)-(c)). The plate form consistently gives higher electrochemical signals than the rod form for all Pd loadings, indicating more superior metal-support interaction at the same metal loading. Also, in Figure 5.6 (c), the absence of a characteristic hump at 0.3 V in Pd/plate Ga_2O_3 may suggest a primary (001) Pd deposition (epitaxyl deposition) instead of mixed Pd phases deposition in Pd/rod Ga_2O_3. Figure 5.6 (d) and (e) illustrate the consecutive scans (all 20 cycles) on representative 5% Pd/rod Ga_2O_3 and 5% Pd/plate Ga_2O_3, respectively, showing the consecutive changes in CV curves before reaching the stable 20th cycle.

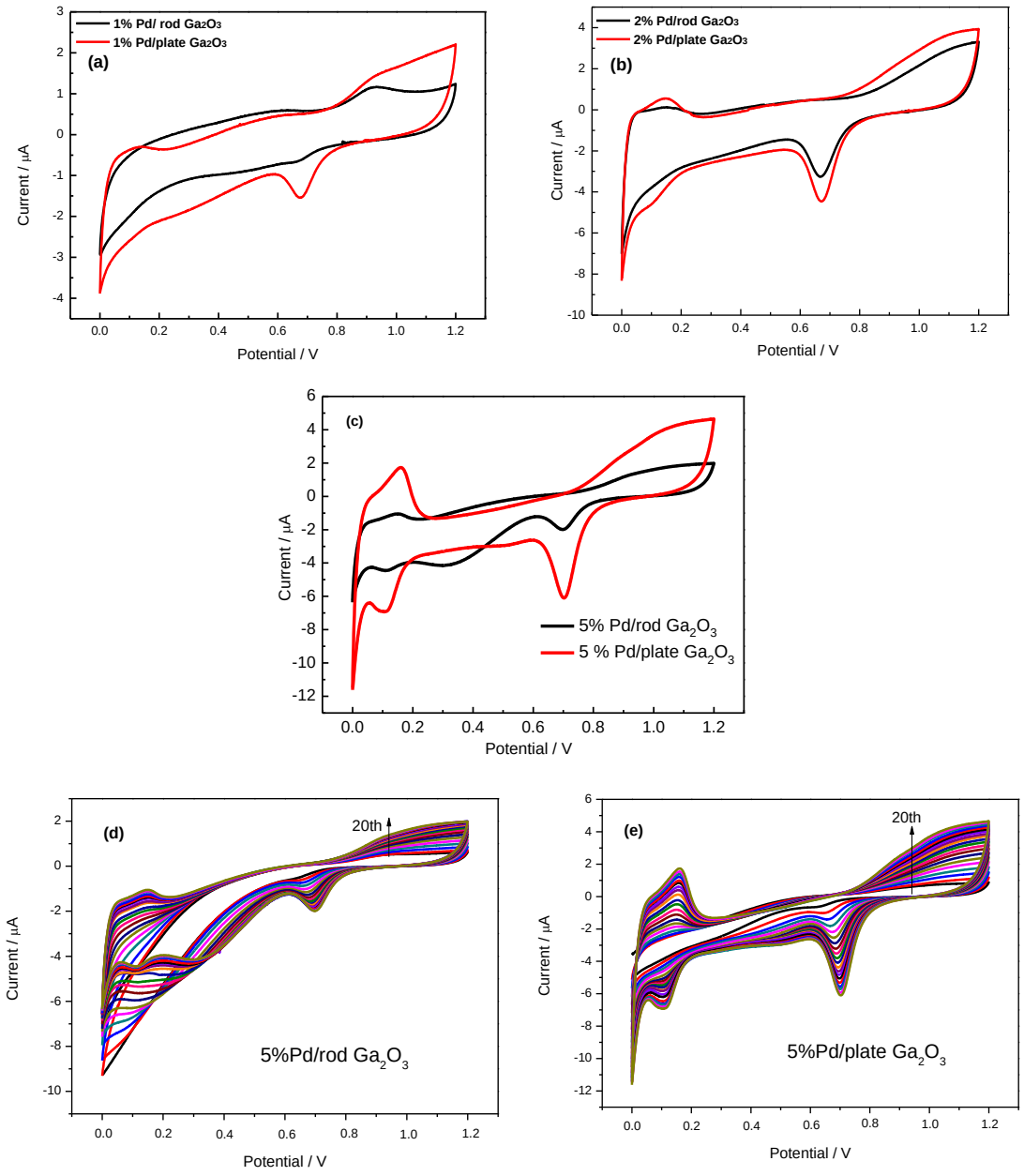

Figure 5.6 Comparison of CV curves of rod and plate forms Ga_2O_3 at (a) 1% Pd, (b) 2% Pd and (c) 5% Pd; representative consecutive CV of all 20 cycles for 5% Pd on rod (d) and plate (e) Ga_2O_3. All the measurements shown were scanned from 0.0 V to 1.2 V (vs. SHE) at 50 mV/s.

Based on the analysis of CV over all Pd doped Ga_2O_3 nanocatalysts, electrochemical oxidative CO stripping was further conducted following the pre-adsorption of CO over the two forms of Ga_2O_3 promoted with 5% Pd which was a more interesting and

important loading level in our study. A peak in the range of 0.7~1.2 V centering around 1.0 V is clearly observed in Figure 5.7 (a) (first cycle scan) due to the oxidation of adsorbed CO on Pd. The calculated electrochemically active surface (EAS_{co}) from the charge passed revealed a surprisingly large difference between the two supported Pd samples, being 0.42 and 0.07 $m^2 \bullet g_{Pd}^{-1}$ for 5% Pd plate Ga_2O_3 and 5% Pd rod Ga_2O_3, respectively (6 times), despite the comparable surface area of their supports. The electrochemical results clearly reflected that the stronger interaction of the Pd with the plate ((002) facet) than rod oxide ((111)/(110) facets), leading to significantly higher electrochemically active sites on the former material. However, it is noted that the nature of electrochemically metal active sites may not necessarily correspond to the same catalytically active sites for methanol synthesis as it is known that synergetic sites created at metal-metal oxide interface may be required for both CO_2 and H_2 activation and catalysis.[2,9] On the other hand, from the Figure 5.7 (a), the measured onset potential for the stripping process is lower for the plate form, being 0.77 ± 0.006 V and 0.83 ± 0.008 V for rod with the $peak_{max}$ shifting 15 ± 3 mV to lower voltage in plate sample. This earlier onset for the plate form indeed shows more chemically active form of surface Pd sites in synergy with this support material compared to the rod form. In addition, for most supported Pd samples, adsorbed CO on Pd is totally stripped off during the first anodic scan. Interestingly, it is noted here that CO stripping signals are still observed for both samples on the second and subsequent scans (higher CO stripping signals for each scan for the plate form). Thus, the results suggest CO_{ad} can be inter-transferred between Pd and Ga_2O_3 sites

presumably via surface carbonate/bicarbonate, resembling the reversible spillover phenomenon in catalysis with strong MSI.[10] Clearly, Ga_2O_3 and particularly its energetic (002) surface with the plate morphology has an extensive influence on the catalytic chemistry of Pd phase.

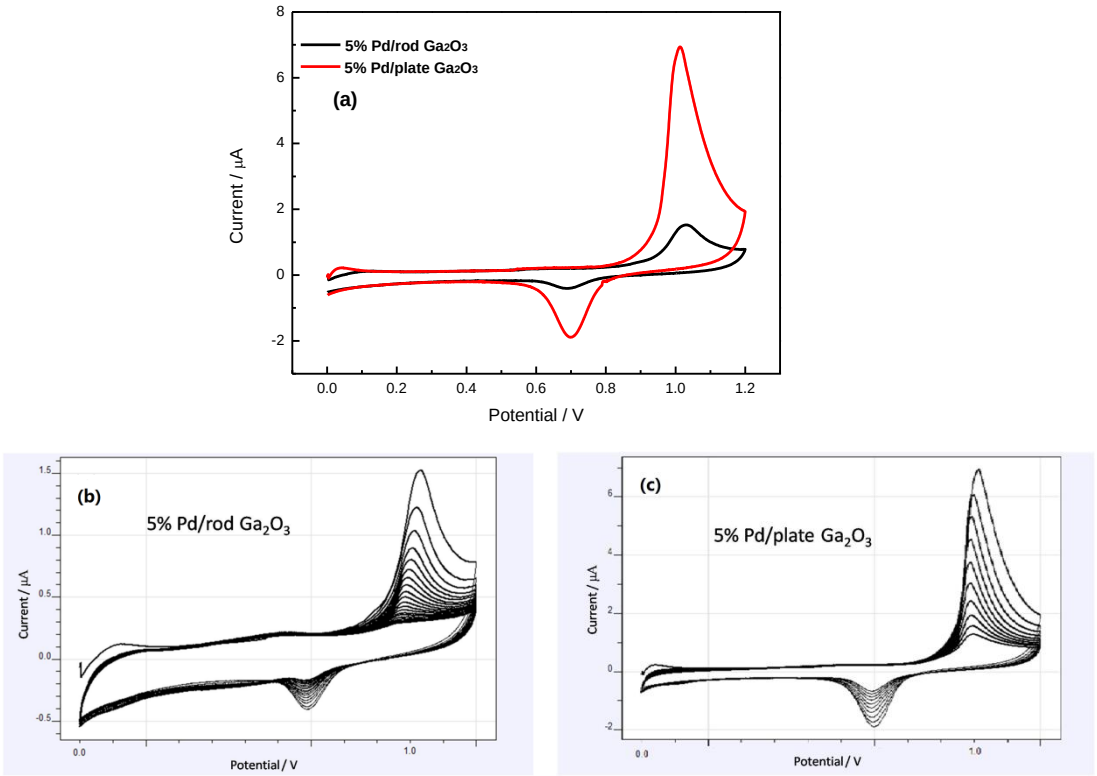

Figure 5.7 Comparison of the first cycle of CO stripping curves of rod and plate forms Ga_2O_3 doped with 5% Pd (a); consecutive CO stripping profiles of rod (b) and plate (c) Ga_2O_3 with 5% Pd loading. Measurements were scanned from 0.0 V to 1.2 V (vs. SHE) at 50 mV/s.

5.4.2 EPR and TPR/D

In order to gauge the intrinsic difference between the surface characteristics for rod and plate Ga_2O_3 nanocrystals and assess their interactions with metal, further material characterisations have been carried out. Electron paramagnetic resonance (EPR) was

used to probe the total unpaired electrons trapped in rod and plate Ga_2O_3 crystals. EPR profiles of plate and rod samples (Figure 5.8 and Table 5.2) clearly reveal that the plate sample gives higher signal of unpaired electrons (4.728 $x10^{16}$ spins per mg) than rod sample (2.076$x10^{16}$ spins per mg). The presence and quantity of spin reflect the degree of structural defects presented in these samples. The g value of 2.30 (plate) and 2.20 (rod) can be attributed to deep trapped electrons from typical oxygen defect sites in semiconductor oxide near the valence band (O_2^- acts as electron acceptor when O_2 molecule from air adsorbs on an oxygen vacancy).[2,9] Interestingly, only plate Ga_2O_3 gives a distinctive signal with g value of 1.96, which is attributed to shallow trapped donor defects near the conduction band. The presence of such donor defects clearly reflects the occupancy of excited electrons in the conduction band, indicating that the (002) surface on the plate form is more defective and electron richer than (111) or (110) surfaces of rod form. Similarly, a plate form ZnO also gave higher EPR signals for the deep trapped acceptors and unique shallow donors as compared to rod ZnO.[2,9] In addition, Yan *et. al.* reported a higher degree of surface defects for plate Ga_2O_3 than powder form by photoluminescence.[11]

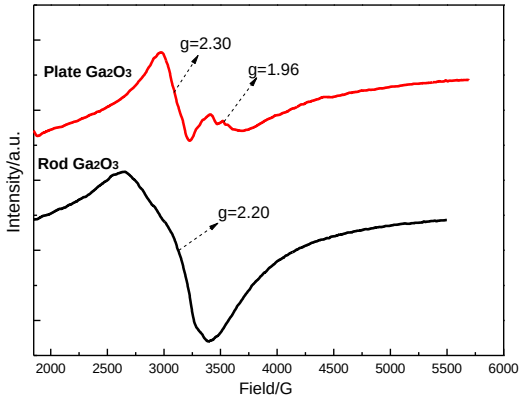

Figure 5.8 EPR spectra of rod and plate Ga_2O_3.

Table 5.2 The quantitative spin number obtained over two pure forms of Ga_2O_3

Samples	Absolute number of spins (/mg)	Absolute number of spins (/mm^3)
Rod Ga_2O_3	$2.076x10^{16}$	$1.055x10^{16}$
Plate Ga_2O_3	$4.728x10^{16}$	$3.402x10^{16}$

The interaction between Pd and the two forms of Ga_2O_3 was then studied by temperature programmed reduction (TPR). It was demonstrated that pure Ga_2O_3 would not undergo reduction in hydrogen until 900 ℃,[12] and this is clearly reflected by the TPR profiles of two pure Ga_2O_3 samples in our study (Figure 5.9 (a) and (b)). Figure 5.9 (a) and (b) also display TPR profiles of both 5% Pd/rod Ga_2O_3 and 5% Pd/plate Ga_2O_3, compared to their undoped samples. Figure 5.9 (a) shows three apparent reduction peaks at 365, 555 and 670 ℃, respectively in the 5% Pd/rod Ga_2O_3. For plate Ga_2O_3, there are four reducing peaks centered at 235, 340, 520 and 640 ℃, respectively presented in Figure 5.9 (b). Further detailed comparison of the two 5% Pd/Ga_2O_3 TPR profiles in Figure 5.9 (c) clearly reveals a stronger interaction between plate Ga_2O_3 ((002) surface) and Pd with all the reduction peaks shifting towards lower temperature than the rod form. It was noted that PdO was readily reduced to Pd^0 at sub-ambient temperature and the observation of a negative peak (hydrogen desorption

from Pd hydride) at 70 ℃ in both profiles clearly suggests the presence of Pd^0. The reduction peaks of Ga_2O_3 in the presence of Pd^0 are thought to be associated with the reduction of surface oxygens to generate oxygen vacancies at low temperatures, followed by deep reduction of lattice oxygen ions at high temperature due to the slow diffusion of lattice ions. No further assignment of the types of oxygen was attempted.

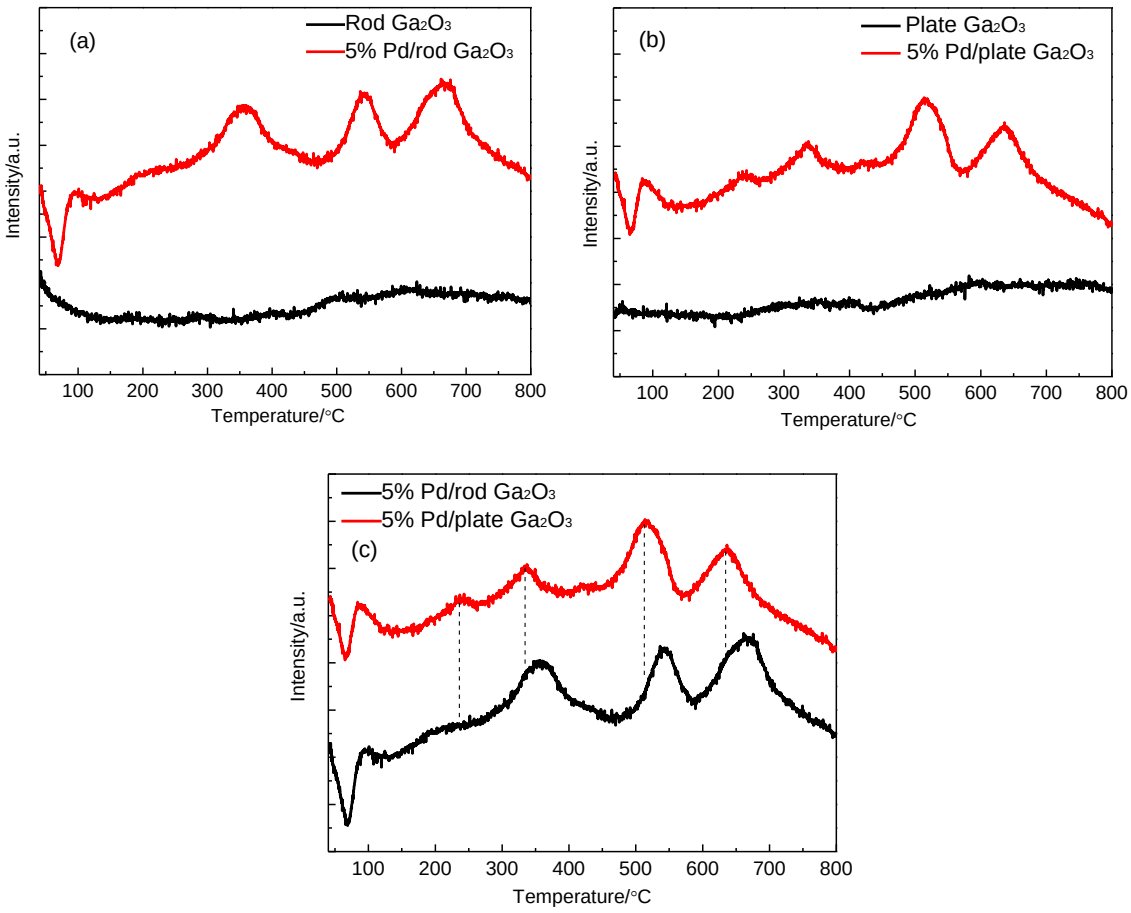

Figure 5.9 TPR profiles of rod Ga_2O_3 with and without 5% Pd (a); plate Ga_2O_3 with and without 5% Pd (b); TPR comparison of 5% Pd on rod and plate Ga_2O_3 (c).

Temperature programmed desorption (TPD) of CO_2 was also carried out on two forms of pure Ga_2O_3 materials to probe their surfaces (Figure 5.10). It is observed that plate form Ga_2O_3 shows a slightly larger desorption peak than rod Ga_2O_3. The scale of the

desorption peak area reflects the capability and amount of CO_2 adsorbed by two forms Ga_2O_3. The higher presence of defective sites, particularly oxygen vacancies on the plate form might be responsible for the difference in the capability and amount of taking up CO_2, since CO_2 would be more favorably adsorbed into oxygen vacancies compared with other sites when contacting the Ga_2O_3 surface. In addition, the temperature at which CO_2 comes off from the Ga_2O_3 in plate form is slightly higher, indicating a moderately stronger interaction between CO_2 and the plate form Ga_2O_3 surface. Detailed results are summarized in Table 5.3.

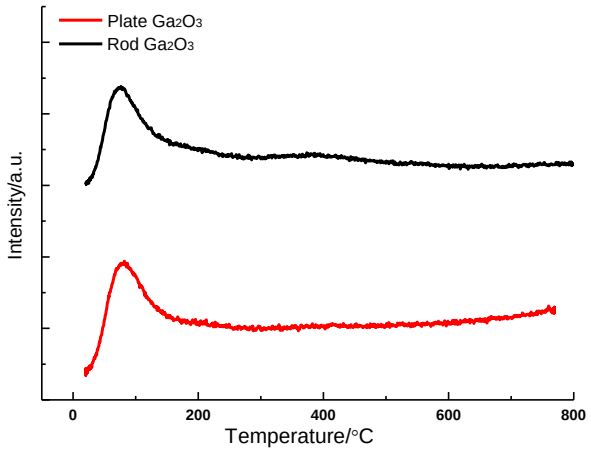

Figure 5.10 CO_2 TPD profiles of pure rod and plate forms of Ga_2O_3.

Table 5.3 Summary of CO_2 TPD data

Samples	Integrated peak area (a.u.)	Peak position (℃)
Rod Ga_2O_3	0.10212	76.47
Plate Ga_2O_3	0.12398	81.51

5.4.3 XPS

X-ray photoelectron spectroscopy (XPS) analysis of rod and plate Ga_2O_3 with and without Pd (5%) were performed to characterize the electronic properties of the Ga_2O_3

surface in the presence of Pd after pre-reduction in diluted H_2 (H_2/N_2=1:2) at 200 ℃ without exposure to air. The measured binding energy (BE) values for all components are based on the reference of the C 1s BE value (284.5 eV). The BE value of O 1s for plate Ga_2O_3 (529.7 eV) is slightly lower than that of rod Ga_2O_3 (529.8 eV), meaning electrons in plate Ga_2O_3 samples are slightly easier to be excited. After doping 5% Pd on both forms, their BE values for O 1s increase, to the values of 531.7 eV (plate) and 531.3 eV (rod), respectively. The larger up-shift of the O 1s BE value on plate form when doped with 5% Pd, indicates a more effective electron transfer from the oxygen on the plate Ga_2O_3 surface with the 5% Pd addition. The detailed comparisons are displayed in Figure 5.11 (a) to (c).

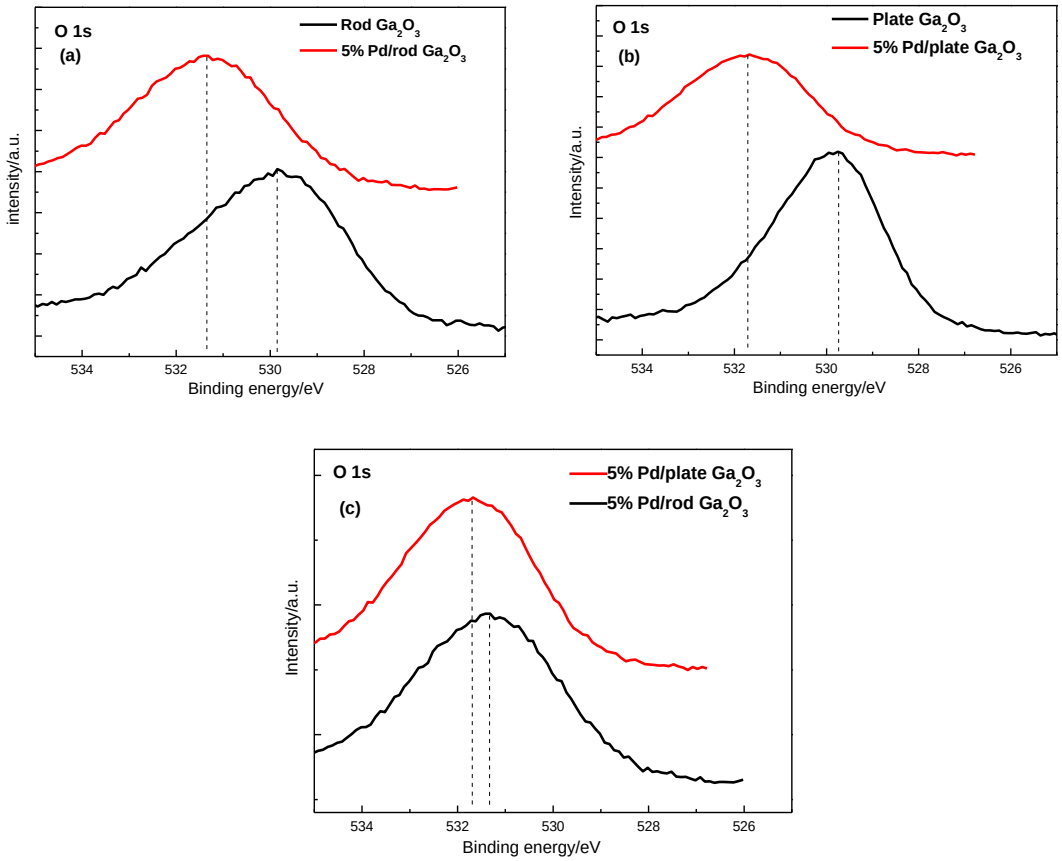

Figure 5.11 XPS data of O 1s for rod form Ga_2O_3 with and without 5% Pd (a); O 1s for plate form Ga_2O_3 with and without 5% Pd (b); comparison of O 1s for rod and plate form Ga_2O_3 with 5% Pd (c).

The Ga 2p 3/2 peak was the dominantly observed peak for analyzing chemical information of Ga for both forms Ga_2O_3. The BEs of Ga 2p 3/2 gave similar values of around 1117.4 eV for the two undoped samples, which was in good agreement with the literature value of 1117.5 eV.[13] After the addition of 5% Pd, there was no apparent change observed for the Ga 2p 3/2 BE on rod form, and the sample still showed only one Ga 2p 3/2 signal, the binding energy of which can be assigned to Ga^{3+}. However, for the 5% Pd/plate Ga_2O_3 sample, a very broad peak is observed in Figure 5.12 (a), which can be resolved into two Ga 2p 3/2 signals (BE values of 1117.4 and 1115.1 eV)

at an area ratio of 43:27. This may be attributed to the co-existence of Ga^{3+} and reduced Ga^{+}/Ga^{0}. Clearly, the strong and extensive interface created between Pd and the plate Ga_2O_3 surface at 5% Pd loading suggested that a deep reduction of the oxide support happened to generate more reduced Ga species from its surface (in agreement with the TPR results). There is also a slight shift in Pd signals (Figure 5.12 (b)) between the two forms, indicating that there might be PdGa alloy formation on the plate form Ga_2O_3, but the signals are too poor to be further ascertained.[14]

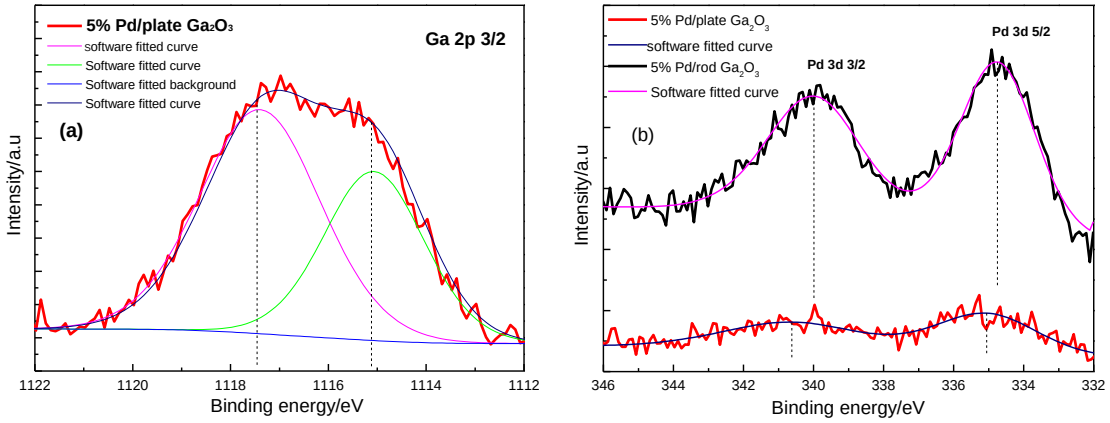

Figure 5.12 XPS data of Ga 2p 3/2 on 5% Pd/plate Ga_2O_3 (a); Pd 3d 3/2 and Pd 3d 5/2 data for both forms of Ga_2O_3 with 5% Pd loading (b).

5.4.4 Computational modeling and calculations

It is becoming clear that the plate form Ga_2O_3 with a higher degree of defects and electron richer (002) surface must exert a stronger electronic interaction with Pd than the rod form (110) or (111) surface and in some cases, leading to a deep reduction of Ga^{3+} to account for superior catalysis. DFT calculations were then carried out to probe the electronic properties of this energetic (002) surface as compared to the (110) and

(111) surfaces of Ga_2O_3.

It is interesting to point out that the (110) and (111) faces of rod Ga_2O_3 are typical normal non-polar surfaces containing equal numbers of cations and anions while the (002) face represents a polar surface for plate Ga_2O_3 with either O anion or Ga cation terminated surfaces.[15,16] Their atomistic models and corresponding calculated density of states (DOS) at different energies are shown in Figures 5.13-5.15. It was noticed that the cation and anion arrangements over the exposed (002) surface of Ga_2O_3 are unbalanced hence giving an overall non-zero polarity in the top layers.[15,16] Depending on the degree of covalency, the coloumbic repulsion between ions of the same charge tends to give rise to a higher surface energy than those of other exposed surfaces. Energetic polar oxide surfaces have not been well studied as metal catalyst supports, but the high methanol yields noted in this work clearly suggested they could be of considerable catalytic interest. It is evident that such an energetic polar oxide (002) surface can interact strongly with deposited Pd metal, thereby imparting superior catalytic performance as demonstrated in the formation of methanol on the plate form of Ga_2O_3.

From results shown in Figure 5.13, it can be seen that a typical (110) non-energetic, non-polar surface (Figure 5.13 (a)) displays a similar DOS pattern compared to bulk Ga_2O_3, as displayed in Figure 5.13 (b). For this (110) non-polar surface, the top occupied valance band is significantly contributed by p-orbitals of O (Figure 5.13 (c)) and the conduction band is dominantly contributed by s and p-orbitals of Ga (Figure 5.13 (d)), with a wide forbidden surface bandgap in between. The line at 0 eV

represents the Fermi level.

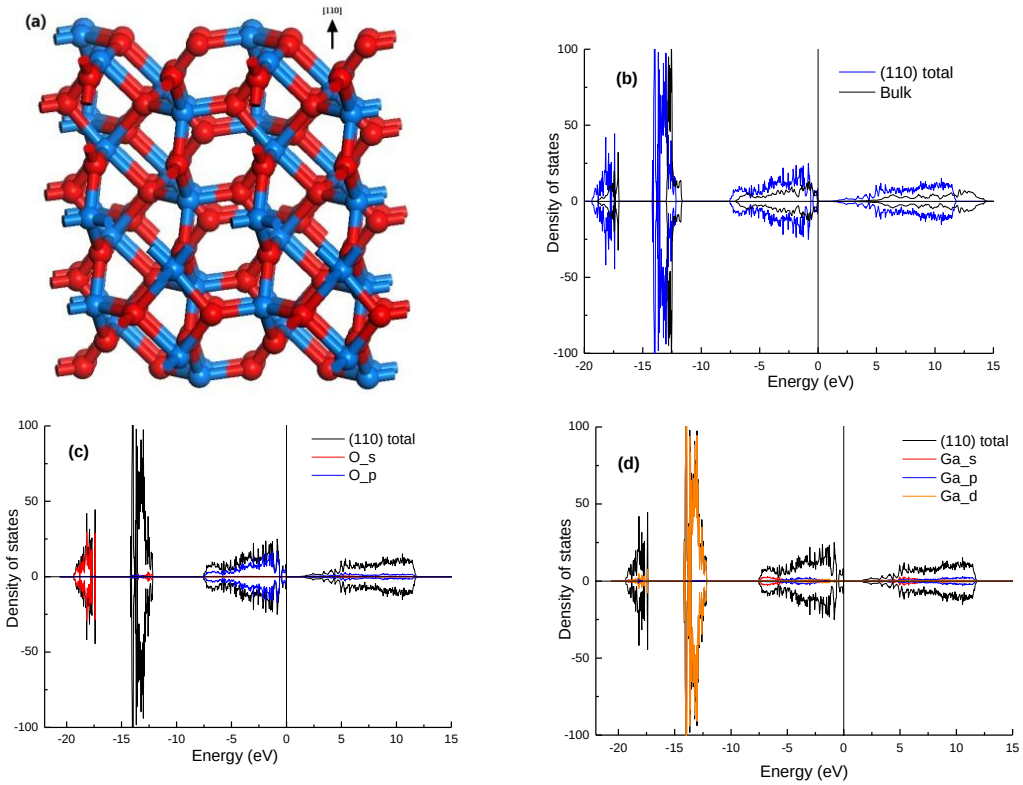

Figure 5.13 Atomistic model showing (110) non-polar surface of Ga_2O_3 (O: red, Ga: blue) (a); DOS of (110) surface in comparison with bulk Ga_2O_3 (b); DOS of (110) surface with orbital contributions from O (c) and Ga (d).

Figure 5.14 displays results for the non-energetic, non-polar (111) surface, which is quite similar to the (110) surface. From the DOS calculations in Figure 5.14 (b), It can be seen that it exhibits a slightly narrower bandgap than the (110) surface, but is still well separated by the Fermi level. As for the orbital influence, those projected DOS profiles of O and Ga contributions (Figure 5.14 (c) and (d)), show similar results to the (110) system.

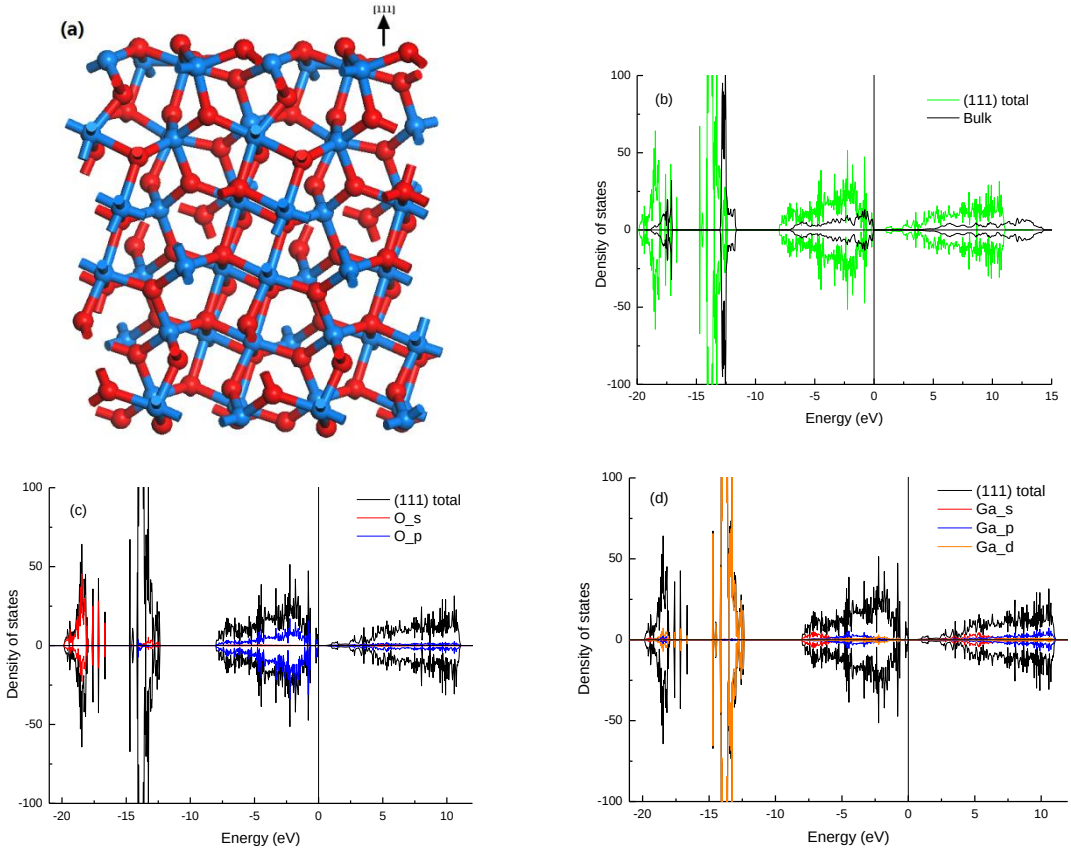

Figure 5.14 Atomistic model showing (111) non-polar surface of Ga_2O_3 (O: red, Ga: blue) (a); DOS of (111) surface in comparison with bulk Ga_2O_3 (b); DOS of (111) surface with orbital contributions from O (c) and Ga (d).

In contrast, calculations for the DOS associated with the polar (002) surface (Figure 5.15 (a) and (b)) clearly reveal some unusual electronic properties. On both terminations, a strong modification of the DOS with respect to bulk Ga_2O_3 takes place. The principal effects consist of an important strong exchange splitting and distortion of the DOS towards higher energy at the top of the valence band (up-shift) due to electrostatic repulsion on the O termination (Figure 5.15 (c)) and a downward shift of the conduction band on the Ga termination ((Figure 5.15 (d)). with a significant reduction in the surface forbidden band gap. The band contributions mainly from

p-orbitals of O (Figures 5.15 (e, f)) and s and p-orbitals of Ga (Figure 5.15 (g, h)) for the surface valence and conduction bands, respectively, are also shown for comparison. As a result, the surface bandgap became much narrower and electrons could be promoted more easily to higher surface bands. It was noted that similar calculations over (002) ZnO and other polar metal oxide surfaces reported the narrowing of band gaps and in some cases, metallation (total disappearance of bandgap) was suggested.[15,16]

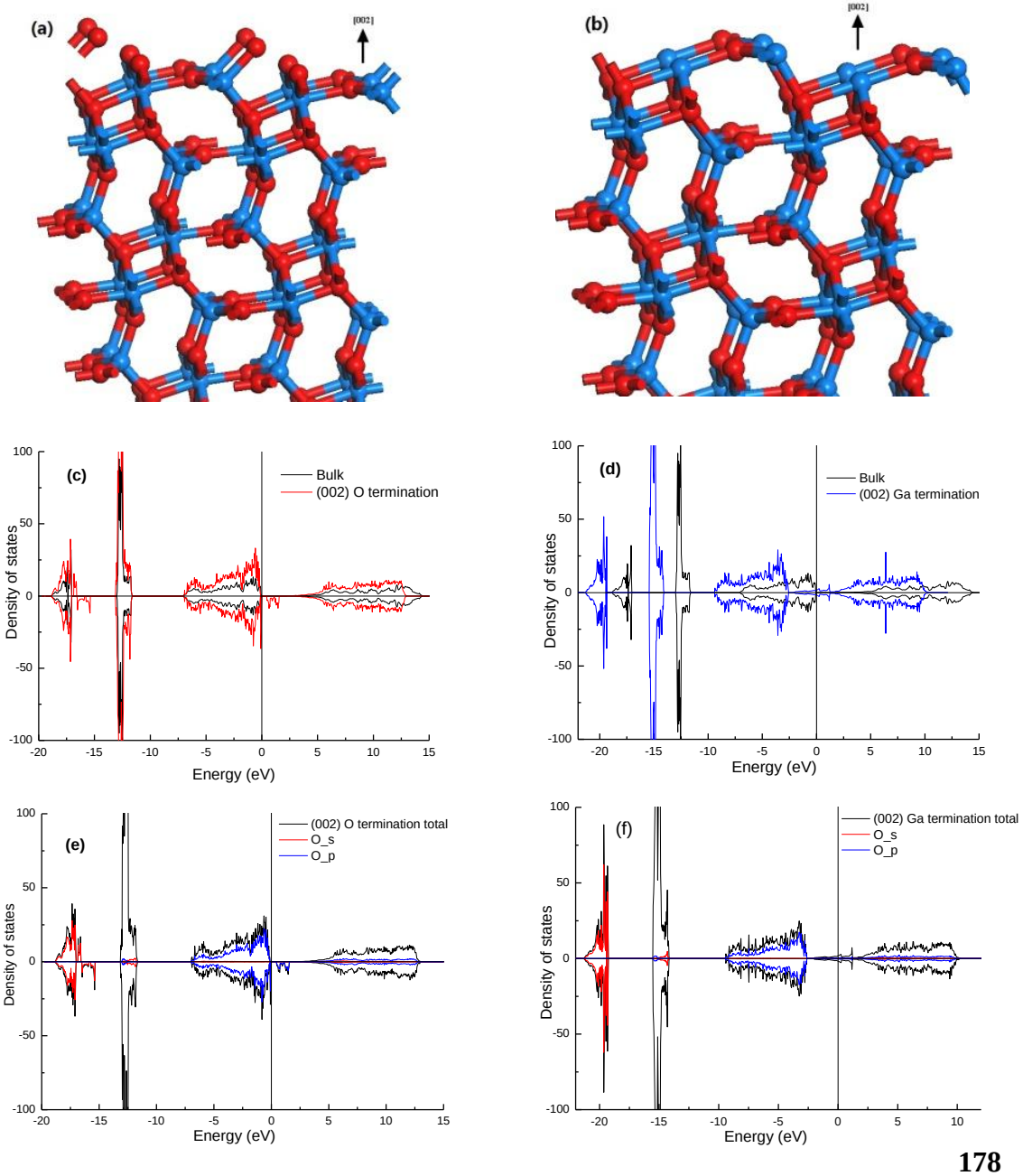

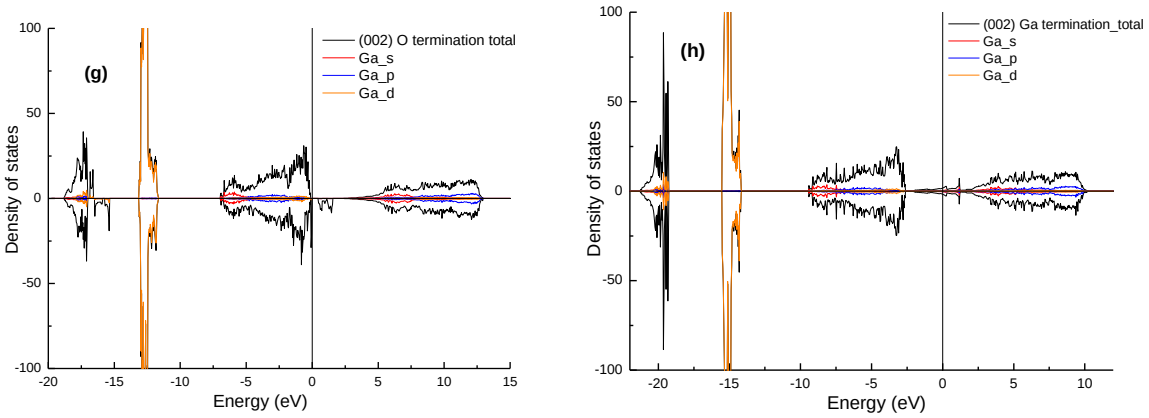

Figure 5.15 Atomistic models showing (002) polar surfaces of Ga_2O_3 with oxygen termination (a) and gallium termination (b) (O: red, Ga: blue); DOS of (002) polar surfaces with O termination (c) and Ga termination (d) in comparison with bulk Ga_2O_3; O orbital contributions to DOS of O terminated (e) and Ga terminated (f) (002) polar surfaces; Ga orbital contributions to DOS of O terminated (g) and Ga terminated (h) (002) polar surfaces.

It is accepted that electrostatic repulsion of the same charged species within the layer on a high energy oxide surface can render instability of its structure. However, the high energetic surface may tend to seek various mechanisms for stabilization, such as selective adsorption of counter-ions, surface reconstruction and excitation of localized electrons to delocalized bands as our calculations presently indicate.[15,16] If the latter takes place, the excitation of electrons to higher conduction bands from localized oxygen anions would facilitate oxygen release to create anion vacancies. Therefore, the minimum energies required have been calculated for the formation of an oxygen vacancy from (002) polar O terminated and (110) and (111) non polar surfaces with active oxygen sites at the lowest coordination. Results were -0.78 eV for the polar (002) surface, and +1.74 eV and +2.94 eV for the (110) and (111) non polar surfaces,

respectively, indicating that the unstable high energy oxide (002) surface was readily prone to produce oxygen vacancies and excited electrons. This mechanism was also well verified by EPR analysis. As mentioned before, the EPR studies on rod and plate Ga_2O_3 indeed confirmed that the plate sample gave a higher signal of unpaired electrons (4.728 $x10^{16}$ spins per mg) than rod samples (2.076$x10^{16}$ spins per mg) due to trapped electrons from surface oxygen defect sites near the valence band.[2.9] In addition, the plate Ga_2O_3 also gave a distinctive signal due to shallow trapped donor defects near the conduction band, indicative of a more electron rich conduction band.

5.4.5 Further discussions

It is therefore evident from our work that it was the instability of this defective (002) Ga_2O_3 polar surface and its high propensity for electron transfer facilitating the interaction with Pd (as a way of stabilization) at their Schottky-Mott interface (the oxide support has a higher conduction band energy than the Fermi-level of the overlying metal).[2,6-7,9] This can lead to higher metal dispersion and enlarge interface, and, in some cases, possible (PdGa) alloy formation from a deep reduction of Ga_2O_3 at the material's interface,[14] giving higher activity and selectivity in methanol production than those of low energy surfaces.

Comparison of the Pd/Ga_2O_3 catalytic data from this thesis with previously studied Cu/ZnO catalysts by our group[2] for the same reaction, might consolidate the argument. It is noted from the Table 5.4 that the present Pd/Ga_2O_3 catalysts are clearly more active for methanol synthesis than the previously reported Cu/ZnO catalysts but with

a slightly lower selectivity. Interestingly, Ga_2O_3 (monoclinic) and ZnO (wurtzite) are structurally very different oxides. Our experiments undoubtedly suggested that the uses of (002) polar surfaces of both these crystal structures, which were seen as the plate forms, comprise alternating oxygen anion and cation layers carrying a non-zero charge of each layer were more superior as supports for metals than corresponding non-polar surfaces, giving higher yields in the methanol synthesis from CO_2 hydrogenation.

Table 5.4 Summary of catalytic performance of 5% Pd on rod and plate Ga_2O_3 crystals in comparison with Cu on rod and plate ZnO

Catalysts	CO_2 Conv. (%)	CH_3OH Select. (%)	CH_3OH Yield (%)
5% Pd/rod Ga_2O_3	11.0	41.3	4.5
5% Pd/plate Ga_2O_3	17.3	51.6	8.9
Cu/rod ZnO/ Al_2O_3 [2]	15.8	41.0	6.5
Cu/plate ZnO / Al_2O_3 [2]	15.5	64.5	10.0

Scheme 5.1 summarizes pictorially the possible electronic interactions between Pd and Ga_2O_3 as well as Cu and ZnO from our recent findings. The band positions are presented using literature bulk values[17,18] with no information on nano-regime. Interestingly, these two pairs previously identified as the most active metal-metal oxide catalysts from empirical screening of large samples actually match well with energy levels with each others. As mentioned before, this can facilitate electron transfer from oxide support to metal at their Schottky-Mott interfaces (the oxide support has a higher conduction band energy than the Fermi-level of the overlying metal). This scheme can also account for further facilitated electron transfer from

downshifted conduction bands of using polar (002) Ga_2O_3 and ZnO surfaces to metals, leading to higher catalytic performance.

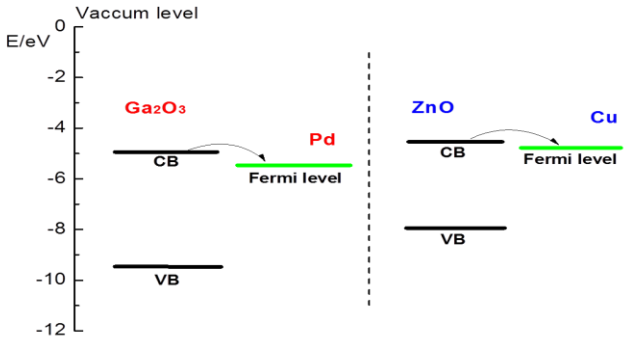

Scheme 5.1 Electronic levels match of Pd-Ga_2O_3 and Cu-ZnO pairs for SMSI.

The mechanism of methanol synthesis from catalytic hydrogenation of CO_2 and nature of active site are still very unclear despite the intense research over the past 40 years. From kinetic and spectroscopic studies, surface stepwise hydrogenations involving formate, methylenebisoxy, methoxy to methanol have been proposed for both Cu/ZnO and Pd/Ga_2O_3 based catalysts.[3,4,19-21] Electron rich surfaces have been found to favor this catalytic hydrogenation.[2,9] The assignments of possible active sites ranging from simple metal sites, sites on small metal islands under high isomorphic strain on support, optimum balance between metallic and partial oxidized species, metal sites decorated with heteroatoms from the extensive oxide support reduction (CuZn and PdGa) and synergetic sites created between metal and support have been suggested.[2-4,9,19-21] In this work, it is stressed that the study did not attempt to address the specific mechanism nor identify exact active sites for this reaction but it has been focused more on the materials interaction between metal and different surfaces of support oxide.

5.5 Conclusion

In conclusion, it is well accepted that the metal-support interaction, which originates from either geometric or/and electronic perturbations between the two catalyst components, plays an important role in heterogeneous catalysis. Here, based on the controllable preparation of Ga_2O_3 nanocrystals with two different shapes (i.e. rod and plate forms), Ga_2O_3 nanocrystals with the majority of their surfaces covered with either (002) polar or (110)/(111) non-polar surfaces were used to host Pd. These materials have been tested for methanol synthesis from CO_2 hydrogenation under industrially applicable conditions, and characterized extensively. It is reported that a significant SMSI between (002) polar surface of plate Ga_2O_3 and Pd promoter leads to higher metal dispersion and facilitated electron transfer between them. It is also suggested that the higher degree of oxygen defects on (002) polar surface for plate Ga_2O_3 could facilitate CO_2 adsorption and its further activation. It is aimed to correlate this SMSI and electron transfer with elementary catalytic steps in the future, which may lead to rational design of superior catalysts for this important process.

5.6 References

1. K. M. K. Yu, I. Curcic, J. Gabriel and S. C. E. Tsang, *ChemSusChem.,* 2008, **1**, 893–899.
2. F. Liao, Y. Huang, J. Ge, W. Zheng, K. Tedsree, P. Collier, X. Hong and S. C. Tsang, *Angew. Chem. Int. Ed.*, 2011, **50**, 2162-2165.
3. M. Saito, *Catalysis Survey from Japan*, 1998, **2**, 175-184.
4. S. E. Collins, D. L. Chiavassa, A. L. Bonivardi and M. A. Baltanas, *Catal. Lett.*, 2005, **103**, 83-88.
5. L. K. Rihko-Struckmann, A. Peschel, R. Hanke-Rauschenbach and K. Sundmacher, *Ind. Eng. Chem. Res.*, 2010, **49**, 11073 – 11078.
6. T. Fujitani and I. Nakamura, *Bull. Chem. Soc. Jpn.*, 2002, **75**, 1393-1398.
7. T. Fujitani, M. Saito, Y. Kanai, T. Watanabe, J. Nakamura and T. Uchijima, *Appl. Catal. A: Gen.*, 1995, **125**, L199-L202.
8. J. A. V. Bokhoven, *ChemCatChem*, 2009, **1**, 363-364.
9. F. Liao, Z. Zeng, C. Eley, Q. Lu, X. Hong and S. C. E. Tsang, *Angew. Chem. Int. Ed.*, 2012, **51**, 5832-5836.
10. W. C. Conner and J. L. Falconer, *Chem. Rev.*, 1995, **95**, 759-788.
11. S. Yan, L. Wan, Z. Li, Y. Zhou and Z. Zou, *Chem. Commun.*, 2010, **46**, 6388-6390.
12. E. Gebauer-Henke, J. Grams, E. Szubiakiewicz, J. Farbotko, R. Touroude and J. Rynkowski, *J. Catal.*, 2007**, 250**, 195-208.
13. Y. Yang, H. Ma, C. Xue, H. Zhuang, X. Hao and J. Ma, *Appl. Surf. Sci.*, 2002, **202**, 295-300.

14. C. D. Wagner, *Faraday Discuss. Chem. Soc.,* 1975, **60**, 291-300.

15. C. Noguera, *J. Phys.: Condens. Matter*, 2000, **12**, R367-R410.

16. J. Goniakowski, F. Finocchi and C. Noguera, *Rep. Prog. Phys.*, 2008, **71**, 1-55.

17. D. S. Ginley, H. Hosono and D. C. Paine, *Handbook of Transparent Conductors*, Springer, 2010.

18. H. L. Skriver and N. M. Rosengaard, *Phys. Rev. B*, 1992, **46**, 7157-7168.

19. X. Liu, G. Lu, Z. Yan, and J. Beltramini, *Ind. Eng. Chem. Res.,* 2003, **42**, 6518-6530.

20. T. Ressler, B. L. Kniep, I. Katsatkin and R. Schlogl. *Angew Chem. Int. Ed.,* 2005, **44**, 4704-4707.

21. M. Behrens, F. Studt, I. Kasatkin, S. Kuhl, M. Havecker, F. A. Pederson, S. Zander, F. Girgsdies, P. Kurr, B. L. Kniep, M. Tovar, R. W. Fischer, J. K. Norskov and R. Schlogl, *Science*, 2012, **336**, 893-897.

Chapter 6 Shape effect of Pd promoted Ga_2O_3 nanocatalysts for H_2 evolution from methanol photodecomposition

Chapter 6 Shape effect of Pd promoted Ga_2O_3 nanocatalysts for H_2 evolution from methanol photodecomposition 186

6.1 Introduction 187

6.2 Photocatalytic performance 189

6.2.1 Effect of reaction time 192

6.2.2 Effect of methanol concentration 194

6.2.3 Comparison with TiO_2 based catalysts 194

6.3 Characterizations and discussions 196

6.3.1 PXRD 196

6.3.2 TEM 198

6.3.3 EPR 201

6.3.4 Raman spectroscopy 203

6.3.5 UV-Visible spectroscopy 205

6.3.6 ssNMR 206

6.3.7 PL and TRPL spectroscopy 209

6.4 Conclusion 216

6.5 References 219

6.1 Introduction

Hydrogen has been identified as a potential energy carrier in many low greenhouse gas (GHG) energy scenarios due to its high energy capacity and environmental friendliness.[1-3] Most of the hydrogen containing compounds in their liquid forms such as biomass molecules, alcohols and even water are potential sources of H_2.[1] During the past 20 years, the technology for generating hydrogen by photocatalytic splitting of water has attracted much attention. However, high energy is required to break up the stable H_2O molecule to form H_2 ($\triangle G$=237.1 kJ/mol)[4] making this process very thermodynamically unfavorable. On the other hand, hydrogen production from photodecomposition of methanol (CH_3OH) requires a much lower decomposition energy ($\triangle G$=16.1 kJ/mol)[5] than water. In addition, the high hydrogen storage capacity in the form of a methanol molecule (4H in each molecule) could enable the liquid methanol molecule under s.t.p. conditions to function as a mobile energy carrier. When required, H_2 can then be generated on-site through methanol decomposition.

As for photocatalytic reactions, the catalyst itself plays a key role in governing activity and selectivity of a target reaction. There have been some intense investigations on the development of TiO_2 based catalysts (e.g. metal doped TiO_2). However, their generally low activity and poor energy conversion have promoted vigorous search for more effective catalysts in this area.

On the other hand, Ga_2O_3 is a chemically and thermally stable semiconductor with a bandgap of 4.9 eV,[6] which is expected to be a good photocatalyst for various applications such as wastewater treatments and the decomposition of aromatic

compounds.[7] Therefore, potentially, Ga_2O_3 based materials could be good candidates for methanol photodecomposition to H_2. It is also well-known that morphology (shape) effect over nanocatalysts is of paramount importance. The activity and selectivity of a reaction are not only governed by chemical composition and size but also by type of exposed surface (different shapes) of the catalyst,[8] and thus controlling the shape of a particle can add an exciting variable in tailoring the properties of nanocatalysts. So far, only few examples of shape effects of single-component metal nanocrystals and semiconductor oxide nanocrystals have been demonstrated, for different catalytic reactions.[8-10] To the best of our knowledge, there is no reported study on shape effect of Ga_2O_3 for photocatalytic decomposition of methanol to H_2.

In this chapter, a fundamental study of the morphological effect of three different forms of Ga_2O_3 (i.e. β-Ga_2O_3 nanorods, β-Ga_2O_3 nanoplates and γ-Ga_2O_3 nanoparticles, respectively) is reported, towards H_2 evolution from the methanol photodecomposition reaction. Pd metal at various loadings was doped as cocatalyst, which enabled investigation of the metal support interaction (MSI) for this target reaction. Apart from the testing, the catalysts were extensively characterized by various techniques including PXRD, TEM, PL & TRPL, EPR, Raman and UV-Vis spectroscopy, and solid state nuclear magnetic resonance (ssNMR) in order to elucidate the shape effect of Ga_2O_3 for this reaction.

6.2 Photocatalytic performance

Three morphologically distinctive forms of Ga_2O_3 (i.e. rod, plate, and particle forms) and their corresponding Pd doped photocatalysts were tested for the methanol photodecomposition reaction under the conditions detailed in Chapter 3. As for the preparation of the catalysts for this study, the wet impregnation method and post-treatments were used which were described in Chapter 3. The Pd loadings were 0.5 wt%, 1 wt%, 2 wt% and 5 wt%, respectively, on the three forms of Ga_2O_3. Their photocatalytic results on methanol decomposition are summarized in Table 6.1 and Figure 6.1.

Table 6.1 Summary of methanol photodecomposition results on three different forms of Ga_2O_3 (i.e. β-Ga_2O_3 rods, β-Ga_2O_3 plates and γ-Ga_2O_3 particles) and with various amounts of Pd. All reaction time was 5 hours

Rod	H_2 (μmol)	CO_2 (μmol)	Plate	H_2 (μmol)	CO_2 (μmol)	Particle	H_2 (μmol)	CO_2 (μmol)
Pure	1594.2	4.6	Pure	2249.8	4.5	Pure	2038.4	20.4
0.5% Pd	4029.2	12.0	0.5% Pd	3217.4	8.2	0.5% Pd	2690.8	18.3
1.0% Pd	3870.3	9.1	1.0% Pd	2510.7	6.9	1.0% Pd	2165.7	6.2
2.0% Pd	1680.7	5.9	2.0% Pd	2314.2	6.8	2.0% Pd	1324.1	5.6
5.0% Pd	1629.0	5.1	5.0% Pd	2294.3	4.9	5.0% Pd	727.2	2.9

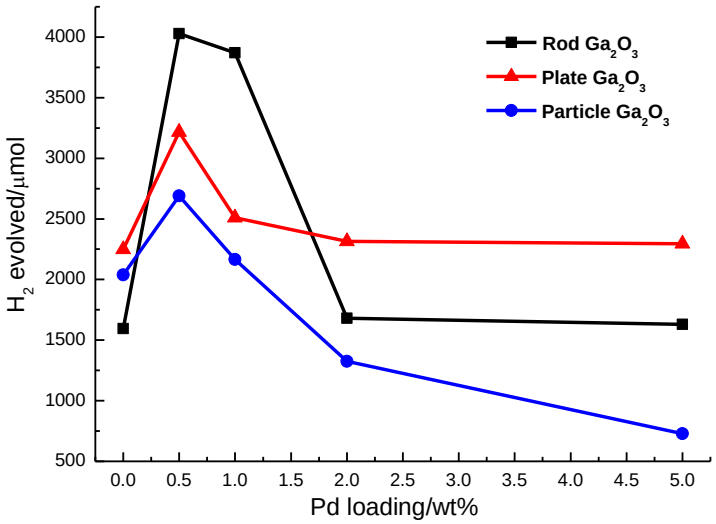

Figure 6.1 H_2 evolved from methanol photodecomposition on rod, plate and particle Ga_2O_3 with various Pd loadings. All reaction time was 5 hours.

The results from the Table 6.1 and Figure 6.1 show that all the three pure Ga_2O_3 materials of different shapes exhibit a considerable activity for H_2 evolution via the decomposition of methanol. Without the addition of Pd, β-Ga_2O_3 plate shows a higher activity than γ-Ga_2O_3 particle and β-Ga_2O_3 rod (plate > particle > rod) for the H_2 photodecomposition reaction, which does not follow the order of their surface area (N_2 BET surface area of particle, rod and plate were 99.45, 21.87 and 16.69 m^2/g, respectively). This clearly suggests the importance of the surface feature of a catalyst for this reaction.

Also as seen from Table 6.1, as soon as Pd metal is loaded onto Ga_2O_3, the activity of the Ga_2O_3 catalysts is altered dramatically. With the incorporation of Pd, all three forms of Ga_2O_3 generally show a very significant enhancement in H_2 production from the methanol decomposition, indicating a synergetic effect of the Pd co-catalyst with Ga_2O_3 (MSI). However, the interaction(s) between Pd and the oxide appears to be

different for different forms of Ga_2O_3. For example, for the Pd loadings of 0.5-1.0%, the activity order is rod > plate > particle. Notice that 1 wt% Pd is commonly found to be the upper limit of metal loading for many photocatalytic reactions.[11,12] At loadings >1.0%, the activity order is changed to plate > rod > particle, suggesting that a number of interplaying factors (surface area, surface feature, crystallinity, interface) could affect the photocatalytic activity.

All the catalysts also show some low levels of CO_2 produced from the catalyzed reaction as the only other gaseous product but there is a strong correlation between CO_2 and H_2 activities. This matches the expectation that the two products are derived from the same decomposition reaction. However, their quantities evolved do not match with the stoichiometric value (CO_2/H_2=1:3), indicating that the photochemical process is a very complex cascade reaction and might not be catalyzed in a simple stoichiometric manner. In addition, analysis of liquid mixture after photoreaction by HPLC revealed only a tiny amount of formaldehyde, suggesting this reaction might have undergone stepwise dehydrogenations before hydrogen and carbon dioxide were formed.

In order to ensure the above measurements were correct, control experiments were carried out (Table 6.2). It is shown that 1% Pd/Ga_2O_3 plate catalyst, in absence of light irradiation, produced no H_2 or CO_2 and a very small amount of H_2 was detected under light without a catalyst. Finally, the same catalyst was tested in 5% CH_4/Ar atmosphere but no gas product was detected. When 100 mL pure H_2O was added to 1% Pd/Ga_2O_3 plate under light irradiation, a very small amount of H_2 (50.4 μmol) was

evolved. The result is in an agreement with literature, showing that Pd/Ga_2O_3 is also capable of water splitting.[13] In the absence of a catalyst, there is no production for H_2. All the control experiments indicate that the vast majority of H_2 is generated from methanol photodecomposition, with only a small contribution from water splitting. The internal gas standard (methane) was stable and hence did not affect the catalytic results.

Table 6.2 Summary of control experiments (reaction time: 5 hours, at 253.7 nm)

Details of control experiments	H_2 (μmol)	CO_2 (μmol)
1% Pd/Ga_2O_3 plate (methanol+H_2O, 1:1 (v/v),100 mL total; 100 mg catalyst; no UV irradiation)	N/A	N/A
Methanol+H_2O (1:1 (v/v), 100 mL total; no catalyst)	1.7	N/A
1% Pd/Ga_2O_3 plate (5% CH_4/Ar; no methanol and no H_2O; 100 mg catalyst)	N/A	N/A
1% Pd/Ga_2O_3 plate (100 mL H_2O; 100 mg catalyst; no methanol)	50.4	N/A
H_2O (100 mL; no catalyst)	N/A	N/A

In further studies, effects such as reaction time and methanol concentration were investigated over the selected 0.5% Pd/γ-Ga_2O_3 catalyst. A comparison to the benchmarked TiO_2 catalysts of various metal dopants was also conducted and the results are presented in the following sections.

6.2.1 Effect of reaction time

The reaction time was investigated using 0.5% Pd/γ-Ga_2O_3 as a selected catalyst. With increasing reaction time, the amount of H_2 evolved from the catalyst increases accordingly (Table 6.3). The linear profile (Figure 6.2) clearly suggests that, under

photoreaction conditions, the catalyst can continuously generate H_2 in a highly active manner even at 14 hours. This reflects the excellent activity and stability of the Pd/Ga_2O_3 catalysts towards this reaction. Also, the Ga_2O_3 based catalysts showed a fast and readily production of H_2 within the first 2 hours of low power UV irradiation. On the other hand, many other types of catalysts have been reported to have longer induction periods before reaching a stable H_2 production rate. [4,11,14]

Table 6.3 Effect of reaction time on methanol photodecomposition. Selected catalyst: 0.5% Pd/γ-Ga_2O_3 particles

Reaction time	H_2 (μmol)	CO_2 (μmol)
2 hours	937.3	0.67
5 hours	2690.8	18.3
8 hours	3678.8	21.4
11 hours	5123.3	24.9
14 hours	6599.2	32.7

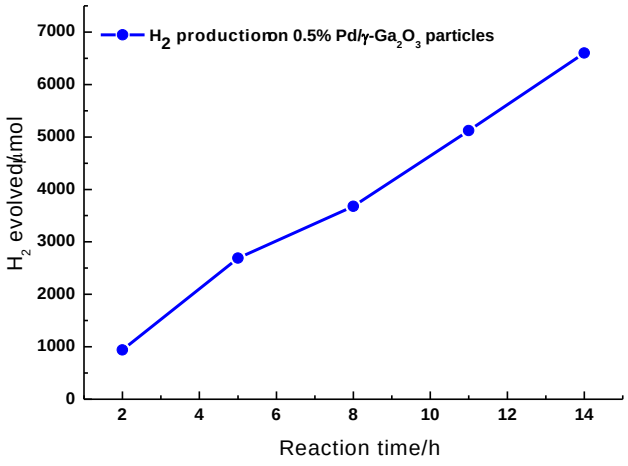

Figure 6.2 Results of H_2 production from methanol decomposition at different reaction time over the selected 0.5% Pd/γ-Ga_2O_3 particle catalyst.

6.2.2 Effect of methanol concentration

Table 6.4 and Figure 6.3 show that the H_2 production is progressively increased at increasing methanol concentration. However, the degree of enhancement is quite small. Nevertheless, this indicates that hydrogen is clearly produced from the methanol decomposition.

Table 6.4 Effect of methanol concentration on methanol photodecomposition (total volume of liquid mixture: 100 mL; reaction time: 5 hours; selected catalyst: 0.5% Pd/γ-Ga_2O_3 particles)

Methanol concentration (v/v)	H_2 (μmol)	CO_2 (μmol)
10%	2493.2	38.2
30%	2567.4	19.4
50%	2690.8	18.3
70%	2930.1	16.8

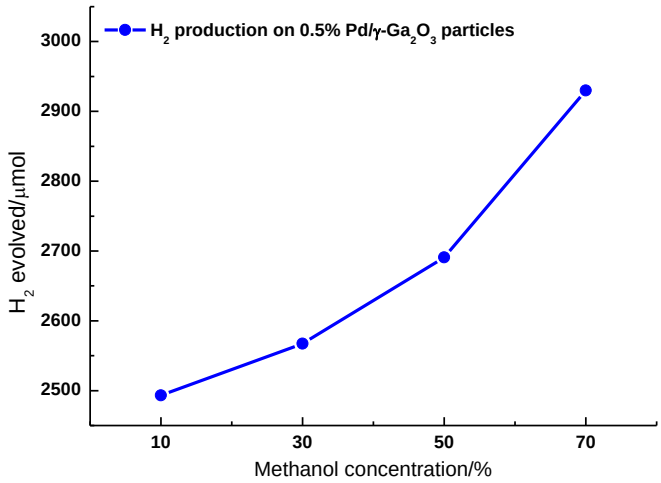

Figure 6.3 Results of methanol concentration effect on H_2 evolution from methanol decomposition over 5 hours. Selected catalyst: 0.5% Pd/γ-Ga_2O_3 particles.

6.2.3 Comparison with TiO_2 based catalysts

A comparative study has been carried out with commercial TiO_2 P25, which is used as

a benchmark reference in many photocatalytic applications, doped with 1 wt% metal. From the results in Table 6.5, it shows that the catalytic performance of TiO_2 P25 doped with metals is generally better (apart from the Ag doped sample) than the corresponding commercial Ga_2O_3 catalysts. The difference in photocatalytic activities could be related to various degree of electron transfer from the semiconductor to the dopant metal. As TiO_2 has a bandgap of around 3.2 eV, it might be better excited by a longer wavelength (350 nm was chosen, with a comparison of using 253.7 nm UV included in Table 6.5). In addition, it is noticed from the table that the Pt metal shows a better activity on TiO_2. But in the case of Ga_2O_3, Pd appears to work better than Pt, suggesting a stronger interaction between Pd and Ga_2O_3. Pure TiO_2 shows very poor performance (i.e. 90.6 μmol H_2), compared to pure Ga_2O_3 particles (2038.4 μmol H_2).

Table 6.5 Methanol photodecomposition on commercial β-Ga_2O_3 and commercial TiO_2 P25 catalysts doped with various metals (1 wt% metal for each catalyst; reaction time: 5 hours; the UV at 253.7 nm, unless indicated)

Catalysts	H_2 (μmol)	CO_2 (μmol)
1% Pd/β-Ga_2O_3 commercial	3005.1	10.8
1% Pt/β-Ga_2O_3 commercial	2132.4	15.1
1% Pd/TiO_2 P25	4920.3	32.0
1% Pd/TiO_2 P25 (350 nm UV)	5090.2	60.9
1% Pt/TiO_2 P25 (350 nm UV)	5687.6	135.9
1% Ag/TiO_2 P25 (350 nm UV)	527.2	N/A
1% Cu/TiO_2 P25 (350 nm UV)	3270.8	17.5
Pure TiO_2 P25 (350 nm UV)	90.6	0.8

6.3 Characterizations and discussions

In order to gain a fundamental understanding about photocatalytic activity and shape relationship of Ga_2O_3, various techniques including PXRD, TEM, PL & TRPL, ssNMR, EPR, Raman and UV-Vis spectroscopy were conducted. Results and discussions are presented in the following sections.

6.3.1 PXRD

The powder X-ray diffractograms of 0.5% Pd doped Ga_2O_3 of different shapes (i.e. rod, plate and particle forms) are shown in Figure 6.4 (a) and (b). 0.5% Pd doped samples were chosen for the PXRD study because they represented the best

photocatalytic performance for each shape. It can be seen from the Figure 6.4 (a) that there is no observable Pd peak, indicating that the Pd particles are smaller than ca. 3 nm in size. Figure 6.4 (b) also reveals that the catalysts are stable and maintain the original structure after 5 hours of light exposure. Figure 6.4 (c) also shows no apparent Pd peak of γ-Ga_2O_3 particles with different Pd loadings until 5% Pd, where two small but distinctive Pd peaks ((111) and (220)) can be detected. This result is similar to those of doped rod form Ga_2O_3 as discussed in Chapter 5. From a PXRD perspective, the plate form Ga_2O_3 appears to show a better Pd dispersion than those of rod and particle forms (no Pd peak even at 5% loading), due to the stronger MSI (Figure 5.1).

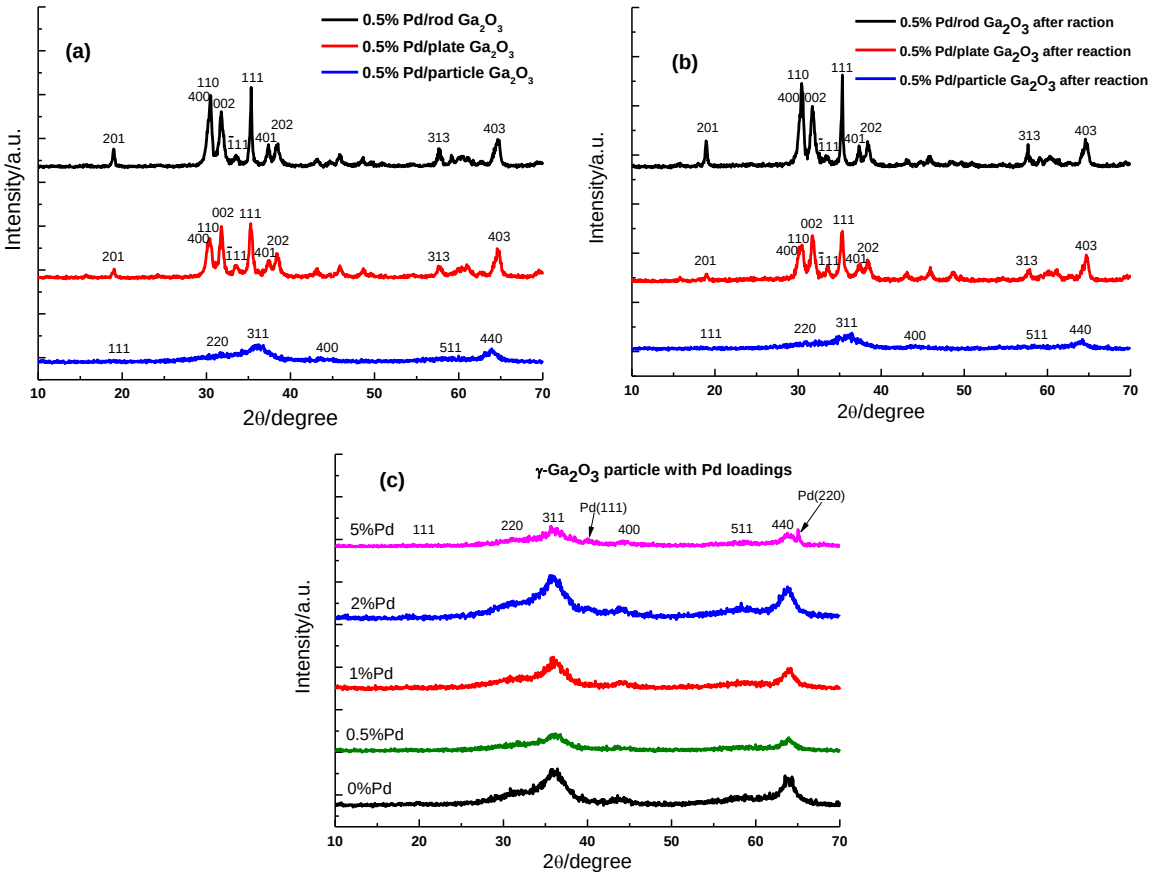

Figure 6.4 PXRD patterns of 0.5% Pd doped Ga_2O_3 before (a) and after (b) reaction; PXRD patterns of particle Ga_2O_3 with Pd loadings before reaction (c).

6.3.2 TEM

TEM analysis was also performed on 0.5% Pd doped Ga_2O_3 for all the three morphologies. The images of a typical 0.5% Pd/Ga_2O_3 rod sample are shown in Figure 6.5 (a)-(d). The small dots representing doped Pd clusters/nanoparticles are observed along the edges of rod shape particles. The enlarged image in the Figure 6.5 (b) clearly reveals that the Pd clusters/nanoparticles are well dispersed on a Ga_2O_3 rod surface and with the sizes ranging from 1-8 nm. A typical high resolution TEM image obtained from the edge of the rod (Figure 6.5 (c)) reveals the fringes of the (110) crystal facet (with d-spacing of 2.94 Å) of Ga_2O_3 rod, which are perpendicular to the rod growth direction [110] as previously reported. The results suggest that the rod grows along the [110] direction and the majority of surfaces identified on the Ga_2O_3 rods are (111) and (110) non-polar facets. Figure 6.5 (d) is a high resolution image from the same region, with the (110) surface identified. In addition, an isolated Pd nanoparticle can be clearly seen, but the lattice fringes of Pd particle are not observed.

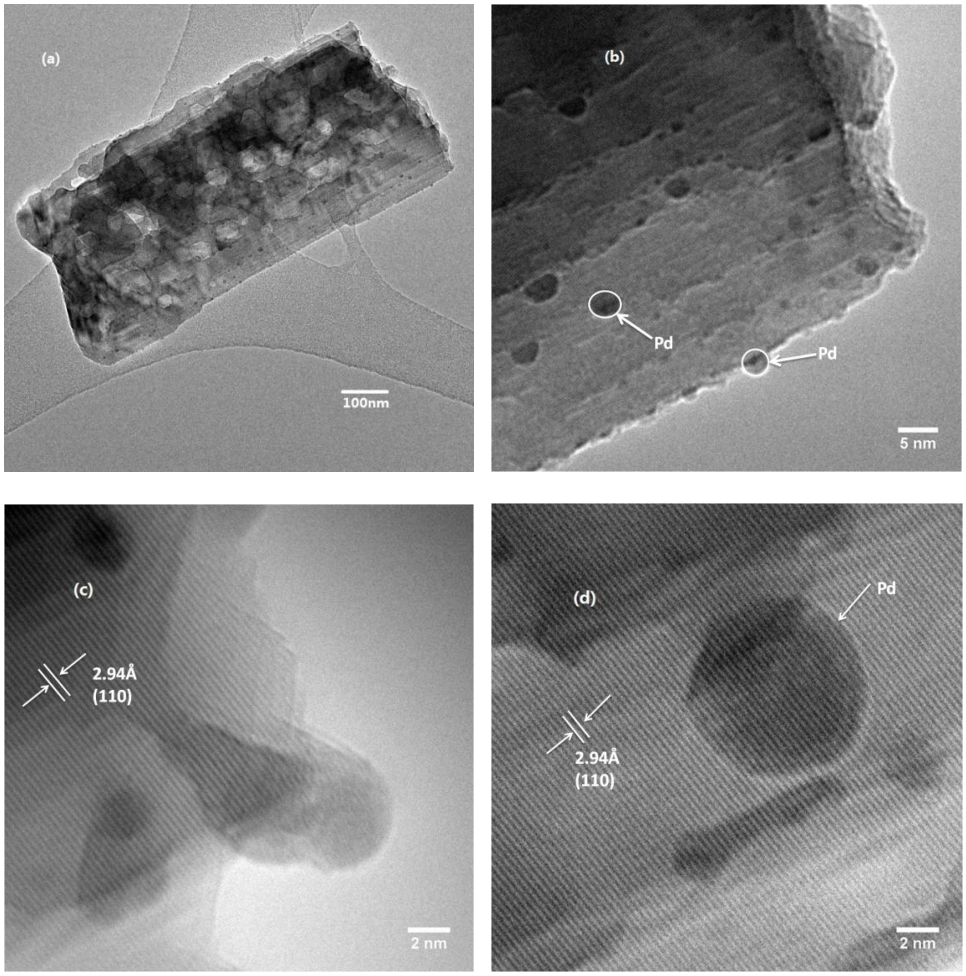

Figure 6.5 TEM image (a) and enlarged image (b) of 0.5% Pd/rod Ga_2O_3. Typical high resolution TEM images of the edges of 0.5% Pd/rod Ga_2O_3 ((c), (d)).

The images presented in Figure 6.6 ((a) and (b)) reflect the structure and morphology of the 0.5% Pd doped plate form Ga_2O_3 catalyst. Previous analysis indicated that the majority of the plate form was rhombic shape with an average diameter of around 150-200 nm. After the Pd doping, some of the plates aggregated, but the individual rhombic particles are still observable, as shown in Figure 6.6 (a). Pd clusters/nanoparticles are seen to be well dispersed on Ga_2O_3 plate surfaces (Figure 6.6 (b)) after the Pd deposition, with the Pd metal sizes ranging from 1-5 nm at the 0.5% Pd loading. The smaller Pd size is attributed to the reduced aggregation by the

SMSI between Pd and the (002) surface of the plate form Ga_2O_3. A representative high resolution TEM image from the plate edge (Figure 6.6 (c)) shows the observed fringes of (002) crystal facet. This more open surface is dominant in population on the plate Ga_2O_3, which agrees well with previous TEM analysis. Pd particles can also be seen on the edges of plate form Ga_2O_3 in this HRTEM.

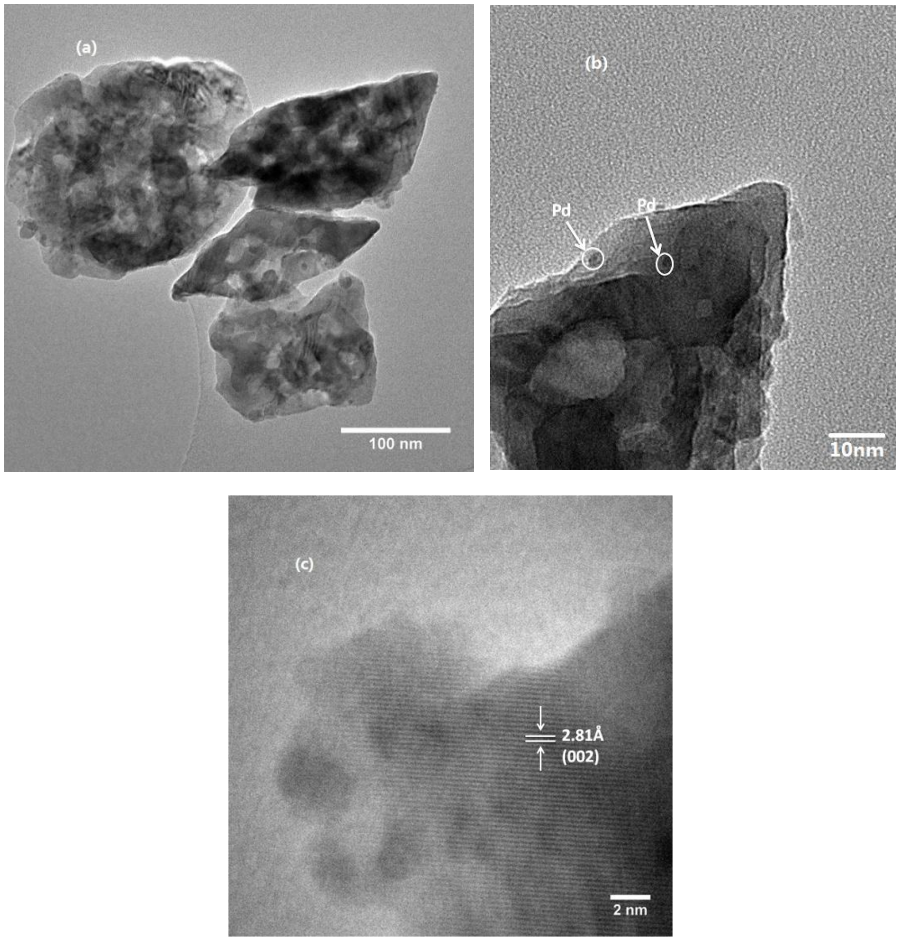

Figure 6.6 TEM image (a) and enlarged image (b) of 0.5% Pd/plate Ga_2O_3. A representative high resolution TEM image near the edge of 0.5% Pd/plate Ga_2O_3 (c).

Figure 6.7 ((a) and (b)) depicts the images of γ-Ga_2O_3 particles with 0.5% Pd deposition. The average particle size of this form of Ga_2O_3 is small, and the particles are homogenously dispersed across the whole field of the imaging area. From Figure

6.7 (a), it can be seen that the particles of the 0.5% Pd/Ga_2O_3 are of about 5 nm in size, which agrees with our previous TEM analysis of the pure Ga_2O_3 particles. Although preliminary diffraction experiments suggested that the Ga_2O_3 particle had a cubic structure, but under the solvothermal synthetic conditions, this growth rate of this particle was greatly inhibited by the presence of a capping agent, and thus produced very small and low crystalline (nearly amorphous in some cases) particles. Because the particle size of the Ga_2O_3 particles is comparable with Pd, it is not easy to differentiate them from each other. The fact of small size and poor crystallinity of this sample is consistent with the XRD result.

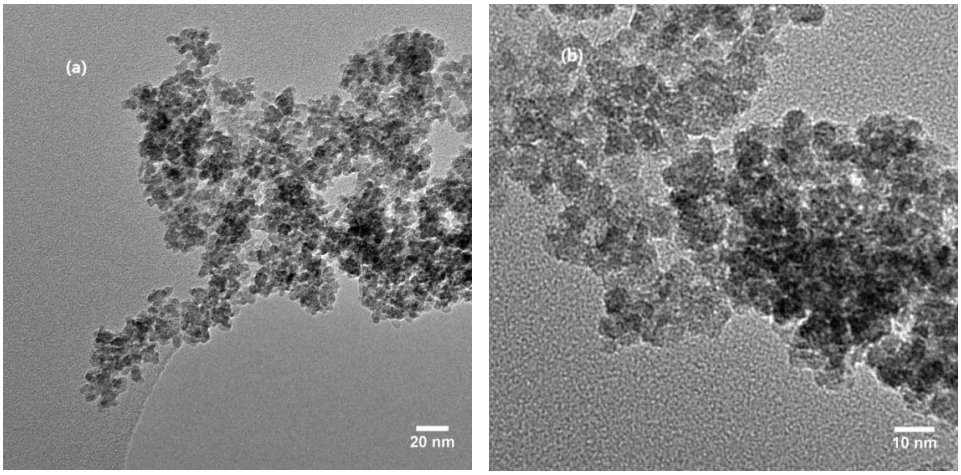

Figure 6.7 TEM image (a) and enlarged image (b) of 0.5% Pd/particle Ga_2O_3.

6.3.3 EPR

The electron paramagnetic resonance study was carried out on the three forms of Ga_2O_3. Figure 6.8 (a)-(c) give the typical single integrated EPR profiles (i.e. absorption patterns). From the characterization, it is found that the rod Ga_2O_3 gives a g value at 2.20 and the plate at 2.30. These similar values suggest the deep trapped

unpaired electrons from oxygen defect sites near the valence band (O_2^- acts as an electron acceptor when an O_2 molecule from air adsorbs on oxygen vacancy).[10,15] Notice that only the plate form of Ga_2O_3 gives a distinctive signal with a g value of 1.96, which is attributed to shallow trapped donor defects near the conduction band. The presence of such donor defects clearly reflects the significant occupancy of excited electrons in the conduction band. In contrast, for the particle Ga_2O_3, it shows a much weaker EPR signal than the other two materials. There is only a small, symmetric absorption peak centered at 3340 G with a g value of 2.0 identified (Figure 6.8 (c)). This value is again derived from the deep trapped unpaired electrons by oxygen defects and similar to those values of the rod and plate Ga_2O_3. The slight difference in the g values suggests the chemical environments of these unpaired electrons are different from each other and thus further understanding with modeling of the g value position and intensity may give important information. However, this study has not yet been conducted before the thesis submission due to other priorities. On the other hand, quantitative analysis of the EPR signals of the 3 Ga_2O_3 based materials without Pd revealed that the number of unpaired electrons in each case was significantly different. The Ga_2O_3 particle gave the spin counts of 2.337×10^{15}/mg or 2.232×10^{15}/mm^3, which was much lower compared to either the rod (2.076×10^{16}/mg or 1.055×10^{16}/mm^3) or plate form (4.728×10^{16}/mg or 3.402×10^{16}/mm^3) Ga_2O_3.

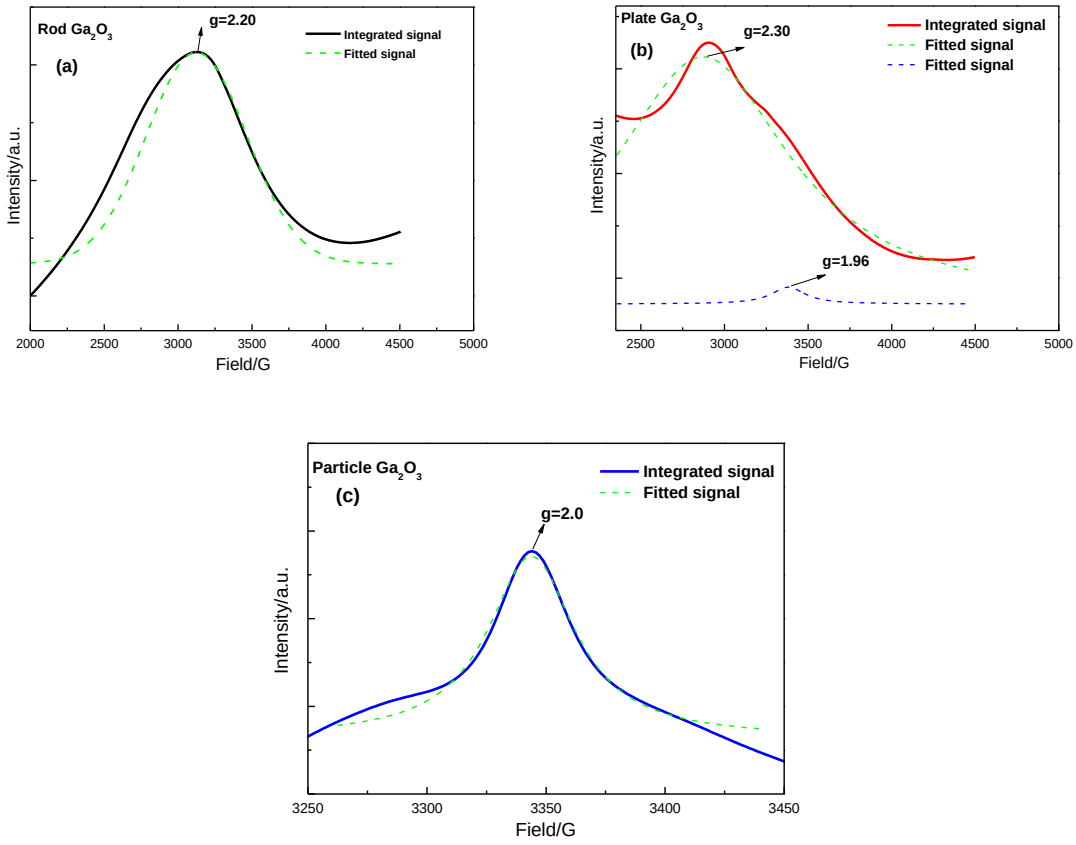

Figure 6.8 The absorption EPR data of rod (a), plate (b) and particle (c) forms Ga_2O_3.

6.3.4 Raman spectroscopy

All the Ga_2O_3 and Pd doped samples were characterized by Raman spectroscopy to probe their structural properties and the results are shown in Figure 6.9 (a)-(c). As for the three pure Ga_2O_3 samples, the rod and plate forms exhibit characteristic Raman active modes which were discussed in detail in Chapter 4. The particle form does not show any lattice vibration mode, indicative of poor crystallinity, which cannot provide a long range order to generate the Raman peaks. For all the three Ga_2O_3, it is interesting to note that the Raman peaks decline rapidly with the addition of Pd and according to its loadings. From the figures, the progressive attenuation of the 200 cm^{-1}

Raman peak size on rod and plate forms can be clearly seen. In this regard, metal doping undoubtedly affects the Ga_2O_3 Raman active modes. Based on the Raman scattering mechanism[16] and the semiconductive properties of Ga_2O_3, one possible explanation is that the SMSI between Pd and Ga_2O_3 with electron transfer may affect the fundamental vibration modes of Ga_2O_3 and transitions between their virtual vibration states. The strong quenching effect of Pd to Ga_2O_3 lattice vibrations could have caused the decline or even total disappearance of some characteristic Raman active modes.

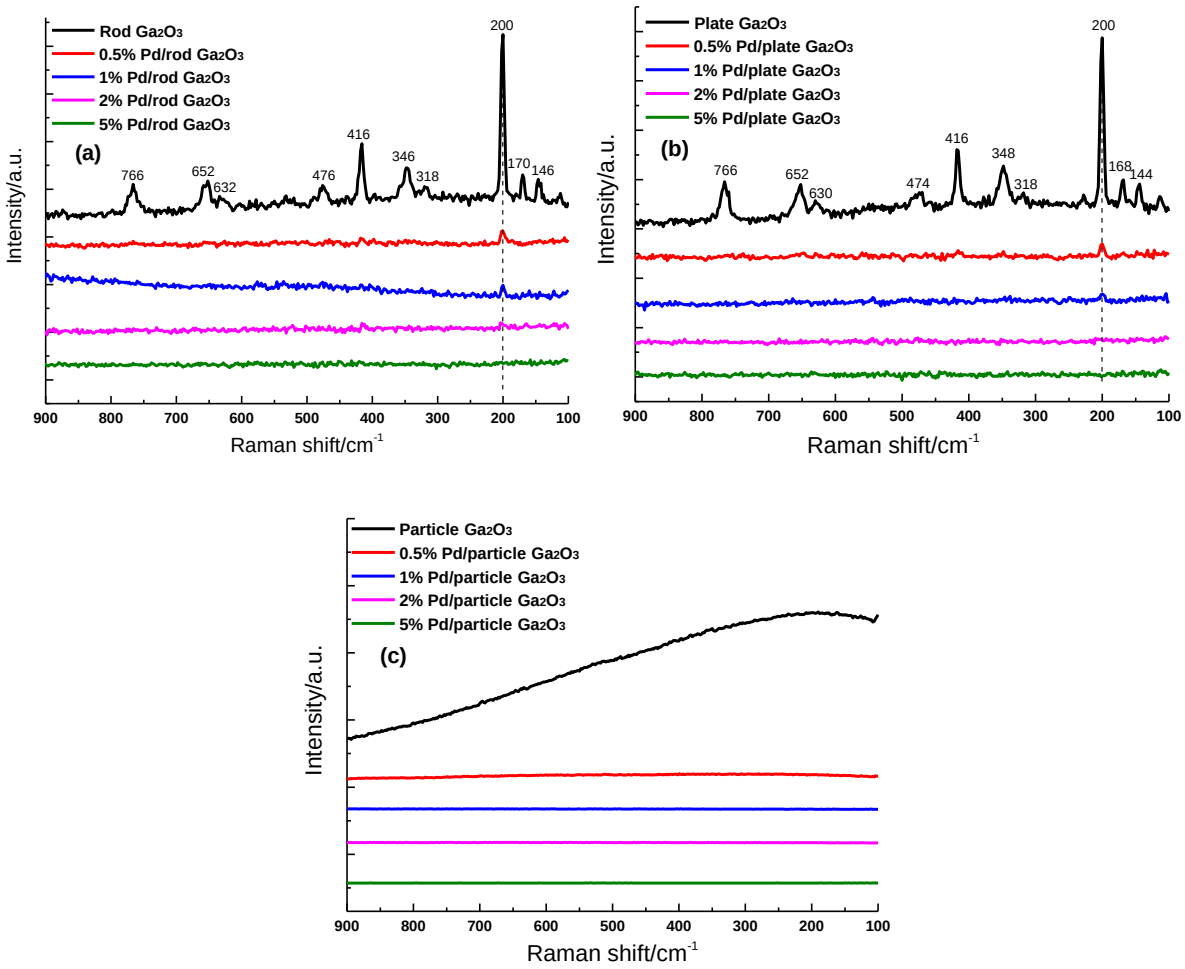

Figure 6.9 Raman spectra of rod (a), plate (b) and particle (c) Ga_2O_3 with Pd loadings.

6.3.5 UV-Visible spectroscopy

UV-Visible absorption spectroscopy was also used to characterize Ga_2O_3 materials with and without Pd doping (Figure 6.10 (a)-(c)). In general, the absorption spectra are similar between the rod and plate form Ga_2O_3 materials, but the small particle Ga_2O_3 shows a slightly higher energy absorption peak. It is because that the average particle size of this form of Ga_2O_3 is much smaller at around 5 nm, accounting for the blue shift of the absorption peak in this case. The bandgaps of these Ga_2O_3 based materials were calculated according to the Kubelka-Munk function[17] and corresponding plots were described in Chapter 4. The derived bandgap values are summarized in Table 6.6. As seen from Figure 6.10 (a)-(c) and Table 6.6 with taken the 0.01eV instrumental error level into account, the bandgap of all forms of Ga_2O_3 with the exception of the plate form do not apparently change with the increase of metal loading until the 5% Pd loading. But the plate form Ga_2O_3 shows an observable progressive peak shift. Such progressive lowering of bandgap by 0.18 eV (5% Pd) might be caused by the stronger MSI between Pd and plate form Ga_2O_3 as compared to the other two forms. Notice that an observable peak at around 300 nm in the particle Ga_2O_3 is thought to arise from absorption by surface organic ligands. A commercial β-Ga_2O_3 powder sample was also measured for comparison and the result is shown in Table 6.6.

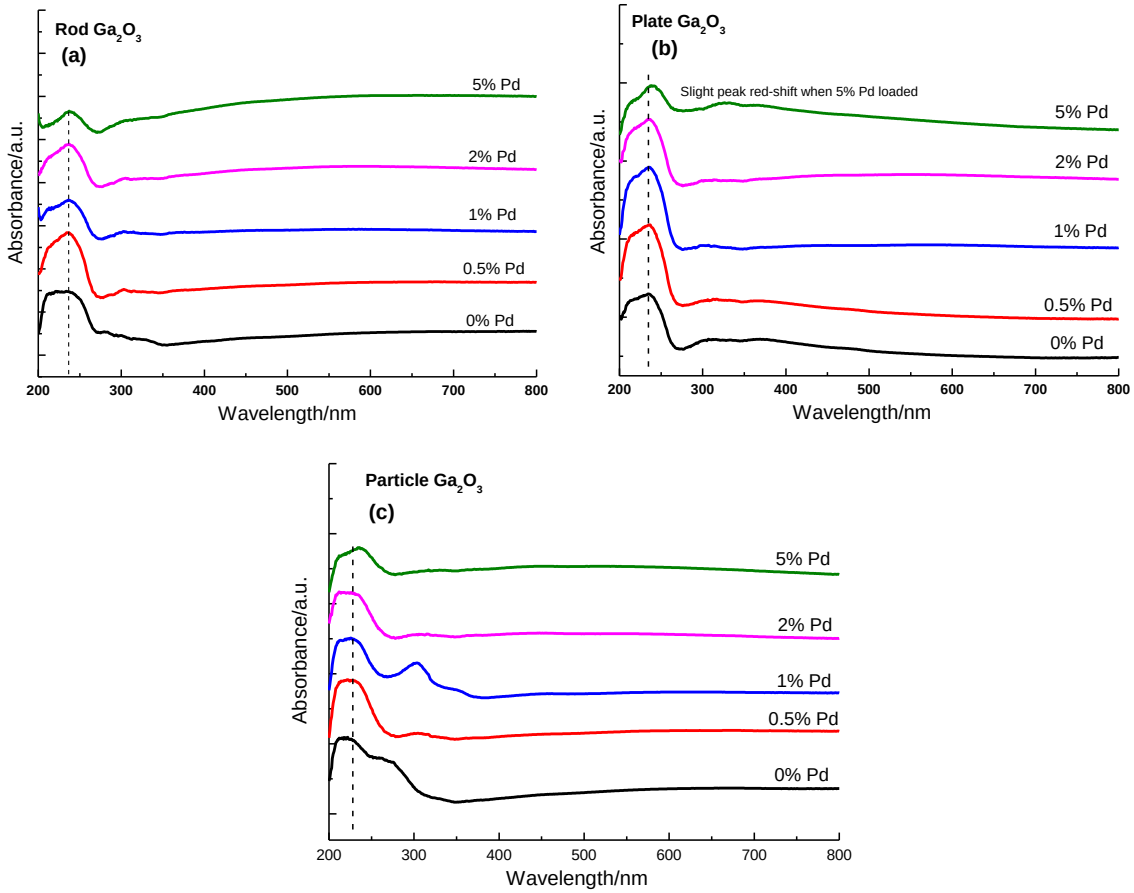

Figure 6.10 UV-Vis spectra of rod (a), plate (b) and particle (c) Ga_2O_3 with Pd loadings.

Table 6.6 Summary of bandgap values of Ga_2O_3 with and without Pd

Samples	Pure (eV)	0.5% Pd (eV)	1% Pd (eV)	2% Pd (eV)	5% Pd (eV)
Rod Ga_2O_3	4.85	4.85	4.85	4.85	4.83
Plate Ga_2O_3	4.87	4.86	4.86	4.85	4.69
Particle Ga_2O_3	5.02	5.02	5.02	5.02	4.92
Commercial Ga_2O_3	4.86	N/A			

6.3.6 ssNMR

The solid state NMR characterization in combination with the use of a chemical probe was carried out to further investigate the surface features of the three morphologically different Ga_2O_3 and the results are shown in Figure 6.11. The probe molecule,

trimethylphosphine (TMP) was employed which can adsorb on Ga_2O_3 surface with its ^{31}P nucleus to give intense signals in ^{31}P NMR spectroscopy. It should be noted that TMP is a basic molecule so that it will selectively adsorb onto a surface Lewis acidic center[18] such as Ga^{3+} ion (TMP has a lone pair of electrons which can form a dative bonding interaction with a vacant orbital of a surface Ga site). From the spectra shown in Figure 6.11, the plate form gives a resonance peak at -51.86 ppm with reference to rod (-45.92 ppm) and commercial Ga_2O_3 (-43.04 ppm). The typical ^{31}P NMR peak of the TMP molecule is at -62 ppm and thus there is a clear reduction in shielding effect to the ^{31}P nuclei causing its downshift due to attachment to the surface Ga^{3+} ion with electron deficiency. Therefore, this molecule can probe the electron density of surface Ga^{3+} ions indirectly, which follows the electron richness order as: plate > rod > commercial sample. Calculations of Bader charge density by DFT have been conducted and the results are shown in Figure 6.12. According to our atomistic models and calculations, there are different surface Ga sites of different coordination numbers. The Ga site with lower coordination number is more electron rich hence giving a higher Bader charge density. It is also anticipated that surface Ga site in close proximity to an oxygen vacancy will also increase its electron density. At this stage, it is not yet able to assign the nature of each individual NMR peak and the broad nature of some peaks may suggest a complex local environment. Nevertheless, notice that all surface Ga sites of the plate form are comparatively more electron rich than those of the rod form with the same coordination number (or defective neighbors), as anticipated from the works mentioned in previous chapters. As a result, the electron

richness order reflected by the NMR chemical shift values could be broadly accounted for. The results are also consistent with the EPR results suggesting the electron richness of the plate form which contains the polar (002) surface. The particle form of Ga_2O_3 shows a very different NMR spectrum from the others. Firstly, the distinctive peak of –62 ppm is due to the physisorption of the TMP molecules (same chemical shift value as the TMP molecule) due to its high surface area (not significant in other samples at room temperature), and the broad peak at -30 ppm is attributed to some highly disordered sites of this sample.

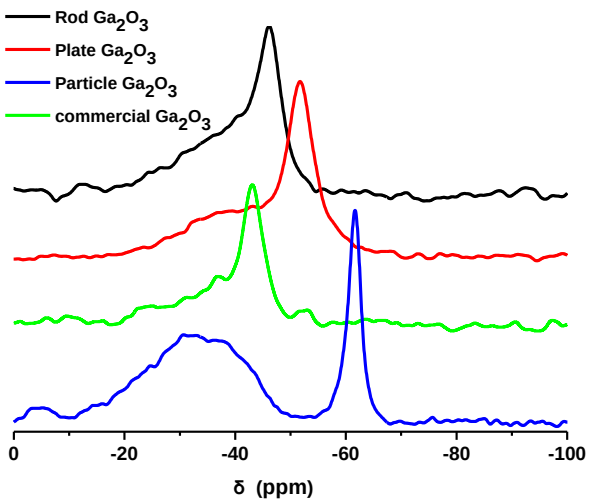

Figure 6.11 ^{31}P ssNMR spectra of four pure Ga_2O_3 samples.

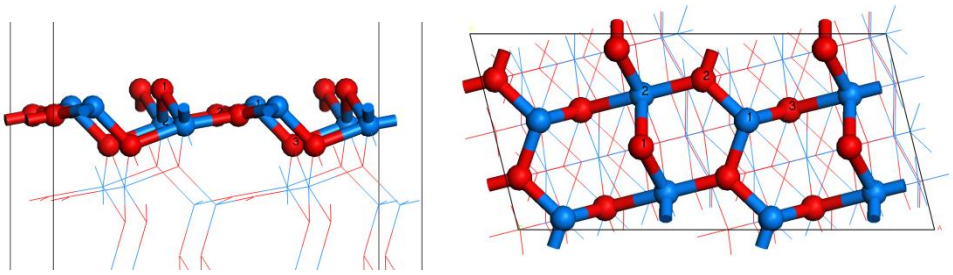

Figure 6.12 (a) The polar Ga_2O_3 (002) with two types of surface Ga ions, namely, octahedral gallium ions and tetrahedral gallium ions; the calculated Bader charge densities are: Ga1 (oct) 11.1862; Ga2 (tetra) 11.2344. The average Bader charge density of Ga_2O_3 (002) is 11.2103 (left: sideview; right: topview; blue: Ga ion; red: O ion).

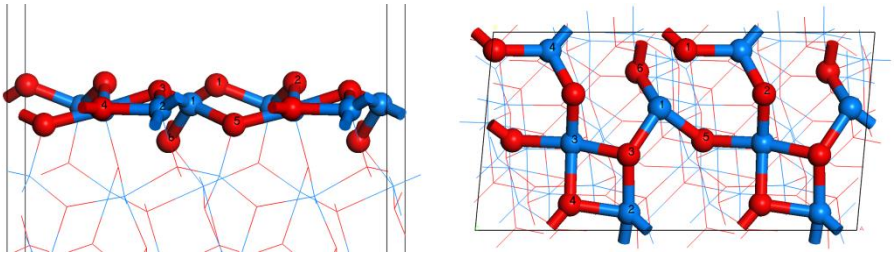

Figure 6.12 (b) The non-polar Ga_2O_3 (111) with four types of surface Ga ions, namely, octahedral gallium ions and tetrahedral gallium ions; the calculated Bader charge densities are: Ga1 (tetra) 11.2282; Ga2 (oct) 11.1775; Ga3 (oct) 11.1575; Ga4 (tetra) 11.2074. The average Bader charge density of Ga_2O_3 (111) is 11.1926 (left: sideview; right: topview; blue: Ga ion; red: O ion).

6.3.7 PL and TRPL spectroscopy

To explore the mechanism, in particular the influence of Ga_2O_3 morphology and interplay between Ga_2O_3 and Pd in photocatalytic activity for the H_2 evolution, static photoluminescence (PL) and time-resolved PL (TRPL) spectroscopy were employed. Figure 6.13 displays static PL spectra and the corresponding PL decay profiles

obtained from TRPL measurement (excitation at 255 nm) for rod, plate, and particle Ga_2O_3 without or with varied levels of Pd loading. TRPL spectra recorded at representative time intervals after the photo-excitation are given in Figure 6.15. It is evident from Figure 6.13 (a)-(c) that all the samples examined exhibit broad emission (~300-650 nm) with λ_{max} at ~470 nm arising due to the recombination of a trapped excited electron by a donor formed by an oxygen vacancy and a hole from an acceptor formed by a gallium ion vacancy or a pair of charged vacancies (gallium-oxygen).[6,19-21] The intensity of the PL, when measured by the integrated area of the TRPL spectra (300-650nm), features decay in extensive timescale spanning tens of μs after the photo-excitation (Figure 6.13 (d)-(f)). Notably, for Ga_2O_3 in all the three shapes, the PL is significantly quenched in the presence of Pd: with the addition of Pd, the intensities of static PL decreases (Figure 6.13 (a)-(c)) and the decay of PL takes place in faster timescale (Figure 6.13 (d)-(f)). This dynamic quenching of PL is most obvious from pure Ga_2O_3 to Ga_2O_3 with 0.5% Pd; higher levels of Pd loading quenches further the PL but to a lesser degree. This quenching effect is thought to be the direct result of the electron transfer from the electrons in the conduction band of Ga_2O_3 to Pd (non-radiative process).

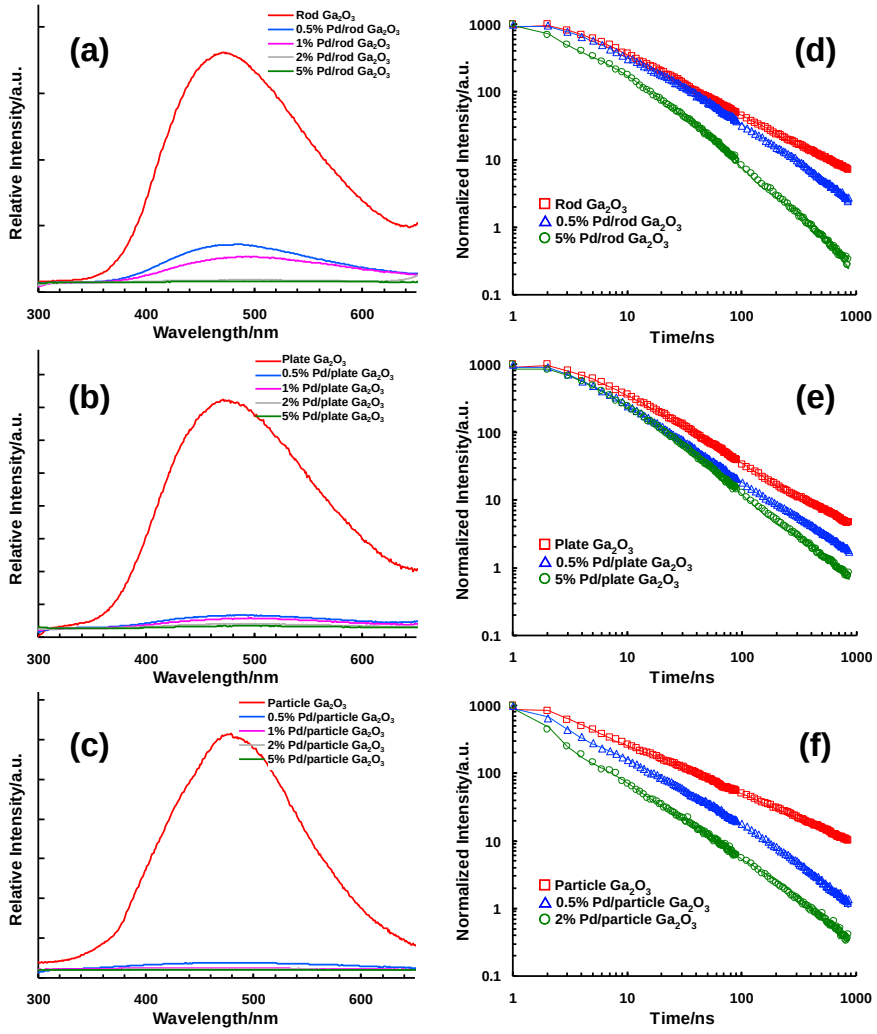

Figure 6.13 Static photoluminescence (PL) spectra ((a)-(c)) and PL kinetic decay curves ((d)-(f)) obtained with excitation at 255 nm in solid state of Ga_2O_3 rod ((a), (d)), plate ((b), (e)), and particle ((c), (f)) without or with varied Pd loadings.

Analysis of PL decay profiles for all the samples investigated revealed complex dynamics that required fitting with multi-exponential functions. This combined with the progressive red-shift as an increase of delay time of the TRPL wavelengths (Figure 6.15) indicates (i) complex energy structure for the donor and/or acceptor states and (ii) involvement of radiative as well as non-radiative processes during the relaxation of carrier states. Figure 6.14 compares the PL decay profiles for pure Ga_2O_3

in the three morphologies and those containing 0.5% or higher (2% or 5%) level of Pd loading. The time constants and related amplitudes derived from the fitting procedure are listed in Table 6.7. As a common feature for all the samples, the decay of PL is dominated (~61 to 89%) by a fast component (τ_1~0.6 to 3.8 ns) and there is a modest contribution (~11 to 37%) due to several to tens of ns components (τ_2~4.7 to 16 ns; τ_3~24 to 83 ns) as well as a small fraction (< ~2%) from a long-lived component with hundreds of ns time constant (τ_4~155 to 674 ns).

Compared to the samples with Pd, the pure Ga_2O_3 in all three forms feature much slower time constants especially the τ_3 and the long-lived component τ_4 with the τ_4 bearing more percentage contribution to the overall decay. It is worth noting that, for pure Ga_2O_3, the τ_3 and τ_4 follow the order (inset in Figure 6.14 (a)): particle (τ_3/τ_4~83/674 ns) > rod (τ_3/τ_4~74/612 ns) > plate (τ_3/τ_4~66/600 ns). This is in line with the order observed for the relative yield of static PL by the three Ga_2O_3 (Figure 6.16). The decrease in PL intensity from γ-Ga_2O_3 to β-Ga_2O_3 agrees with the literature.[22] Given that plate Ga_2O_3 holds the highest concentration of defect sites (EPR and ssNMR studies), the PL and TRPL data here would suggest that the defects in plate Ga_2O_3 accelerate the non-radiative in relation to radiative decay of the carrier states.

On the other hand, the markedly faster PL decay showed by samples containing Pd is clear evidence for the presence of extra non-radiative decay which can be attributed to rapid transport of excited mobile electrons from Ga_2O_3 to Pd. This electron transfer, referring to our previous studies,[10,15,23] facilitates a higher catalytic activity, rendering

an effective switch of the major radiative relaxation to a faster catalytic process of the carriers which in the current case is to promote H_2 evolution from methanol photodecomposition. The photo-induced electron transfer may thus constitute a key factor for the pronounced improvement in the activity showed by the Pd loaded (0.5%) Ga_2O_3 compared to the pure Ga_2O_3. In addition, it is interesting to note the following trends in the carrier lifetime for Ga_2O_3 in the three forms with varied levels of Pd loading. When measured by the average time constant (τ_{av}, Table 6.7), the carrier lifetime follows rod (~15.2 ns) > plate (~10.3 ns) > particle (~6.0 ns) for the samples with 0.5% Pd (Table 6.7 and the inset in Figure 6.14 (b)) and plate (~9.2 ns) > rod (~4.2 ns) > particle (~1.9 ns) for the 5% (rod and plate) or 2% (particle) Pd/Ga_2O_3 (Table 6.7 and inset in Figure 6.14 (c)). Such trends are respectively in the same order as the relative activity showed by samples with the corresponding Pd loading towards the H_2 evolution (the activity was rod > plate > particle for 0.5% Pd loading, and changed to plate > rod > particle for 5% or 2% Pd loading). This seems to imply that, apart from the electronic interaction (electron transfer from Ga_2O_3 to Pd), an adequately long carrier lifetime is also important for promoting this photocatalytic performance. Within this context, the general decrease in the activity exhibited by samples with higher level (> 0.5%) of Pd could be due to the shorter carrier lifetimes. In particular, the less shortening in the lifetime upon increase of Pd loading showed by the plate (10.3/9.2 ns for 0.5%/5% Pd loading) than rod Ga_2O_3 ((15.2/4.2 ns for 0.5%/5% Pd loading) might account for the reversed order in the activity displayed by the two forms with low (0.5%) *vs* high (5%) level of Pd loading.

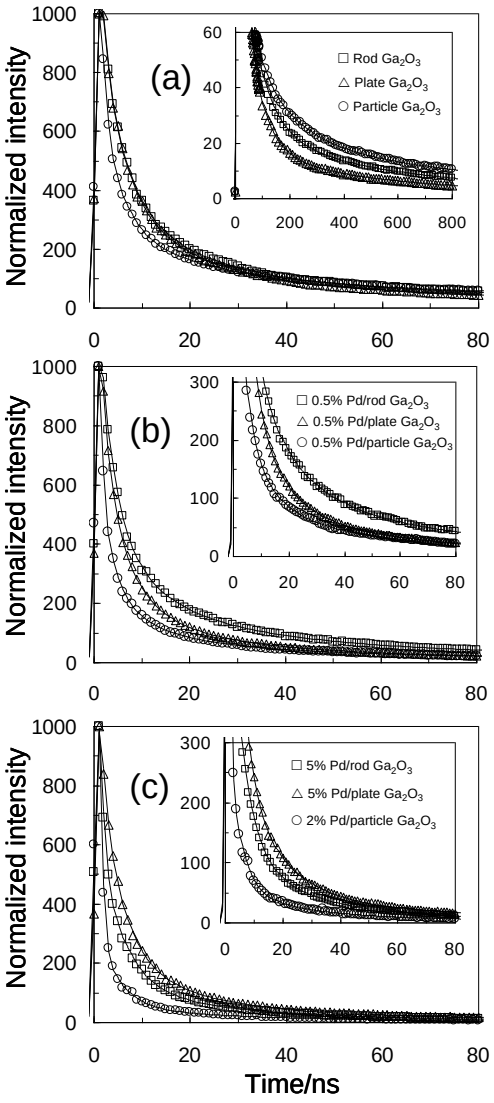

Figure 6.14 Comparison of luminescence decay profiles obtained with 255 nm excitation of solid state Ga_2O_3 rod (□), plate (Δ) and particle (○) without (a) or with increasing Pd loadings ((b),(c)). The solid lines are the fittings of experimental data.

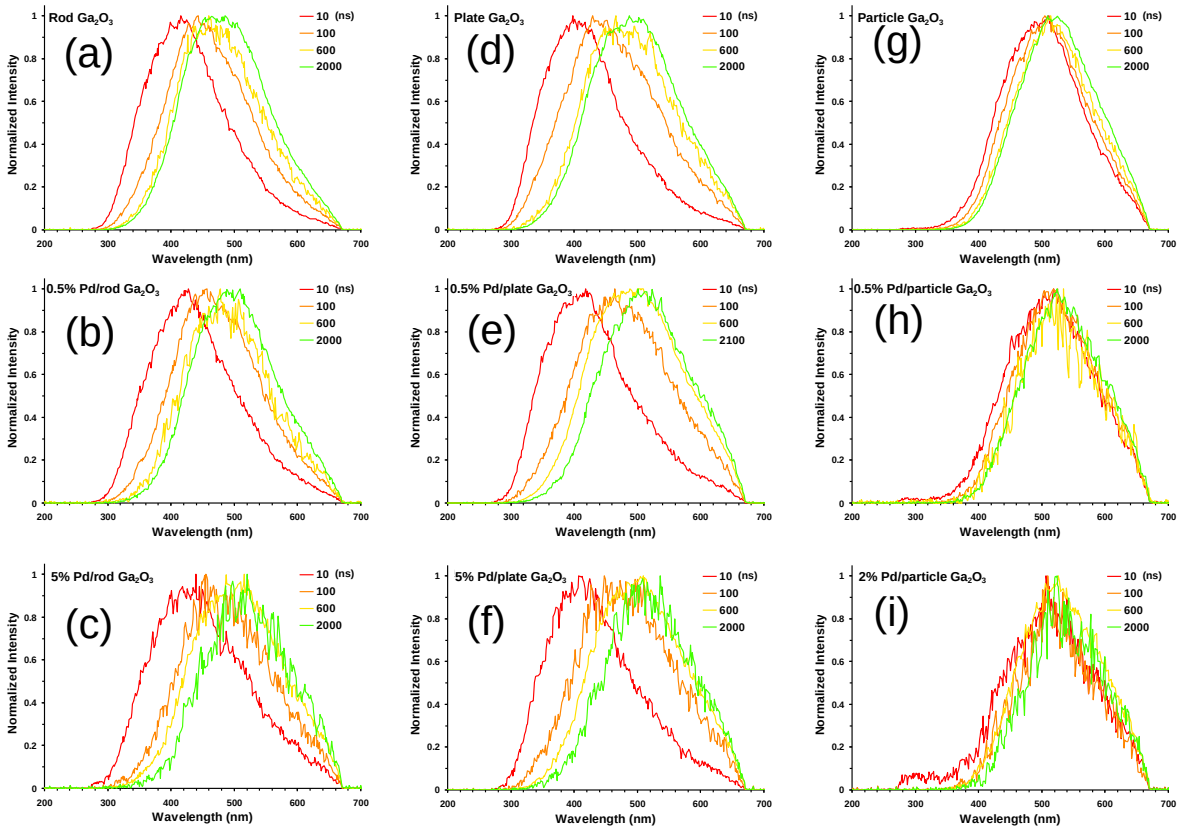

Figure 6.15 Time-resolved photoluminescence spectra recorded at the denoted time intervals after excitation at 255 nm for rod ((a)-(c)), plate ((d)-(f)) and particle ((g)-(i)) Ga_2O_3 without and with varied Pd loadings.

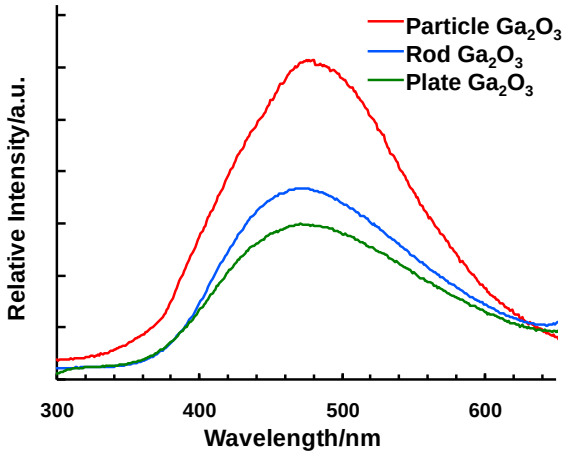

Figure 6.16 Static photoluminescence spectra recorded with 255 nm excitation of solid state Ga_2O_3 in rod, plate and particle forms.

Table 6.7 Kinetic analysis of ns-TRPL decay profiles (τ: time constant; a: associated amplitude)

	τ_1/ns	(a_1)	τ_2/ns	(a_2)	τ_3/ns	(a_3)	τ_4/ns	(a_4)	τ_{av}/ns
Rod Ga_2O_3	3.7	(0.612)	14.9	(0.295)	74	(0.073)	612	(0.018)	23.1
Plate Ga_2O_3	3.8	(0.645)	15.8	(0.269)	66	(0.073)	600	(0.012)	18.8
Particle Ga_2O_3	2.3	(0.725)	15.5	(0.195)	83	(0.058)	674	(0.020)	23.3
0.5%Pd/rod Ga_2O_3	3.3	(0.680)	16.0	(0.238)	62	(0.067)	350	(0.014)	15.2
0.5%Pd/plate Ga_2O_3	2.8	(0.676)	10.6	(0.250)	42	(0.064)	334	(0.009)	10.3
0.5%Pd/particle Ga_2O_3	1.0	(0.773)	7.2	(0.175)	42	(0.045)	300	(0.007)	6.0
5%Pd/rod Ga_2O_3	0.8	(0.685)	5.6	(0.260)	30	(0.052)	241	(0.003)	4.2
5%Pd/plate Ga_2O_3	2.9	(0.645)	9.9	(0.280)	39	(0.069)	332	(0.005)	9.2
2%Pd/particle Ga_2O_3	0.6	(0.885)	4.7	(0.093)	24	(0.019)	155	(0.003)	1.9

6.4 Conclusion

In summary, the shape effect of Ga_2O_3 (i.e. rod, plate and particle forms) and their Pd doped samples has been studied for the methanol photodecomposition reaction to H_2. The photocatalytic results and characterizations suggested a complex nature of this reaction, which was not only dependent on the shape of catalyst particle but also on other factors such as crystallinity, type of metal dopant and its concentration.

First, for pure Ga_2O_3, the plate form with predominant polar (002) surface was found to be more active for methanol photodecomposition to H_2 than the particle form and the rod form with non-polar surfaces (plate > particle > rod) in contradiction to their difference in the order of BET surface area. PXRD, UV-Vis and Raman have indicated that the internal bulk feature was likely to be identical for these three forms, which implied that the surface feature was clearly an overwhelming factor. The EPR

and ssNMR indeed suggested that the plate form with the (002) polar surface was more electron rich and more defective than the other forms to account for the activity difference. Based on all these results, it was suggested that such defective and charge separated surface feature (polar charge separation) would promote the non-radiative catalytic recombination of excitons in relation to the radiative recombination.

The addition of Pd on Ga_2O_3 of different shapes has shown some very interesting responses. First, the introduction of Pd metal on Ga_2O_3 should provide catalytically more active sites for enhanced hydrogen production and methanol oxidation. However, the exciton lifetime was another important contrasting factor that needed to be considered. The longer lifetime could facilitate a more efficient 'sites separation' for simultaneous photocatalytic reduction and oxidation reactions to take place. Clearly, when Pd was introduced on Ga_2O_3, there was also a rapid charge transfer due to the formation of Schottky junctions between metal and conduction band (electron transfer from excited electrons of oxide to metal) as well as metal and valance band (electron transfer from metal to the holes of oxide). Thus, the electron rich Fermi status of the metal phase could rapidly neutralize the generated excitons upon irradiation, as evidenced by the Raman and TRPL (ns timescale with quenching signals). As a result, there were clear trends of increasing quenching (PL signal attenuation) and decreasing exciton lifetime (τ_{av}) at increasing Pd content for each form of Ga_2O_3. Therefore, the plate form with electron richer surface would encourage an effective electron transfer leading to the formation of smaller Pd particles at higher dispersion on this surface indicative of a SMSI as shown by PXRD and TEM. But at higher Pd loading, the

plate form appeared to sustain a longer lifetime for photocatalysis (i.e. the decay for exciton lifetime was much slower as compared to other forms). Overall, the introduction of metal sites to promote photocatalysis at the interface could be offset by shortening of exciton lifetime and the extent of photocatalysis would depend on the type of catalyst surface and crystallinity. In the future, more detailed mechanistic studies should be conducted to lead to the rational design of effective photocatalysts for this important reaction.

6.5 References

1. X. Chen, S. Shen, L. Guo and S. S. Mao, *Chem. Rev.*, 2010, **110**, 6503-6570.
2. A. Zuttel, A. Borgschulte and L. Schlapbach, *Hydrogen as a Future Energy Carrier,* Wiley-VCH: Weinheim, Germany, 2008.
3. N. Z. Muradov and T. N. Veziroglu, *Int. J. Hydrogen Energy,* 2008, **33**, 6804-6839.
4. H. J. Choi and M. Kang, *Int. J. Hydrogen Energy,* 2007, **32**, 3841-3848.
5. M. S. Park and M. Kang, *Mater. Lett.*, 2008, **62**,183-187.
6. S. Yan, L. Wan, Z. Li, Y. Zhou and Z. Zou, *Chem. Commun.*, 2010, **46**, 6388-6390.
7. Y. Hou, L. Wu, X. Wang, Z. Ding, Z. Li and X. Fu, *J. Catal.*, 2007, **250**, 12-18.
8. R. Narayanan and M. A. El-Sayed, *J. Phys. Chem. B*, 2005, **109**, 12663 – 12676.
9. A. McLaren, T. Valdes-Solis, G. Li and S. C. Tsang, *J. Am. Chem. Soc.*, 2009, **131**, 12540 – 12541.
10. F. Liao, Y. Huang, J. Ge, W. Zheng, K. Tedsree, P. Collier, X. Hong and S. C. Tsang, *Angew. Chem. Int. Ed.*, 2011, **50**, 2162-2165.
11. K. Domen, A. Kudo, A. Shinozaki, A. Tanaka, K. I. Maruya and T. Onishi, *J. Chem. Soc., Chem. Commun.,* 1986, 356-357.
12. W. C. Lin, W. D. Yang, I. L. Huang, T. S. Wu and Z. J. Chung, *Energy & Fuels*, 2009, **23**, 2192-2196.
13. Y. Sakata, Y. Matsuda, T. Nakagawa, R. Yasunaga, H. Imamura and K. Teramura, *ChemSusChem,* 2011, **4**, 181-184.
14. J. W. Park and M. Kang, *Int. J. Hydrogen Energy*, 2007, **32**, 4840-4846.

15. F. Liao, Z. Zeng, C. Eley, Q. Lu, X. Hong and S. C. E. Tsang, *Angew. Chem. Int. Ed.*, 2012, **51**, 5832-5836.
16. F. Fan, Z. Feng and C. Li in *Characterization of Solid Materials and Heterogeneous Catalysts,* ed. M. Che and J. C. Vedrine, Wiley-VCH Verlag GmbH & Co. KGaA., 2012, Volume 1, pages 49-87.
17. F. C. Jentoft in *Characterization of Solid Materials and Heterogeneous Catalysts,* ed. M. Che and J. C. Vedrine, Wiley-VCH Verlag GmbH & Co.KGaA., 2012, Volume 1, pages 89-147.
18. H. M. Kao and C. P. Grey, *Chem. Phys. Lett.*, 1996, **259**, 459-464.
19. T. Wang, S. S. Farvid, M. Abulikemu and P. V. Radovanovic, *J. Am. Chem. Soc.*, 2010, **132**, 9250-9252.
20. L. Binet and D. Gourier, *J. Phys. Chem. Solid,* 1998, **59**, 1241-1249.
21. T. Harwing and F. Kellendonk, *J. Solid State Chem.*, 1978, **24** , 255-263.
22. T. Wang and P. V. Radovanovic, *J. Phys. Chem. C,* 2011, **115**, 18473-18478.
23. X. Zhou, J. Qu, F. Xu, J. Hu, J. S. Foord, Z. Zeng, X. Hong and S. C. E. Tsang, *Chem. Commun.*, 2013, **49**, 1747-1749.

Chapter 7 Conclusion and perspective

Chapter 7 Conclusion and perspective.....221

7.1 Conclusion 222

7.2 Perspective 224

7.1 Conclusion

Within the scope of this thesis, the shape effects of Pd promoted Ga_2O_3 nanocatalysts have been studied for two important heterogeneous catalytic reactions, namely, methanol synthesis from CO_2 hydrogenation and methanol photodecomposition for H_2 evolution. To the best of our knowledge, this is the first catalytic study regarding the two related areas. Three different shapes of Ga_2O_3 (i.e. rod, plate and particle forms) and their Pd doped catalysts have been synthesized by nano-chemical approaches in the first place.

For the reaction of methanol synthesis from CO_2 hydrogenation, the investigation has been carried out on the shape effect of rod and plate form β-Ga_2O_3 and their Pd doped samples. From the catalytic testing and characterization, it was found that a low indexed (002) polar Ga_2O_3 surface was dominant on the plate form. Such a surface is more unstable hence giving a higher degree of oxygen defects and mobile electrons in the conduction band than those of the non-polar (111) and (110) surfaces on the rod form. It is reported in this thesis that a significant SMSI between the (002) polar Ga_2O_3 surface predominant on the plate form and Pd gave higher metal dispersion and facilitated electron transfer, for higher methanol yield and selectivity in this catalytic CO_2 hydrogenation reaction.

For the reaction of methanol photodecomposition to generate H_2, the investigation has been carried out on the shape effect of all three Ga_2O_3 morphologies (i.e. rod and plate β-Ga_2O_3, and particle γ-Ga_2O_3) and their Pd doped samples. The complex nature of this cascade photocatalytic reaction (non-stoichiometric) was first identified. Despite

the difficulties in understanding the reaction mechanisms for a number of complex reactions, it was interesting to note that, for pure Ga_2O_3, the radiative recombination rate of excitons followed the order: plate > rod > particle. This was in line with the order of the concentration of defect sites (EPR and ssNMR studies) for the three Ga_2O_3 materials. Thus, the highest defect concentration in the plate Ga_2O_3 with polar surface clearly accelerated the non-radiative decay in relation to radiative decay of the carrier states to the greatest extent. Thus, this form of Ga_2O_3 gave the highest photocatalytic H_2 production from methanol. On the other hand, the markedly faster PL decay shown by samples containing Pd was evidence for the presence of extra non-radiative decay which can be attributed to rapid transportation of excited mobile electrons from Ga_2O_3 to Pd. This electron transfer facilitated a further increase in catalytic activity, rendering an effective switch of the major radiative relaxation to a faster catalytic process of the carriers which in the current case was to promote H_2 evolution from methanol photodecomposition. The photo-induced electron transfer might thus constitute a key factor for the pronounced improvement in the activity shown by the Pd loaded (0.5-1.0%) Ga_2O_3 compared to pure Ga_2O_3. Apart from this electronic interaction (electron transfer from Ga_2O_3 to Pd), it was found that an adequately long carrier lifetime was also important for promoting this photo-catalytic performance. The higher content of Pd (>1%) can reduce the photocatalytic activity for H_2 production over the Ga_2O_3 due to shortening of the lifetime of excitons and thus giving an overall volcanic response in activity to increasing Pd content.

7.2 Perspective

With the rapid development of nanotechnology, research activities in heterogeneous catalysis can be boosted to a more fundamental level. A more thorough understanding on surface features of catalysts and advances in elucidation of the mechanisms for various important catalytic reactions in future, will lead to a new era of rational design of highly active and selective catalysts for various industrial applications, to meet more challenges in environment and energy in the future. I believe that the work presented in this thesis may contribute towards the future development in this new area.